

ELECTRON SPECTROSCOPY OF TRANSITION METAL
OVERLAYERS ON LOW-INDEX SILVER AND
COPPER CRYSTAL SURFACES

Graham C. Smith

A thesis submitted to the University of Leicester
for the degree of Doctor of Philosophy

November
1982

UMI Number: U333566

All rights reserved

INFORMATION TO ALL USERS

The quality of this reproduction is dependent upon the quality of the copy submitted.

In the unlikely event that the author did not send a complete manuscript and there are missing pages, these will be noted. Also, if material had to be removed, a note will indicate the deletion.



UMI U333566

Published by ProQuest LLC 2015. Copyright in the Dissertation held by the Author.
Microform Edition © ProQuest LLC.

All rights reserved. This work is protected against
unauthorized copying under Title 17, United States Code.



ProQuest LLC
789 East Eisenhower Parkway
P.O. Box 1346
Ann Arbor, MI 48106-1346

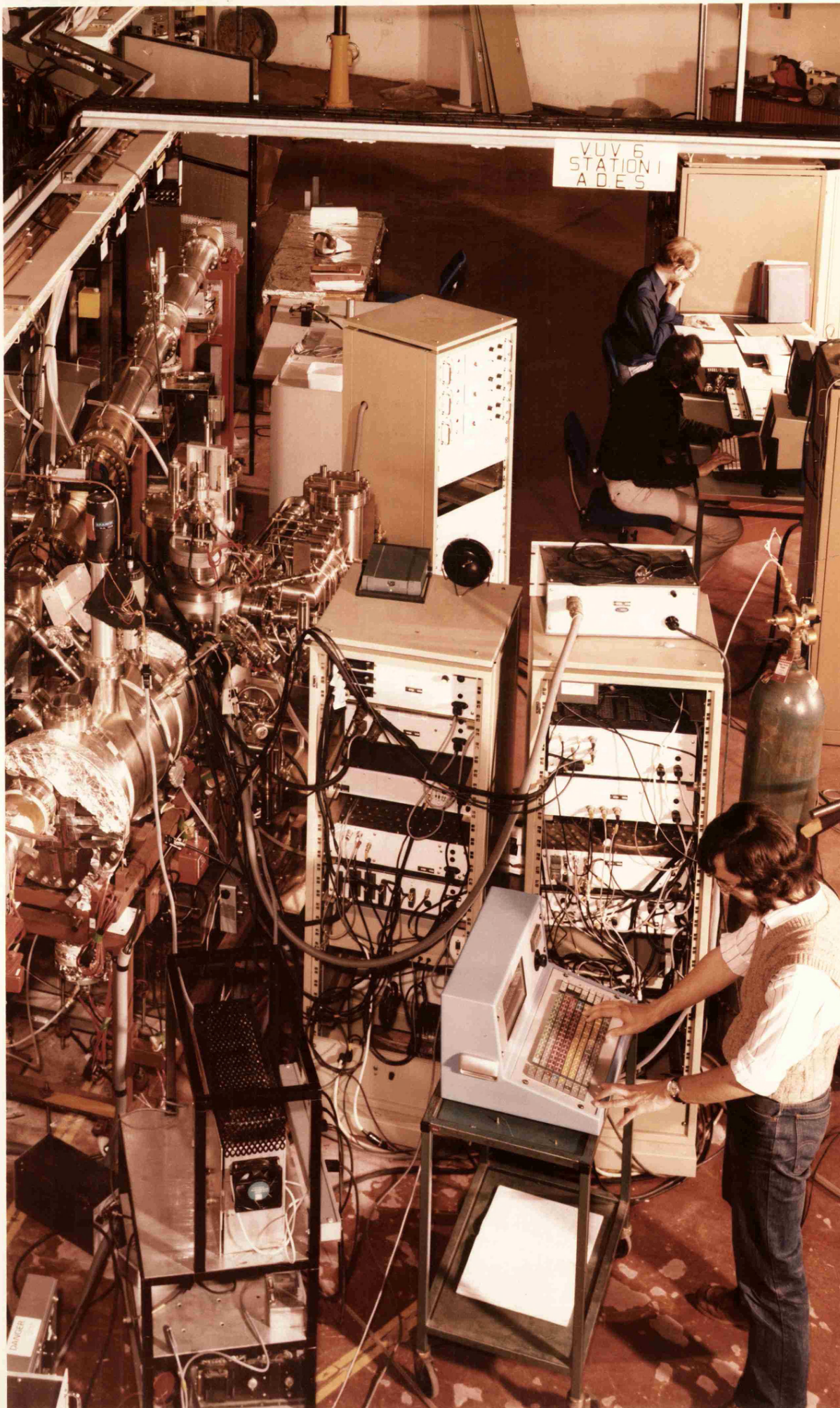


THESIS
661215

X752926291

frontispiece

Daresbury Synchrotron Radiation Source Beam line
VUV6 during experiments carried out by members
of the Leicester University Condensed Matter
Physics Research Group presented in this thesis.



Contents

	<u>Page</u>
Abstract	
Acknowledgements	
Chapter 1 : <u>Introduction</u>	1
Chapter 2 : <u>Surface and Overlayer Geometry and Electron States : Electron Spectroscopies</u>	4
2.1 Introduction	5
2.2 LEED	6
2.3 Auger Spectroscopy	8
2.3.1 The Auger Process	8
2.3.2 Overlayer Structure from Auger Spectroscopy	9
2.4 Mechanics of Overlayer Growth	11
2.5 Energy Bands in Crystalline Solids	14
2.5.1 Methods of Band Calculations	16
2.5.2 Surface Effects	19
2.5.3 Thin Film and Layer Calculations	21
2.6 The Work Function	22
2.7 Work Function Change on Metal Adsorption	24
2.8 Theory of Photoemission	26
2.8.1 Three Step Model	27
2.8.2 One Step Model	28
Chapter 3 : <u>Experimental Techniques</u>	33
3.1 Introduction	34
3.2 ADES-1 at Daresbury	35
3.3 Sample Manipulation	36
3.4 Monitoring LEED Patterns	37
3.5 Detection of Auger Electrons	37
3.6 Photoelectron Analyser	39
3.7 Ultra-Violet Discharge Source	40
3.8 Synchrotron Radiation	41
3.8.1 Properties of Synchrotron Radiation	41
3.8.2 Daresbury Synchrotron Radiation Source	43
3.9 Beam Line and Monochromator	43
3.10 Data Collection	44
3.11 Leicester Chamber	45
3.12 Crystalline Surface Preparation	46
3.13 Overlayer Growth - General Considerations	48
3.14 Transition Metal Vapour Source	50

	<u>Page</u>
Chapter 4 : <u>Photoemission from the Clean Crystal Surfaces: Copper, Silver and Palladium</u>	52
4.1 Introduction	53
4.2 Photoemission from Transition and Noble Metals	54
4.3 The Copper (100) Surface	60
4.4 The Silver (100) and (111) Surfaces	63
4.4.1 HeI Spectra	64
4.4.2 Synchrotron Radiation Spectra	67
4.5 The Palladium (111) Surface	69
Chapter 5 : <u>An Electron Spectroscopic Study of Palladium Overlayers on Silver (100) and (111)</u>	74
5.1 Introduction	75
5.2 LEED and AES Results	76
5.3 Normal Emission Photoelectron Spectra	78
5.4 Work Function	81
5.5 Isolated Palladium Resonance	83
5.6 E-k Dispersion Relations for Palladium Monolayers	85
5.7 Photoemission Calculations	88
5.8 Discussion	89
5.9 Summary	91
Chapter 6 : <u>An Electron Spectroscopic Study of Palladium Overlayers on Copper (100)</u>	93
6.1 Introduction	94
6.2 LEED and AES Results	95
6.3 Coverage Calibration	96
6.4 Photoemission Spectra	98
6.5 Photoemission Calculations	99
6.6 Discussion and Summary	100
Chapter 7 : <u>An Electron Spectroscopic Study of Copper Overlayers on Silver (100)</u>	102
7.1 Introduction	103
7.2 LEED and AES Results	104
7.3 Coverage Calibration	105
7.4 Normal Emission Photoelectron Spectra	106
7.5 Dispersion Relation for the Monolayer	110
7.6 Photoemission Calculations	112
7.7 Discussion and Summary	117

	<u>Page</u>
Chapter 8 : <u>An Electron Spectroscopic Study of Iron Overlayers on Silver (100)</u>	120
8.1 Introduction	121
8.2 LEED and Auger Spectroscopy	122
8.3 Growth Mode	122
8.4 Work Function	123
8.5 Photoemission at 21.2 eV (HeI)	125
8.5.1 Three Monolayer Coverage	126
8.5.2 One Monolayer Coverage	128
8.6 Photoemission at 40.8 eV (HeII)	129
8.7 Photoemission Calculations	130
8.7.1 Three Monolayer Coverage	131
8.7.2 One Monolayer Coverage	133
8.8 Photoemission Using Synchrotron Radiation	133
8.8.1 The 3s Levels	134
8.8.2 Valence Band Emission	136
8.9 Summary	138
Chapter 9 : <u>An Electron Spectroscopic Study of Nickel Overlayers on Silver (100)</u>	141
9.1 Introduction	142
9.2 LEED and Auger Spectroscopy	143
9.3 Growth Mode	143
9.4 Photoemission Spectra	145
9.5 Photoemission Calculations	148
9.6 Magnetism in Overlayers	149
9.7 Summary	153
Chapter 10: <u>Discussion, Summary and Conclusions</u>	155
10.1 Introduction	156
10.2 Overlayer Growth Modes	156
10.3 Overlayer Electronic Structure	159
10.4 Two-Dimensional Energy Bands	161
10.5 Surface States	163
10.6 Calculation of Photoelectron Spectra	165
10.7 Suggestions for Further Work	167
10.7.1 Experimental Development	168
10.7.2 Theoretical Development	170
References	172
Appendix 1 : Publications	184
Appendix 2 : Data set for Photoemission Calculations	186

ABSTRACT

The growth and electronic structure of Fe, Ni, Cu and Pd overlayers on Ag (100) and Pd overlayers on Ag (111) and Cu (100) have been investigated using LEED, Auger electron spectroscopy (AES) and angle resolved photoemission spectroscopy (ARPES). Calculations of the photoemission spectra from the adsorbed overlayers and the clean substrates are reported.

LEED and AES showed that Pd was initially adsorbed on Cu (100) as a $c(2 \times 2)$ surface alloy whereas the other overlayer-substrate combinations formed pseudomorphic monolayers. Pd on Ag (100) and Ag (111) showed continuous layer growth but for Fe and Ni islands were formed after three monolayers and for Cu after two monolayers had been deposited. The differences in growth mode can be understood in terms of a classical theory in which lattice mismatch plays an important role.

ARPES from the clean Cu (100), Ag (100), Ag (111) and Pd (111) surfaces at 21.2 eV photon energy can be interpreted by direct transitions from calculated ground state band structures. For clean Ag (100) and Pd (111) normal emission photoelectron spectra were recorded over the energy region 40 to 120 eV. Spectra were calculated using the time reversed LEED description and good agreement between theory and experiment obtained.

The development of overlayer structure through characteristic phases of different dimensionality was followed using ARPES. At low coverages a single spin-orbit split Pd resonance on Ag (100) occurred, and a similar exchange-split Fe resonance was observed. For Cu and Pd monolayers on Ag (100) the experimental two-dimensional band structures were in fair agreement with calculated isolated monolayer bands. Photoemission calculations reproduced the spectra from these adsorbed monolayers

using bulk atomic potentials, particularly good agreement being obtained for the Cu monolayer. ARPES using synchrotron radiation identified the magnetic state of the Fe monolayer on Ag (100) and a valence band exchange splitting of 1.8 to 1.9 eV was inferred. Magnetic ordering in the Ni monolayer on Ag (100) was also indicated. Throughout the study the orientation and lattice expansion imposed on the overlayer by the substrate was shown to have a significant effect on overlayer electronic structure.

ACKNOWLEDGEMENTS

I wish to express my gratitude and thanks to Dr. C. Norris for his supervision and guidance during the course of this work. I also thank the U.G.C. for financial support in the form of a Research Demonstratorship.

The experimental work of this thesis was greatly assisted by collaboration with Drs C. Binns and H.A. Padmore, to whom I give sincere thanks. I also thank Drs D. Norman and J.B. West of Daresbury Laboratory. The theoretical aspect of this work was conducted through the Theory Group at Daresbury and I wish to acknowledge the help of Drs N. Kar and P. Durham in this respect. Numerous fellow physicists have been of assistance in discussions of ideas presented in this thesis; special thanks are due to Drs G.P. Williams, M-G Barthes-Labrousse, C-G Larsson and S.J. Gurman. The iron and nickel monolayer band structures in Chapters 8 and 9 were provided by Dr. J. Noffke of the Institut fur Theoretische Physik, Clausthal, to whom I am grateful.

Without expert technical assistance from the Physics Department of Leicester University this work could not have proceeded and I am especially grateful to Mr. J.S.G. Taylor.

My parents have provided continuous support and encouragement throughout my education and it is impossible for me to express sufficient thanks to them. My thanks must also go to Ruth Mitchell for her good humour and understanding during the course of this work.

Finally, I would like to thank Mrs. M.E. Garner for typing this thesis, and Mr. J.F. Kerruish for reprographic work.

CHAPTER 1INTRODUCTION

Ultra-thin layers of metals supported on metal substrates are a class of adsorption systems of considerable fundamental and technological interest. The systems represent an approach to low dimensionality, where dramatic changes in electronic structure including magnetism occur. This is brought about by the lack of translational symmetry normal to the surface and by the reduction in coordination number which affects electron bandwidths, degeneracies and state densities. Using these overlayers, theories of crystal growth and the effect of lattice mismatch and the different free energies of the substrate and adsorbate may be investigated. Information on surface phase transitions is also obtained.

Commercial interest in ultra-thin metal layers has focussed on catalysis, where the presence of a monolayer of adsorbed material can dramatically alter catalytic reaction rates (see for example Sachtler et al 1981). El-Batanouny et al (1981) have shown that the presence of a single palladium monolayer on niobium (110) caused a rapid increase in the rate of uptake of hydrogen. This was associated with an increase in the density of states at the Fermi level and clearly illustrates the importance of electronic structure measurements on these systems. Applications are also found as electrically active surface layers for electron emitters, chemically passive coatings and magnetic films.

A supported metal monolayer forms the basic unit of a Layered Ultra-thin Coherent Structure (LUCS) of the type now attracting increasing theoretical and experimental investigation (Schuller 1980, Jarlberg and Freeman 1980). Such structures, formed from repeating sandwiches of alternating epitaxial films, have been shown to exhibit unusual superconducting and magnetic properties (Banerjee et al 1982, Brodsky and

Freeman 1980). A thorough understanding of the properties of the unit "building block" is fundamental to investigations of the properties of these new materials.

Metallic monolayers are convenient experimentally in that they do not usually poison the vacuum or react with the substrate in a damaging way. The deposition of simple compact epitaxial layers is accurate and controllable using MBE (molecular beam epitaxy) technology. In addition, the contribution of a single layer to surface properties may be investigated.

This thesis presents the results of electron spectroscopic investigations of the growth and electronic structure of nickel, iron, copper and palladium overlayers on silver (100), and palladium overlayers on silver (111) and copper (100). These overlayer/substrate combinations were chosen to emphasise the aspects of low dimensionality and magnetic behaviour evident in transition metal overlayers. For these studies silver is a suitable substrate for several reasons. It is well characterized (Christensen 1972, Courths et al 1981). It presents a wide, 4 eV, window below the Fermi level in which to monitor the development of the overlayer electronic structure, and it is immiscible with many of the elements of the first row of the transition metal series.

The (100) surface gave the possibility of simple epitaxial overlayer structures with mismatches of $\sim 10\%$ with the (100) faces of the overlayer materials. The silver (111) and copper (100) surfaces gave additional structural variations. The palladium and copper adsorbates are both well understood materials whose d-bands show little overlap with the silver 4d bands and for which the experimental derivation of the overlayer band structure was possible. For copper the 11.5% mismatch relative to the substrate was a further factor whose effects on the overlayer electronic structure were investigated. Recent experiments

concerning the magnetic properties of thin iron and nickel films have produced controversial results which appear to depend upon the orientation, geometry and thickness of the film (Binns et al 1982, Keune et al 1977, Bergmann 1981, Gradman and Isbert 1980). The importance of clean, well characterized surfaces and overlayers for reliable results must be emphasized. For these reasons electron spectroscopic studies using surface sensitive techniques of iron and nickel layers on silver (100) were undertaken.

The growth and structure of metal overlayers, the electronic properties of bulk materials and their modifications at surfaces, and the theory of electron spectroscopies are described in Chapter 2. The experimental techniques employed in this work are discussed in Chapter 3. Chapter 4 describes photoemission studies of the clean copper (100), silver (100) and (111), and palladium (111) surfaces. The results of electron spectroscopic studies of the growth and electronic structure of the systems palladium on silver (100) and (111), palladium on copper (100), copper on silver (100), iron on silver (100) and nickel on silver (100) are described and discussed in Chapters 5 to 9 respectively. The work is discussed and summarized, and conclusions drawn, in Chapter 10.

CHAPTER 2
SURFACE AND OVERLAYER GEOMETRY AND
ELECTRON STATES: ELECTRON SPECTROSCOPIES

- 2.1 Introduction
- 2.2 LEED
- 2.3 Auger Spectroscopy
 - 2.3.1 The Auger Process
 - 2.3.2 Overlayer Structure from Auger Spectroscopy
- 2.4 Mechanics of Overlayer Growth
- 2.5 Energy Bands in Crystalline Solids
 - 2.5.1 Methods of Band Calculations
 - 2.5.2 Surface Effects
 - 2.5.3 Thin Film and Layer Calculations
- 2.6 The Work Function
- 2.7 Work Function Change on Metal Adsorption
- 2.8 Theory of Photoemission
 - 2.8.1 Three Step Model
 - 2.8.2 One Step Model

CHAPTER 2

SURFACE AND OVERLAYER GEOMETRY AND
ELECTRON STATES: ELECTRON SPECTROSCOPIES2.1 Introduction

The behaviour of metal overlayer systems is one of the remaining outstanding problems of condensed matter physics. Frequently the geometric structure taken by the adsorbate in a particular overlayer-substrate combination, and hence the local atomic environment, is unknown. Calculations of the electronic structure are complicated by lack of translational symmetry in the direction normal to the surface and the resulting breakdown of the Born-von Karmen periodic boundary conditions. For realistic results in borderline situations such as this self-consistency of the calculation becomes critically important. Effort has recently been expended on finding new ways of calculation in which this may be achieved more readily than previously.

The most powerful method available for the determination of electronic structure is photoemission, particularly when used in conjunction with a synchrotron radiation source; this is the technique of the present work. For the study of the geometric structure of overlayers and surfaces a variety of procedures are available. LEED spot intensity analysis, with the application of a suitable reliability factor, has been successfully used in many cases. Surface EXAFS, although capable of giving the required information, is rather difficult experimentally and requires the use of a synchrotron radiation source. Similar comments apply to grazing-incidence Bragg scattering. The use of photoelectron diffraction originally held great promise but is complicated both experimentally and in the theoretical analysis of the results.

A standard routine laboratory determination of overlayer periodicity and growth mode is obtained using combined LEED and Auger

spectroscopy while growing the overlayer in situ. Simple kinematical LEED analysis gives the periodicity of the growing layer whose coverage and structure is obtained by Auger intensity analysis using the same piece of equipment. This technique was used in the present work.

Thus, this chapter falls naturally into two halves, dealing respectively with the determination of overlayer geometry and growth mode, and with the electronic structure of surfaces and overlayers. LEED and Auger spectroscopy are the subjects of sections 2.2 and 2.3, with the mechanics of overlayer growth considered in section 2.4. Energy bands in crystalline solids and their modification at surfaces and in layers are discussed in section 2.5. The work function of a surface gives information concerning its state, and the work function change on metal adsorption is an important effect. These are considered in sections 2.6 and 2.7. Interpretation of angle-resolved photoelectron spectra within the framework of both the three-step and one-step models is discussed in section 2.8.

2.2 Low Energy Electron Diffraction

The high atomic scattering cross-section for electrons of energy less than 1000 eV suggests that Low Energy Electron Diffraction (LEED) should be extremely sensitive to surface atomic arrangement. This has been known for some time, indeed Davisson and Germer used the technique in 1927 to demonstrate the wave nature of the electron. Because of its surface sensitivity LEED may be considered as the two-dimensional analogue of X-ray diffraction. Emergent angles of diffracted beams may be found using the Ewald Sphere construction (see for example Wormald 1973). For angles 2θ between incident and scattered beams and diffraction from a square lattice of side a for any particular reciprocal lattice rod $(h k)$ and wavelength λ .

$$a = \frac{(h^2 + k^2)^{\frac{1}{2}} \lambda}{\sin \theta}$$

Evaluation of beam intensities, however, is a much more difficult problem since there is significant elastically reflected flux from the second and subsequent underlying layers and multiple scattering becomes important in the calculation. Measurement of LEED beam intensities as a function of energy (structure plot) or azimuthal angle (Renninger plot or rotation diagram) can yield much useful information. For example the relaxation of the outermost layer to the vacuum may be obtained, or adsorbate sites (e.g. bridge, hollow or atop) ascertained.

Beam intensities were not evaluated in the present work and the reader is referred elsewhere for a full description of dynamical LEED theory (e.g. Pendry 1974).

At this stage a brief description of the notation in use for surface structures is called for. By analogy with bulk crystallography two dimensional periodic structures may be grouped into five types of surface net which may be generated by unit translations of their primitive vectors \underline{a}_1 and \underline{a}_2 . In the case of an adsorbed monolayer having unit mesh, \underline{b}_1 and \underline{b}_2 it is convenient to relate this to the substrate unit mesh by means of the transformation matrix M such that

$$\underline{b} = M \underline{a}$$

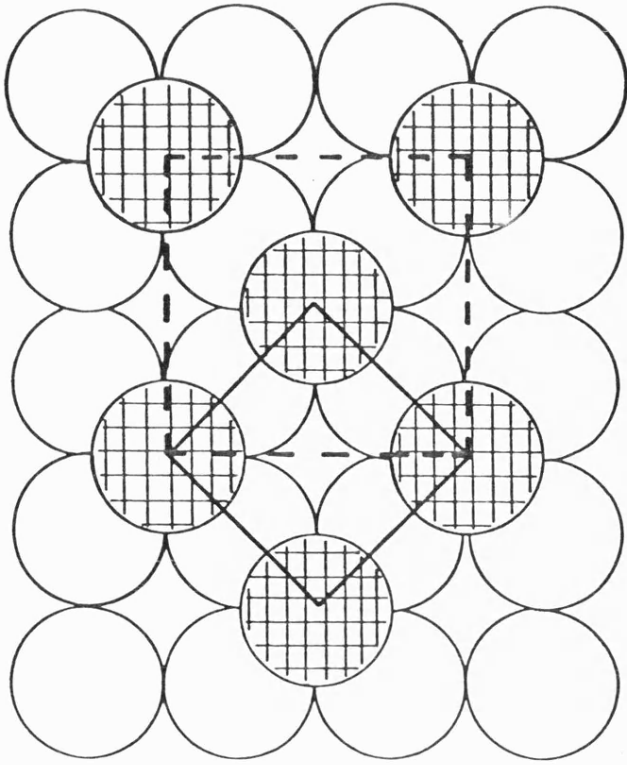
$$b_1 = m_{11} a_1 + m_{12} a_2$$

$$b_2 = m_{21} a_1 + m_{22} a_2$$

The areas of the two meshes A and B are related by

$$A = B \det M$$

Although the matrix notation is simple and general many observers use the notation of Wood (1964). Here the overlayer and substrate meshes are related by the ratio of the lengths of the translation vectors and by a rotation R (degrees) through an expression of the



$\left(\begin{array}{c} | \\ | \\ | \\ | \end{array} \quad \begin{array}{c} | \\ | \\ | \\ | \end{array} \right)$ structure

- - - - = c (2 x 2)

——— = $(\sqrt{2} \times \sqrt{2}) R 45^\circ$

Fig. 2·1

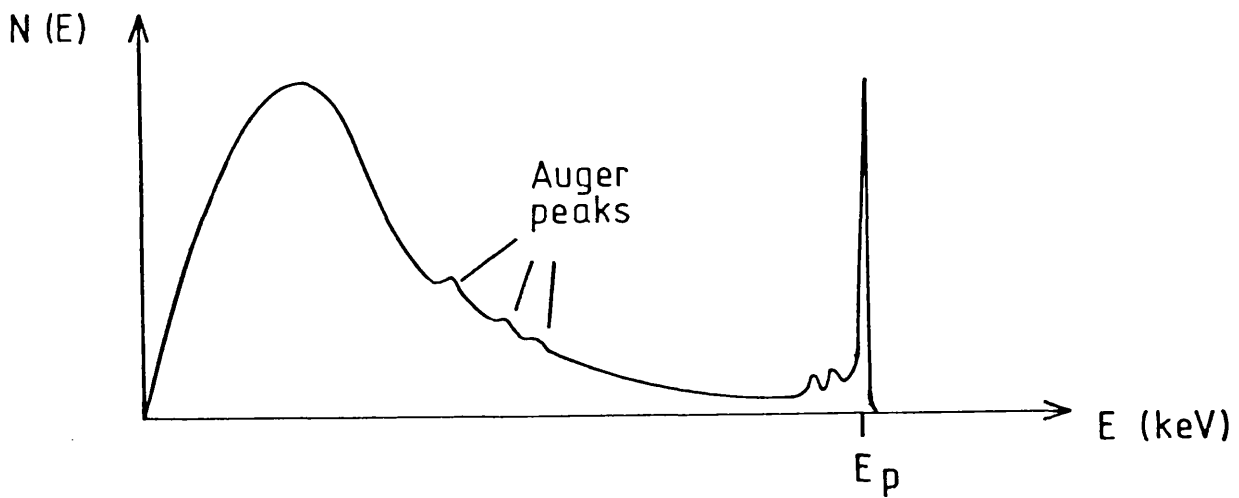
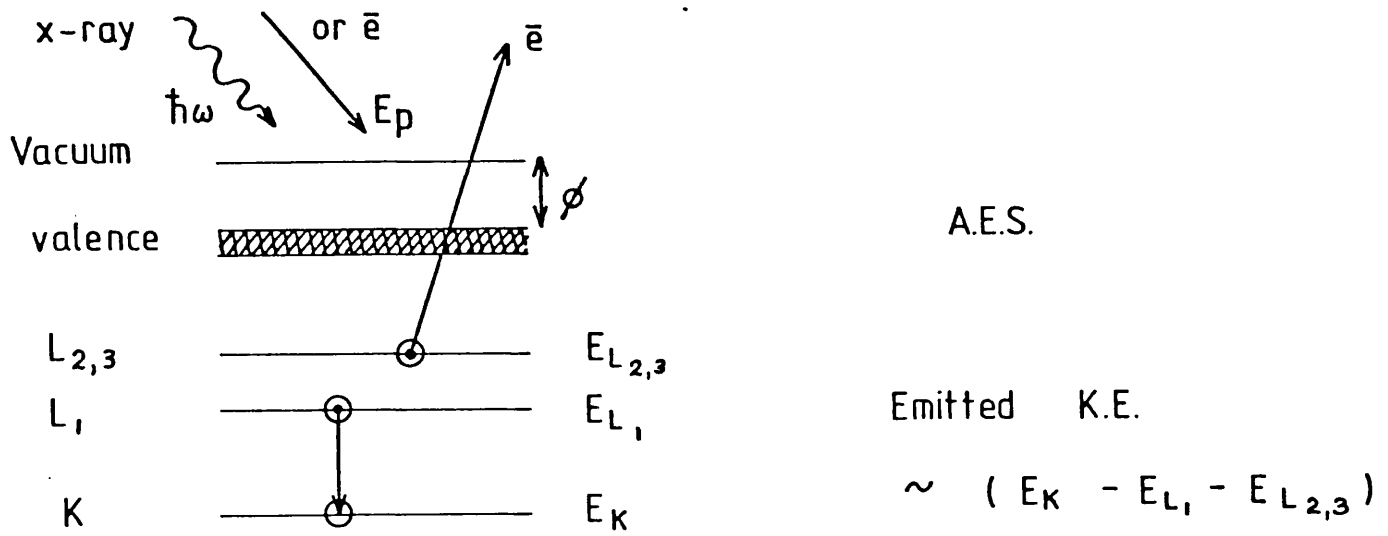
form $(a_1 / b_1 \times a_2 / b_2)R$. A lower case p or c is used as a prefix to indicate a primitive or centred mesh respectively. The often observed $(\sqrt{2} \times \sqrt{2}) R 45^\circ$ structure may therefore also be described as $c(2 \times 2)$. This is illustrated in figure 2.1.

2.3 Auger Spectroscopy

2.3.1 The Auger Process

In the Auger event (Auger 1925) a core hole produced in an atom by an incident energetic particle (typically an electron of energy 1 keV) is filled by an electron from a higher level. The excess energy, a characteristic of the atom, is carried by an emitted (Auger) electron. This is shown in figure 2.2. The Auger electron is denoted by $W_p X_q Y_r$ where, in X-ray notation (K, L, M etc) W is the level of the initial hole, X is the level from which the hole is filled and Y is the level of the emitted electron. The orbital quantum numbers of the levels are represented by p, q and r. For example $L_1 = 2S$, $L_2 = 2P_{1/2}$, $L_3 = 2P_{3/2}$ etc. For a level in the valence band the suffix is dropped and the letter V used in place of X or Y as the case may be.

Electrons from any region of the valence band may contribute to a $W X V$ transition, in which case the peak structure should resemble the valence band density of states (DOS). Auger transitions, however, occur in very short times typically of the order of 10^{-16} s. The resultant lifetime broadening of the order of 6 eV makes extraction of the valence band DOS difficult and this is not usually attempted. Peaks of greater width result from Coster-Kronig transitions of the form $W_p W_q Y_r$ when the initial hole is filled by an electron with the same total momentum but greater angular momentum. This is a very fast process, resulting in broadening of several tens of eV.



The Auger Process

Fig. 2.2

Creation of the core hole causes a redistribution of the Coulomb field in which the electrons move and the consequent shift in energy levels affects the expected energy values of Auger electrons. Approximating $E(Z)$ by the mean of $E(Z)$ and $E(Z+1)$ using the following formula (Chung and Jenkins 1970) has been found to give sufficiently accurate Auger energies for most purposes.

$$E_{WXY}(Z) = E_W(Z) - \frac{1}{2}(E_X(Z) + E_X(Z + 1)) - \frac{1}{2}(E_Y(Z) + E_Y(Z + 1))$$

If the two final state levels are both in the valence band then the electron gas screens the Coulombic interaction and the simple expression

$$E_{WVV}(Z) = E_W(Z) - 2 E_V(Z)$$

gives a reasonable approximation to WV Auger energies. Relaxation effects have been discussed recently by Ohno and Wendin (1982).

The set of discrete lines found in the Auger spectrum form a characteristic "fingerprint" of an element. Peak intensities can be used to estimate the concentration of surface contaminants, for example 0.1% of a monolayer of carbon being detectable.

2.3.2 Overlayer Structure from Auger Spectroscopy

Structural information concerning the growth mode of a metal overlayer may be obtained by plotting the substrate and overlayer Auger intensities as a function of deposition time, to give a so-called AS-t plot (Rhead 1976). In the case of the perfect layer-by-layer mode (see section 2.4) the simple model proposed by Jackson et al (1973) indicates that a series of straight lines separated by well-defined changes of gradient is seen. In this model a crystal is regarded as a set of atomic planes labelled 1, 2, n oriented parallel to the surface. The production of a back scattered Auger current due to an incident electron beam penetrating the crystal is described in terms of the

probabilities of a primary electron reaching the n th layer, of an Auger electron being produced there, and of this Auger electron passing through $(n-1)$ layers before reaching the surface and escaping into vacuum. Summing the contributions from n layers gives

$$I_n = I_\infty (1 - (1 - I_1 / I_\infty)^n) \quad (2.3.1)$$

where I_1 is the current from one monolayer and I_∞ the current obtained from bulk material.

This may be applied to the layer growth of material A arriving at constant rate R at the surface of material B. The initial Auger current is given by

$$I_A = R S_1 I_1 t$$

where S_1 = sticking coefficient of A on B

I_1 = current from one monolayer of A

t = elapsed time

After time t_1 , one monolayer of A is complete and the second monolayer develops, giving a current

$$I_A = I_1(1 - \theta) + I_2 \theta$$

where θ = fractional coverage of second layer

$$= R S_2(t - t_1)$$

S_2 = sticking coefficient of A on A

and I_2 is given by (2.3.1) with $n = 2$.

Substitution for I_2 gives

$$I_A = I_1 \left[1 + \theta \left(1 - \frac{I_1}{I_\infty} \right) \right]$$

showing a linear increase in current as the second layer develops. For an integral number n deposited layers the Auger current is given by (2.3.1) with

$$n = 1 + R S_2(t_n - t_1)$$

where t_n = time of completion of n th monolayer. The dependence is piece-wise linear.

Using similar reasoning Venables et al (1980) have considered the Stranski-Krastanov growth mode in which monolayer growth is followed by island formation (see section 2.4). The experimentally observed change in gradient in the AS-t plot on monolayer completion and commencement of islanding is predicted by the theory.

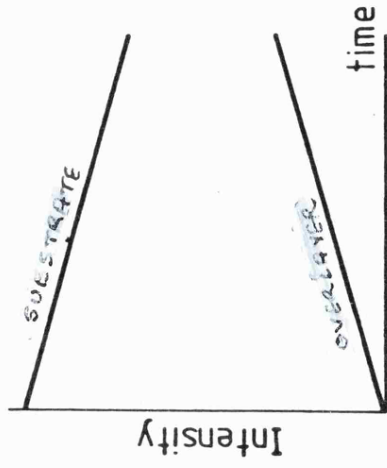
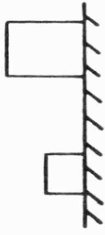
These phenomenological models have proved adequate for many systems but fail when back scattering effects from the substrate are much larger than from the overlayer deposit (Tokutako et al 1979) or when diffraction effects predominate (Barthès and Rhead 1980). In the strong back-scattering case Tokutako et al (1979) have developed a model for Auger current including the attenuation of the primary beam, and back-scattering and forward-scattering effects from the substrate and deposit which predict a maximum in the overlayer Auger signal in certain cases, for example Be overlayers on Cu (Goto et al 1975). Using only measured secondary electron coefficients the theory allows estimation of the deposit thickness in Auger signal in thin film growth.

In the case of Au substrates Barthès and Rhead (1980) have pointed out that 72 eV $N_{6,7}VV$ Au Auger electrons have a wavelength equal to the Au atomic radius. This coincidence leads to large diffraction effects in the surface layers and may account for the discrepancies observed between different experiments with Au substrates. The effect has recently been turned to advantage and structural information resulting from diffraction and anisotropic emission effects obtained from angle resolved Auger electron spectra (Koshikawa et al 1981).

2.4 Mechanics of Overlayer Growth

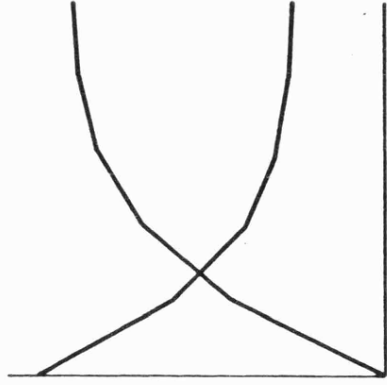
A classification scheme for the growth of thin overlayer films was proposed by Bauer (1958). The validity of this scheme was established in a later review when further experimental evidence became

Volmer - Weber



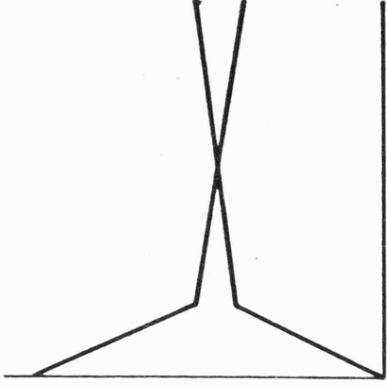
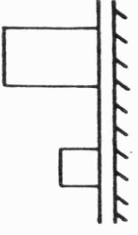
island growth on
substrate

Frank - van der Merwe



layer growth

Stranski - Krastanov



island growth on
adsorbed layer

Overlayer Growth Modes

Fig. 2.3

available (Bauer and Poppa 1972). The scheme distinguishes between three basic growth mechanisms: the Volmer-Weber, Frank-van der Merwe and Stranski-Krastanov modes. These are illustrated in figure 2.3, together with their corresponding AS-t plots. In principle the Volmer-Weber mode should occur when the surface energy of the film is large compared to the substrate, and the other modes should be typical of the reverse case - a low surface energy film on a high surface energy substrate. In the latter case a low strain energy in the film compared with the surface energy of the film should result in layer by layer (Frank-van der Merwe) growth and in the case of large strain energy Stranski-Krastanov growth should occur. These considerations apply for conditions of ideal overgrowth, i.e. no chemical reactions, alloying or electron bombardment induced phenomena occurring during growth.

For the case of transition metal overlayers on metal surfaces, overlayer and substrate surface energies tend to be approximately equal so growth is dependent upon the strain in the overlayer. Strain results from the lattice mismatch between overlayer and substrate and the critical values beyond which layer growth cannot be sustained were obtained by Frank and van der Merwe (1949) in an extension of their theory of one-dimensional dislocations. They considered a classical model consisting of identical balls connected by identical springs arranged in a straight line to which their motion was constrained, at the same time being acted upon by a force varying periodically along the line, initially taken to be sinusoidal. Extending to two dimensions and treating the balls as overlayer atoms and the source of the potential as the substrate enabled identification of the dislocation density.

$$P_0 = a / (b - a)$$

where a = substrate natural lattice spacing
 b = overlayer natural lattice spacing

and the effective length of a dislocation

$$\lambda_0 = (\mu a^2 / 2W)^{\frac{1}{2}}$$

where μ = force constant of the springs

$\frac{1}{2}W$ = amplitude of the substrate potential.

By considering equilibrium at zero temperature the stability limit

$$0 \leq \lambda_0 / P_0 \leq 1$$

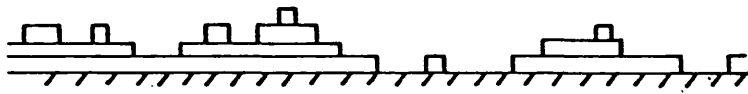
was defined, giving the critical misfit for layer growth where the temperature can be reduced sufficiently to inhibit thermal activation of dislocation formation. The state of lowest energy at finite temperature was found as

$$\lambda_0 / P_0 \leq 2 / \pi$$

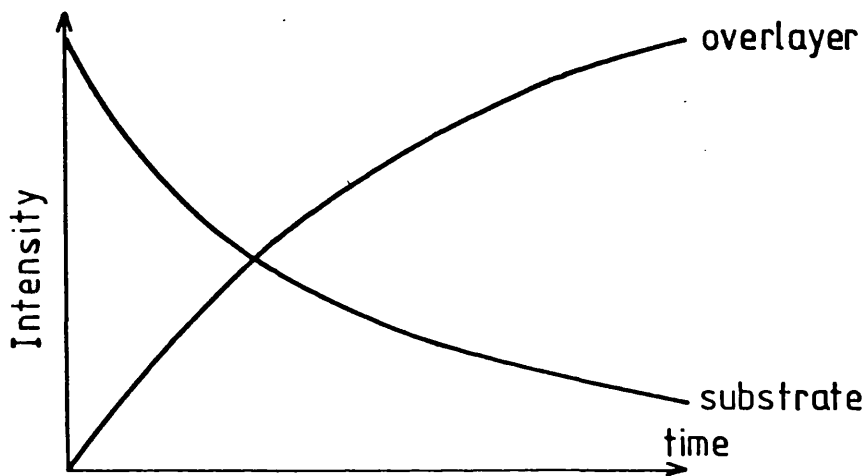
Using a Lennard-Jones force law (Lennard-Jones 1940) λ_0 was evaluated as ~ 7 , giving the critical misfits $\% \leq 1 / P_0 \leq 14\%$, depending on temperature. Woltersdorf (1981) has pointed out that the Frank-van der Merwe paper contained a numerical error and the correct value for λ_0 is ~ 8.8 , so the critical misfits are 7% and 11% respectively. For misfits greater than these the Stranski-Krastanov mode may frequently be observed and this has recently been demonstrated by Guglielmacci and Gillet (1980, 1981, 1982a, 1982b) in their investigation of the effect of temperature on the pseudomorphic growth of Ag on Pd(100). From 20°C to 100°C layer by layer growth was observed. Between 100°C and 200°C growth of two monolayers was followed by islanding. Between 200°C and 300°C islands were formed after deposition of one monolayer and for temperatures between 300°C and 600°C direct growth of islands (crystallites) on the substrate was observed.

The critical conditions may be expected to change with film thickness, for instance a 2-layer film will have a critical misfit $1 / \sqrt{2}$ times that of a monolayer film since $\lambda_0 \propto \mu^{\frac{1}{2}}$ and μ may be taken

Simultaneous Multilayer Growth



$$\theta_n = 1 - e^{-Jt} \sum_{m=1}^n \frac{(Jt)^{m-1}}{(m-1)!}$$



layer growth on incomplete
underlying layers

Fig. 2·4

as proportional to thickness. Obviously the strain permissible in a thin film cannot persist to thick layers and relaxation to a bulk lattice constant must occur, as has been experimentally observed for Pd / Ag(111) and Pd / Au(111) by Burland and Dobson (1981).

In the experimental situation a crystal surface is exposed to an arriving vapour flux and the case of crystal growth by vapour deposition on to a perfect, i.e. dislocation free, crystal surface has been considered by Kashchiev (1977). In this case Frank-van der Merwe growth may be expected since the surface energies of overlayer and substrate are equal and the mismatch is zero, as they are the same material. Kashchiev found that during growth of the n th layer small amounts of the $(n + m)$ th layer where $m = 1, 2, 3 \dots$ were present. This was due to the reduced diffusion coefficient over a step and the resulting surface consists of a series of terraces. In the extreme case where an atom is restricted to the terrace on which it is initially adsorbed the fractional coverage of the n th layer ($n \geq 1$) is given by

$$\theta_n = 1 - e^{-Jt} \sum_{m=1}^n \frac{(Jt)^{m-1}}{(m-1)!}$$

where J = arrival rate (monolayers per unit time)

t = exposure time

The situation is illustrated in figure 2.4, and the corresponding AS-t plot shown. In this so-called "simultaneous multilayer" growth mode no structure is observed in the Auger signal decay and an independent coverage calibration is required. This has been observed for the case of Ni overlayers on Ag(111) (Barthès and Rolland 1980).

2.5 Energy Bands in Crystalline Solids

In general the analysis of the results of electron spectroscopy relies heavily on the concept of discrete energy bands in solids. The theory of band structure is elaborated in many standard texts, for example

Ziman (1972), Blakemore (1974), Kittel (1976). The essential features relevant to the present work are summarized here. For a thorough treatment see, for example, Pincherle (1971), Haug (1972), Altmann (1970).

To obtain energy bands from first principles it is necessary to solve Schrodinger's equation within the crystal

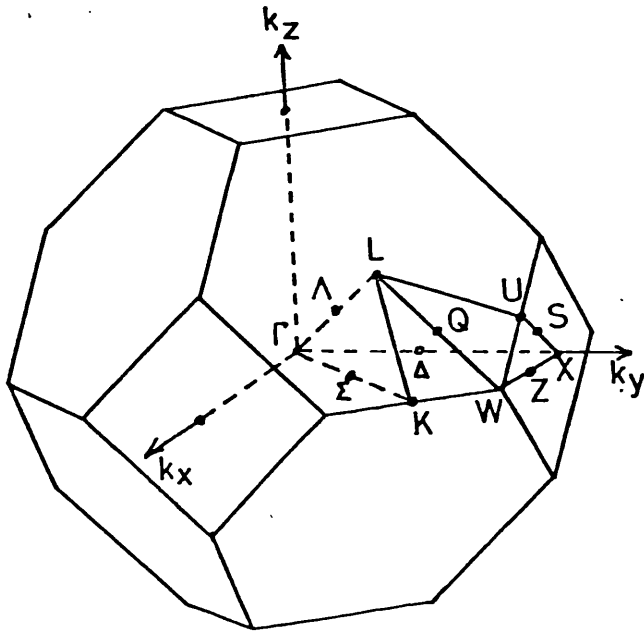
$$\left[-\frac{\hbar^2}{2m} \nabla^2 + V(\underline{r}) \right] \psi_{\underline{n}\underline{k}}(\underline{r}) = E_{\underline{n}\underline{k}} \psi_{\underline{n}\underline{k}}(\underline{r}) \quad (2.5.1)$$

Application of the Born-Oppenheimer approximation (Born and Oppenheimer 1927) allows the valence electrons to be taken as being in the field of fixed ion cores. To give the system wavefunction separable solutions the independent particle approximation (or Hartree approximation, Hartree 1928) is invoked so a single electron which experiences an average static potential due to all other electrons and ions may be considered. The effect of these other electrons is taken into consideration by incorporation of two further terms, the exchange and correlation corrections. The exchange term may be derived from the Pauli exclusion principle (Slater 1951)

$$V_X(r) = -\frac{3}{2} \alpha e^2 (\int \rho(\underline{r}) / \pi)^{\frac{1}{2}} \quad (2.5.2)$$

where $\rho(\underline{r})$ is the charge density in the valence and conduction bands and $\alpha = 1$ (Slater 1951), or $\frac{2}{3}$ (Gaspar 1954, Kohn and Sham 1965), or some intermediate value (Snow 1968).

For fcc metals such as considered in this thesis the muffin tin approximation is usually made. A spherically symmetric potential around each nucleus is assumed, with a constant potential region between the nuclei. The spherical part is often constructed using the standard Mattheis (1964) prescription in which the potential is approximated by a superposition of spherically symmetric atomic potentials calculated from self-consistent Hartree-Fock solutions for the atom. The one-electron non-relativistic muffin-tin potential may thus be written:



fcc BZ

FIG. 2.5

$$\begin{aligned}
V(r) = & -\frac{2Z}{r} + \frac{8\pi}{r} \int_0^r r^2 \rho(r) dr + 8\pi \int_r^R r \rho(r) dr \\
& + \frac{CZ_{\text{OUT}}}{a} + \mu_{\text{xc}} [\rho(r)] - \mu_{\text{xc}} [\rho_{\text{OUT}}] \quad (2.5.3)
\end{aligned}$$

for $r < R$ and is zero for $r > R$ (Janak 1974). The potential is in Rydbergs if the electronic charge density $\rho(r)$ is in atomic units (electrons / Bohr³) and R is the muffin-tin radius. μ_{xc} is the exchange-correlation potential, Z_{OUT} is the interstitial charge per unit cell and ρ_{OUT} is the interstitial charge density. The contribution of the interstitial charge density to the electrostatic part of the muffin tin potential is given by CZ_{OUT} / a with $C = 3.116686$ (simple cubic), 4.085521 (bcc) or 4.832066 (fcc) Rydberg-Bohr.

2.5.1 Methods of Band Calculations

As a consequence of periodicity the wavefunctions are in the standard Bloch (1928) form and may be evaluated within the reduced zone scheme. The fcc Brillouin Zone (BZ) is shown in figure 2.5. The wavefunctions $\psi_{\underline{k}}(\underline{r})$ are evaluated in terms of a set of basis functions such that

$$\psi_{\underline{k}}(\underline{r}) = \sum_j C_j(\underline{k}) \chi_j(\underline{k}, \underline{r}) \quad (2.5.4)$$

From equations (2.5.1) and (2.5.4) is obtained a linear homogeneous set of equations and for each \underline{k} value

$$\sum_j \{H_{ij}(\underline{k}) - E(\underline{k}) O_{ij}(\underline{k})\} C_j(\underline{k}) = 0 \quad (2.5.6)$$

with

$$H_{ij}(\underline{k}) = \int \chi_i^*(\underline{k}, \underline{r}) | -\nabla^2 + V(\underline{r}) | \chi_j(\underline{k}, \underline{r}) dr \quad (2.5.7)$$

$$O_{ij}(\underline{k}) = \int \chi_i^*(\underline{k}, \underline{r}) \chi_j(\underline{k}, \underline{r}) dr \quad (2.5.8)$$

$H_{ij}(\underline{k})$ and $O_{ij}(\underline{k})$ are elements of the energy and overlap matrices respectively. For non-trivial solution

$$\text{Det} \left| H_{ij} - E O_{ij} \right| = 0 \quad (2.5.9)$$

The left hand side of (2.5.9) is known as the secular determinant.

A different determinant is generated by each \underline{k} value, hence solution of (2.5.9) for all \underline{k} gives the band structure $E_s(\underline{k})$.

The various methods that are available for solution of the band structure differ mainly in their choice of basis functions. An intuitively favourable approach is to use the Linear Combination of Atomic Orbitals (LCAO) technique, which is based upon the tight binding approximation. A trial wavefunction involving a combination of atomic orbitals $\phi_a^{(j)}(\underline{r} - \underline{\ell})$ centred on the atom at ℓ is used.

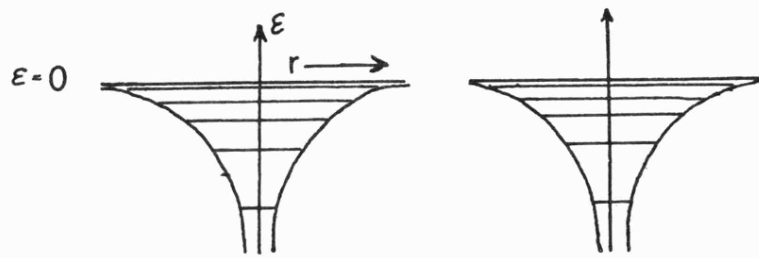
$$\psi_{\underline{k}}(\underline{r}) = \sum_{\ell j} e^{i \underline{k} \cdot \underline{\ell}} \beta_j \phi_a^{(j)}(\underline{r} - \underline{\ell}) \quad (2.5.10)$$

The energy is minimized by suitable choice of coefficients β_j . The technique has been used for metal surfaces and overlayers with some success, especially in a parametrized form where fits to experimental data are used (for example, Bisi and Calandra 1977), but there are objections to its use. It is clear that, once a solid has been formed by bringing together free atoms there is overlap within the interstitial regions and the individual atomic orbitals in (2.5.10) no longer exist. This is shown pictorially in figure 2.6. An attempt is being made to represent Bloch functions in the potential $V(\underline{r})$ by the eigenstates of a different potential satisfying different boundary conditions. This may be overcome by adding plane wave like terms to the sum (2.5.10) and excluding all orbitals that actually disappear in the overlap of atomic wavefunctions (figure 2.6).

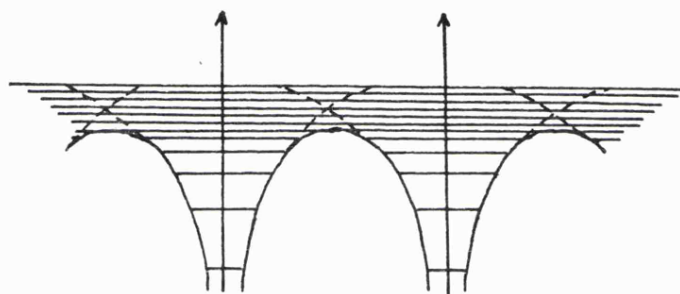
Consider a set of Bloch functions constructed from strongly localized core states

$$b_{t,\underline{k}} = \sum_{\ell} e^{i \underline{k} \cdot \underline{\ell}} b_t(\underline{r} - \underline{\ell}) \quad (2.5.11)$$

The higher valence states must be orthogonal to $b_{t,\underline{k}}$ since they are



bound atomic orbitals of free atoms



Bloch states of a crystal

FIG. 2.6

solutions of the same Schrodinger equation. This leads to a choice of an orthogonalized plane wave (OPW) for the basis function $\chi_{\underline{k}}$ (Herring 1940).

$$\chi_{\underline{k}}(\underline{r}) = e^{i \underline{k} \cdot \underline{r}} - \sum_{\underline{t}} \langle b_{\underline{t}, \underline{k}}, e^{i \underline{k} \cdot \underline{r}} \rangle b_{\underline{t}, \underline{k}} \quad (2.5.12)$$

Again, a variational method is used to minimize the expectation value of the energy and determine the coefficients $C_j(\underline{k})$ in (2.5.4). The approximation process converges rapidly and has been successfully used for metals and semiconductors. The method does not deal elegantly with d-bands, however, and these are best considered within the framework of the Augmented Plane Wave (APW) technique due to Slater (1937).

In the APW method the muffin tin potential (2.5.3) is used with a flat interstitial region as shown in figure 2.7. The Schrodinger equation may be solved exactly in spherical harmonics within the muffin tin and matched to plane waves in the volume between the spheres. Within each sphere

$$\phi(\underline{r}) = \sum_{\ell m} C_{\ell m} R_{\ell}(r, \epsilon) Y_{\ell m}(\theta, \phi) \quad (2.5.13)$$

where $Y_{\ell m}(\theta, \phi)$ is a spherical harmonic for the direction θ, ϕ of \underline{r} and R_{ℓ} is the solution of the radial equation

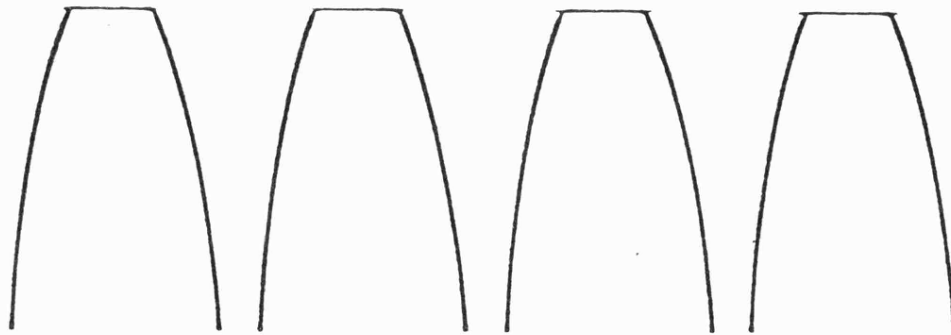
$$-\frac{1}{r^2} \frac{\partial}{\partial r} \left(r^2 \frac{\partial R_{\ell}}{\partial r} \right) + \left(\frac{\ell(\ell+1)}{r^2} + V(r) \right) R_{\ell} = \epsilon R_{\ell} \quad (2.5.14)$$

in atomic units.

The coefficients $C_{\ell m}$ are chosen so that $\phi(\underline{r})$ matches to a single plane wave $\exp(i \underline{k} \cdot \underline{r})$ at $r = R_s$ and the augmented plane wave $\chi(\underline{r})$ defined

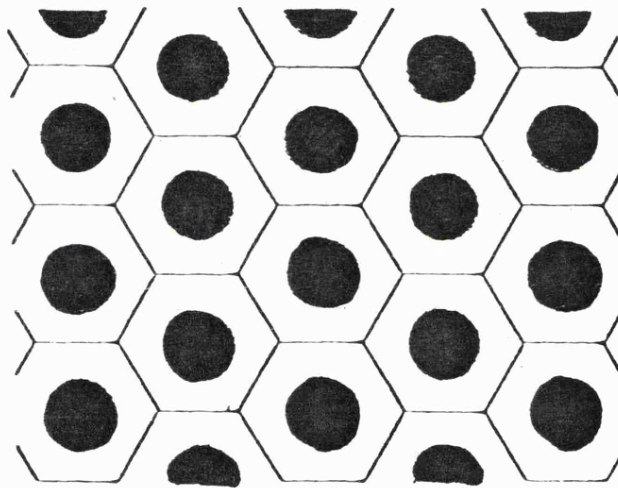
$$\chi_{\underline{k}}(\underline{r}) = e^{i(\underline{k} \cdot \underline{r})} \phi_{\underline{k}}(\underline{r} - \underline{l}) \quad (2.5.15)$$

As before, the $\chi(\underline{r})$ are used as basis functions, the variational principle is applied to obtain the wavefunction $\psi_{\underline{k}}(\underline{r})$ in (2.5.4) and the secular



(a)

■ Core region
 □ Interstitial region



(b)

(a) The muffin-tin potential, plotted along a line of ions. (b) The muffin-tin potential is constant (zero) in the interstitial regions and represents an isolated ion in each core region.

FIG. 2.7

determinant (2.5.9) evaluated to give the band structure.

An alternative method of band structure calculation originally proposed by Korringa (1947) and independently by Kohn and Rostoker (1954) is also in much use. Known as the KKR or Green's function method, it uses an offset muffin-tin potential. Inside the MT sphere the wavefunctions are expanded radially and the Schrodinger equation transformed into an integral equation

$$\psi_{\underline{k}}(\underline{r}) = \int_{\Omega} G_{\underline{k}}(\underline{r}, \underline{r}') V(\underline{r}') \psi_{\underline{k}}(\underline{r}') d\mathbf{r}' \quad (2.5.16)$$

with $G_{\underline{k}}$, the Green's Function, the solution of

$$(-\nabla^2 + E) G_{\underline{k}}(\underline{r}, \underline{r}') = \delta(\underline{r} - \underline{r}') \quad (2.5.17)$$

As $V(\mathbf{r})$ is absent in (2.5.17) the secular matrix may be factored into potential dependent and a structure dependent components. This has the advantage that once the crystal structure dependent matrix elements have been computed they can be used to perform band structure calculations with different potentials. This is especially important where the potential is iterated to self-consistency in the course of a calculation.

2.5.2 Surface Effects

In the preceding section periodic boundary conditions inside an infinite crystal were used in the derivation of energy bands. Termination of the crystal potential causes a perturbation of the

band structure near the surface of a real crystal and may give rise to so-called surface states or surface resonances. For the case of a semi-infinite crystal with one surface the one-electron momentum vector \underline{k} may be factorized into components parallel and perpendicular to the surface, $\underline{k}_{//}$ and \underline{k}_{\perp} respectively. \underline{k}_{\perp} may take complex values $\underline{k}_1 + i \underline{k}_2$ and substitution into Bloch condition leads to a term $\exp(-\underline{k}_2)$. Thus the wavefunction decays into the vacuum resulting in formation of a state due to the presence of the surface. This is shown in figure 2.8.

True surface states exist in the gaps which may occur when the bulk band structure is projected onto the surface Brillouin zone (S B Z). The SBZ for the (100) and (111) faces of an fcc crystal are given in figure 2.9.

The existence of a wavefunction localized at the surface of a semi-infinite crystal was first shown by Tamm (1932) but the nature of the state is very dependent on the form of the surface barrier and it is only recently that realistic calculations have been made. An abrupt step barrier is extremely unsatisfactory; the form of the surface potential needed to reproduce experimentally-observed surface states on Cu(111) has been considered by Gurman (1976).

Using a self-consistent local orbital (SCLO) method of calculation Smith et al (1980) have found a large density of surface states on the Ag(100), Pd(100), Ni(100) and Cu(100) surfaces. States both in the band gaps and in the d-band region (surface

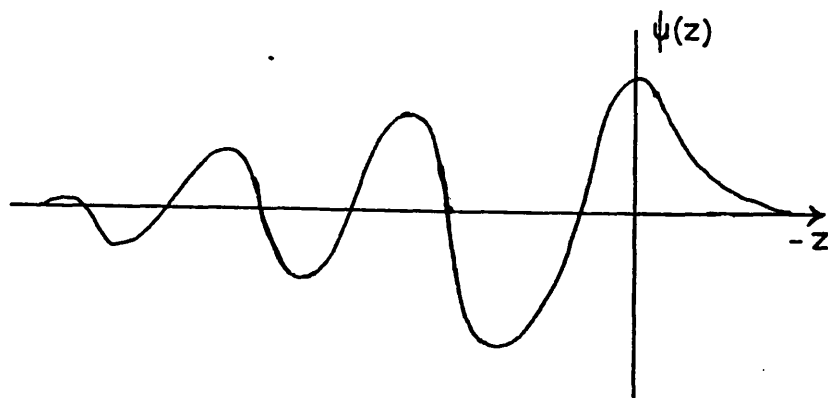


Figure 2.8 Schematic representation of the decay of a wavefunction $\psi(z)$ into the vacuum at a surface.

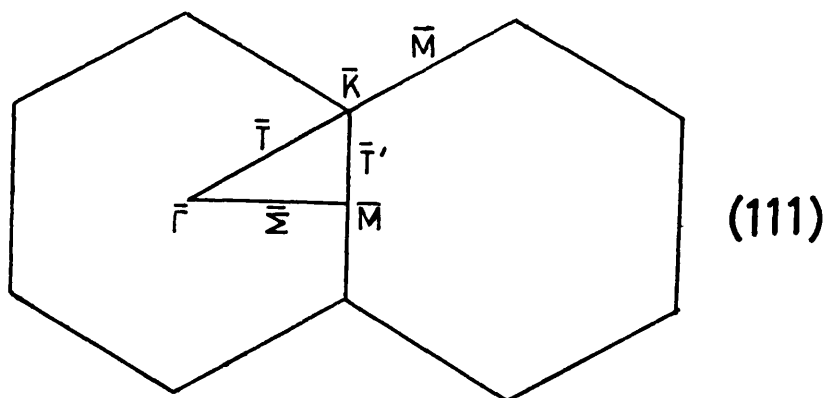
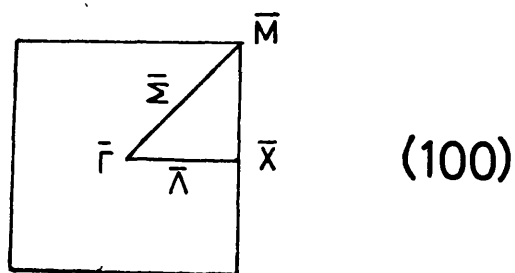


Figure 2.9 The FCC Surface Brillouin Zones

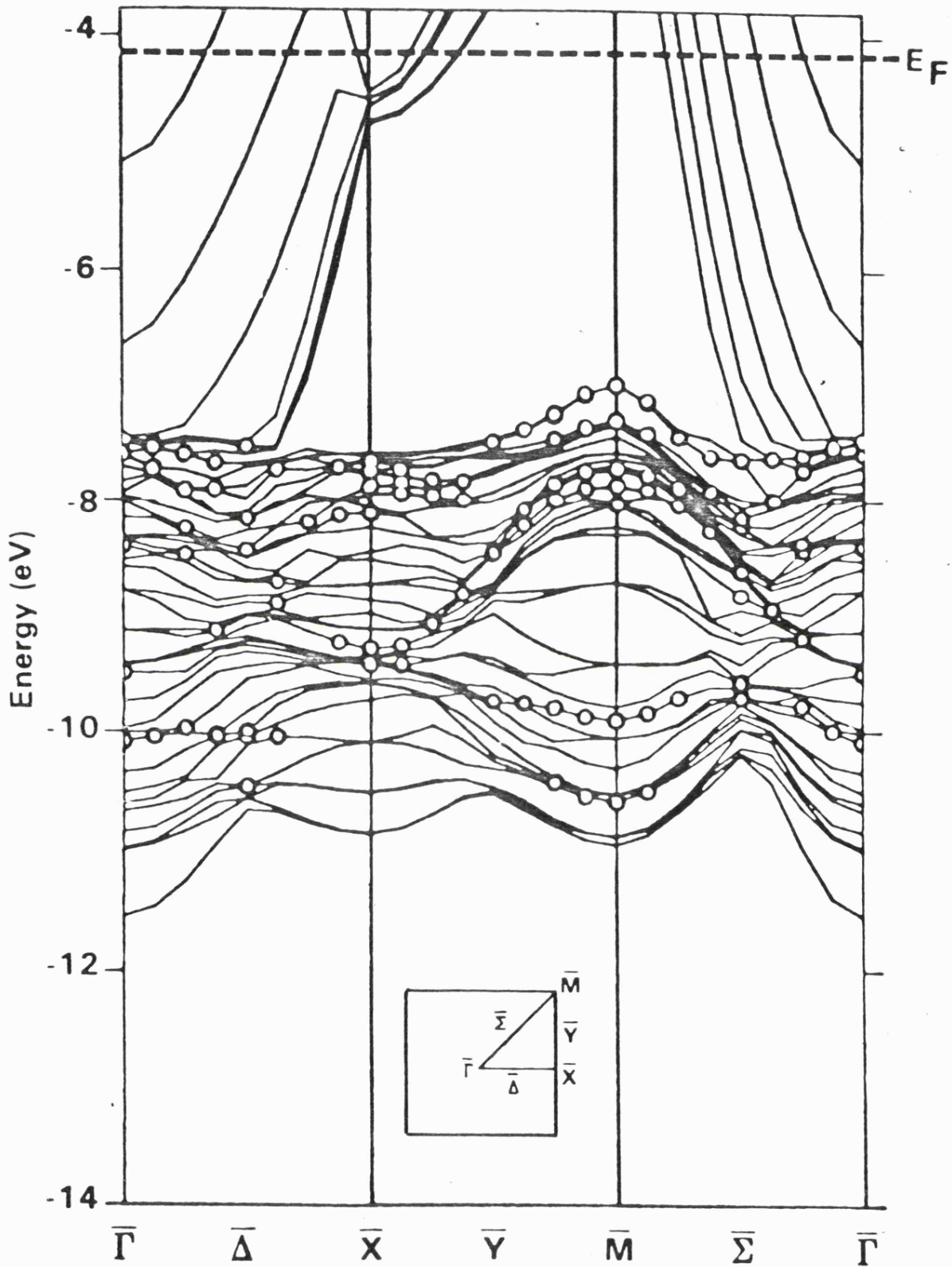
resonances) were found. For Cu(100) this was used to explain the large attenuation of photoemission near the top of the d-band on chemisorption (Tibbets et al 1977). Similar attenuation for Ag(100) was seen in the present work, and is discussed in chapters 4, 5, 6 and 7. The surface electronic structure of Ag(100) given by Smith and co-workers is reproduced in figure 2.10.

2.5.3 Thin Film and Layer Calculations

Due to the localized nature of d-electrons a thin slab of a transition metal may well reproduce an essentially bulk electronic structure after inclusion of typically only seven or nine layers (Wang and Freeman 1979). Taking a thin layer reduces the complexity of calculation and self-consistency may be achieved more readily than for the bulk case. Wang and Freeman (1980) have presented ab initio spin polarized self-consistent LCAO energy bands for ferromagnetic 3d transition metal films. For Ni(100) nine layers were found to be sufficient to accurately determine the energy dispersion and spatial character of surface states and their effect on surface magnetism, electron spin polarization and average exchange splittings. In the case of Fe(100) seven layers were adequate.

Smith et al (1980) used a seven layer slab for the prediction of surface states on Ag(100) whereas Yokoyama et al (1981) used five layers in their self-consistent investigation of the electronic structure and spin polarization of V(100).

As an approach to the electronic structure of an adsorbate it is instructive to consider the case of an isolated monolayer. This is



Surface band structure along high - symmetry directions for the 7 - plane Ag(100) slab. Open circles represent states highly localised in the surface plane.

FIG. 2.10

especially true when a relatively inert substrate is used and the point is elaborated in subsequent chapters. Noffke and Fritsche (1981) have presented self-consistent spin polarized calculations of the energy bands of unsupported Fe, Cu, Ni and Pd(100) monolayers using the Linear Rigorous Cellular (LRC) method (Fritsche et al 1979, Hermann et al 1980). The isolated copper monolayer has been the subject of intense investigation, with controversy surrounding the possibility of d-band holes and the behaviour of the band width and position with thickness (Arlinghaus et al 1979).

In all recent layer calculations the importance of self-consistency is emphasized. This appears to be a critical factor with profound changes often being found on going to a self-consistent result.

2.6 The Work Function

In the photoemission experiment the maximum kinetic energy of a photoemitted electron is given by

$$E_{\text{Kin}_{\text{max}}} = h\omega - \phi$$

where ϕ , the work function, is the energy difference between the Fermi level and the vacuum level. Calculation of the work function is conceptually simple; it is the difference between E_N , the ground state energy for the neutral N-electron solid, and E_{N-1} the ground state energy for the solid with N-1 electrons and charge +1. Unfortunately, the quantum mechanical calculation of ϕ is a complex many body problem which cannot be solved except by making drastic approximations. In principle the calculation yields the internal work function - $\bar{\mu}$ ($\bar{\mu}$ = chemical potential)

$$E_N - E_{N-1} = -\bar{\mu}$$

however a real surface does not have the same charge distribution as a bulk plane. There is redistribution of charge at the surface, resulting

in a dipole, D as shown in figure 2.11.

$$\begin{aligned} \Phi &= -\bar{\mu} + D \\ \text{or} \quad \Phi &= \phi - \mu + D \end{aligned}$$

when ϕ is the average self-consistent electrostatic potential of the electron in the solid. Exchange and correlation effects are included in the term μ .

Writing Φ in terms of averages leads to the expectation that reasonably accurate work functions of simple metals may be obtained using a uniform positive-background or Jellium model. In this model the lattice of positive ions is replaced by a uniform background charge with an abrupt cut-off at the surface. Such a calculation has been carried out by Lang and Kohn (1971). Deep in the interior of the metal the electron density has a constant value \bar{n} and $\bar{\mu}$ takes the simple form

$$\bar{\mu} = \frac{1}{2} k_F^2 + \mu_{xc}(\bar{n})$$

where $k_F = (3\pi^2 \bar{n})^{1/3}$, the bulk Fermi wave number

μ_{xc} = exchange and correlation part of the chemical potential of an infinite uniform electron gas.

$$= \frac{d}{dn} \left[n \epsilon_{xc}(n) \right]$$

$\epsilon_{xc}(n)$ = exchange and correlation energy per particle of the uniform gas.

From the many body theory of the electron gas (Pines 1963) $\epsilon_{xc}(n)$ may be expressed as

$$\epsilon_{xc}(n) = -\frac{0.458}{r_s} - \frac{0.44}{(r_s + 7.8)}$$

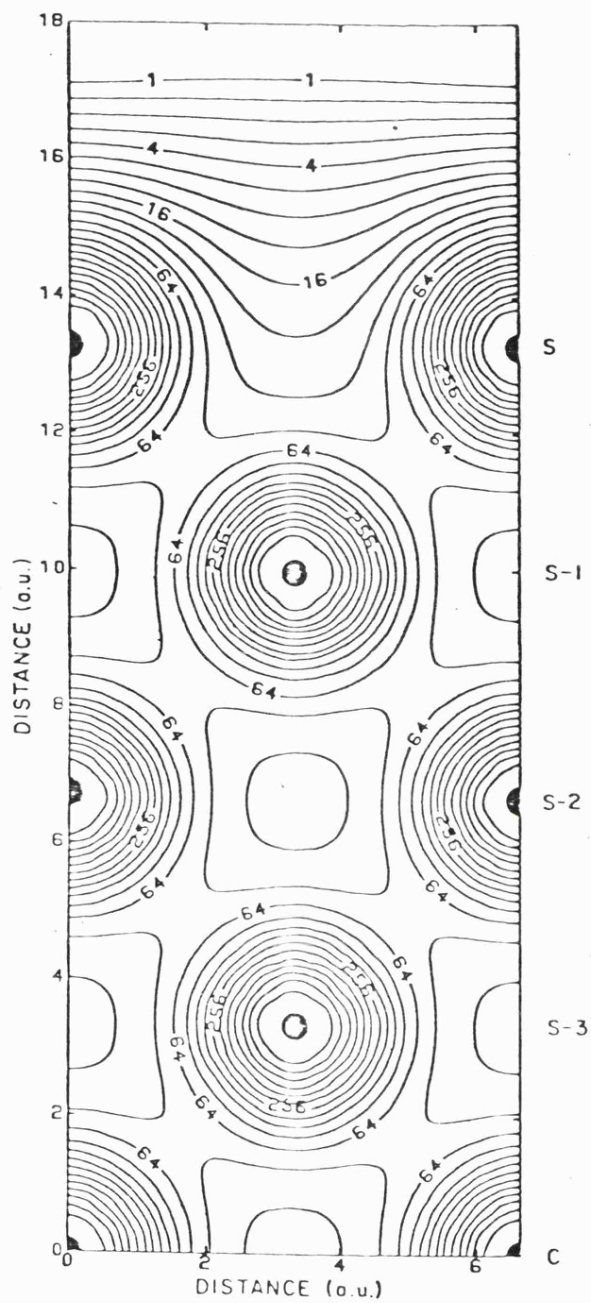
with r_s , the Wigner-Seitz radius, given by

$$\frac{4}{3} \pi r_s^3 = \frac{1}{\bar{n}}$$

The double layer dipole contribution D may be evaluated using

Poisson's equation

$$D = 4 \pi \int_{-\infty}^{+\infty} x [n(x) - n_+(x)] dx$$



Self consistent charge density map in units of .001 a.u. on the Ni(110) plane. Each contour line differs by a factor of $\sqrt{2}$.

FIG. 2.11

where $n(x)$ and $n_+(x)$ are respectively the electron and positive background charge densities.

Theoretical values using the uniform positive background model are compared with experimental results for simple metals in figure 2.12. Also shown are the results of an ion-lattice model in which the Jellium model was improved by replacement of the uniform positive background by ion pseudopotentials of the form employed by Ashcroft and Langreth (1967). The difference between this potential and the uniform positive background provides a perturbation on the work function, and is seen to improve agreement between theory and experiment.

The situation is not so satisfactory for the transition metal surfaces. The localization of the d-electrons breaks down the approximations of the Jellium model and the presence of surface states strongly affects the dipole contribution. A full self-consistent calculation of the surface states is necessary before an accurate value of ϕ can be expected. The majority of transition metal band structure calculations have been of the APW type using a muffin-tin potential with the energy zero chosen to be at the energy of the flat interstitial regions, so no information on the work function is obtained. It is, however, possible to extract the work function when a slab calculation is performed. The self-consistent local orbital method of Smith et al (1980) yielded a value of 4.2 eV for the face of a nine-layer (100) slab of Ag, in reasonable agreement with the accepted value of 4.64 eV (Dweydari and Mee 1975). These authors also report a theoretical value of 5.6 eV for Cu(100) (Gay et al 1977), in rather less good agreement with the experimental value of 4.77 eV (Tibbets et al 1977).

2.7 Work Function Change on Metal Adsorption

The situation regarding the theory of the work function change experienced by a metal surface on adsorption of a metal overlayer is

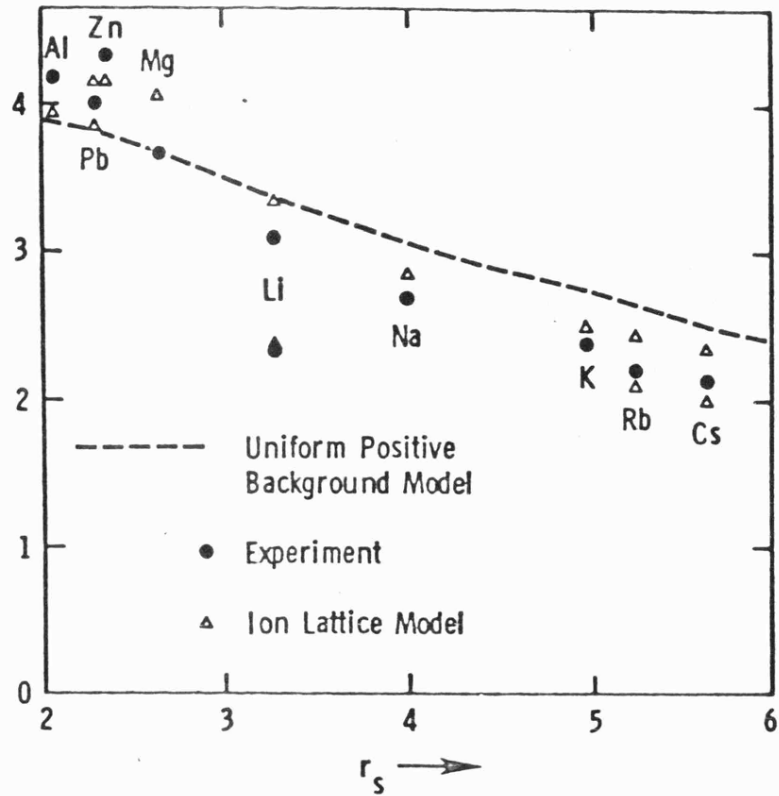


Figure 2.12 The variation of work function with electron density

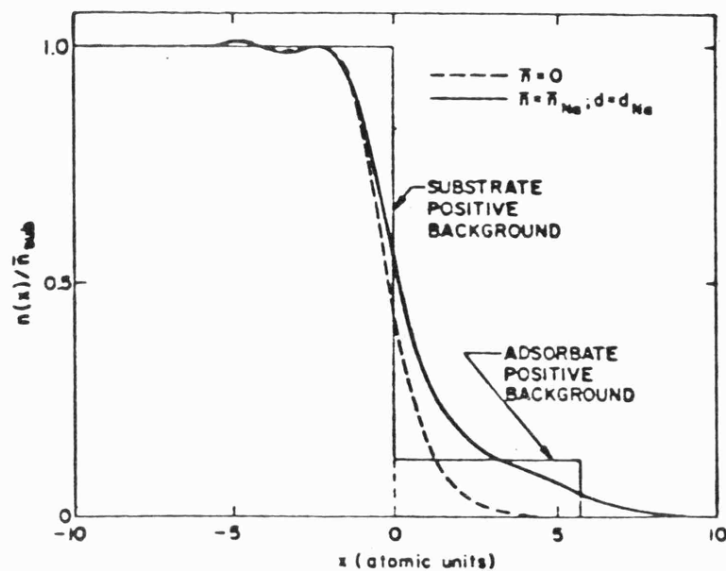


Figure 2.13 Self consistent electron density distribution $n(x)$ for bare substrate model and for a model of substrate with a full layer of adsorbed Na atoms

analogous to that of bulk metal surfaces. Alkali adsorption is quite well understood, with the Jellium model (Lang 1971) as well as various other methods (Muscat and Newns 1974, Gyftopoulos and Levine 1962) being applicable, whereas transition metal overlayers cause greater theoretical difficulty and the problem does not yet appear to have been tackled.

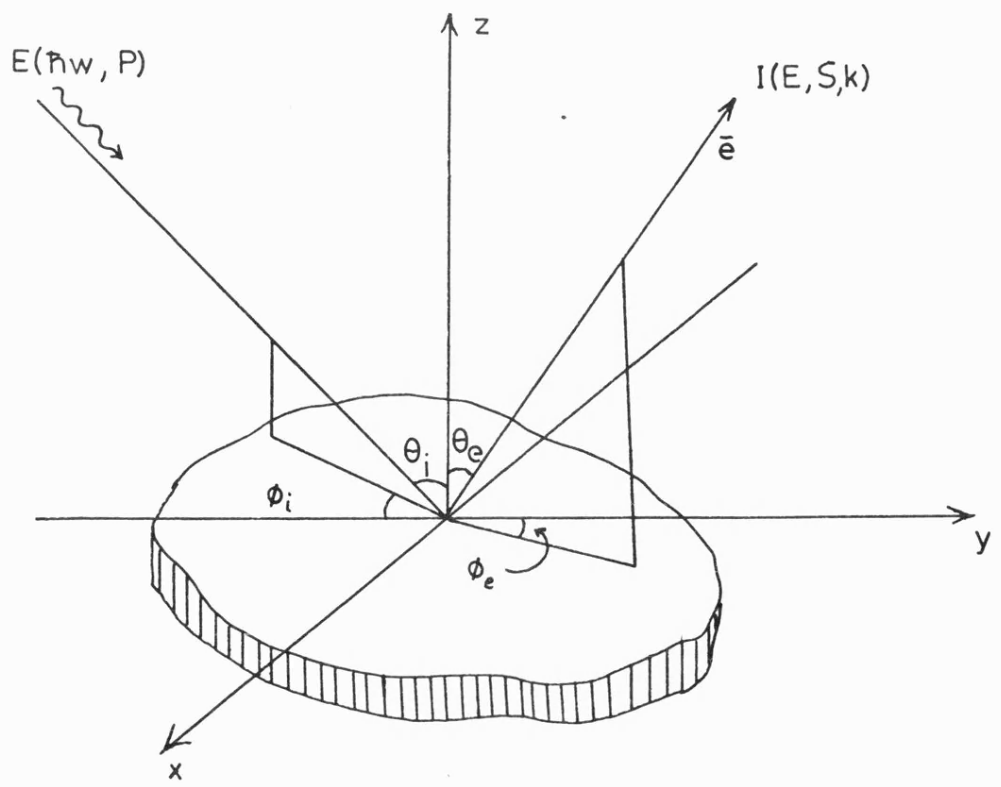
It is well known that alkali metal adsorption onto a close-packed metal surface results in an initial rapid decrease of Φ . With increasing coverage a minimum is reached, after which Φ rises and the bulk alkali value occurs at completion of the first monolayer of adsorbed atoms. The phenomenon was first described quantum-mechanically by Gurney (1935). The adsorbed atom valence electron energy level lying in the vicinity of the substrate Fermi level was viewed as being broadened by the presence of the substrate. The position of the level relative to the Fermi energy determined the fractional occupation of this level which in turn governed the degree of ionization and hence the strength of the dipole moment per adatom. Each dipole is depolarized by the electric field due to all the others, hence the greater the coverage the greater the depolarization. The minimum occurs at the coverage at which the relative decrease in dipole moment per atom (dp/p) balances the relative increase in number of dipoles (dN/N). The model, though conceptually satisfying, involves a good deal of complexity in its application (see Muscat and Newns 1974, for a similar approach).

The alternative method of Lang (1971) was to treat a much simpler model exactly. The model used was an extension of the uniform positive background described in the previous section by addition of a uniform charge density layer at the surface to represent the adsorbate. The adsorbate positive background and resulting self-consistent charge

density are shown in figure 2.13. The calculation proceeded in the same manner as for the clean substrate, the only difference being the form of the electrostatic potential. The theory was found to predict the trend of both the decrease in the minimum of the work function and the decrease in the coverage at which this occurred for the series Li, Na, K, Cs. At one monolayer coverage the bulk value was obtained, as observed experimentally. Although the replacement of an array of adsorbate ions by a continuous charge distribution is a severe approximation for a sparse array, the low coverage results were also in fair agreement with experiment.

2.8 Photoemission

The photoemission experiment is summarized in figure 2.14. Light of energy $\hbar\omega$ and polarization P impinges upon the sample surface at incident angle θ_i and azimuthal angle ϕ_i . The system responds to this excitation by emission of electrons of energy E and spin polarization S at a certain emission angle θ_e and azimuthal angle ϕ_e . There have been two theoretical approaches to the interpretation of such an experiment, based on the one electron model involving direct transitions between states of the crystal or on the results of scattering theory such as used in the analysis of LEED beam intensities. These are known respectively as the three-step and one-step models. Both were used in the analysis of data presented in this thesis. Their use in the interpretation of experimental data is discussed in sections 2.8.1 and 2.8.2 below. It is not intended to present the full theory of each model since this is not necessary for an understanding of the experimental results, and in any case may be found in several reference works and review articles (for example, Feuerbacher et al 1978, Cardona and Ley 1978, Pendry 1976).



The Photoemission Experiment

FIG. 2.14

2.8.1 The Three-Step Model

Since the work of Berglund and Spicer (1964) experimental valence band photoemission spectra have almost universally been interpreted in terms of the three step model. In this model the photoemission process is factorized into three steps:

- 1) optical excitation of an electron,
- 2) transport through the solid, including the possibility of inelastic scattering, and
- 3) escape through the sample surface into the vacuum.

The primary photoelectron energy distribution (for a given symmetry direction of the BZ) may thus be written down as

$$I_p(E, \hbar\omega) = P(E, \hbar\omega) T(E) D(E)$$

where $P(E, \hbar\omega)$ = distribution of photoexcited electrons
 $T(E)$ = transport function
 $D(E)$ = escape function.

Under the assumption that the inelastic scattering probability may be described by an isotropic mean free path $\lambda_e(E)$, $T(E)$ is given by

$$T(E) = \frac{\lambda_e(E) / \lambda_{ph}(\hbar\omega)}{1 + \lambda_e(E) / \lambda_{ph}(\hbar\omega)}$$

where $\lambda_{ph}(\hbar\omega)$ is the attenuation length of the incident photons at energy $\hbar\omega$. For typical ultra-violet energies $T(E)$ is ~ 0.1 and is a slowly varying function of energy.

For electrons of energy $E > E_F + \phi$ excited into plane wave-like final states $E = \hbar^2 k^2 / 2m$ an escape cone of angle θ relative to the surface normal is defined:

$$\cos \theta = \left(\frac{\phi + E_F}{E} \right)^{\frac{1}{2}}$$

If the distribution of electrons within the solid is isotropic then the escaping fraction is given by

$$D(E) = \frac{1}{2}(1 - \cos \theta) ; E > E_F + \phi$$

$$= 0 ; E < E_F + \phi$$

This is also a smoothly varying function of E . While $D(E)$ and $T(E)$ may be expected to distort the energy distribution of emitted electrons, any sharp structure in $I_p(E, \hbar\omega)$ must result from structure in $P(E, \hbar\omega)$. $P(E, \hbar\omega)$ is given through k -conserving transitions from occupied states E_i into unoccupied states E_f . Thus

$$P(E, \hbar\omega) \propto \sum_{i,f} \int d^3k | \langle f | \underline{p} | i \rangle |^2 \delta [E_f(\underline{k}) - E_i(\underline{k}) - \hbar\omega] \delta [E_f(\underline{k}) - E]$$

For a constant dipole matrix element $M_{if} = \langle f | \underline{p} | i \rangle$ the so-called energy distribution of the joint density of states (EDJDOS) is obtained

$$P(E, \hbar\omega) \propto \sum_{i,f} \int d^3k \delta [E_f(\underline{k}) - E_i(\underline{k}) - \hbar\omega] \delta [E_f(\underline{k}) - E]$$

and the photoelectron energy distribution curve is a distorted version of the initial and final state densities.

The model predicts a feature in the energy distribution curve (EDC) when an occupied state at energy E_i is separated from an unoccupied state at the same \underline{k} (in the reduced zone scheme) at energy E_f such that $E_f - E_i = \hbar\omega$, the photon energy. As direct transitions at specific points in $E - \underline{k}$ space may be identified the theory lends itself to the use of photoelectron spectroscopy as a tool for band structure mapping. This is discussed further in chapter 4.

2.8.2 The One-Step Model

In order to describe the photoemission process as the response of an interacting multi-electron system to an electromagnetic field two different formalisms have been used. The quadratic response formalism developed by Ashcroft and Schaich (1969) has been shown to be equivalent to the methods of Lippmann and Schwinger (1950) and Gellmann and Goldberger (1953) based upon formal scattering theory (Schaich and Ashcroft 1971). Pendry (1976) has presented a solution of the one-step model which has

been incorporated into a computer program (Hopkinson et al 1976). In this model the initial states are calculated with the effect of the surface included and so surface states emerge naturally. The effect of crystal symmetry is included in the calculation of matrix elements between the appropriate wave fields. The attenuation and redistribution of photoemitted intensity due to scattering of the outgoing electron by the ion cores is also introduced.

Following Hopkinson et al (1979), the number of electrons emitted per photon per unit solid angle per unit energy is:

$$I = \underbrace{[2(E+\omega - V_{or})]}_{(1)} \underbrace{\frac{1}{2} \cos\theta}_{(2)} \times \underbrace{[2(E+\omega)]}_{(3)} \underbrace{\cos\theta}_{(4)} \times \frac{2N\Omega}{(2\pi)^2} \times \frac{I(k_{\parallel}, E+\omega - V_{or})}{(N\Omega)^2} \quad (2.8.1)$$

Atomic units are used ($e = h = m = 1$, unit of distance = Bohr radius, unit of energy = Hartree, $c = 137.036$). The \underline{A} vector of the incident radiation is described by

$$A = \frac{1}{(N\Omega)} \underline{a} \cos(\underline{q} \cdot \underline{r} - \omega t)$$

$$\underline{q} \cdot \underline{a} = 0$$

and the equation has been normalized to unit photon per unit time

$$|\underline{a}|^2 = \frac{8\pi c}{\omega \cos\theta}$$

Ω = area of one unit cell

$(N\Omega)$ = area of surface illuminated.

Term (1), with θ the polar angle of the escaping electron, represents the velocity of the escaping electron normal to the surface. Term (2) is the projection of unit solid angle onto the k_{\parallel} plane. Term (3) is the density of states in k_{\parallel} space and includes a factor of 2 to allow for spin. The last term, (4) is the density of an outgoing

wave of wave-vector $k_{//}$ at a plane $z = z_0$ outside the surface.

Energy E is referred to the muffin-tin zero and V_{or} is the height of the surface barrier.

$k_{//}$ is defined by the energy and polar coordinates of the electron in vacuo

$$k_{//x} = \left[2(E + \omega - V_{or}) \right]^{\frac{1}{2}} \sin\theta \cos\phi$$

$$k_{//y} = \left[2(E + \omega - V_{or}) \right]^{\frac{1}{2}} \sin\theta \sin\phi$$

The photocurrent may be obtained by constructing the outgoing state, measured in the experiment

$$\langle \underline{r} | \underline{k}_{//}, E + \omega \rangle = L^{-3/2} \exp(i \underline{k}^- \cdot \underline{r})$$

$$\text{where } \underline{k}^{\pm} = (k_{//x,y} \pm \left[2(E + \omega) - |k_{//}|^2 \right]^{\frac{1}{2}})$$

and L is a characteristic dimension of the experiment.

Inside the crystal the state is a linear combination of Bloch waves of energy $E + \omega$ and component of crystal momentum vector parallel to the surface $k_{//}$ which are so constructed as to match at the surface to the wavefunction outside. Writing the initial state as $|j, E\rangle$ gives (Pendry 1976) an emitted state of the form

$$\sum_{\underline{k}} - \frac{iL}{k_z^+} | \underline{k}_{//}, E + \omega \rangle \langle \underline{k}_{//}, E + \omega | \Delta | j, E \rangle$$

and summing the photocurrent from each state gives

$$I(k_{//}, E + \omega) = \sum_j \frac{L}{k_z^+} | \langle \underline{k}_{//}, E + \omega | \Delta | j, E \rangle |^2 \quad (2.8.2)$$

which forms term (4) in (2.8.1) above. Δ is the perturbing term in the Hamiltonian

$$\Delta = \frac{1}{2c} (\underline{p} \cdot \underline{A} + \underline{A} \cdot \underline{p})$$

If a choice of gauge is made such that

$$\nabla \cdot \underline{A} = 0$$

and \underline{p} commutes with \underline{A} then it can be shown that

$$\Delta = \frac{\underline{A} \cdot \nabla V}{\omega c}$$

Thus the potential plays a dual role both as a source of photocurrent and as a scatterer.

(2.8.2) forms the basis of the so-called static method of calculation in which stationary states at initial and final energies are found and then a matrix element calculated. This procedure is inefficient in that all Bloch waves with energy $E + \omega$ and parallel momentum k_{\parallel} are calculated but only a single linear combination of them is used to find the matrix element. Recently more economic methods have been introduced, in which only the required final state is calculated. In the method suggested by Pendry (1975) evolution of the final state wave field produced by the incoming photons from the valence and conduction bands at each point in the crystal is followed out of the crystal taking into account all scattering events on the way. An alternative, equivalent, method has been proposed by Liebsch (1974). In the scattering method the emergent wave state is equivalent to a time-reversed LEED state, and LEED programs are incorporated in the computation.

The computer implementation of this model of photoemission is available through the theory group of Daresbury Laboratory (SERC) and is known as PEOVER. The program, as used in this work, runs on the CRAY-1 computer and is also IBM 370/165 compatible. The program takes as input the substrate crystal structure and the geometry of any over-layers together with the appropriate muffin-tin potentials, initial and final state lifetimes, and control parameters; and calculates the photocurrent emergent in a particular direction and energy range for a given photon energy and incident beam direction. Examples of its

use are given in the following chapters.

Most of the information required to determine the Bloch waves at a particular energy is available in the program so a section was added to complete the calculation. The electron and hole lifetimes and all beam angles are set to zero and the band structure may then be obtained by searching for zeros in the imaginary part of \underline{k} .

A typical input data set consisting of overlayer and substrate geometry and potentials, and output information, is given in Appendix 2.

CHAPTER 3
EXPERIMENTAL TECHNIQUES

- 3.1 Introduction
- 3.2 ADES-1 at Daresbury
- 3.3 Sample Manipulation
- 3.4 Monitoring LEED patterns
- 3.5 Detection of Auger Electrons
- 3.6 Photoelectron Analyser
- 3.7 Ultra-Violet Discharge Source
- 3.8 Synchrotron Radiation
 - 3.8.1 Properties of Synchrotron Radiation
 - 3.8.2 Daresbury Synchrotron Radiation Source
- 3.9 Beam Line and Monochromator
- 3.10 Data Collection
- 3.11 Leicester Chamber
- 3.12 Crystalline Surface Preparation
- 3.13 Overlayer Growth - General Considerations
- 3.14 Transition Metal Vapour Source

CHAPTER 3
EXPERIMENTAL TECHNIQUES

3.1 Introduction

The spectroscopic techniques used in this work are concerned with electrons produced at the surface of a solid sample by electron or photon incidence emitted with energies in the range 10 to 400 eV. The electron inelastic mean free path data reproduced in figure 3.1 (Seah and Dench 1979) show a minimum in this energy range. Electrons in this range which escape without loss of energy originate from the top few atomic layers of the material. The techniques are therefore surface sensitive and necessitate the use of ultra high vacuum (UHV). The production of UHV is standard laboratory practice and is described in many textbooks (see for example Redhead 1968, Yarwood 1967).

Kinetic theory of gases shows that the average number of gas atoms sticking unit area of a metal sample in unit time is given by

$$\bar{n} = 2.89 \times 10^{22} p(MT)^{-\frac{1}{2}} \text{ cm}^{-2} \text{ s}^{-1}$$

where p = pressure (torr)

M = molecular weight

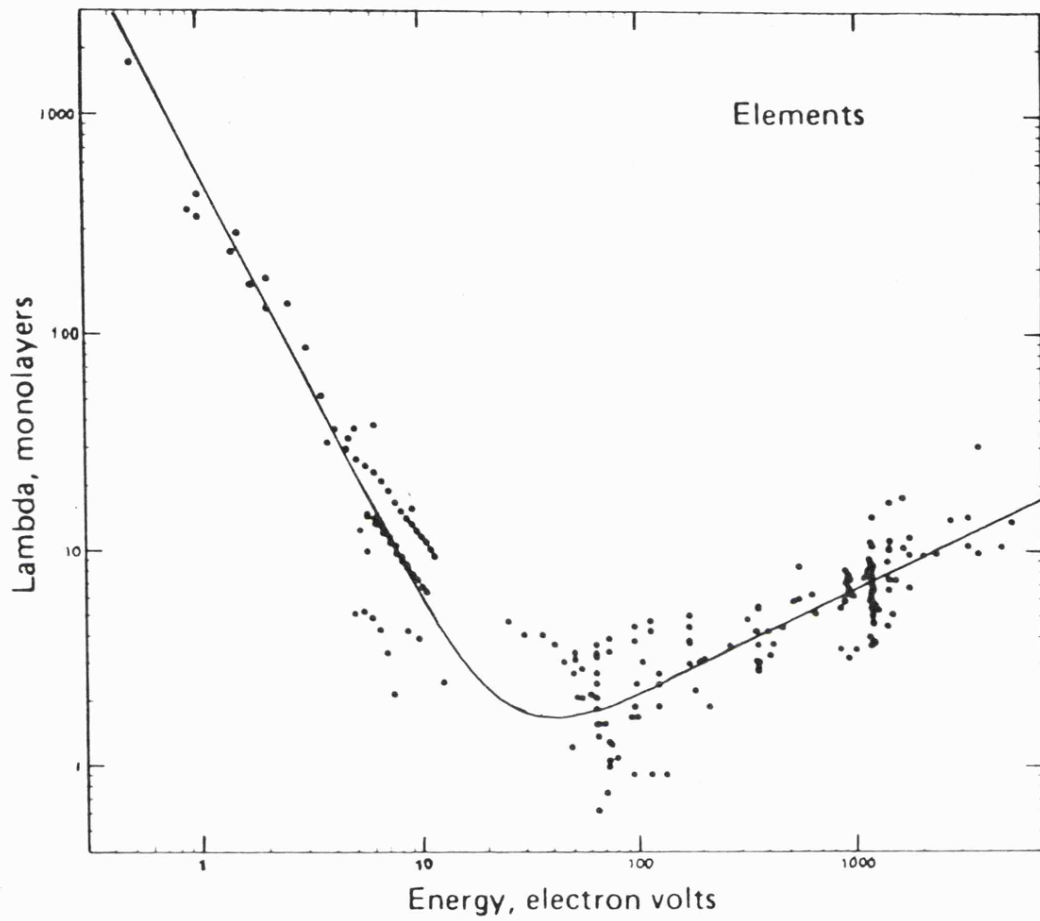
T = temperature (K)

Assuming a mean molecular weight of 28 for air at room temperature gives

$$\bar{n} \sim 10^6 s \text{ monolayers s}^{-1}$$

where s = sticking coefficient.

If s is unity a monolayer of nitrogen would be adsorbed in an hour at 3×10^{-10} m bar, the typical ambient pressure. s , however, is strongly dependent on the nature of the adsorbate, the substrate, and the substrate temperature. For the single crystal surfaces of copper, silver and palladium at room temperature no significant surface contamination (i.e. $\leq .01$ ml) was found after eight hours. The ultrathin transition metal



Experimental measurements of imfp's in monolayers, for elements

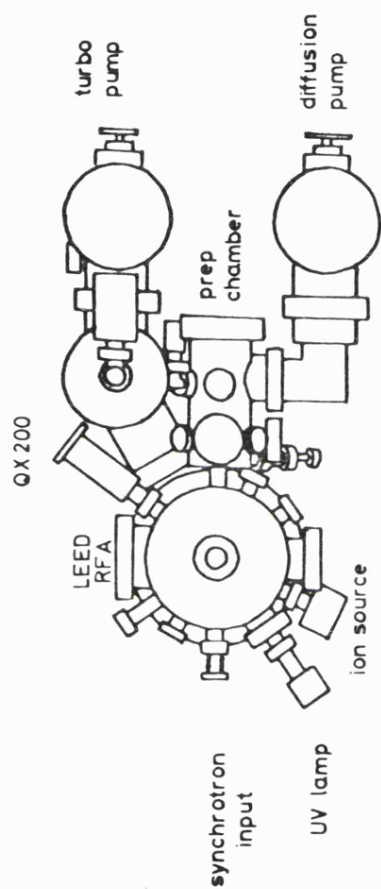
FIG. 3.1

overlayers were more reactive and showed signs of deterioration after three to four hours at 3×10^{-10} mbar.

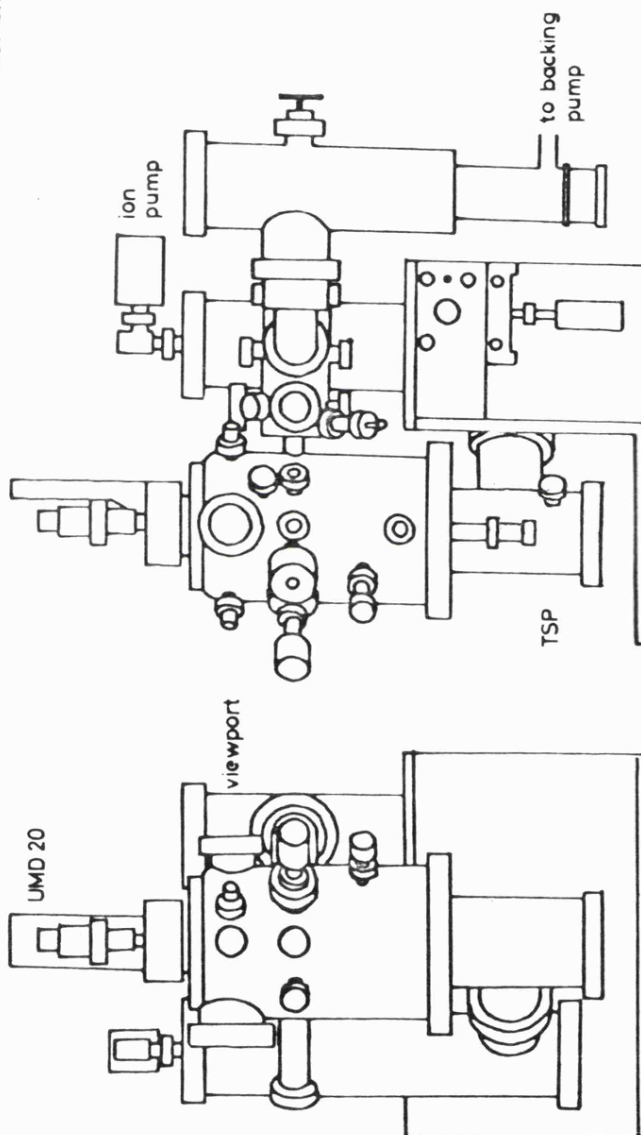
Most of the work described in this thesis was carried out at the Science and Engineering Research Council (SERC) Daresbury Laboratory, using a modified Vacuum Generators ADES 400 angle resolving electron spectrometer. Data were recorded with both synchrotron radiation from the newly commissioned Synchrotron Radiation Source (SRS) and ultra-violet radiation obtained from a noble gas discharge source. The Daresbury chamber and the different spectroscopic techniques are discussed in sections 3.2 to 3.10. Crystal preparation and some of the characterization of overlayer growth modes was done at Leicester using a chamber described previously (Binns 1981). The general features of this chamber are given in section 3.11. Production of the single-crystal copper (100), silver (100) and (111), and palladium (111) surfaces is discussed in section 3.12. The general principles of vapour deposition and the form of the metal vapour source used in this study are described in sections 3.13 and 3.14.

3.2 ADES-1 at Daresbury

The VG ADES 400 electron spectrometer, modified to accept synchrotron radiation at 1m beam height, is shown schematically in figure 3.2. The main chamber body was fabricated from mu-metal to minimize stray electromagnetic fields and has two experimental levels. The upper level was equipped with 4-grid electron optics and integral electron gun for LEED and Auger spectroscopy, high current electron gun and detector for physical imaging, QX-200 quadrupole mass spectrometer, and could accommodate up to three of the high temperature metal vapour sources developed at Leicester. At the lower level were an argon ion gun, a noble gas discharge source, an X-ray source (removed when the



gas manifold and differential pumping not shown



ADES spectrometer

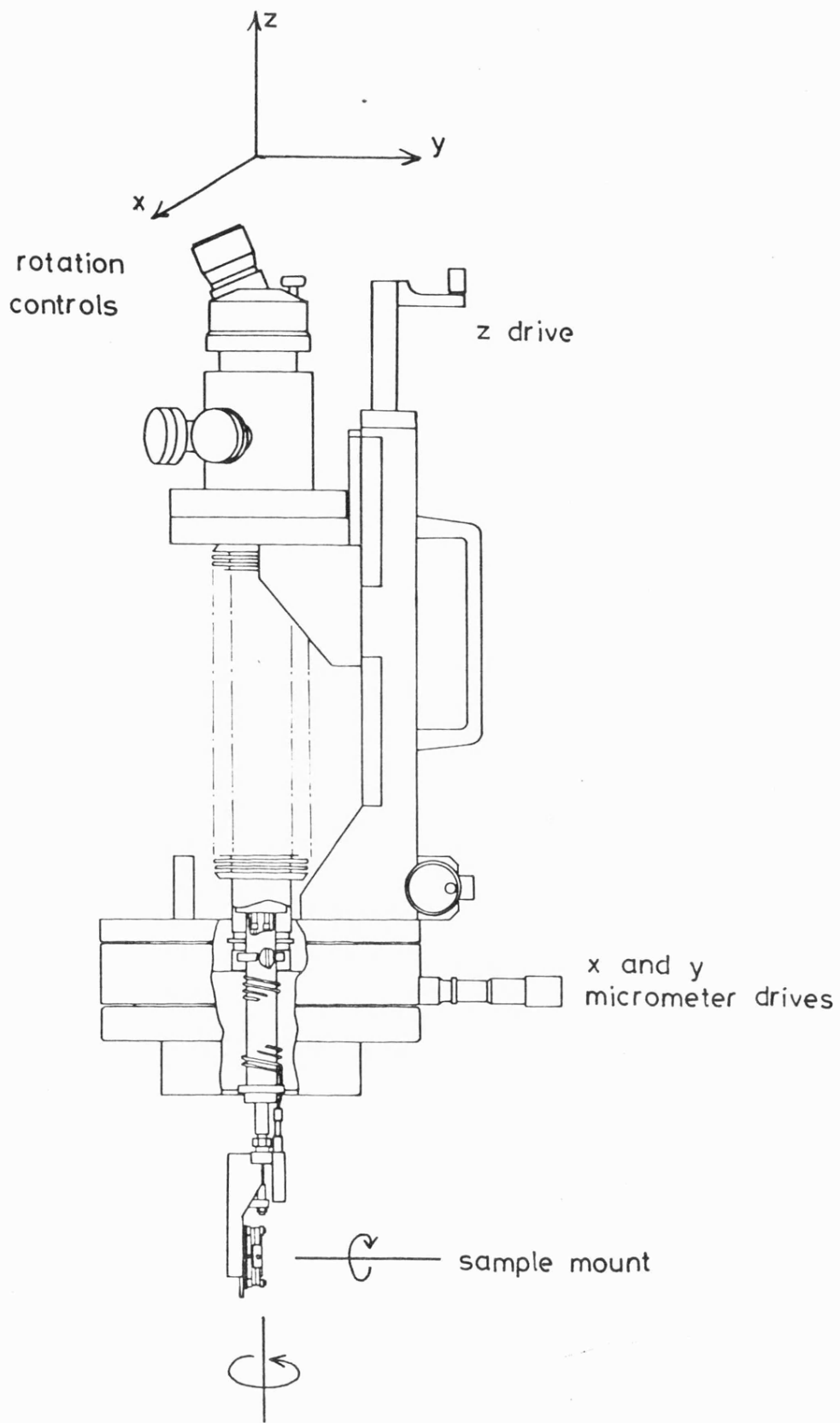
FIG. 3.2

chamber was installed on the synchrotron beam line) and the photoelectron analyser. Also shown in the figure is the sample preparation chamber, which was not used in this work.

The pumping system was chosen to give a clean residual atmosphere. The system was pumped from atmospheric pressure to 10^{-2} mbar by a trapped rotary pump. Turbomolecular pumping on the main chamber and diffusion pumping on the preparation chamber then took the pressure down rapidly to 1×10^{-7} mbar. To remove adsorbed gases from the chamber walls and achieve ultimate pressure bakeout, typically at 200°C for 12 hours, was necessary. This was followed by thorough outgassing of all hot filaments and, after cooling, pressures below 1×10^{-10} mbar were obtained. Cooling the top of the turbomolecular pump with liquid nitrogen was found to have no effect on the chamber pressure. The best recorded pressure was 3×10^{-11} mbar, at the X-ray limit of the gauge. Residual gas analysis using the QX200 quadrupole mass spectrometer showed the typical UHV atmosphere to be composed of mainly hydrogen and methane. Smaller traces of CH_3 , OH , H_2O , N_2 , CO and CO_2 were also observed.

3.3 Sample Manipulation

The single crystal substrates were mounted on the VG UMD20 sample manipulator shown in figure 3.3. Micrometer drives controlled the X and Y translation and up to 15 cms of vertical movement was possible. The crystal could also be rotated about the vertical axis of the manipulator and azimuthally about an axis normal to the manipulator axis. The alignment of the crystal on the manipulator was checked prior to mounting in UHV by reflecting laser light from the surface onto a suitable plane approximately 5 m away while operating the azimuthal drive. Small packing pieces were used behind the crystal mount and adjusted until movement of the reflected laser spot with azimuthal rotation corresponding



• sample manipulator

FIG. 3.3

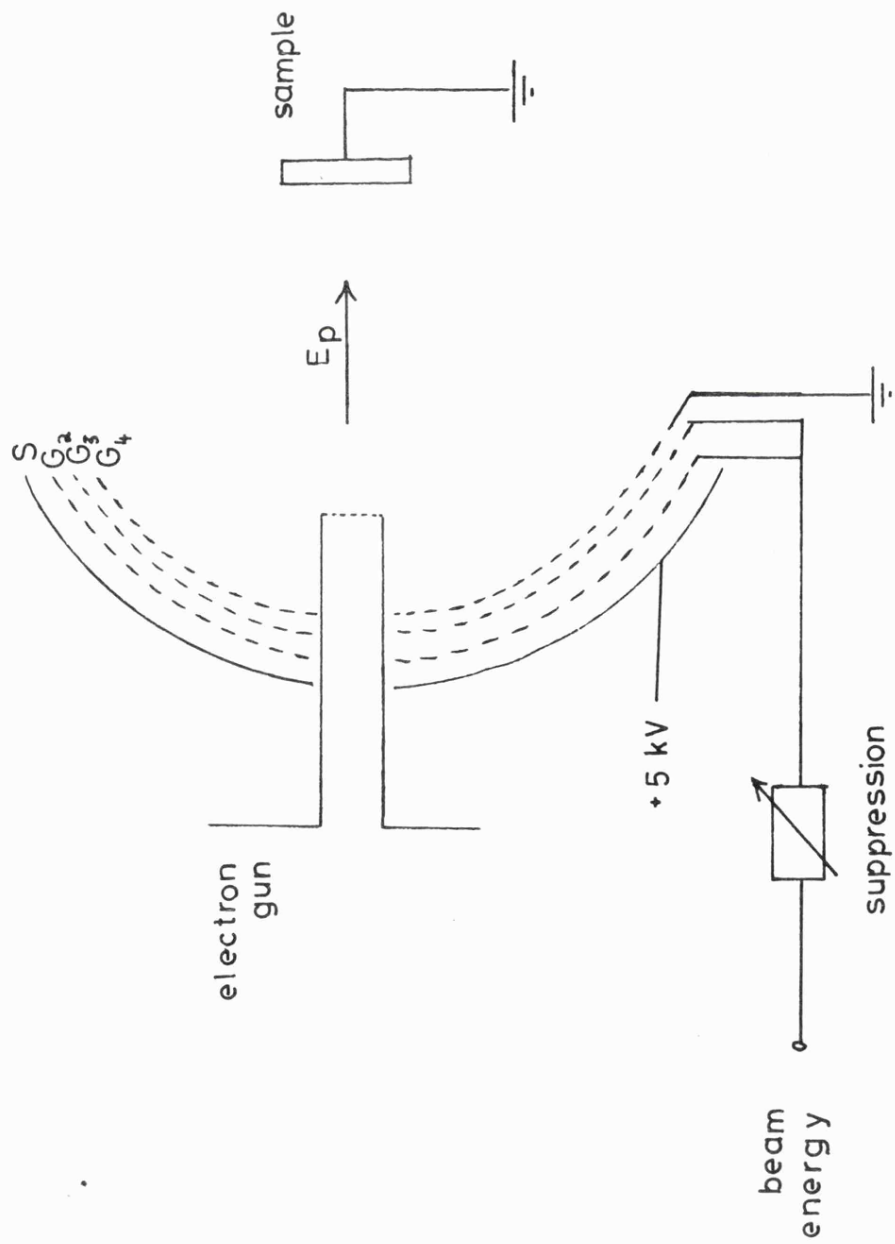
to $\pm \frac{1}{2}^\circ$ was obtained. The sample temperature could be varied between room temperature and 600°C by a resistive heater, and cooling by liquid nitrogen was also available.

3.4 Monitoring LEED Patterns

Low energy electron diffraction (LEED) as first described by Davisson and Germer (1927) enabled monitoring of the crystalline perfection of the substrate and the periodicity of the ordered overlayers during deposition experiments. The standard 3-grid LEED arrangement is shown in figure 3.4. G_2 , G_3 and G_4 are concentric fine stainless-steel meshes of spherical section and 90% optical transparency and S is a phosphor-coated aluminium screen. The sample and G_4 are at earth potential, G_2 and G_3 are held slightly lower than the beam potential and S is raised to + 5kV. Inelastically scattered secondary electrons cannot pass G_2 and G_3 and the elastically scattered ones which do so are accelerated and cause fluorescence on S, resulting in display of the diffraction pattern.

3.5 Detection of Auger Electrons

The detection of Auger electrons was demonstrated by Lander (1953) with the use of a 90° spherical electrostatic analyser and by Thorp and Scheibner (1967) using a LEED system as a retarding field analyser (RFA), where a small modulating voltage was applied to the retard grid and the collector tuned to the frequency of the applied signal in a manner similar to that described by Lebler and Simpson (1958). Although of interest, the technique appeared to have limited application due to its apparent lack of sensitivity until it was noted (Harris 1968) that electronic differentiation of the energy distribution function



Low Energy Electron Diffraction Optics

FIG. 3.4

greatly enhanced the Auger spectrum detectability.

The conventional 3-grid LEED optics can be used as an RFA in this differentiating mode when connected as shown in figure 3.5 (Weber and Peria, 1967). A ramped negative voltage V_E applied to G_3 results in a current reaching the collector given by the transfer characteristic

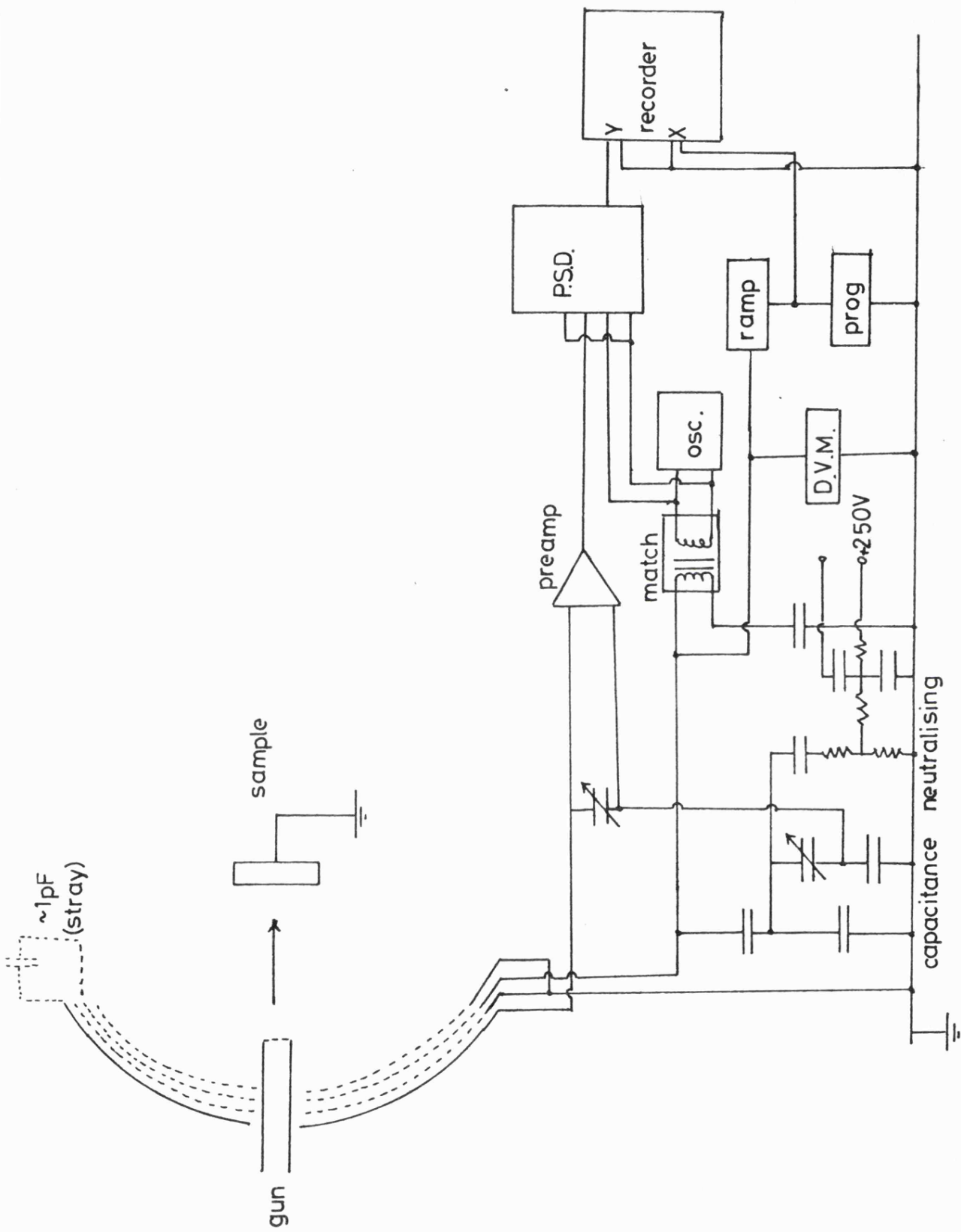
$$I(E) = \int_E^{\infty} N(E) dE$$

where $E = eV_E$ and $N(E)$ is the energy distribution of electrons leaving the sample. For a small modulation voltage $k \sin \omega t$ added to V_E expansion of $I(E)$ as a Taylor series gives

$$I(E) = I(V_E) + KN(E) \sin \omega t + \frac{k^2}{4} \frac{dN(E)}{dE} (1 - \cos 2\omega t) + \dots$$

So, to obtain the energy distribution curve $N(E)$ the component of $I(E)$ at frequency ω is detected, and the differentiated curve $dN(E) / dE$ is obtained by detecting the component at 2ω , using the phase-sensitive detector. Unwanted pick-up due to the stray capacitance between G_2 and G_3 is avoided by use of the capacitance-neutralizing de Sauty bridge circuit included in figure 3.5.

The resolution and sensitivity of such a detector have been considered by Taylor (1969) and the instrumental line-width $\Delta E / E$ shown to be a constant for a particular instrument, except at lower energies. At higher energies resolution is mainly limited by the non-perfect potential variation in the grids as these are not true equipotential surfaces due to the finite spacing between their wires; and by deviation of the grids from ideal spherical geometry. The energy base width of a monoenergetic beam entering the analyser must be at least equal to the peak-to-peak modulation amplitude, hence at lower energies the modulation-broadening limit is approached and $\Delta E \sim$ constant. A resolution $\Delta E = 13$ eV at 356 eV ($\Delta E / E = 4\%$) and $\Delta E = 5$ eV at 47 eV ($\Delta E / E = 11\%$) was obtained.



R.F.A. for Auger electron detection

FIG. 35

3.6 Photoelectron Analyser

The ADES angle resolving photoelectron energy analyser was of the double focus hemispherical mirror type with 150° deflection and is similar in operation to that described by Lindau and Hagstrom (1971); it is shown in figure 3.6. A comparison of the performance of different analysers has been given by Heddle (1971). The analyser acts as a narrow pass filter, transmitting only electrons with an energy HV where V is the potential difference between the inner and outer hemispheres and H is a constant determined by the physical dimensions of the analyser. For a retarding voltage R applied between the sample and the electrical centre point of the hemispheres then photoelectrons of kinetic energy K given by

$$K = R + HV + W$$

will reach the detector, where W is a constant arising from the difference in work function between the sample and the various materials of the analyser. Generally W is referred to as the work function of the spectrometer.

In practice the analyser has a finite resolution and lets through electrons in an energy range $e \pm de$ and it can be shown that

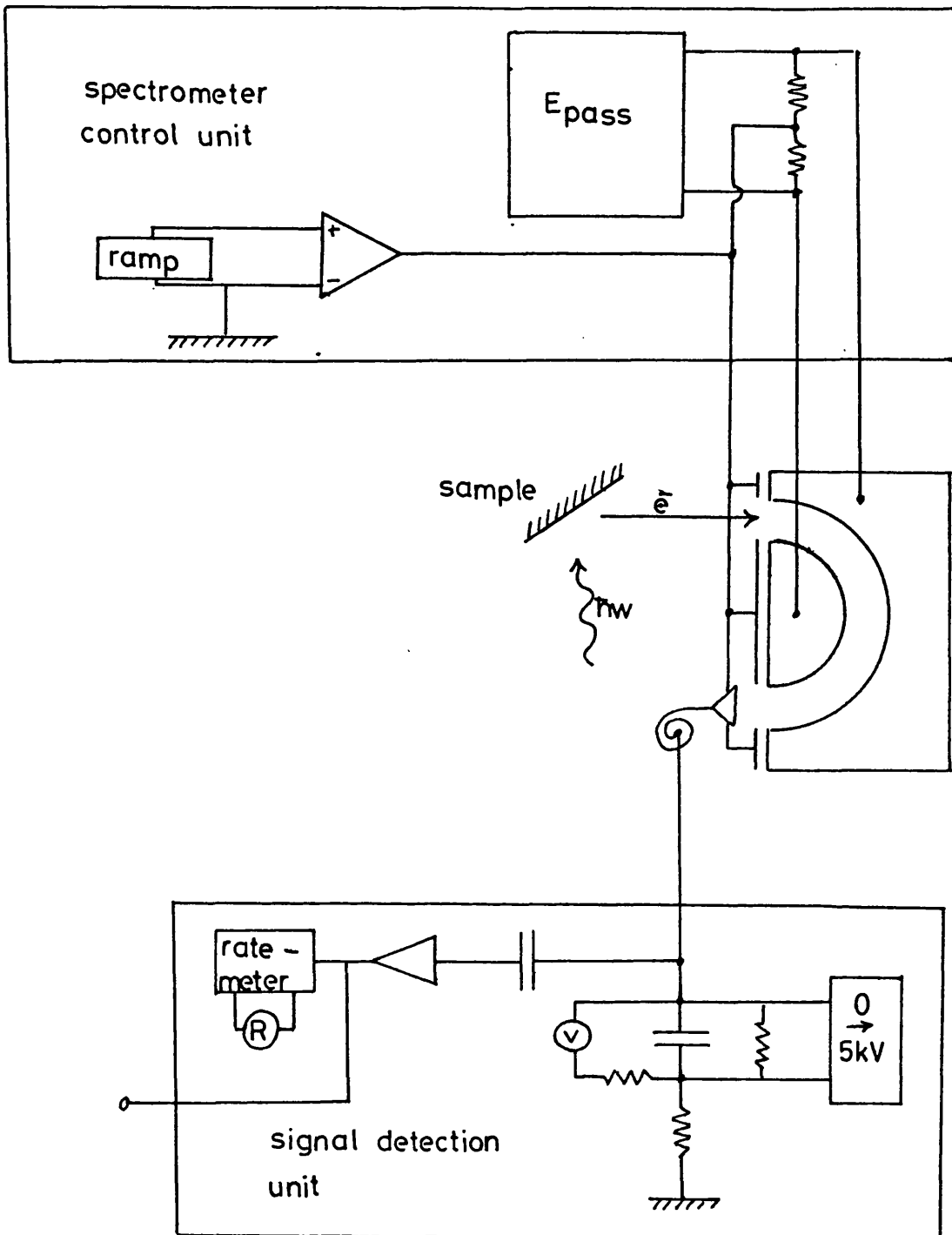
$$\frac{de}{e} \sim \frac{dr}{r} + \alpha^2$$

where r = mean radius of the hemispheres

dr = slit width

α = half angle of electron admission.

Hence resolution decreases with increasing kinetic energy. Operating at a 10 V pass energy with a He I (21.2 eV) line source gave an energy resolution of approximately 120 meV. With synchrotron radiation of 100 eV the resolution was approximately 0.3 eV. Angle resolution from



Hemispherical Photoelectron Analyser

FIG. 36

a point source was defined by the entrance slits to be $\pm 2^\circ$. For an extended source which occurred when the synchrotron light illuminated the whole sample this increased to $\pm 10^\circ$. In later experiments a collimator was attached to the exit slit of the monochromator to reduce the spot size. The implications of finite resolution on analysis of angle resolved photoemission data are discussed in chapter 4, section 4.2.

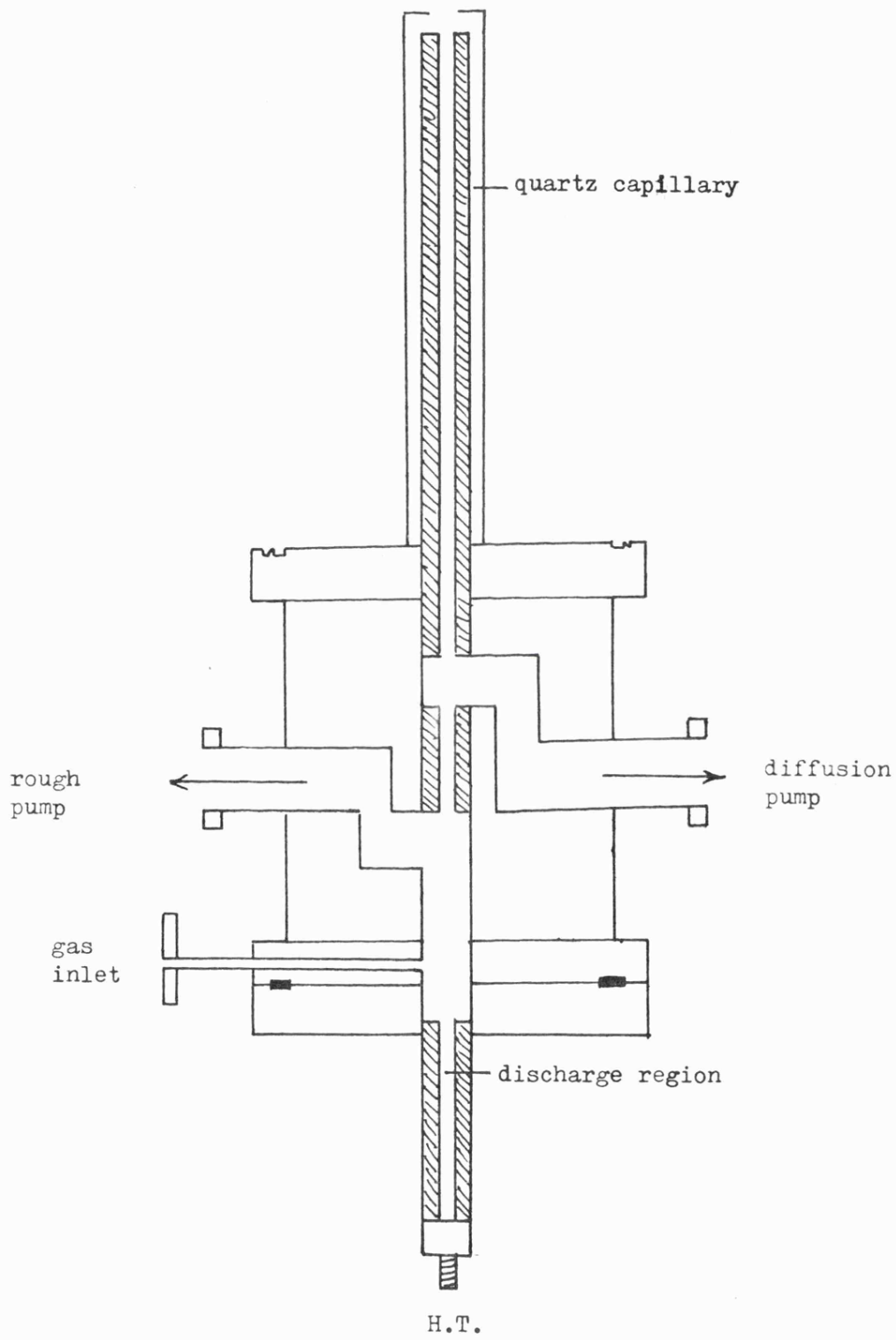
3.7 Ultra-Violet Light Source

Low energy fixed wavelength radiation was provided by a conventional noble gas discharge source. A number of transitions in rare gas atoms give rise to a line discharge in the ultra violet region of interest in valence band photoemission; a summary of the more useful lines is given in figure 3.7. The helium singlet 2p-singlet 2s (HeI) transition at 21.2 eV (584 Å) gives a very intense, narrow ($< .01 \text{ Å}$) line and was found most useful in the fixed wavelength studies of the present work. The problem of transmission of the light (for which no suitable window materials exist) into the UHV chamber is overcome by using a windowless source and differentially pumping the light guides, which have low gas conductance. Such a scheme, as used on the ADES spectrometer, is shown in figure 3.8. The lamp gas is purified by passing through a liquid nitrogen cooled sorb trap before reaching the discharge region, maintained at $\sim .05$ mbar by rough pumping. Chamber pressures in the 10^{-10} mbar range are maintained by a second diffusion pumped stage reaching $\sim 5 \times 10^{-8}$ mbar. After striking the discharge intense HeI emission was obtained using a discharge current of 60 mA and a voltage of 600 V.

Ultra-Violet Gas Discharge Lines

Discharge Conditions	Transition	Wavelength (nm)	Energy (eV)	Approx. Intensity
~ 1.0 Torr	HeI 2p - 1s	58.435	21.217	$I_0 \sim 10^{10} - 10^{11} \text{ s}^{-1}$
	HeI 3p - 1s	53.705	23.086	0.02 I_0
~ 0.5 Torr	HeII 2p - 1s	30.378	40.812	0.1 - 0.5 ($I_0/4$)
~ 0.5 Torr	NeI $3s(3/2) - 2p^6$	74.372	16.670	0.4 I_1
	$3s(1/2) - 2p^6$	73.590	16.848	$I_1 \sim 10^{10} - 10^{11} \text{ s}^{-1}$
~ 0.1 Torr	NeII $2s2p^6(1/2) - 2p^5(1/2)$	46.239	26.813	0.05 I_1
	$2s2p^6(1/2) - 2p^5(3/2)$	46.073	26.910	0.1 I_1
~ 0.5 Torr	ArI $4s(3/2) - 3p^6$	106.666	11.623	0.07 I_2
	$4s(1/2) - 3p^6$	104.822	11.828	I_2
Impurities	O I	130.22	9.52	
	N I	113.41	10.93	
	H I (Ly α)	121.57	10.2	

Figure 3.7



Noble Gas Discharge Lamp

FIG. 3.8

3.8 Synchrotron Radiation

Although much useful information may be obtained using noble gas discharge sources the most promising light source for photoemission is the dedicated synchrotron storage ring. The advantages of intensity, turnability and polarization of the synchrotron radiation source have often been discussed (see for example Kunz 1979). The photoemission facility at the Daresbury Synchrotron Radiation Source (SRS - SERC Daresbury, Warrington, Cheshire) is described below.

3.8.1 Properties of Synchrotron Radiation

Synchrotron radiation, whose properties may be calculated using classical electrodynamics (see for example Jackson 1962), arises when electrons moving with almost the velocity of light are deflected by magnetic fields. For a particle travelling in a circular orbit the radiation pattern is similar to an antenna and radiation at the frequency of revolution is produced. Concentration of charge at discrete points (each particle acting as an independent emitter) moving with relativistic velocities leads to strong enhancement of higher order harmonics and so the emitted spectrum may be considered to be a dense continuum extending from the revolution frequency to very high optical frequencies. The polarization and collimation properties of the radiation are shown in figure 3.9a.

The angular distribution of power P has been shown to take the following form (Tombouljian and Hartman 1956)

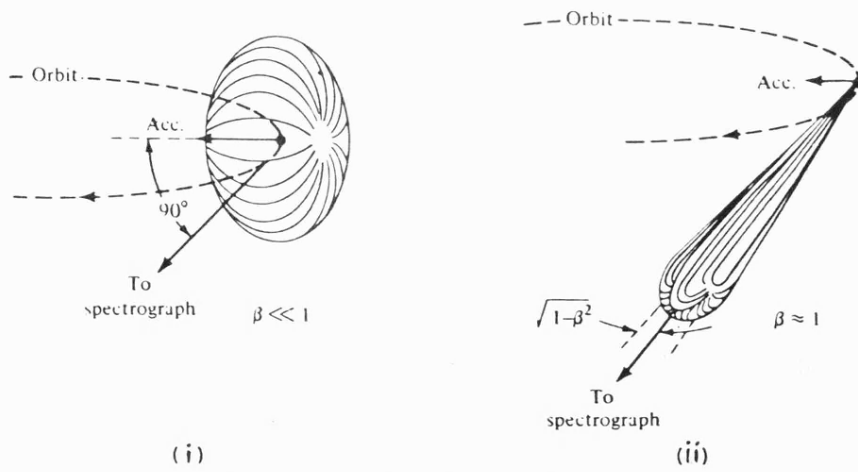
$$P(\psi, \lambda) = \frac{8\pi R e^2 c}{3\lambda^4} \alpha^{-4} (1 + x^2)^2 \left[K_{\frac{2}{3}}^2(\xi) + \frac{x^2}{(1+x^2)} K_{\frac{1}{3}}^2(\xi) \right] \quad (3.8.1)$$

where $x = \alpha \psi$

$$\xi = [2\pi R / 3\lambda]^{-3} (1 + x^2)^{3/2}$$

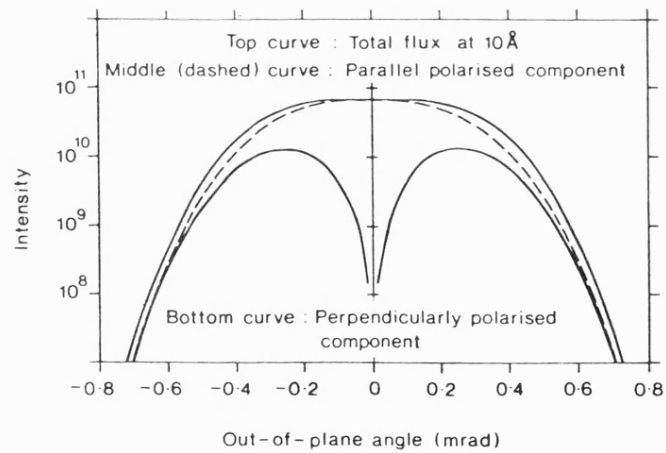
$$\alpha = E / (mc^2)$$

(a)



Angular intensity distribution of slow (i) and relativistic (ii) electrons on a circular orbit. The dipole pattern (i) is strongly distorted (ii) into the forward direction because of the relativistic speed of the electron; β , velocity in units of c . (From Tomboulian and Hartman 1956)

(b)



Angular distribution of polarisation components of 10 \AA radiation from the SRS. Intensity is in units of photons/s/mA beam/mrad horizontal/mrad vertical within 0.1% bandwidth, for SRS operation at 2 GeV and 1.2 T.

FIG. 3.9

R = radius of orbit

E = particle kinetic energy

$K_{\frac{2}{3}}(\xi)$, $K_{\frac{1}{3}}(\xi)$ = modified Bessel functions of the second kind.

$P(\psi, \lambda)$ = power ($\text{erg sec}^{-1} \text{rad}^{-1}$) emitted at azimuthal angle ψ relative to the plane of the orbit per unit wavelength interval at wavelength λ .

The equation is valid for a single electron travelling in a circular orbit. In the optical range the power emitted by several electrons may be simply added since the distribution of electrons around the orbit is random on the scale of the wavelengths emitted (Kunz 1978).

The first term in large parenthesis in (3.8.1) gives the power of the component of radiation with the electric field E parallel to the plane of the orbit and the second term gives the component with E perpendicular to the plane. It follows that in the plane of the orbit radiation is 100% linearly polarized and is right and left hand elliptically polarized above and below the plane respectively. The actual values of angular distribution of components obtained from the Daresbury SRS with 10 Å radiation is shown in figure 3.9b.

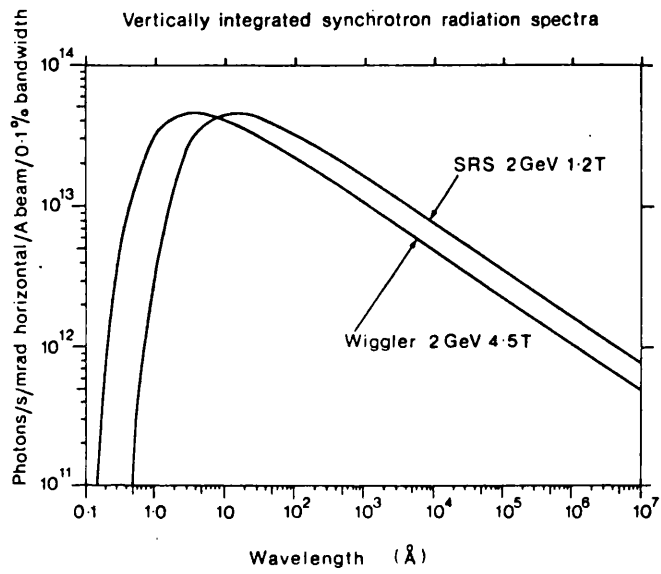
Integrating $P(\psi, \lambda)$ over all ψ and plotting as a function of λ shows a maximum in $P(\lambda)$ near λ_c , the critical wavelength (figure 3.10). λ_c is defined as

$$\begin{aligned} \lambda_c &= \frac{4\pi R}{3} \alpha^{-3} \\ &= 5.59 R(\text{m}) |E(\text{GeV})|^{-3} \end{aligned}$$

giving a critical photon energy

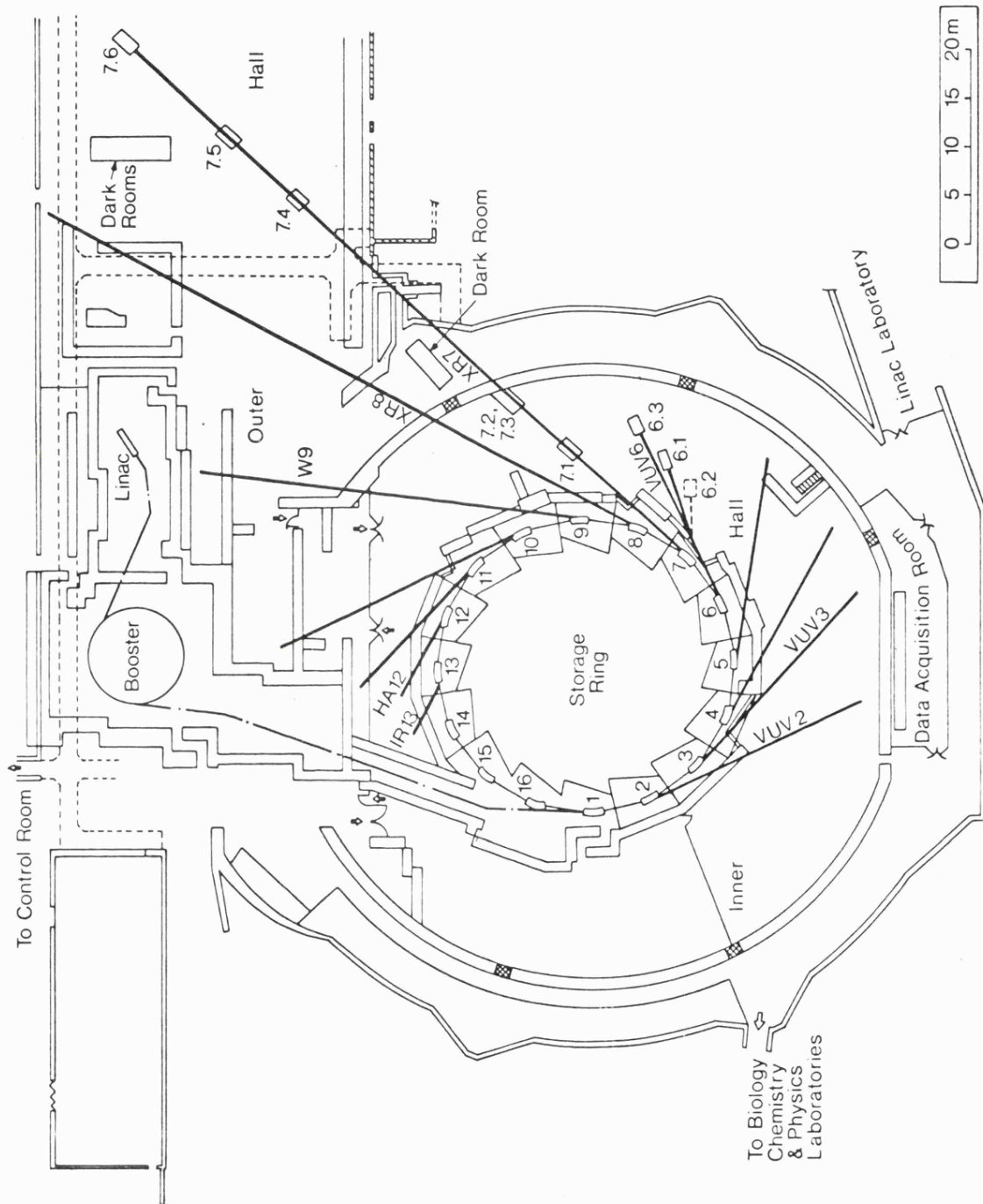
$$\epsilon_c = 2.22 \times 10^3 |E(\text{GeV})|^3 |R(\text{m})|^{-1}$$

Useful intensities are available up to $\epsilon \approx 4 \epsilon_c$.



Spectral curves from normal bending magnet (1.2 T) and from 4.5 T wiggler magnet, for a 2 GeV 1 A beam in the SRS. (The wavelength scale in Å may be converted to other units by use of the relations: $1000 \text{ \AA} \approx 100 \text{ nm} = 0.1 \mu = 12.399 \text{ eV}$).

FIG. 3.10



Plan of the Daresbury Synchrotron Radiation Source

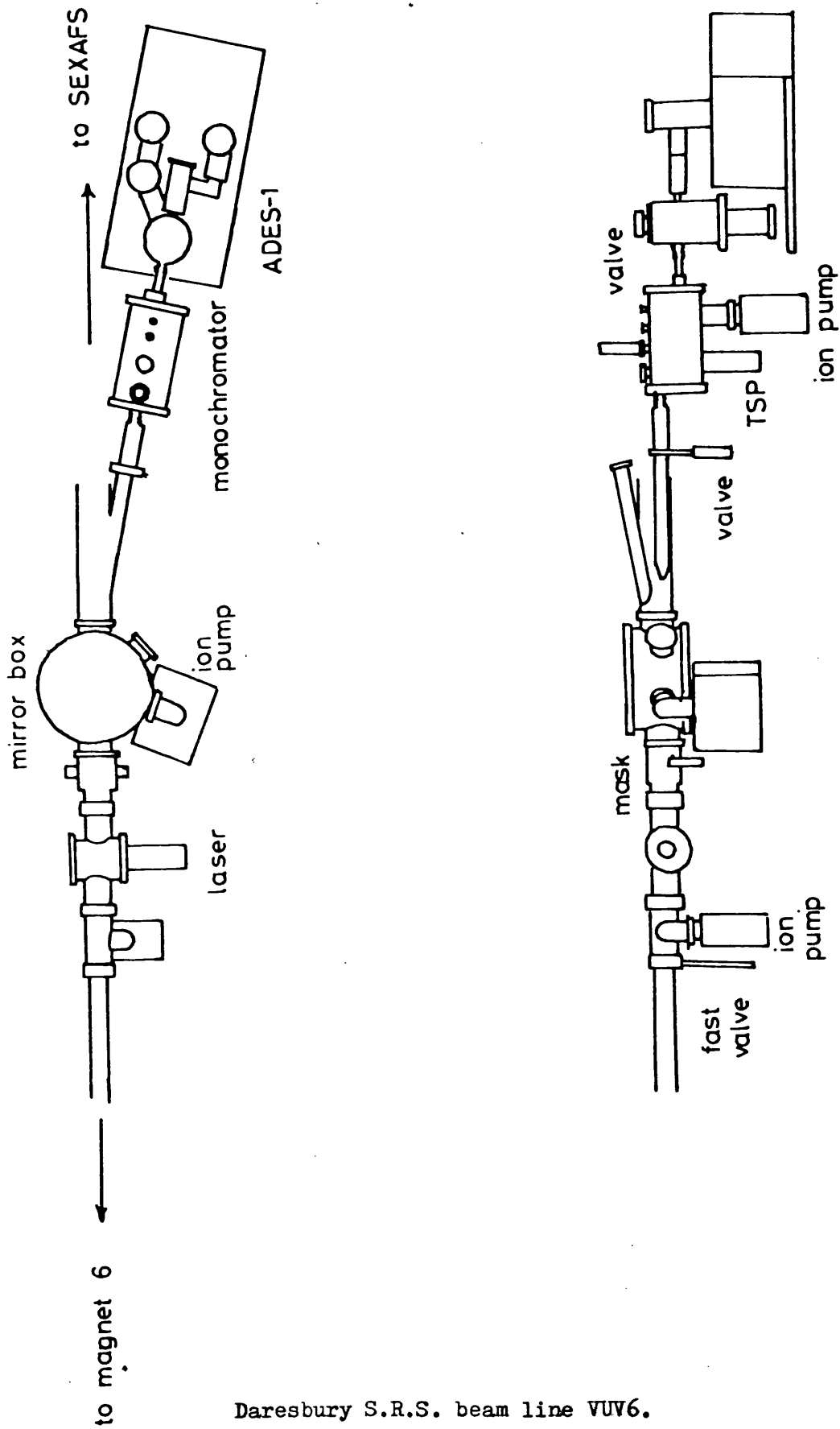
FIG. 3.11

3.8.2 The Daresbury Synchrotron Radiation Source

An overview of the design of the SRS is given in figure 3.11. Electron pulses of 10 - 15 MeV, 20 mA at a 10 Hz repetition frequency are produced in the linear accelerator (linac) and injected into the booster synchrotron, which takes 53 electron bunches and accelerates them up to 600 MeV using a 500 MHz rf field. The maximum field of the booster bending magnets is 0.786T and the bending radius is 2.55m. The average radius is 5.06 m. From the booster synchrotron electron bunches travel through the transfer path to the 15 m radius storage ring. By successive injections 160 bunches at a current of up to 1.0 A are accepted (stacking). These are then accelerated up to the maximum design energy of 2.0 GeV (ramping) and, if stable, the beam is stored. At ring vacuums in the 10^{-10} mbar range beam lifetimes of 8 - 10 hours are obtained (Munro 1981).

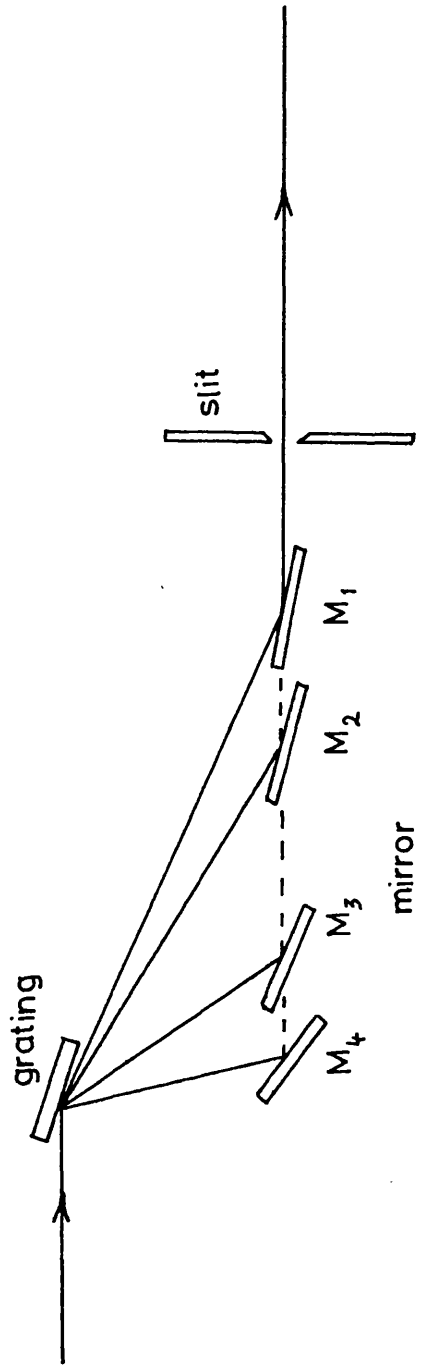
3.9 Beam Line and Monochromator

The continuous spectrum of synchrotron radiation emitted tangentially at the site of the bending magnets requires monochromatization before use in a photoemission experiment. Howells (1980) has reviewed vacuum ultra-violet (VUV) monochromator techniques and the proposed instrumentation at the SRS has been discussed by Codling (1980). The photoemission experiments of the present work were carried out on beam line VUV6, tangential to magnet 6 (figure 3.11), shown schematically in figure 3.12. Three experimental stations are planned, of which two (ADES and SEXAFS) are shown in the figure. After emerging from the shield wall synchrotron radiation passes the water cooled adsorbers (installed to protect closed valves from the radiation) and enters the



Daresbury S.R.S. beam line VUV6.

FIG. 3.12



VUV6 MONOCHROMATOR

FIG. 3.13

mirror box. Here it is split into three beams, directed towards the Surface - EXAFS station and the two angularly dispersive electron spectrometers (ADES 1 and ADES 2). Experiments were performed using the ADES 1 equipment.

The monochromator in use with the ADES 1 spectrometer was a plane grating instrument of the Miyake type (Miyake et al 1969) as described by West et al (1974) and Howells et al (1978). The optical layout of the instrument is shown in figure 3.13. The plane grating has a square wave profile (phase type) and is a master ruled at $632 \text{ lines mm}^{-1}$. Higher spectral orders are rejected by selective reflections from one of the four spherical mirrors shown in the figure which may be tilted until light diffracted from the grating passes through the exit slit. The exit slit is adjustable from $10 \mu\text{m}$ and the dispersion of the instrument is approximately 6 \AA mm^{-1} on all ranges. The variation in output intensity with energy on all four ranges is shown in figure 3.14.

3.10 Data Collection

It was found that the Auger spectra produced at Daresbury and plotted directly onto an X-Y recorder were of sufficiently high quality that no signal averaging or processing of any kind was required. At Daresbury the photoelectron spectrometer could be operated in either manual or computer controlled mode. The HeI spectra produced under manual control were adequate for most purposes but whenever possible computer control was used, and always for other noble gas discharges and synchrotron radiation.

A block diagram of the analyser and computer control circuitry is shown in figure 3.15. Software stored on the system desk enabled the LSI-11 to set up the required parameters and control the start, finish and pass energies of the analyser, together with the counting time,

MONOCHROMATOR OUTPUT

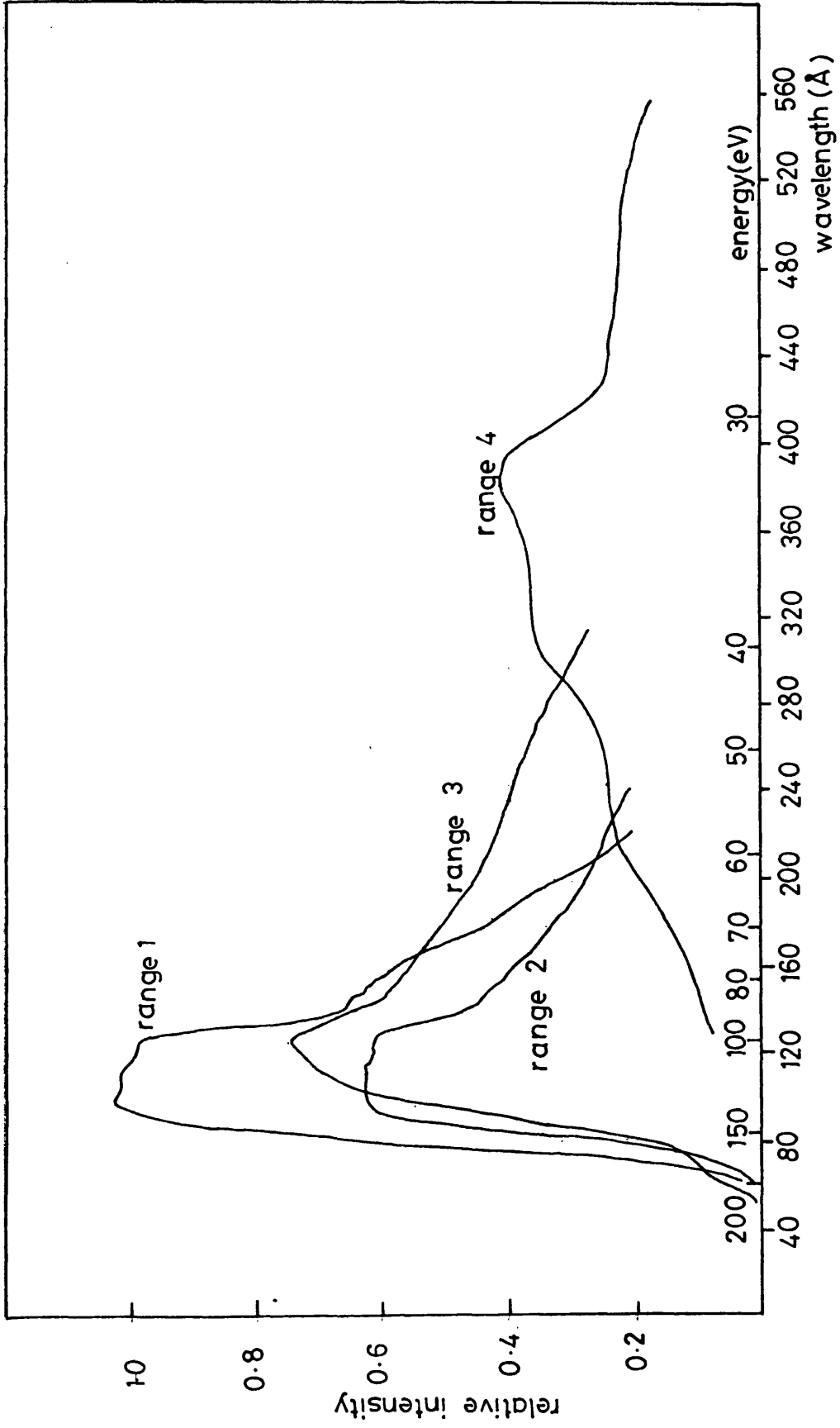


FIG. 3.14

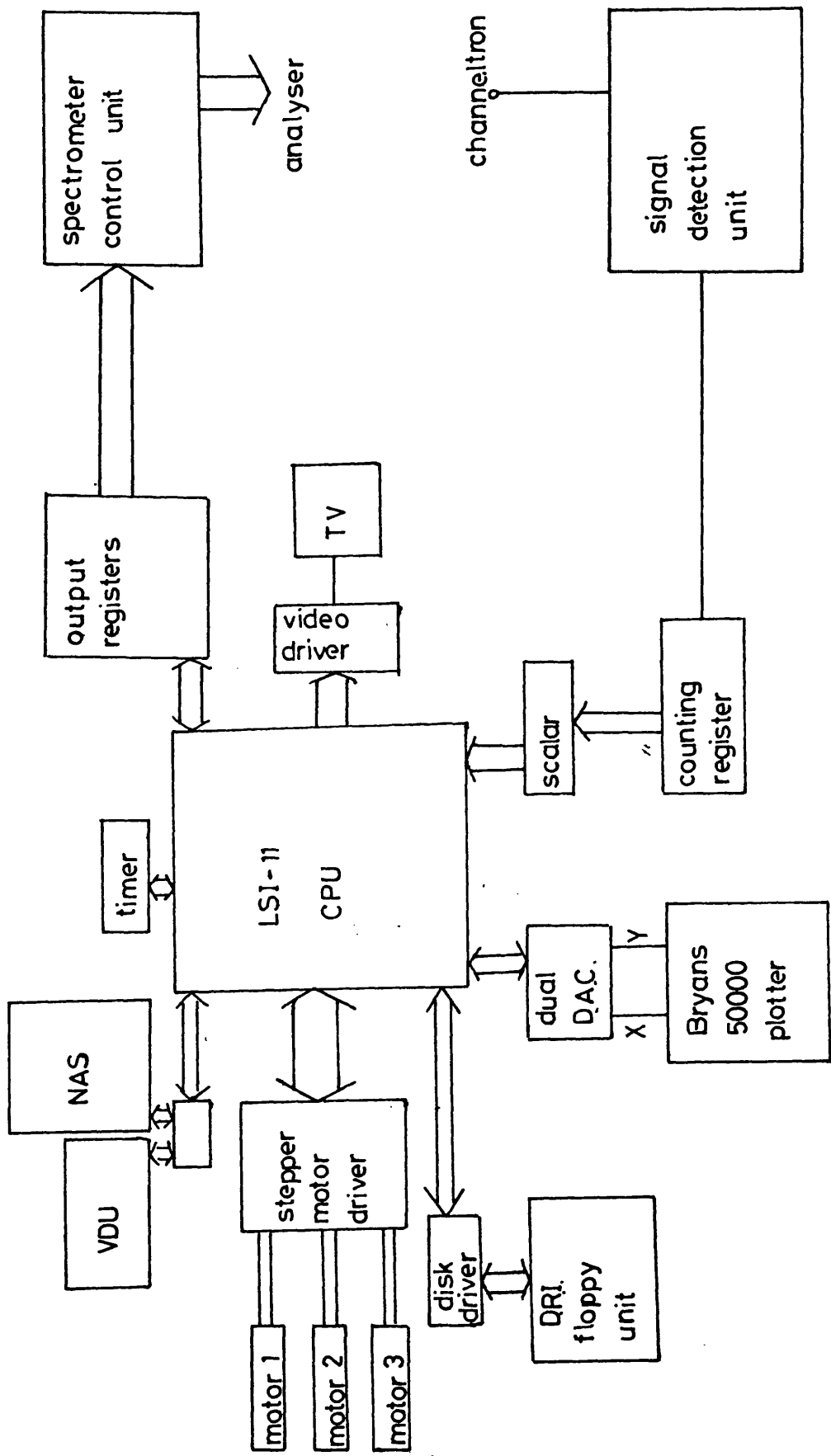


FIG. 3.15

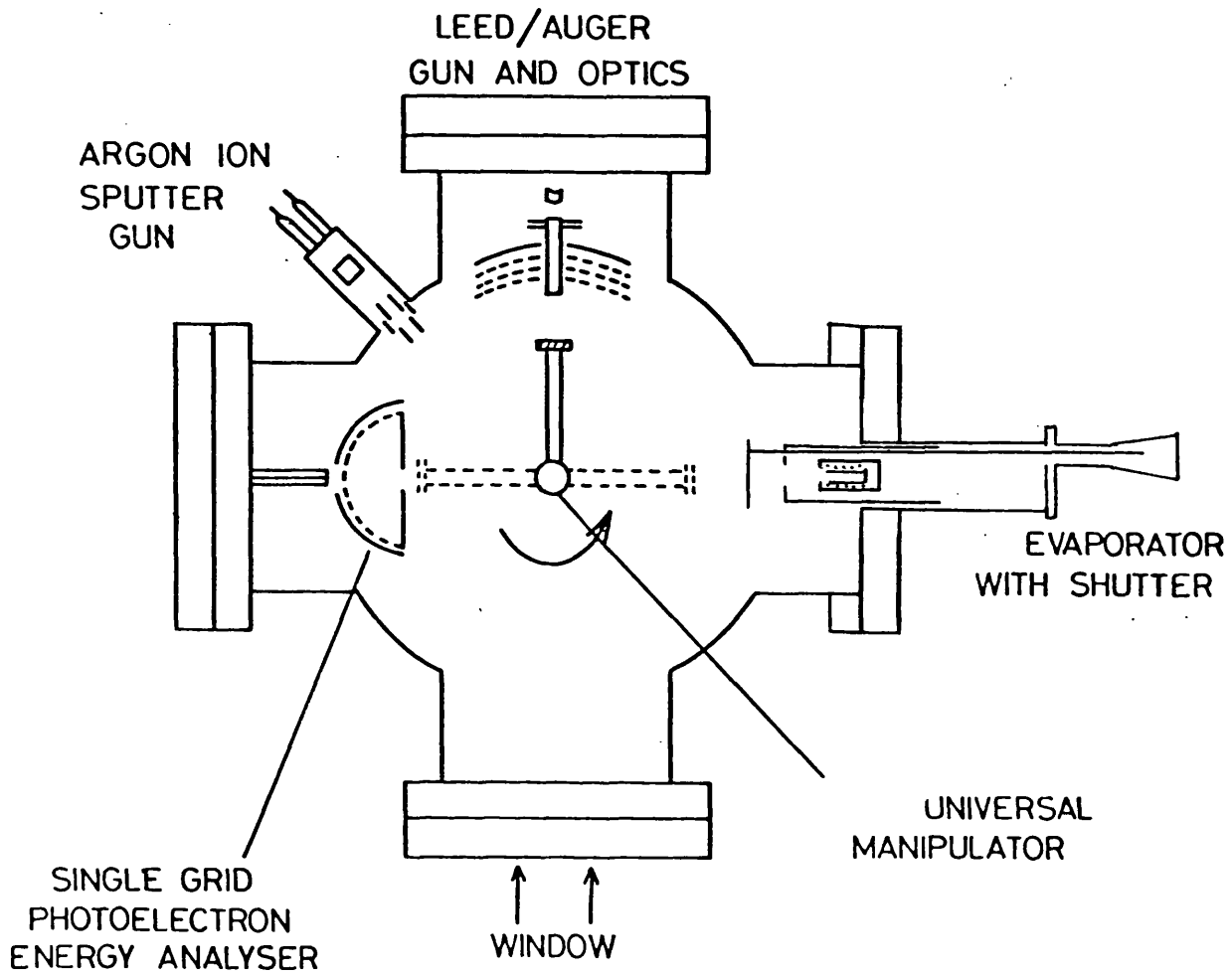
ANALYSER COMPUTER CONTROL

number of scans and energy width of the input counting register. The minimum energy increment of 0.05 eV was used for all high resolution scans. Data were outputted onto the TV display and the number of counts accumulated shown on the VDU as the spectra were scanned, with the display driver routines operating during the channeltron recovery time so as not to slow down data taking. After multi-scanning the final averaged spectrum was displayed and the accumulated data dumped onto the current data disk. For most purposes the spectra were plotted on the X-Y recorder but for further processing data were transferred to the NAS 7000 mainframe computer. At the time of writing final commissioning of the stepper motor drives was not complete so the spectrometer could not be used in the constant initial or constant final state modes. All data were in the form of energy distribution curves (EDC's), where the energy distribution of photoelectrons at a fixed photon energy were measured.

3.11 The Leicester Chamber

Work at Leicester was carried out using the LEED / Auger and angle-integrating photoemission system described by Binns (1981) after replacement of the electron gun power supply, provision of a high temperature metal vapour source and certain improvements and modifications to the pumping system. The basic arrangement is shown in figure 3.16.

Using the Vacuum Generators UMD 1 manipulator the sample could be rotated between the angle-integrating photoemission system, the Ar⁺ ion gun, the LEED / Auger gun and optics, and the metal vapour source. Angle integrated photoemission spectra are of limited use and



Resources available within the Leicester chamber

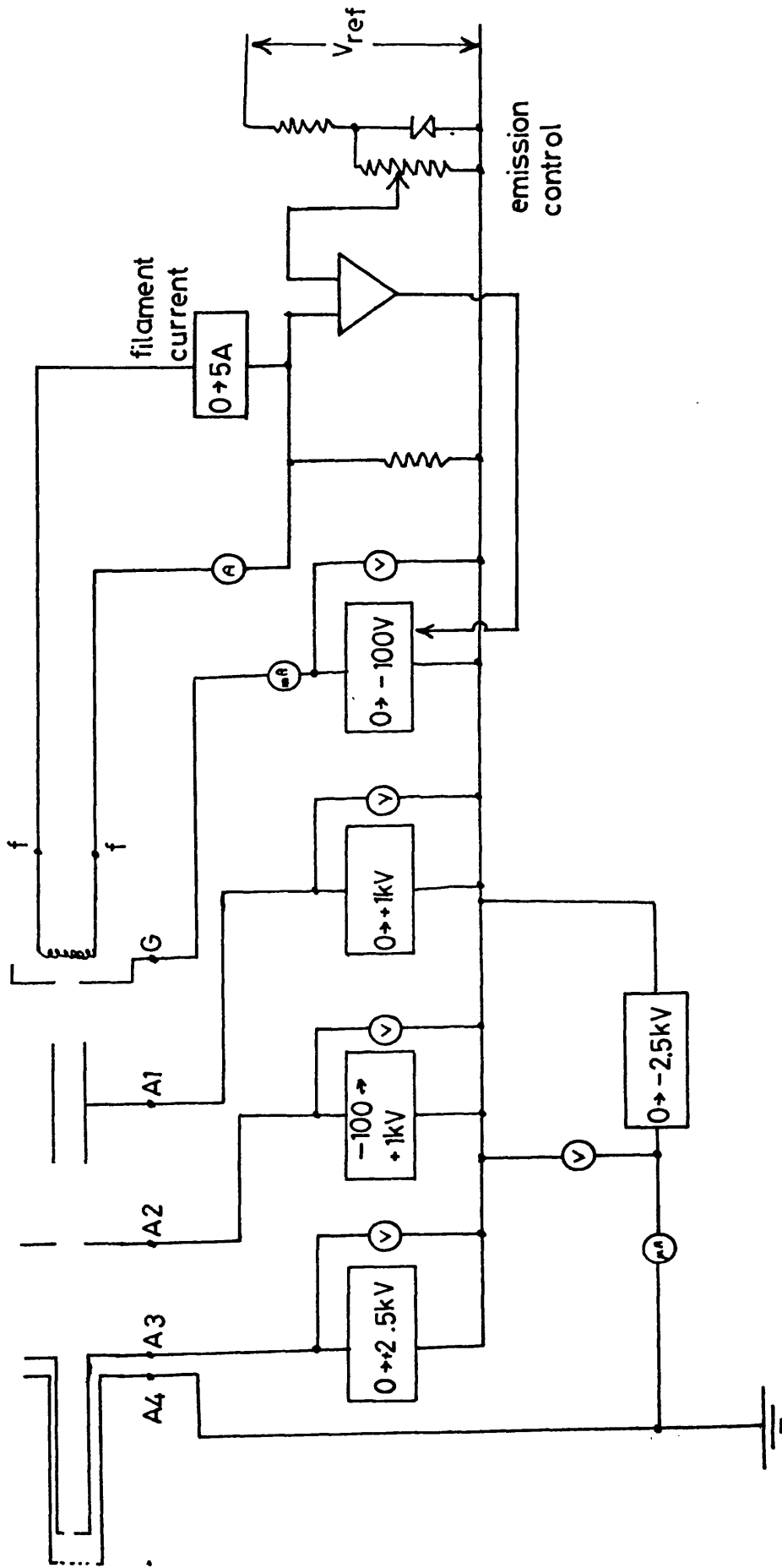
FIG. 3.16

are not to be presented in this work. To minimize oil contamination, initial rough pumping was by carbon vane pump to ~ 100 mbar followed by liquid nitrogen cooled sorb pumps to $< 10^{-3}$ mbar after which the triode ion pump could be started. The liquid nitrogen trapped diffusion pump was valved into the chamber during Ar^+ bombardment only. Ar poisoned the ion pump so the ion pump valve was kept closed during this operation. After bakeout pressures in the low 10^{-10} mbar range were routinely obtained.

To improve the performance of the system the electron gun power supply described was designed and constructed. The design, based on modular "Brandenburg" high voltage units, is shown in figure 3.17. In order that the electron beam may enter a field free space within the chamber the final accelerating anode must be at earth potential, hence the filament was floated down to the (negative) beam energy and all other voltages referenced to this. The electron beam is emission current stabilized using an operational amplifier based feedback circuit to control the Wehnheldt voltage. During operation with a filament current of 2.2 A a stable beam of between 50 V and 2.4 kV with an emission current of 1 mA could be obtained.

3.12 Crystalline Surface Preparation

All substrate materials used in this work were obtained commercially in 99.998% pure single crystal form from Metals Research Ltd. The copper specimen was spark cut to $\pm 1^\circ$ of the (100) plane by the suppliers; the silver (100), silver (111) and palladium (111) specimens were spark cut from the boule by the Centre for Materials Science of Birmingham University.



ELECTRON GUN CONTROLLER

FIG. 3.17

Although accurate to $\pm 1^\circ$ of the required orientation the spark cut surfaces contained numerous imperfections and further work to obtain good atomically smooth surfaces was necessary. The samples were mechanically polished with successively finer grades of carborundum down to 1200 grade, then with a sequence of $8\ \mu$, $3\ \mu$ and $1\ \mu$ diamond polishing cloths until a good optically smooth mirror finish with no discernible imperfections was produced. This completed the pre-UHV preparation of the silver and palladium specimens but the copper surface was further improved by electropolishing. A rapidly stirred solution of 2 parts concentrated orthophosphoric acid (H_3PO_4) to 1 part deionized water contained in an ice-bath at a current density of $2.6\ \text{A dm}^{-2}$ for one minute was used. This was followed by repeated washings in 10% orthophosphoric acid and in deionized water.

The crystals were then individually mounted in UHV and taken through repeated cycles of Ar^+ ion bombardment with a 1 keV beam of $10\ \mu\text{A}$ for 25 minutes followed by annealing at $500\text{-}600^\circ\text{C}$ for 30 minutes until no impurities were detected by Auger spectroscopy (AES). Further annealing at 500°C for 40 hours in UHV followed by a final bombard / anneal cycle completed the preparation of the surfaces. A review of preparation methods of atomically clean surfaces has been given by Musket et al (1982).

During subsequent experimental runs clean, well ordered surfaces, as determined by LEED and AES, were routinely prepared in situ by Ar^+ bombard / anneal cycles. The copper (100) specimen proved easiest to clean, requiring a 1 keV beam for 5-10 minutes and annealing at 500°C for 30 minutes. The silver specimens required a 2 keV beam for 15 minutes and an anneal at 600°C for 30 minutes. Routine cleaning of palladium (111) was more complex, requiring bombardment at 2 keV for

30 minutes to remove deposited metal overlayers, followed by a bombardment at 2 keV for 10 minutes while at 500°C. After a five minute anneal it was then bombarded further, while hot, with a 1 keV beam for five minutes, followed by a four minute anneal at 500°C. It was then allowed to cool and when the pressure had reached the low 10^{-9} mbar range it was heated rapidly up to 300°C. After final cooling this process produced good quality surfaces. Palladium is a rather reactive material and during the anneal stages of cleaning tended to adsorb gas from the residual atmosphere. This was removed by light bombardment, after which a further anneal was required to repair damage done by the bombardment, the final rapid heating to 300°C thermally desorbed gas (especially hydrogen) which may have contaminated the surface during cooling after the final anneal.

3.13 Overlayer Growth, General Considerations

Some of the theoretical aspects of overlayer growth were considered in the previous chapter. Interpretation of growth modes of the overlayer-substrate combinations presented in this thesis was dependent on the production of meaningful Auger signal vs time (A s - t) plots, obtained by measuring overlayer and substrate Auger emission intensities as a function of overlayer deposition time. The quality, or signal to noise ratio, of an As-t plot is dependent on two factors:

- (i) accurate sample translation between the evaporation source and electron optics, and
- (ii) the characteristics of the vapour source.

Condition (i) is achieved using a suitable manipulator with micrometer drives. The second condition has been the subject of much recent research

due to the emerging importance of Molecular Beam Epitaxy (MBE) as a growth technique for semiconductors (see for example Bachrach 1980, Pamplon 1980). In this technique the different constituents of the required solid are deposited simultaneously from separate sources onto the growth surface. For reproducible materials the deposition rate, and hence the source temperature, must be stable and the beam profile known.

The rate of evaporation, W (g sec cm^{-2}), from a metallic surface as a function of temperature T is given by

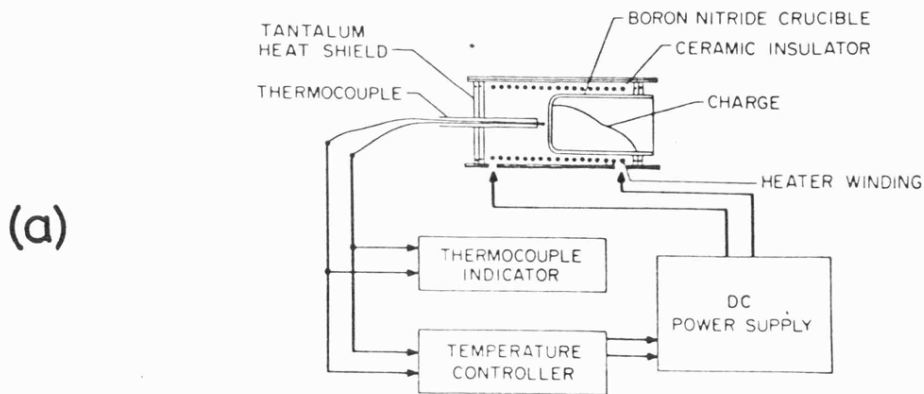
$$\log W = A - B / T - \frac{1}{2} \log T + C \quad (3.13.1)$$

(Dushman 1949) with A , B and C constants for a given material. Values for the materials used in the present study are given in the table below:

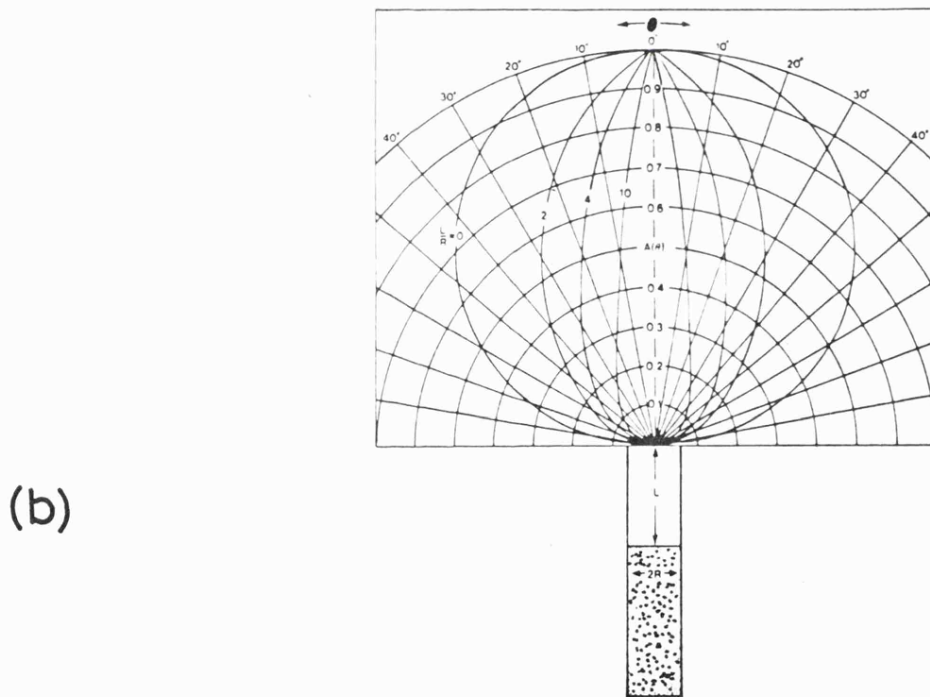
Material	A	B	C
Mn	12.25	1.410×10^4	-3.3641
Cu	12.81	1.806 "	-3.3322
Pd	11.46	1.923 "	-3.2199
Fe	12.63	2.000 "	-3.3605
Ni	13.28	2.184 "	-3.3497
V	13.52	2.662 "	-3.3805

Substitution leads to the conclusion that for small ($\sim 3\%$) variations in W the temperature must be controlled to within 1°C . This implies the need for either a thermally massive source or a feedback stabilized heater supply. A typical arrangement is shown in figure 3.18a.

The rate of arrival of material at the growth surface must be constant over the area under investigation. For a point source the distribution is spherical and no problem is encountered provided the collimation does not reduce the beam area below that of the sample, and



Schematic of a typical MBE evaporation source in use today with the associated circuitry. A pyrolytic boron nitride crucible is heated by a well-insulated oven. The thermometer is closely coupled and with a proportional controller maintains a stable temperature.



Evaporation angular distribution function on a polar plot parameterized as a function the source diameter r to collimation length l ratio. $l/r = 0$ corresponds to a full crucible.

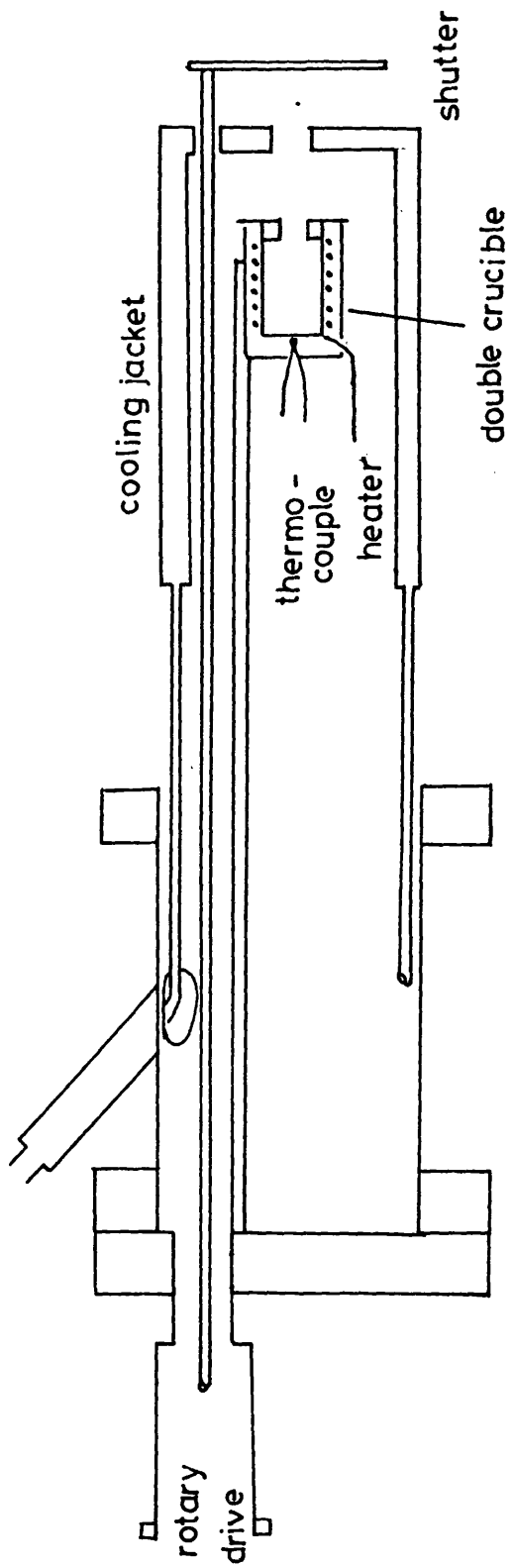
FIG. 3.18

the sample is sufficiently far from the source, and small enough, that the spherical contours of equal flux approximate to a plane at the sample surface. The distribution obtained from the source type shown in figure 3.18a is given in figure 3.18b, and is seen to be non-spherical. For a suitably small ratio L / R the distribution, or beam profile, will be approximately constant over a small area in direct line of sight from the source.

3.14 Transition Metal Vapour Source

The considerations described in the previous section have been incorporated into the design of the water cooled UHV compatible Knudson cell type device shown in figure 3.19. The inner crucible has a machined screw thread into which the tungsten heater filament is wound. Collimation of the atom beam is by means of the cap on the double crucible and the exit orifice of the water cooled jacket. The rotary-driven shutter enabled interruption of the vapour flux, and evaporant temperature was monitored using the chromel-alumel thermocouple held in contact with the base of the inner crucible. The crucible was found to be of sufficient thermal mass that no temperature-stabilization circuitry was required. When driven from a Farnell TSV 70 stabilized power supply temperatures could be maintained to within 1°C for periods of several hours, once time had been allowed for the device to reach thermal equilibrium.

For UHV operation thorough outgassing was found to be essential. Immediately after bakeout the evaporator was run up to the required temperature without water cooling for about half an hour, then allowed to cool after which water cooling at mains pressure was applied and the crucible heated to operating temperature and run for several hours.



METAL VAPOUR SOURCE

FIG. 3.19

After outgassing chamber pressures of 5×10^{-10} mbar could be maintained with the evaporator at typically 900°C .

The temperature, coverage rate and power input required for the various evaporants are shown in the table below. The estimated variations in coverage rate, ΔW , for a 1°C change in temperature, obtained using equation (3.13.1) are given.

Evaporant	T($^{\circ}\text{C}$)	P(W)	dep.rate (ml/hr)	$\Delta W(\%)$
Mn	500	21	5	5.2
Cu	750	44	6	3.9
Pd	850	70	8	3.4
Fe	900	80	8	3.3
Ni	950	104	5	3.3

Beam uniformity was investigated by evaporating from the source with the substrate placed in direct line of sight of the centre of the crucible. On checking the coverage of evaporated material using Auger spectroscopy, no measurable variation was found on traversing the electron beam across the sample.

CHAPTER 4

PHOTOEMISSION FROM THE CLEAN COPPER, SILVER
AND PALLADIUM CRYSTAL SURFACES

- 4.1 Introduction
- 4.2 Photoemission from Transition and Noble Metals
- 4.3 The Copper (100) Surface
- 4.4 The Silver (100) and (111) Surfaces
 - 4.4.1 Helium-I Excitation
 - 4.4.2 Synchrotron Radiation Excitation
- 4.5 The Palladium (111) Surface
- 4.6 Summary

CHAPTER 4

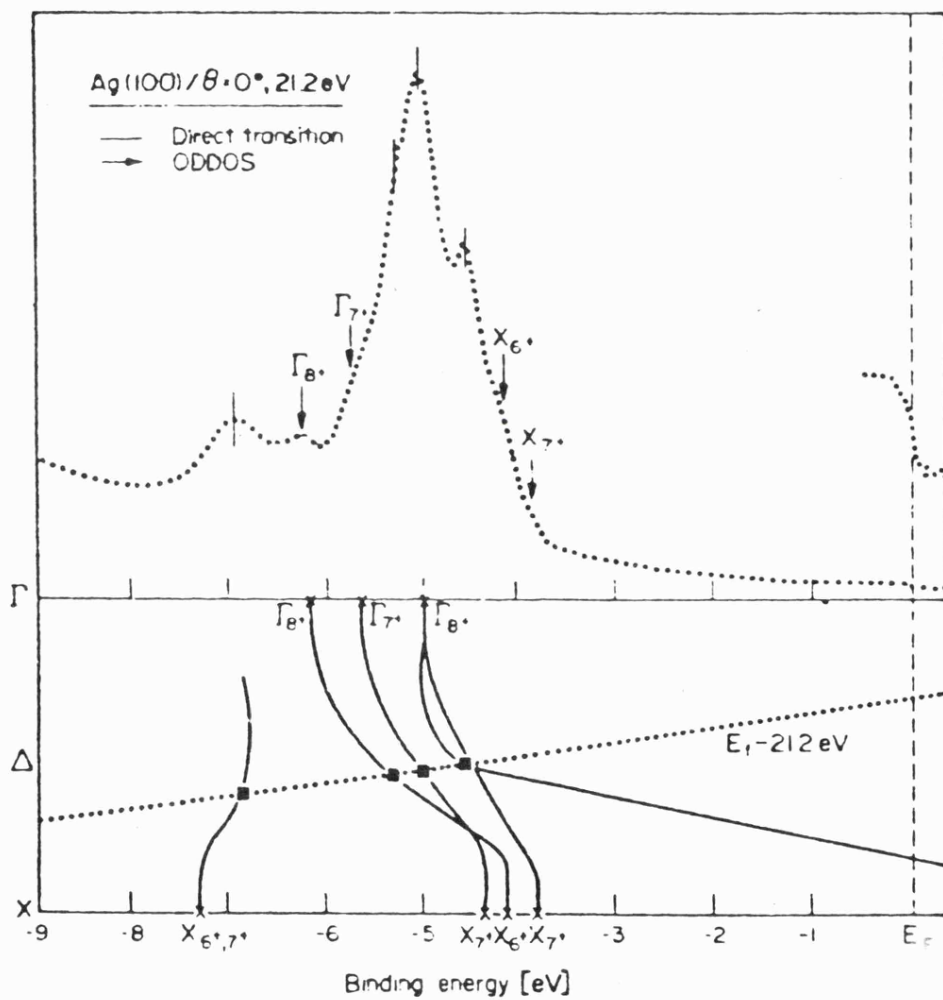
PHOTOEMISSION FROM THE CLEAN COPPER, SILVER
AND PALLADIUM CRYSTAL SURFACES4.1 Introduction

In a study of thin adsorbed overlayers it is essential to have a good understanding of the electronic properties of the particular substrate used. To this end, photoemission measurements have been made of the single crystal copper (100) silver (100) and (111), and palladium (111) surfaces. Angle-resolved spectra at 21.2 eV (Helium-I radiation) were taken for a range of azimuthal and emission angles. Comparison with band structures, both published and calculated using PEOVER as described in chapter 2, enabled the majority of spectral features to be understood in terms of the direct (k-conserving) transition model. In addition, synchrotron radiation was used and spectra were taken in normal emission from the silver (100) and palladium (111) surfaces in the energy range 40-120 eV. Although initial-state band structure mapping to free-electron like final states has been shown to be possible in this energy range (Thiry et al 1979) the stringent angular resolution requirements could not be met sufficiently well to enable accurate mapping with the present equipment. Instead, interpretation proceeded via the one-step time-reversed LEED formalism using the PEOVER program of Hopkinson et al (1980). Reasonable overall agreement between theory and experiment was achieved; peak position and intensity variations with photon energy were predicted.

4.2 Photoemission from Transition and Noble Metals

Although angle-integrated photoemission measurements provide an overview of electronic structure through the simultaneous detection of photoelectrons originating from many parts of the Brillouin Zone (BZ) the importance of angle-resolved measurements was pointed out as long ago as 1964 (Kane 1964). The first high-resolution angle-resolved energy distribution curves (EDC's) for copper were reported by Lindau and Hagstrom (1971). The three-step model for photoemission is usually invoked to explain structure in the EDC's, with peaks appearing at the energy of an initial state above which there occurs a suitable final state for photon-excitation in the calculated band structure in the direction under investigation. This interpretation is illustrated for normal emission ($\theta_e = 0^\circ$) from silver (100) at 21.2 eV (He I) in figure 4.1 (Courths et al 1981). Features in the spectrum marked as direct transitions are due to transitions from the indicated initial states to points on the free-electron like final state curve displaced in energy by 21.2 eV. This procedure is well established (Courths et al 1982, Westphal et al 1980, Nilsson and Dahlback 1979, Roloff and Neddermeyer 1977, and many other authors) although the nature of the final state, i.e. free-electron like or calculated bulk state, has been vigorously investigated (Liebowitz and Shevchik 1978a, Weeks 1978, Shevchik and Liebowitz 1977).

Also shown in figure 4.1 are features marked "ODDOS", or one-dimensional density of states. This refers to an alternate view of photoemission in the ultra violet (UPS) regime which holds that the spectra measure the density of bulk states along the direction of the emitted electron with initial-state structure being lost due to broadening of the final states. In practice both direct-transition



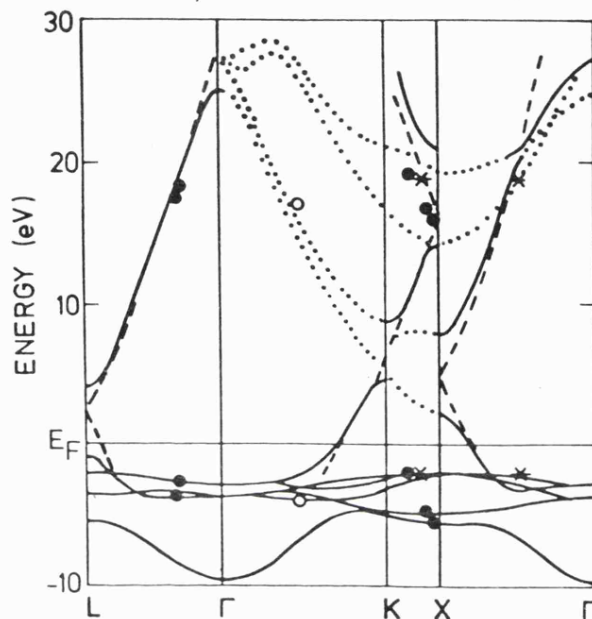
Normal emission photoelectron spectrum from Ag(100) after Courths et al (1981), unpolarised He I radiation.

FIG. 4.1

and DOS-derived structures are seen in the spectra with the direct-transition features dominating by approximately one order of magnitude in intensity (Courths et al 1981). For the (100) and (111) surfaces of noble metals direct transitions have been clearly shown to be dominant whereas on the (110) faces strong contributions to the spectra were found which could not be accounted for by direct \underline{k} -conserving transitions (Heiman et al 1976). Normal emission UPS spectra of the (111), (100) and (110) faces of iron at 21.2 eV (He I) and 40.8 eV (HeII) were measured by Schulz et al (1979). The spectra from all three faces at both photon energies were very similar and resembled the UPS and XPS spectra obtained from polycrystalline iron. In addition, many of the spectral features could not be explained by direct transitions using the band structure of Tawil and Callaway (1973) and this led to the conclusion that, for this material, the spectra provided a measure of the DOS. The results of Schulz and co-workers, together with other evidence, are discussed further in chapter 8.

In the direct transition model it is normal to resolve the one-electron crystal momentum vector \underline{k} into components parallel and perpendicular to the surface, $\underline{k}_{//}$ and \underline{k}_{\perp} respectively. On crossing the surface barrier $\underline{k}_{//}$ is conserved but \underline{k}_{\perp} is not. In the simplest experimental configuration emitted electrons are collected normal to the surface and $\underline{k}_{//}$ is zero. \underline{k}_{\perp} may then be obtained by a fit to the theoretical band structure or by considering the free-electron like final states as described above. Interpretation, however, is in general more complicated at off-normal emission angles where $\underline{k}_{//}$ varies as a function of emitted electron kinetic energy. In this case the simplest situation is that of a two dimensional system in which the energy bands are a function of $\underline{k}_{//}$ only. A feature at kinetic energy E_{kin} seen in

Band structure of Cu by Janak et al (1975).
 The broken line is the free electron parabola.
 Experimental points obtained using two surfaces
 as shown below.



Method used to determine $E(k)$ absolutely from photoemission
 measurements on two surfaces. O.S. = Optical surface,
 F.S. = Fermi surface.

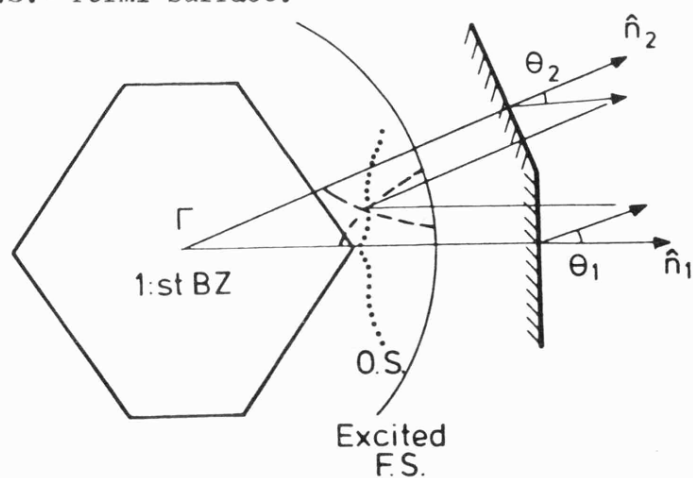


FIG. 4.2

the spectrum at emission angle θ_e gives rise to a point in $E - \underline{k}_{//}$ space through the relation

$$k_{//} = \frac{1}{\hbar} \sqrt{2m E_{kin}} \sin \theta_e .$$

This procedure has been used to determine the two-dimensional dispersion of a segregated copper layer on the (111) surface of a Cu Ni alloy (Heimann et al 1981) but the results presented in the following chapters of this thesis represent the first experimental E vs $\underline{k}_{//}$ relationships for transition metal monolayers (Smith et al 1982). Surface state dispersion curves may also be mapped using this procedure (for example Heimann et al 1979).

In the bulk material the indeterminacy of \underline{k}_{\perp} has to be overcome if experimental band structures are to be obtained. Kane (1964) suggested an energy coincidence method using two crystal faces which has been used recently (Nilsson and Dahlback 1979, Lindroos et al 1981). The method is in principle exact and involves searching for emission angles θ_e at which an energy coincidence occurs for a given structure in the spectra measured on two different faces of a single crystal sample. Having obtained the energy coincidence it is then a geometric problem to obtain \underline{k}_{\perp} involved in the transition. Since $\underline{k}_{//}$ is conserved then \underline{k} can be determined and, as a consequence, the initial and final energies E_i and E_f as well as \underline{k} are obtained from the experiment. The energy bands $E(\underline{k})$ for occupied and unoccupied states may then be mapped out without prior assumptions. Copper in particular has been the subject of thorough examination using this technique (Lindroos et al 1981, Nilsson and Dahlback 1979). Results for palladium have also been presented (Asonen et al 1980). The method, together with the results of Nilsson and Dahlback, is illustrated in figure 4.2. An alternative approach to

angle-resolved spectra involving measurements at constant $\underline{k}_{//}$ has also been applied to copper (Pessa et al 1979).

In the case of a material such as silver where the initial state bands are rather flat it may not be possible to determine energy coincidences sufficiently accurately to enable reliable band mapping (Christensen 1981a). In such cases the Appearance Angle Method (AAM) recently suggested by Christensen (1981b) may be applicable. The appearance angle for a certain interband transition at a specific photon energy and relating to a specific low-index crystal face is defined as the external emission angle θ_a at which the specific transition appears in angle resolved photoemission spectra taken with fixed photon energy when varying the detector angle in a plane of high symmetry. Optical interband transitions observed in ARPES with $\theta_e = \theta_o$ occur at points in \underline{k} -space defined by intersections between the emission plane, the constant energy difference contour (CEDC) for $E_f(\underline{k}) - E_i(\underline{k}) = h\omega$ and the constant emission angle contour (CEAC) of the final state band f for $\theta_e = \theta_o$. This is illustrated in figure 4.3 for transitions between bands 6 to 7 with $h\omega = 16.85$ eV in gold (110). If the emission plane is chosen to be of high symmetry then transitions with $\theta = \theta_a$ must take place on a symmetry line of the BZ. Therefore identification of θ_a provides the required $\underline{k}_{//}$ and E_{kin} to obtain a point on an experimental band structure. To apply the method it must be known in advance that the CEDC and the CEAC will touch for $\theta = \theta_a$ at a point on the symmetry line, although it is not necessary to accurately know the band structure. The gold (110) data of Hansson and Flodstrom (1978) has proved suitable for this kind of analysis and it has also been applied to copper (Courths 1981).

The use of synchrotron radiation as a light source for photoemission has resulted in a proliferation of experimental results. Due to

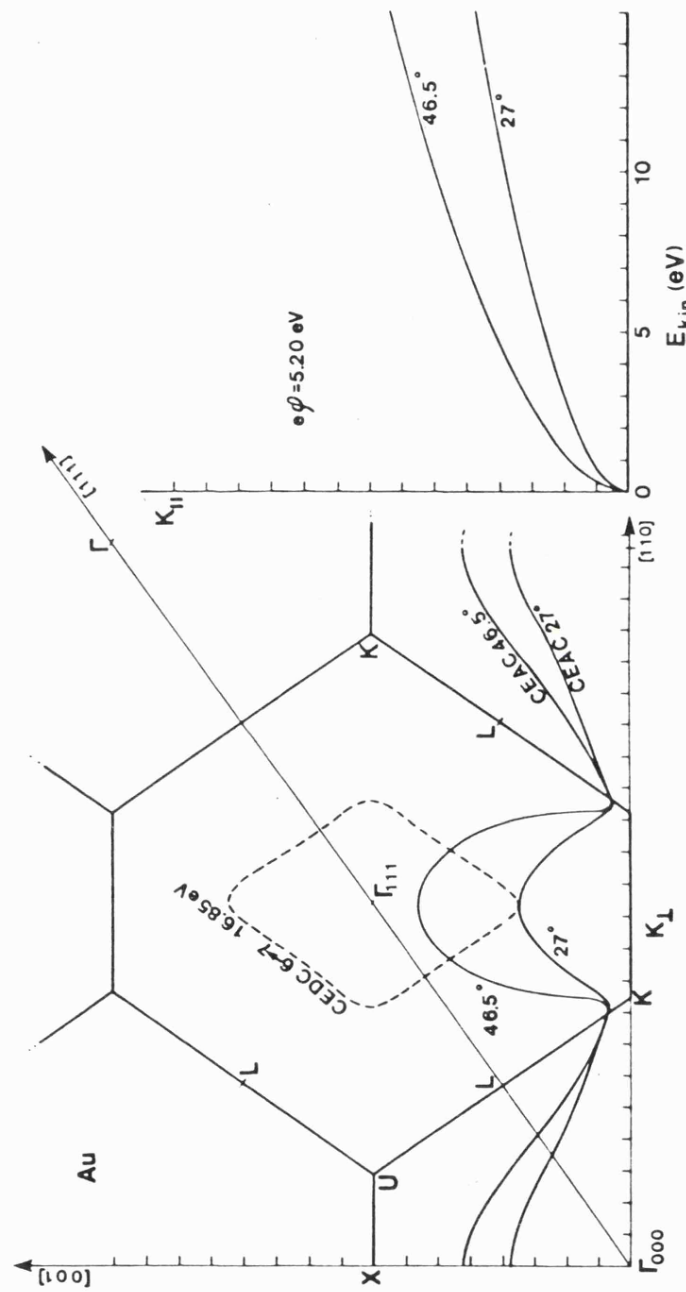


FIG. 4.3

$\Gamma K L U X$ section of the f.c.c. reciprocal space. The dashed curve is the constant energy difference contour for transitions from band 6 to band 7 in gold, the energy separation being 16.85 eV. Two constant-emission-angle contours (CEAC) of band 7 are shown with full lines. The emission angles are $\theta = 46.5^\circ$ and 27° , the latter being the (calculated) appearance angle.

the continuum of available radiation the historical separation of UPS and XPS no longer applies with the result that one may pass from the band structure regime through a region where increasingly large samples of the BZ are obtained to the point where the XPS limit is reached and the spectra represent the DOS. At low photon energies ($\lesssim 35$ eV) it is customary to use calculated or semi-empirical final states to produce an experimental initial state band structure via the direct-transition model. Accurate dispersion relations have been obtained for palladium (111) (Himpsel and Eastman 1978), nickel (110) (Heimann et al 1981), silver (111) (Wehner et al 1979), iron (111), cobalt (0001) and nickel (111) (Eastman et al 1980), and iridium (111) and (100) (van der Veen et al 1980).

At intermediate photon energies ($40 \text{ eV} < \hbar \omega < 140 \text{ eV}$) band structure mapping is still feasible. The final state is not a bound state of the system but is an evanescent decaying electronic wave function matched to a free electron in vacuo at the surface. As a result free electron like final states may be used and the bands obtained from features in normal emission spectra using

$$\frac{\hbar^2 k_{\perp}^2}{2m} = E_{\text{kin}} + U_0 \quad (4.1)$$

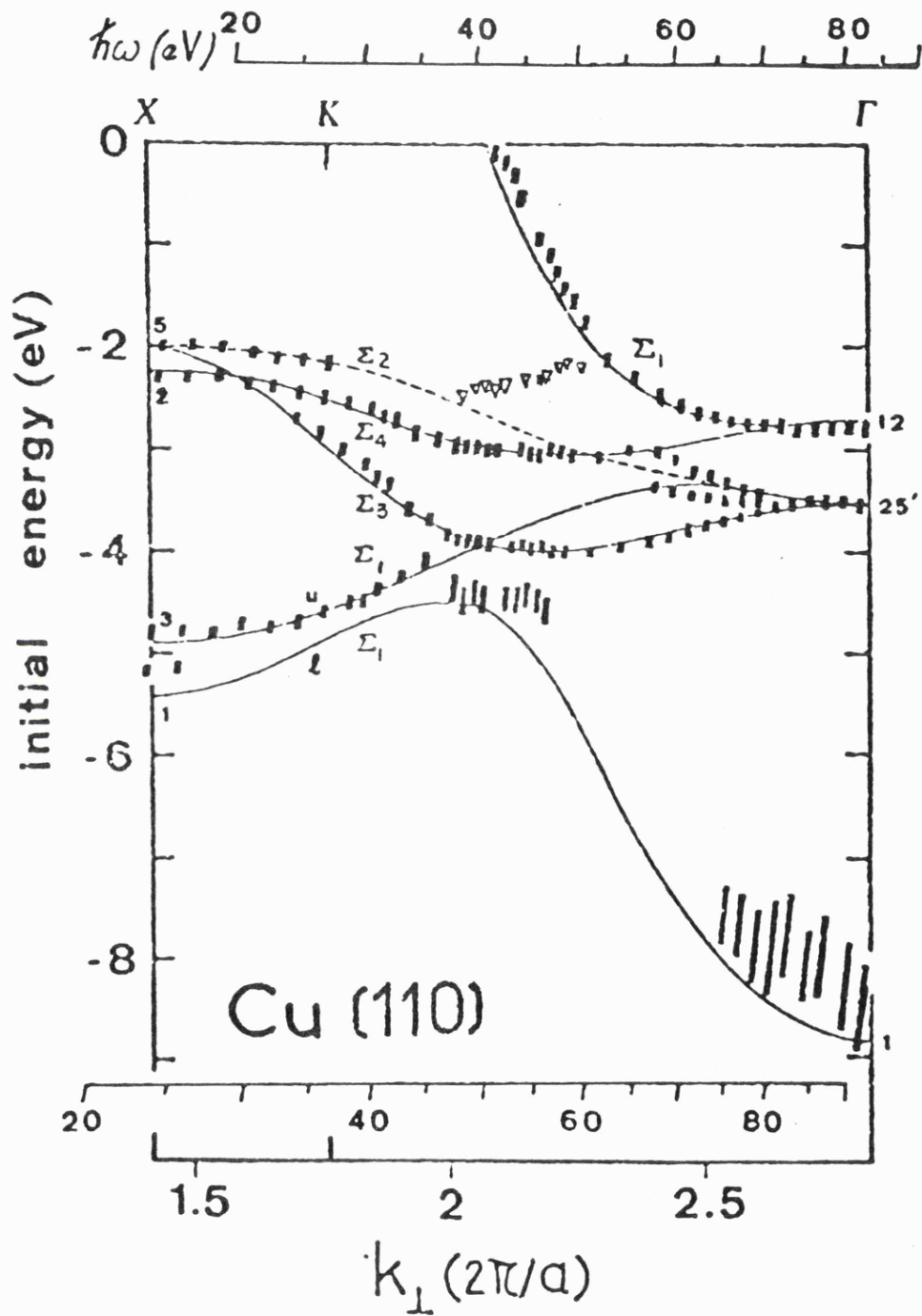
where U_0 is the internal potential.

In normal emission a non-perfect analyser accepts electrons with a small k_{\parallel} component.

$$k_{\parallel} = \frac{1}{\hbar} \sqrt{2m E_{\text{kin}}} \sin \theta_e$$

For finite angular and energy resolution $\Delta \theta$ and ΔE

$$\Delta k_{\parallel} = \frac{\sqrt{2m}}{\hbar} \left[\frac{\sin \theta_e}{2\sqrt{E_{\text{kin}}}} \Delta E + \sqrt{E_{\text{kin}}} \cos \theta_e \Delta \theta \right]$$



Experimentally determined valence band for Cu along the KX line, after Thiry et al(1979). The full lines correspond to the band structure calculation of Burdick (1963).

FIG. 4.4

In normal emission $\sin \theta_e = 0$, $\cos \theta_e = 1$ so

$$\Delta k_{\parallel} = \frac{1}{\hbar} \sqrt{2m E_{\text{kin}}} \Delta \theta \quad (4.2)$$

For typical values of $\Delta \theta = \pm 2^\circ$, $E_{\text{kin}} = 100$ eV this gives

$$\Delta k_{\parallel} = 0.18 \text{ \AA}^{-1}$$

This corresponds to $\sim 15\%$ of a typical fcc transition metal BZ dimension. Coupled with momentum broadening due to the minimum in the electron mean free path at these energies and lifetime broadening due to the hole created in the valence band, this has serious consequences for the prospect of accurate band structure mapping in this regime and places stringent requirements on angular resolution. In their work on copper Thiry et al (1979) required an angular resolution of $\pm \frac{1}{2}^\circ$ for accurate band structure mapping. Varying the emission angle by $\frac{1}{2}^\circ$ was shown to produce noticeable effects in the EDC structure. Their results for the Γ KX direction in the range 15 - 100 eV are shown in figure 4.4 as an example of the accuracy that may be achieved.

In spite of the success of the direct transition model it is clear that it has several inherent limitations. A fundamental objection is that band structures are normally based on ground state potentials and represent steady-state solutions. The experiment gives the spectral distribution in an excited state having a finite lifetime. Further, a model based on a bulk band structure is unable to account for processes involving states other than eigenstates of the infinite crystal, so that surface states for instance cannot be reproduced. A different approach is to obtain the photoelectron spectral distribution using the time-reversed LEED description. This has the added advantage that the intensity information content of the spectra is included;

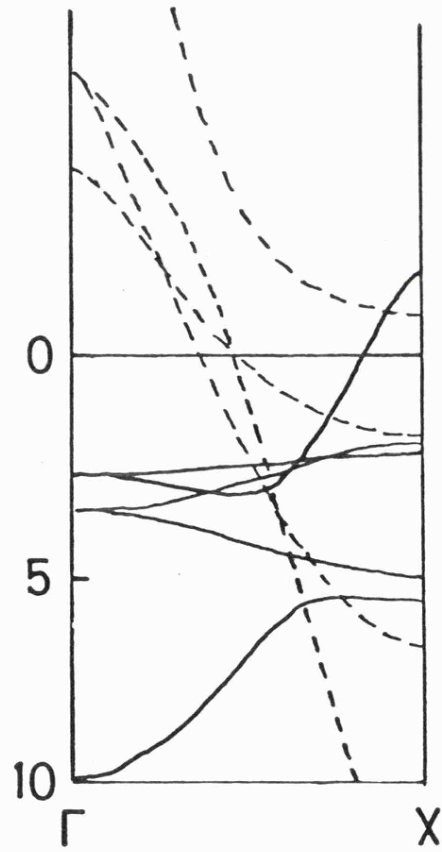
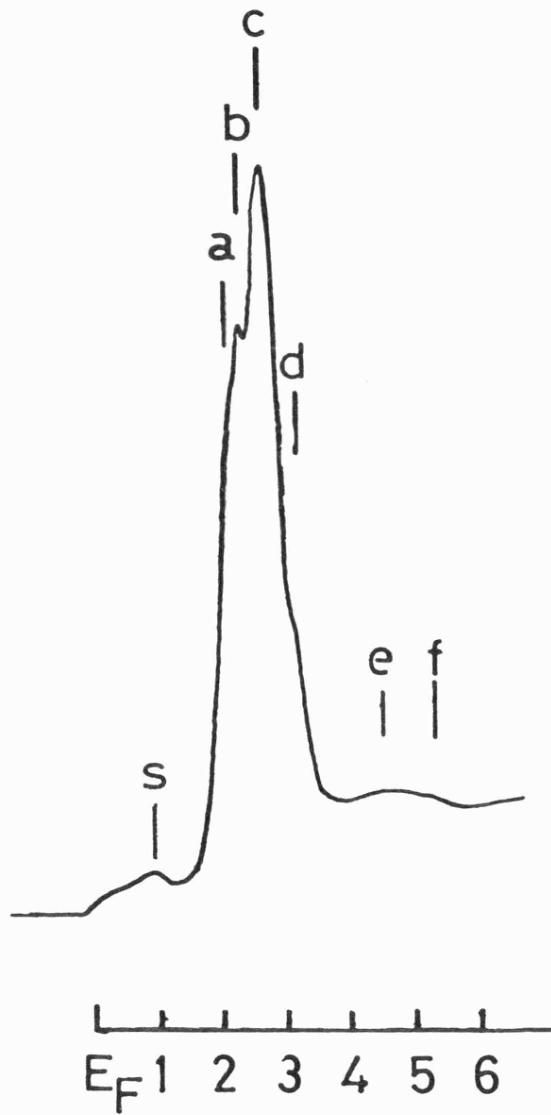
band structure mapping takes no account of this. The formulation by Pendry (1976) has proved most useful with results obtained for copper (111) (Nilsson et al 1980), copper (100) and nickel (100) (Pendry and Titterton 1978, Kanski et al 1980), silver (100) (this chapter, section 4.4.2 and Padmore et al 1982) and palladium (111) (this chapter, section 4.5 and Binns et al 1982).

4.3 The Copper (100) Surface

Photoemission spectra at $\hbar\omega = 21.2$ eV (HeI radiation) were taken of the copper (100) surface prepared as described in chapter 3, section 3.12, using the ADES-1 spectrometer at Daresbury. Throughout the experiments described in this section the photon beam was incident at 20° off normal and the analyser, surface normal and photon beam were in a specified high-symmetry plane. Copper (100) is a well characterized surface and angle-resolved spectra have been previously reported (Heimann et al 1979) but it was thought worthwhile repeating these measurements for two reasons. First, the data represented a stringent test of the previously untried ADES spectrometer and, second, the spectra were required for a comparison of clean and adsorbate covered surfaces.

The normal emission spectrum recorded for copper (100) at 21.2 eV is shown in figure 4.5. Also shown in the figure is the calculated band structure for copper in the Γ -X direction (Burdick 1963). The full lines represent initial states and the broken lines the final states being shifted downwards in energy by the photon energy. Direct optical \underline{k} -conserving transitions are thus possible when the initial and shifted final state bands intersect. The relatively flat nature of the initial state bands compared with the rapidly dispersing final states,

Cu(100)
21.2eV



NORMAL EMISSION, Cu(100)

FIG. 4.5

Photoemission from Cu (100) at 21.2 eV, normal emission

Feature	Interpretation	Binding energies (eV)		
		present data	Westphal et al	Burdick
s	Satellite, and direct transition from s-band	1.0	-	1.2
a	ODDOS	$2.16 \pm .01$	$2.15 \pm .05$	-
b	direct transition	$2.37 \pm .04$	$2.50 \pm .05$	2.55
c	direct transition	$2.69 \pm .04$	$2.77 \pm .03$	2.81
d	direct transition	$3.17 \pm .03$	$3.15 \pm .08$	3.15
e	direct transition	$4.62 \pm .05$	-	4.71
f	direct transition	$5.43 \pm .08$	-	5.81

Figure 4.6

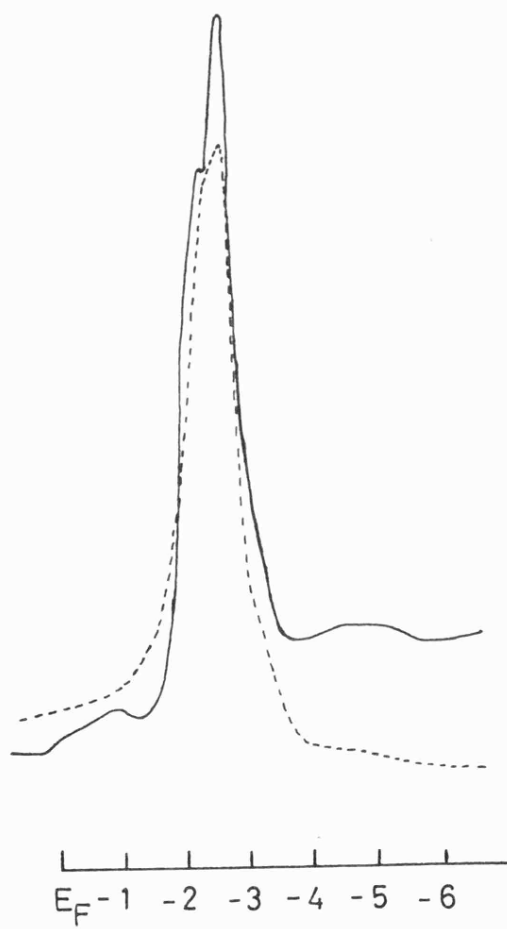
together with the effects of finite experimental resolution, suggest that only one spectral feature per initial state band is expected. The spectrum shows several prominent peaks and shoulders, labelled a to f and s. Inspection of the band structure indicates the direct transition origin of features b, c, d, e and f. The shoulder labelled a is due to a combination of the top d-band edge at the X-point and a surface resonance which is located very close to this band edge (Gay et al 1979). As such, this represents a weak DOS feature. The structure at s is due at least in part to a satellite of the He I resonance line which occurs at 23.09 eV and reflects the strong d-band peaks b and c. An alternative explanation is a direct transition from the copper s-band; without the use of a monochromator on the noble gas discharge lamp these two views cannot be distinguished. The high resolution data of Westphal et al (1980) is in agreement with the results presented here. Features s, a, b, c and d were identified and interpreted in the same manner. The authors, however, did not identify features e and f, although their direct-transition origin is quite clear. Initial state energies for the present data, the data of Westphal et al, and the predicted energies using Burdick's band structure are given in figure 4.6. It can be seen that the non-self consistent non-relativistic band structure calculation gives a reasonably accurate determination of the energies of the direct-transition features in the spectrum.

The time-reversed LEED formalism of Pendry (1976) (the PEOVER program referred to earlier) was used to calculate the normal emission spectrum from copper (100) at 21.2 eV. The Chodorow potential was used (Chodorow 1939). The calculated spectrum is compared with experiment in figure 4.7, together with the PEOVER band structure. In the calculated spectrum the s and p polarized components were added together

———— = experiment

----- = theory

Cu(100)



PEOVER energy bands

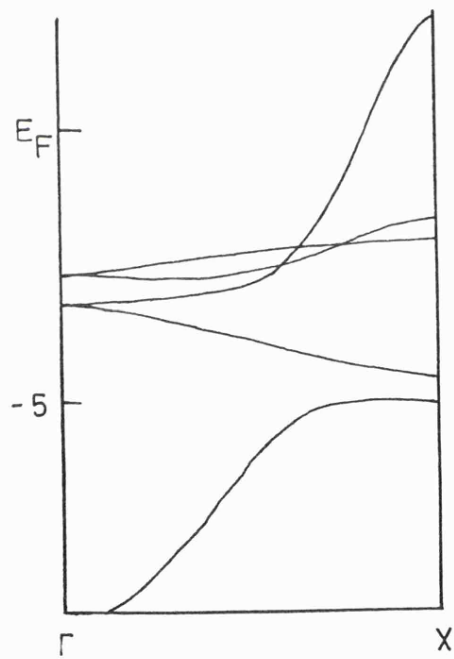


FIG. 4.7

to simulate an unpolarized source. PEOVER is not expected to function extremely well at low photon energies, due at least in part to the constant initial and final state lifetimes approximation (Pendry and Titterton 1978) but the agreement between theory and experiment is quite encouraging. The d-band maximum is located at the correct energy and is broadened into two features, corresponding to b and c in the experimental spectrum. Shoulder d is visible and a small feature approximately mid-way between features e and f is also predicted. The DOS structure a is not reproduced and neither, of course, is the satellite feature s, although considerable s-band emission is indicated. These results, coupled with inspection of the calculated initial state band structure, which agrees in all respects with the self-consistent band structure of Moruzzi et al (1978), give confidence in both the one-step model of photoemission implemented in PEOVER and in the suitability of the Chodorow potential for copper.

Off normal emission spectra were taken for the two principle symmetry planes of the copper (100) surface. These are presented in figure 4.8, and are similar in all respects to those given by Heimann et al (1979). Azimuthal angle $\phi = 0^\circ$ corresponds to emission in the (100) plane containing the Γ , X, W and K points of the BZ, and $\phi = 45^\circ$ to the $(0\bar{1}1)$ plane containing Γ , L, U and X. Heimann and co-workers were also in possession of Cu (110) data and were thus able to perform an analysis based upon the energy coincidence method to determine E vs \underline{k} relationships. The sharp feature observed at higher emission angles in the (100) mirror plane was found to lie within an energy gap of the PBBZ. This feature exhibited two-dimensional dispersion and was sensitive to surface contamination, and was interpreted as a surface state. Exposure of the surface to dry air also resulted in a reduction in intensity of the

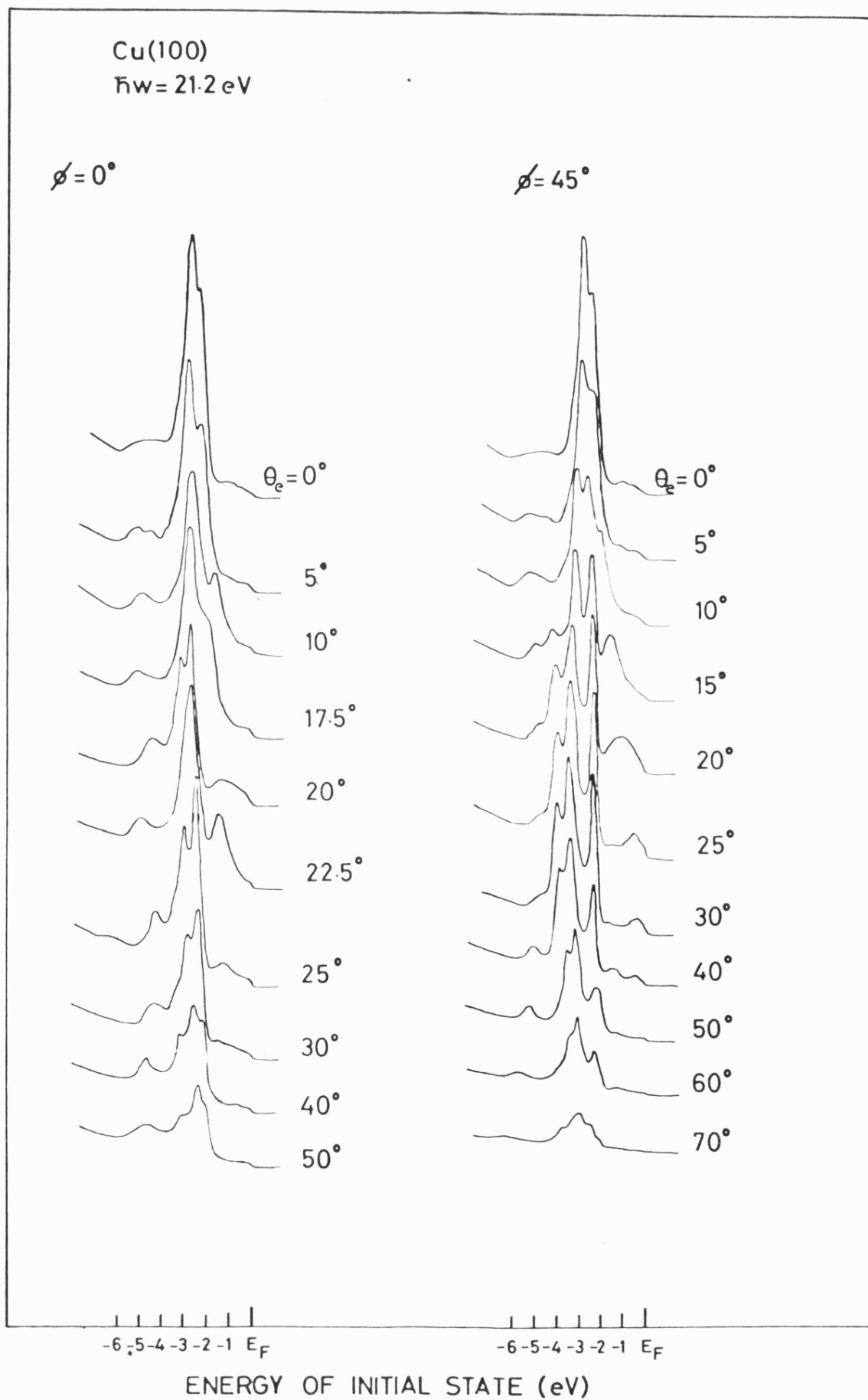


FIG. 4.8

leading d-band maximum observed at and near normal emission. This behaviour is indicative of bulk states with an enhanced surface amplitude on the clean metal, and such surface resonances have been predicted by Gay et al (1979) for a wide region of the SBZ near the top of the copper d-bands. Similar preferential attenuation was observed in the present work, both on exposure to poor vacuum conditions over long periods of time and on palladium adsorption (chapter 6).

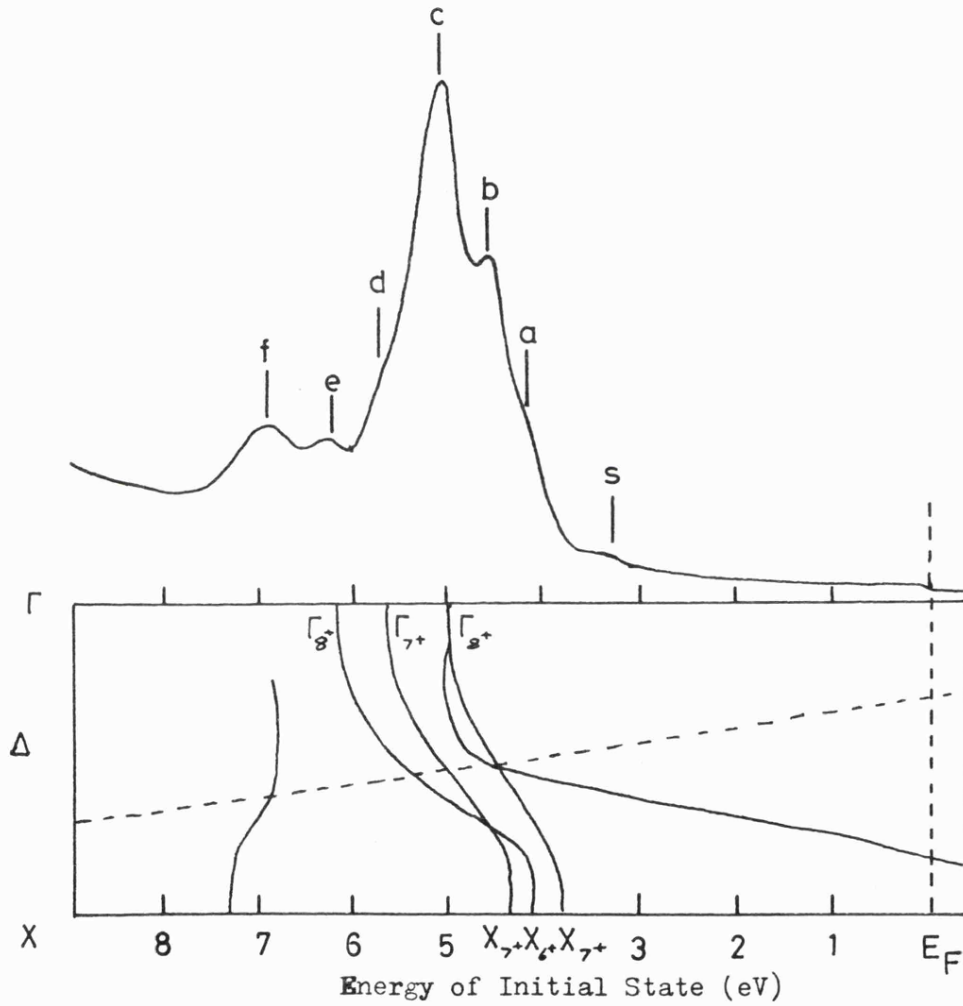
Since the band structure of copper is well known it was not thought worthwhile undertaking an appearance angle analysis of the angle resolved copper data. Such a study has now been carried out (Courths 1981) and Burdick's (1963) band structure shown to be accurate.

4.4 The Silver (100) and (111) Surfaces

The electronic properties of silver have not been investigated as thoroughly by photoemission as copper. A number of studies have been carried out; the definitive work being possible the band structure mapping of Courths et al (1981). Off normal emission spectra were used to determine experimental final-state dispersions and then peaks in the normal emission spectra observed at various noble gas discharge energies assigned to initial states using the direct transition model. Slight deviations of up to 0.4 eV from the theoretical bands of Christensen (1972) were found. The situation with regard to surface states is still rather controversial (Lindroos et al 1982, Smith et al 1980).

In the present work data were taken using the He-I resonance line at 21.2 eV and synchrotron radiation in the energy range 40 to 120 eV. The results are discussed separately in sections 4.4.1 and 4.4.2.

Ag(100), 21.2 eV.
 Normal Emission



Experimental band structure for silver along the Γ - Δ -X direction (Courths et al 1981)

FIG. 4.9

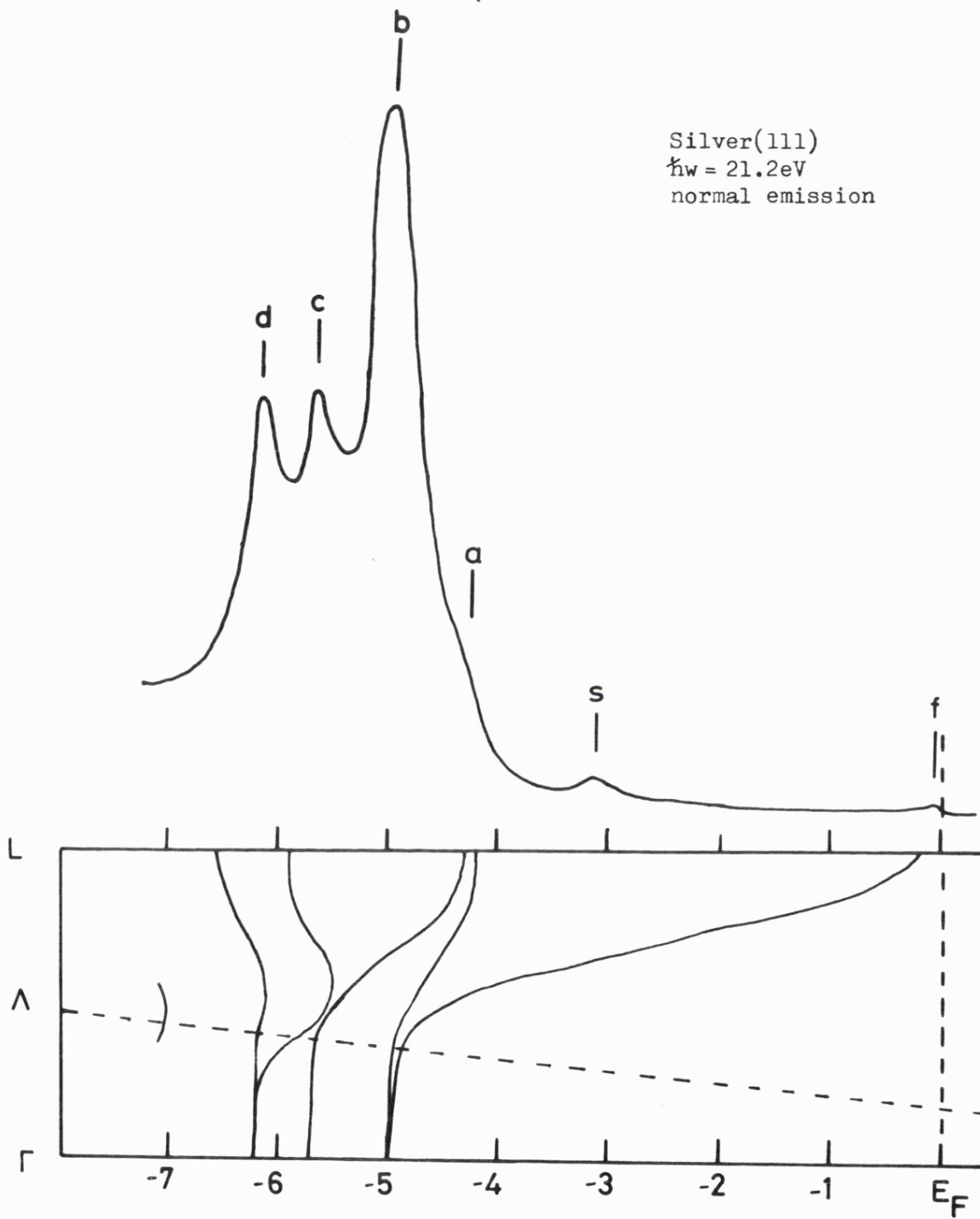


FIG. 4.10

4.4.1 He-I Excitation

The normal emission results for silver (100) and (111) are shown in figures 4.9 and 4.10 respectively, along with the experimental band structure of Courths et al (1981) for the appropriate crystal symmetry direction. The dotted lines represent the experimental final state bands shifted down in energy by the photon energy. The spectra are in excellent agreement with the high resolution data of Roloff and Neddermeyer (1977).

For the (100) case inspection of the bandstructure identifies features b, c and f as due to direct transitions from the initial state bands to the nearly-free-electron like final state, and features a, d and e as due to the high DOS at the X_6^+ , Γ_7^+ and Γ_8^+ points respectively. Structure s is due to the He I- β satellite line at 23.09 eV.

The three most intense features in the (111) spectrum, labelled b, c and d, are clearly due to direct transitions from the experimental initial bands. Shoulder a results from the high DOS at the top of the d-band at Γ . The peak labelled f was also observed by Roloff and Neddermeyer (1977) and as it occurs in the L-gap was attributed to a surface state. Changing the photon energy caused no dispersion of this feature, as expected for a surface state. The structure labelled s is again due to the He I- β satellite line.

The energies and origins of the features in the 21.2 eV normal emission spectra from the (111) and (100) surfaces of silver are summarized in figure 4.11.

The PEOVER calculated normal emission spectrum for Ag(100) is shown against the experimental curve in figure 4.12. An inner potential

Normal Emission Photoemission from Silver at 21.2 eV

Surface	Feature	Energy (eV)	Interpretation
(100)	s	3.19	satellite
	a	4.17	ODDOS from X_6
	b	4.60	direct transition
	c	5.06	direct transition
	d	5.69	ODDOS from Γ_7
	e	6.36	ODDOS from Γ_8
	f	6.90	direct transition
(111)	f	0.10	surface state in L-gap
	s	3.05	satellite
	a	4.32	ODDOS from Γ_8
	b	4.92	direct transition
	c	5.60	direct transition
	d	6.13	direct transition

Figure 4.11

Ag(100), $hw = 21.2\text{eV}$

THEORY

EXPERIMENT

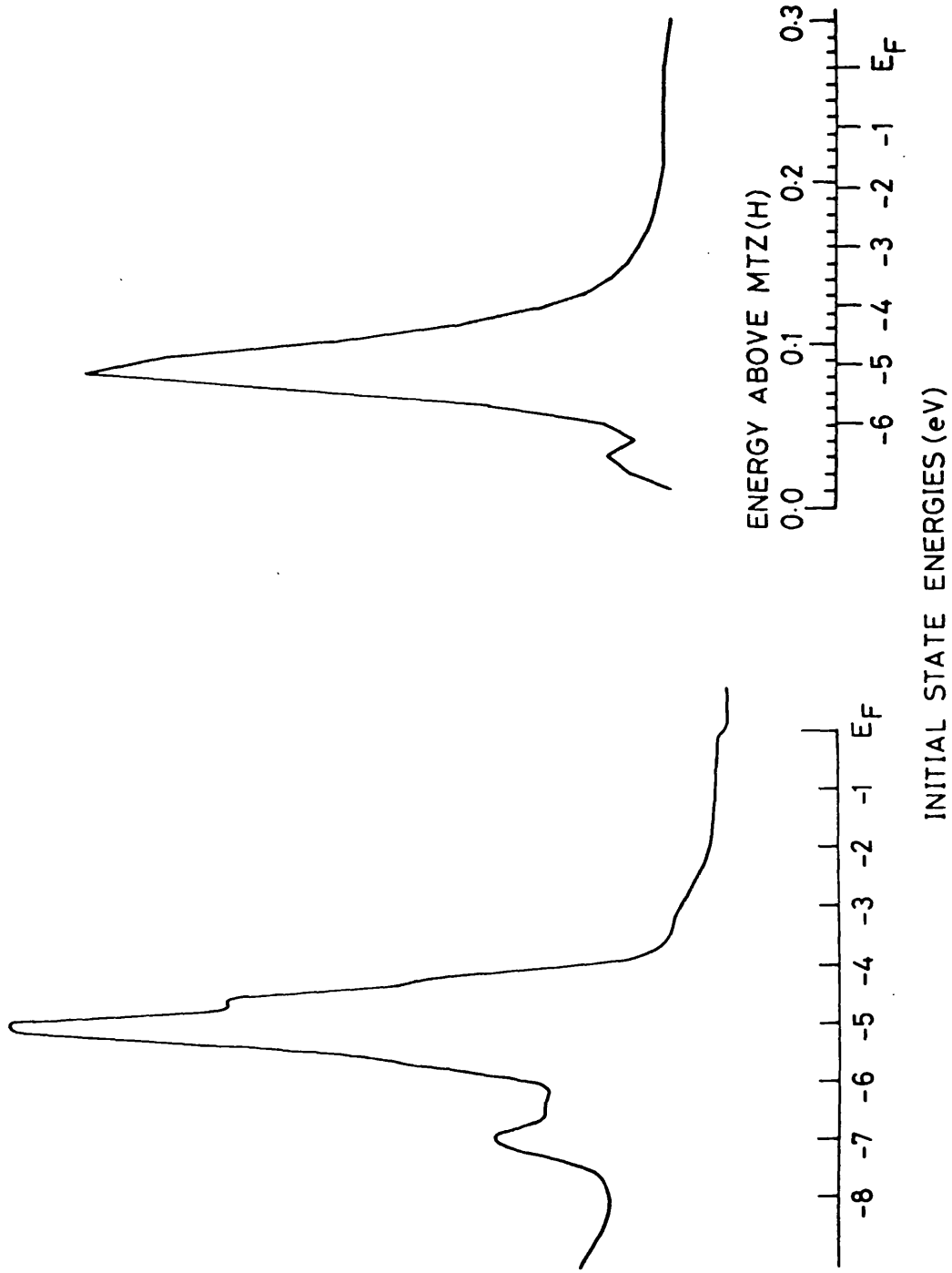


FIG. 4.12

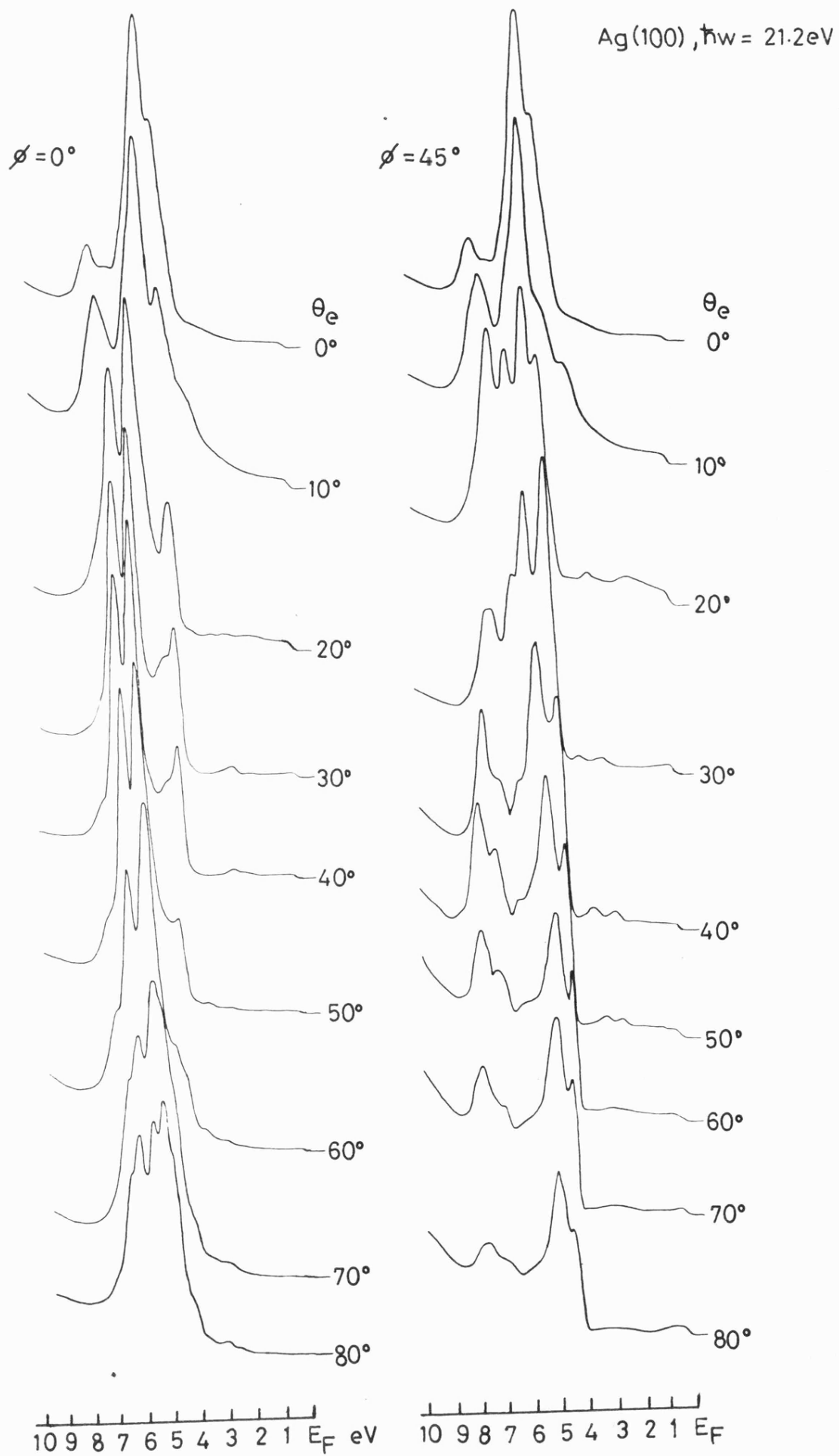


FIG. 4.13

of $0.42H$ was used and electron and hole lifetimes were taken as $.10H$ and $.01H$ respectively, representing realistic values. The potential was obtained from a self-consistent atomic potential and transformed to muffin-tin form using the method of Mattheiss (1964) and is the same as that used by Padmore et al (1982). As in the case of copper, agreement between theory and experiment is quite good with the intense direct-transition features b, c and f being accurately located and the correct spectral shape obtained.

Off normal spectra for the two principal symmetry axes of the (100) and (111) surfaces of silver are shown in figures 4.13 and 4.14 respectively. All spectra compare favourably with published data, where these are available for comparison (Spears et al 1980, Liebowitz and Schevchik 1978, Lindroos et al 1982). As in the case of copper a detailed analysis of the spectra in terms of appearance angles or energy coincidences was not attempted. The energy coincidence method has already been used by Courths et al (1981) in their accurate determination of the experimental band structure of silver.

Recently, controversy has centred around the possibility of surface states on silver (100). The self consistent local orbital calculations of Smith et al (1980) suggest that surface states in the s-d gap may be a universal feature of the noble metal (100) surfaces. In particular, for silver a relatively large fraction of electrons were predicted to be in surface states and surface resonances which resulted from a rise in potential of the outermost layer. A further calculation by Arlinghaus et al (1981) using the same technique predicted a concentration of surface states at the top of the d-bands with one well separated surface band running in the s-d gap at \bar{M} . The photoemission measurements of Lindroos et al (1982), however, showed no evidence for

Ag(111), 21.2eV

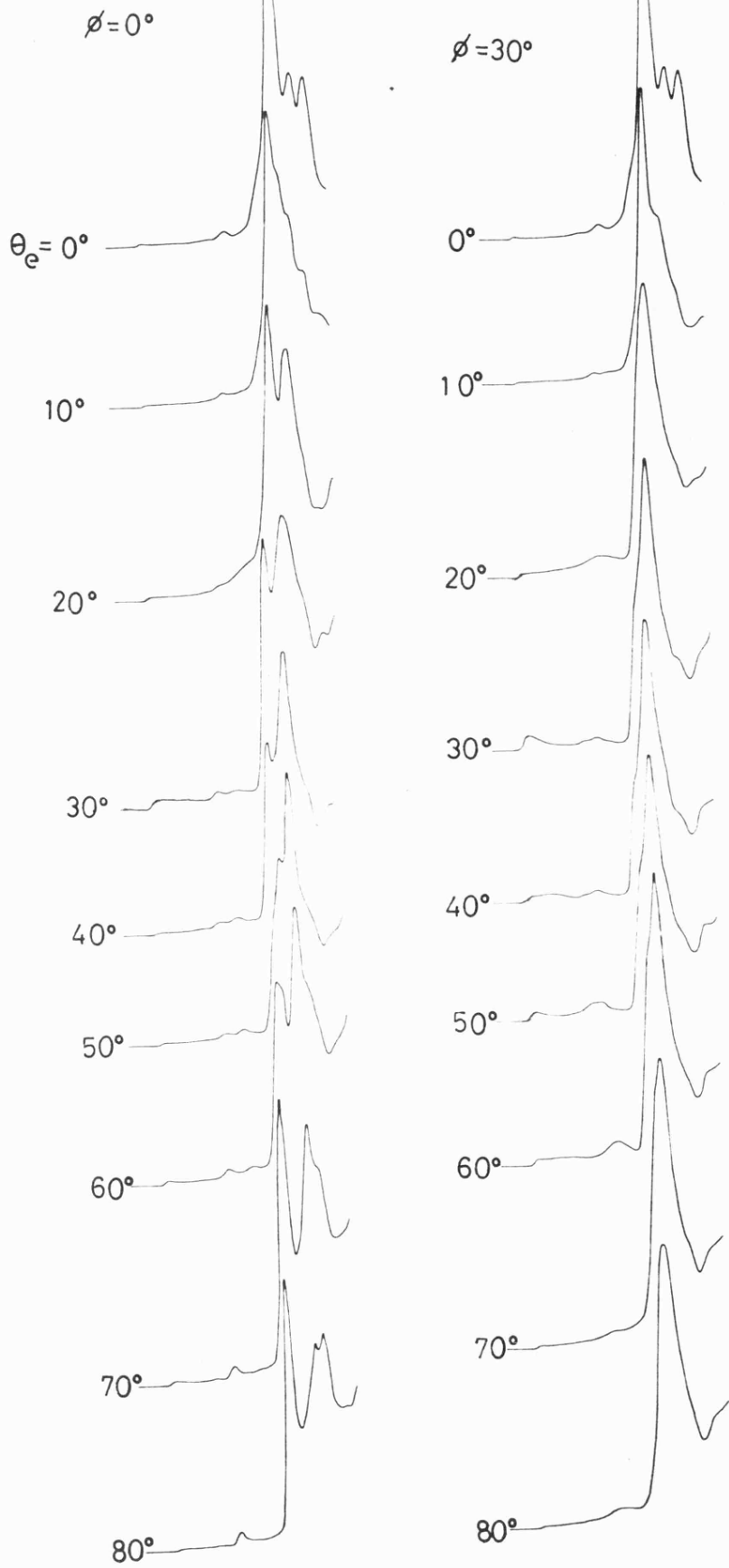


FIG. 11

surface states at or near \bar{M} . Referring to figure 4.13, the sharp leading edge feature at -4.0 eV in the curve recorded for the 45° azimuth with an emission angle of 50° , corresponding to the region of the SBZ in question, is the result of direct transitions very close to the maximum of the d-bands at the X-point in the bulk BZ. Lindroos et al found it possible to produce an additional surface state peak in the theoretical spectra for this emission angle by the application of a 0.5 eV surface potential shift. The absence of this peak in the experimental spectrum was seen as implying an over-estimation of the surface potential shift in the SCLO calculations of Arlinghaus et al (1981). Evidence for the existence of surface resonances on silver (100) was found by Lindroos et al. The results are in agreement with the evidence from photoemission measurements on palladium overlayers on silver (100) discussed in chapter 5 and in Smith et al (1982).

The question of surface states on silver (100) is further complicated by the recent visible and infra-red electroreflectance measurements of Kolb et al (1981). A surface state was observed 0.7 eV below E_F at \bar{X} in the SBZ, corresponding to the gap in the bulk band structure at the L point. No evidence to support this view was found in the photoemission measurements of the present work.

For the (111) surface the surface state observed in normal emission (feature "f" in figure 4.10) has already been discussed. The feature was too weak to enable its dispersion to be mapped out using the off-normal spectra (figure 4.14). No other surface states have been reported for the silver (111) surface; the work of Leibowitz and Shevchik (1978b) indicated there was no significant modification of the bands at the surface and no conclusive signs of surface states were found.

4.4.2 Synchrotron Radiation Excitation

Angle resolved photoemission spectra were taken of the silver (100) surface using the facilities of the Daresbury Synchrotron Radiation Source described in chapter 3. The work described in this section and in Padmore et al (1982) formed the first angularly resolved photoemission study of silver at high photon energies although low energy experiments on several low-index faces have been reported previously (Wehner et al 1979, Spears et al 1980, Courths et al 1981).

Figure 4.15 shows the photoelectron spectra recorded at normal emission for photon energies up to 100 eV. The curves are plotted against the energy of the initial state with the Fermi level at zero and are normalized with respect to the incident photon flux. The synchrotron radiation was incident on the sample at 60° to the normal in the horizontal plane and thus corresponded to mixed s and p polarization.

As with the work of Thiry et al (1979) on copper (110), the spectra change continuously up to the highest photon energy. There is a steady decrease in the area under the region of the 4d band between -4 and -7 eV, reflecting the drop in 4d photoionization cross section as the Cooper minimum is approached. Five separate features in this binding energy region can be discerned at approximately -4.1, -4.9, -5.5, -6.0 and -7.1 eV. They exhibit considerable modulation in their relative intensities. In particular, the -7.1 eV feature which appears as a weak shoulder at $h\nu = 40$ eV increases in strength to a maximum between 80 and 90 eV, after which it drops away. Similar observations have been reported in UPS from other metals such as copper (Louie et al 1980), nickel (Guillot et al 1977) and palladium (Nilsson et al 1981).

Ag(100)

NORMAL EMISSION

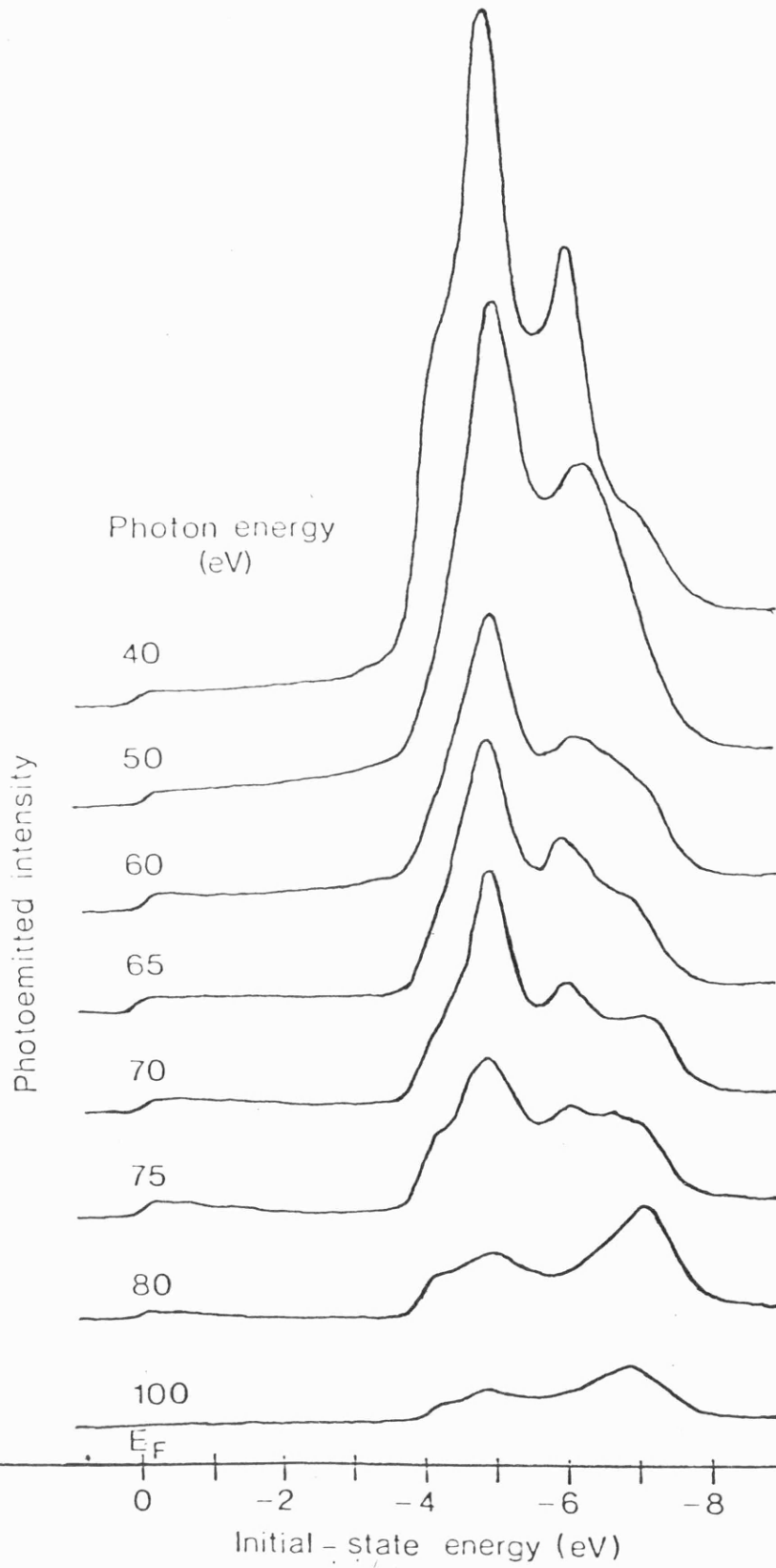


FIG. 4.15

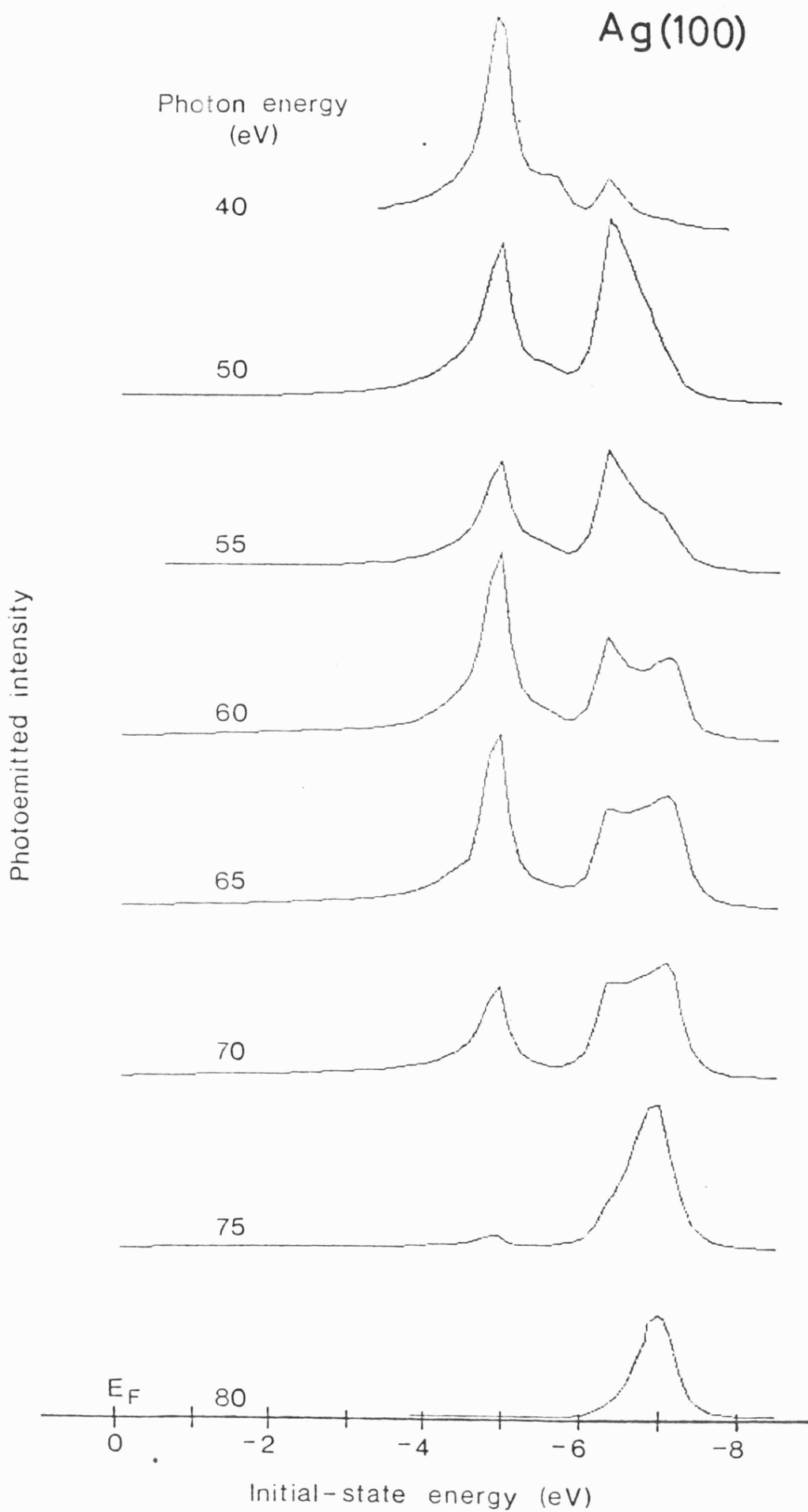


FIG. 4.16

None of the observed valence band peaks show any significant dispersion with varying photon energy. This is a combination of three effects: (i) relatively flat initial state bands; (ii) energy and \underline{k} -broadening in the final state (due to finite electron and hole lifetimes); and (iii) limited experimental angular resolution. In consequence of the first two effects the energy distribution curves in normal emission tend to reflect the one-dimensional density of states along a characteristic \underline{k}_z range. The finite angular resolution gives an additional \underline{k} integration which fixes the spectral weight to the high density of states region within the probed \underline{k} space.

Figure 4.16 shows spectra calculated using the time reversed LEED method. The position of the Fermi level is predicted indirectly via the internal potential U_0 and the work function ϕ and so the energy scale has been adjusted so that the main peak in the 40 eV photon energy curve is aligned with the strong peak at -4.9 eV in the corresponding experimental result. At this photon energy the theory gives a good representation of the experiment. All features are reproduced except for the shoulder at -4.1 eV. This has been observed in low photon energy spectra by Courths et al (1981) and was attributed to non direct transitions from a high density of states close to the X point of the bulk BZ. A similar structure in the copper (111) spectra was given the alternative interpretation of a surface state by Nilsson et al (1980). This state was produced in calculations using a slightly modified atomic potential in the surface layer.

As the photon energy is increased to 80 eV, the same general trends in both theory and experiment are seen. There is no significant movement in energy of the features and there is a rapid increase in the relative strength of the -7.1 eV peak, with an accompanying decrease in

the peak at -4.9 eV above 70 eV photon energy, the theory shows a more exaggerated behaviour with only a single peak at 80 eV, whereas two peaks are observed in the experiment. The agreement between experiment and theory could be improved here by using a more realistic part of the d-state cross section (Nilsson et al 1981, Wendin 1981). Using the same computational method as here, it has been shown by Kanski et al (1980) for nickel and by Nilsson et al (1980, 1981) for copper and palladium that strong intensity modulations can be understood in terms of the single particle approximation. The lower (here -7.1 eV) peak in particular fits a description in terms of ordinary interband transitions.

Thus it appears that the main features of photoemission from silver in the range $40 \text{ eV} \leq \hbar\omega \leq 80 \text{ eV}$ can be described by the one-step photoemission theory with a non-relativistic potential. The discrepancies between theory and experiment may be due to the spin-orbit interaction which, at a value of 0.45 eV at the Γ point in silver, is not sufficiently small for relativistic terms to be ignored. A d-state cross section properly corrected for many-body effects could also play an important role. For narrow band materials a more complete analysis, such as is possible with the one-step photoemission theory, can be the only way that useful information about the crystal potential can be derived from photoemission data. The lack of perfect resolution is not critical and information contained in the intensity of peaks is not ignored, as in the band structure approach.

4.5 The Palladium (111) Surface

Angle resolved photoemission spectra were taken of the palladium (111) surface using He I radiation and synchrotron radiation in the energy range 40 to 120 eV from the Daresbury SRS. Photoemission from palladium (111) in the 40 to 90 eV photon energy range was

Palladium(111)
 $\hbar\omega = 21.2\text{eV}$
normal emission
— = experiment
- - - = theory

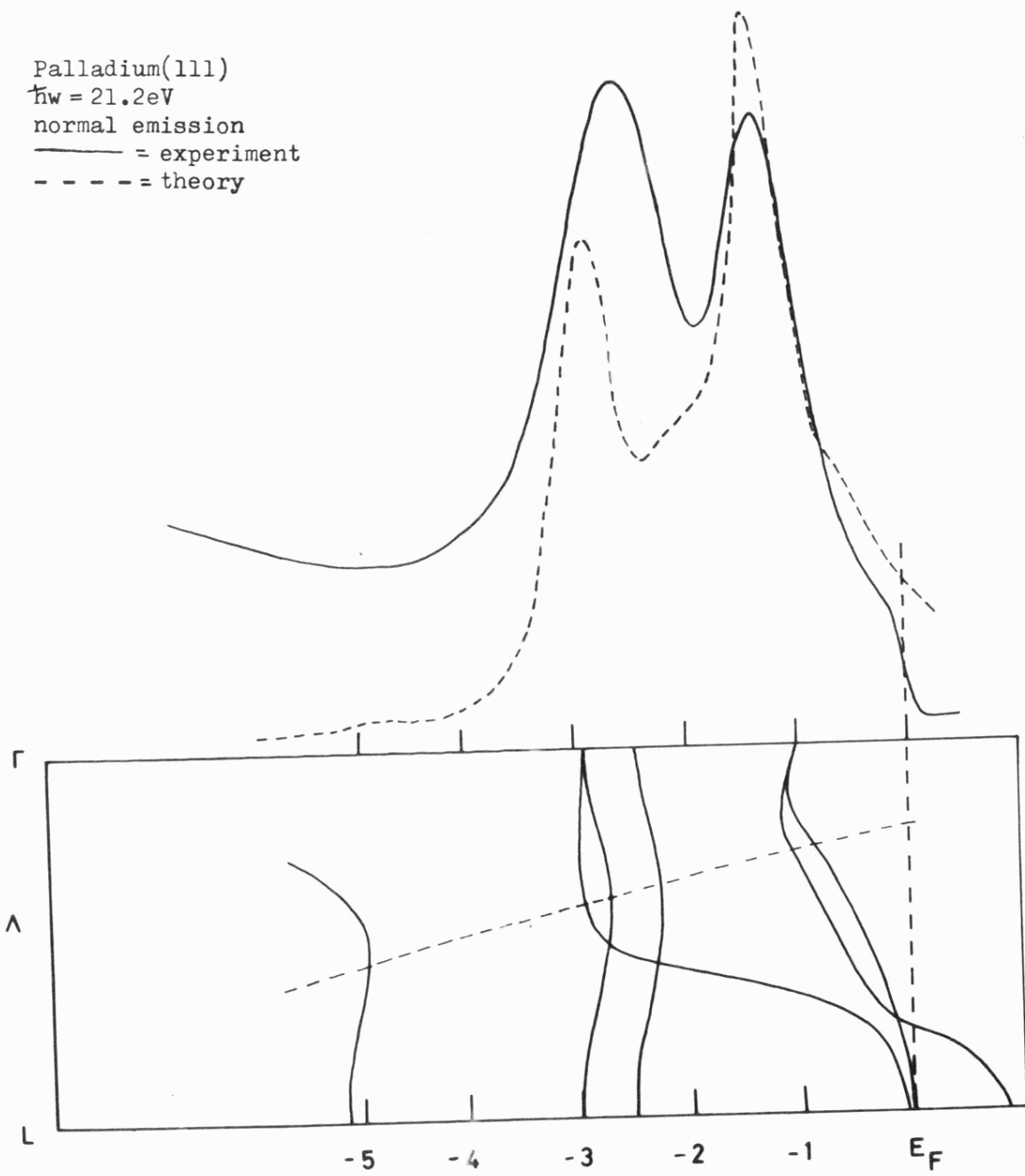


FIG. 4.17

investigated by Nilsson et al (1981) but constant initial energy (CIE) curves were measured and these authors did not present the spectra in the form of EDC's. Several low energy studies of this crystal face have been reported (Lloyd et al 1977, Asonen et al 1980, Himpsel and Eastman 1978).

The normal emission HeI spectrum for palladium (111) is shown in figure 4.17, together with the calculated normal emission spectrum using PEOVER and the experimental band structure of Asonen et al (1980). The experimental spectrum is in good agreement with that obtained by Lloyd et al (1977). The two dominant spectral features at -1.24 and -2.36 eV correspond to direct transitions from the initial state bands, and are also reproduced in the calculated spectrum. The lowest initial state band, of s origin, does not appear to give rise to a feature in the spectrum; this is presumably due to a low cross section for emission from this band at this energy.

Figure 4.18 shows normal emission spectra in the energy range 40 to 120 eV taken of the palladium (111) surface using synchrotron radiation. The photon beam was incident at 60° off normal, corresponding to mixed s and p polarized components. Rather more dispersion of the spectral features with photon energy than in the case of silver (100) was seen and there seemed to be some prospect of band structure mapping as discussed in section 4.2. The ADES analyser angular resolution of $\pm 2^\circ$ (chapter 3 section 3.6), however, is quoted for a point source and rises to approximately $\pm 6^\circ$ for an extended source such as was the case on the Daresbury beam line VUV6. For this value of $\Delta\theta$ equation (4.2) gives values of Δk_{\parallel} ranging between 25% and 40% of the BZ, depending upon the photon energy used. This clearly restricts the accuracy of band structure mapping using this experimental arrangement. Experimental points in $E - \underline{k}_{\perp}$ were obtained using equation (4.1) with U_0 , the inner

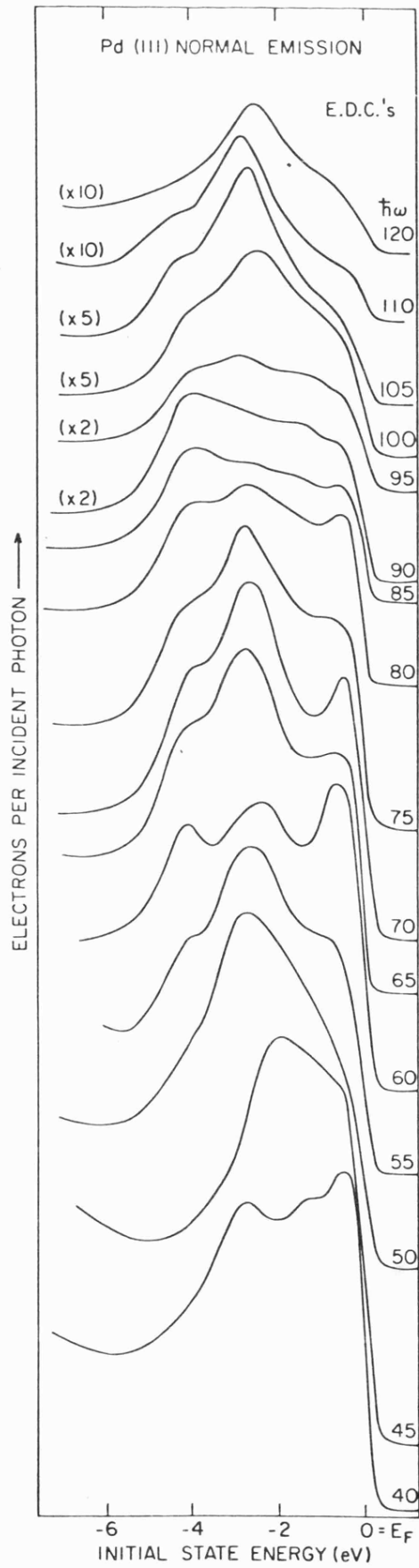
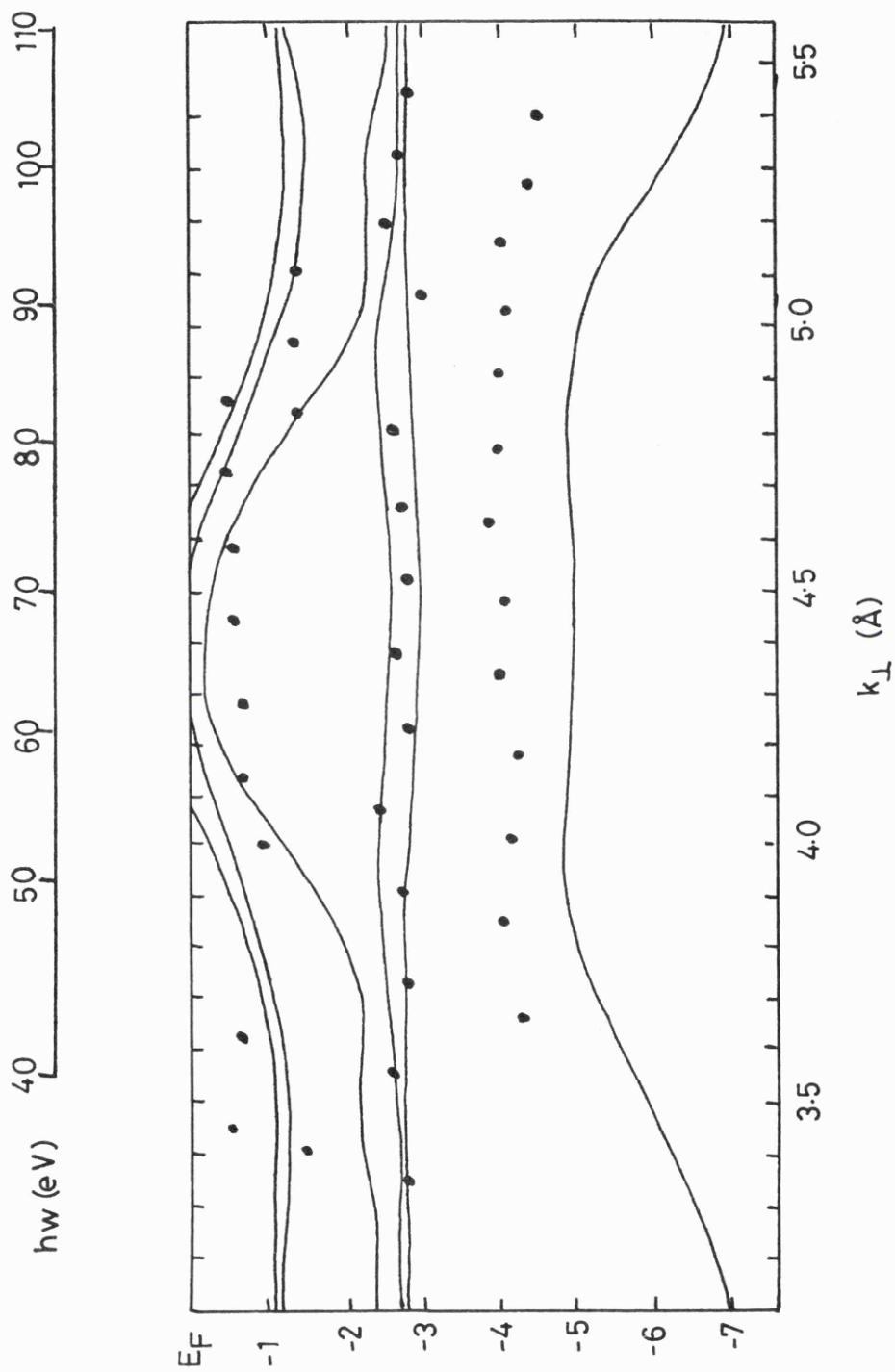


FIG. 4.18



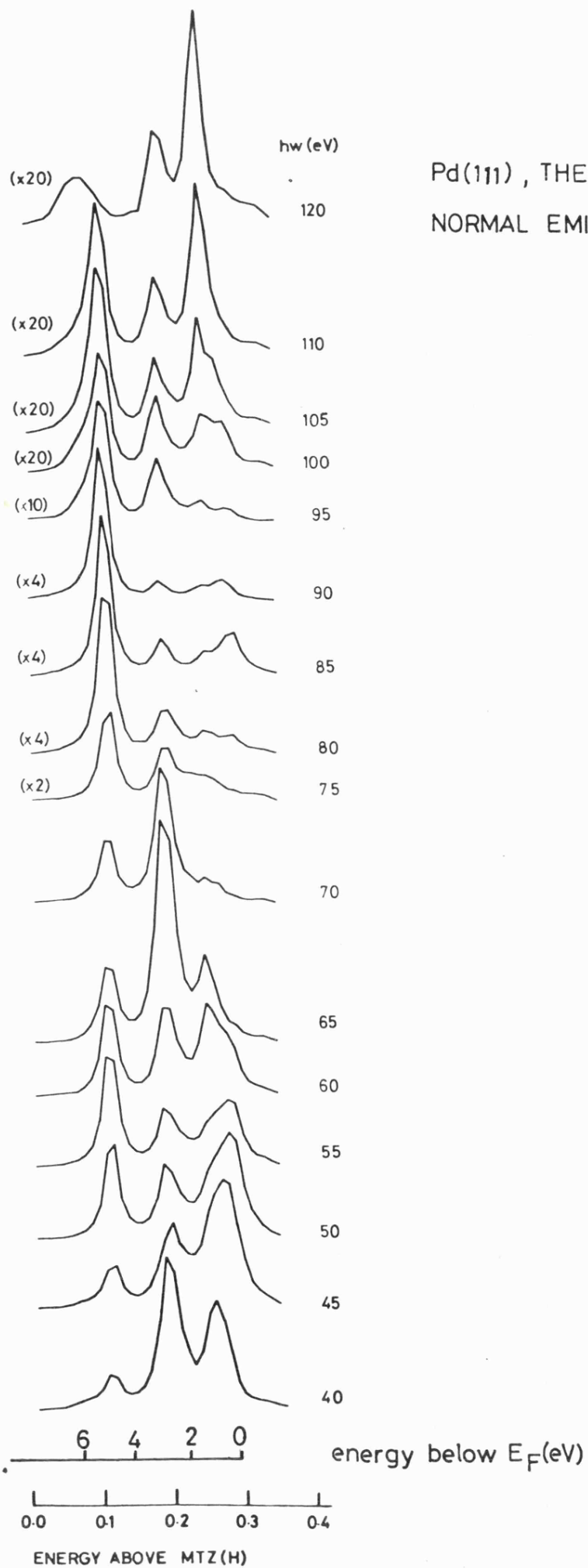
Pd(111) : • = experiment
 — = Christensen (1976)

FIG. 4.19

potential, taken to be the energy difference between the bottom of the first free-electron-like band in Christensen's (1976) RAPW calculation and the vacuum level, after Thiry et al (1979). The results are shown superposed on Christensen's band structure in figure 4.19. The effect of \underline{k} -broadening is immediately apparent on inspection of this figure; the points are spread around the region of the energy bands without following them accurately. The band structure used here has been shown to follow well the experimental initial state bands obtained using the energy coincidence method (Asonen et al 1980).

An interesting point arises concerning the lower 5 s derived band. This feature was not observed in earlier low energy studies due to the energy dependent cross section for photoemission but is seen here at approximately -4 eV. The highest point of the lowest calculated band is -4.8 eV and this appears to indicate a large (0.8 eV) error in the calculation, however, this is unlikely as its accuracy for the higher bands is well established. It is more probably an effect of the integration over the whole BZ resulting from the poor angular resolution with the extended source and represents the contribution due to a high DOS at this energy in some region of the BZ for which the band structure is not calculated. This illustrates further the importance of angular resolution for band structure mapping.

Calculations using the time-reversed LEED derivation of photocurrent directly from the potential were carried out in the same manner as for silver (100) (preceding section) and the resulting theoretical spectra are presented in figure 4.20. A muffin-tin potential obtained from the atomic potential by the Mattheis (1964) scheme was used (P. Durham, private communication) and the surface barrier of 0.42 H was taken to be at a distance corresponding to the muffin-tin radius from the centre of the surface layer. The agreement between



Pd(111) , THEORY
 NORMAL EMISSION

FIG. 4.20

Comparison of Theoretical and Experimental
Binding Energies for Pd (111)

h (eV)	Experimental Binding energy (eV)			Theoretical Binding energy (eV)				
40	.55	1.52	2.80	.81	2.56	4.76		
45	.65	2.65		.48	2.44	4.90		
50	2.80	4.35		.27	2.72	4.76		
55	.98	2.75	4.13	.20	2.65	4.76		
60	.70	2.44	4.20	1.09	2.58	4.76		
65	.65	2.85	4.30	1.09	2.58	4.76		
70	.50	2.65	4.00	.95	2.58	4.76		
75	.55	2.80	4.05	0.00	.95	2.58	4.69	
80	.45	2.75	3.90	0.00	1.02	2.52	4.80	
85	.50	1.42	2.65	4.00	0.10	1.09	2.72	4.90
90	.65	1.40	4.00	0.27	1.09	2.72	4.90	
95	1.40	3.00	4.10	0.14	1.09	2.72	4.79	
100	2.50	4.05		0.27	1.09	2.79	4.76	
105	2.70	4.40		0.54	1.09	2.72	4.76	
110	2.80	4.50		1.09	2.67	4.83		
120	.70	2.73		0.00	1.16	2.58	5.58	

Figure 4.21

theory and experiment is of similar order to that observed for silver (100). The trends with changing photon energy are well reproduced, in particular the change from three to four features with increasing photon energy, and the sudden intensity maximum in the central -2.8 eV feature around 70 eV are predicted in the theoretical curves. The highest binding energy peak also follows the experimental result in dispersing to higher binding energies at higher photon energy. A comparison of the energies of the theoretical and experimental spectral features is given in figure 4.21, relative to a Fermi energy positioned 0.29 H above the muffin-tin zero in the theory. There seems to be no clear shift of E_F (i.e. variation in step height or work function) in the theory that will improve agreement. It is possible that at the higher energies the predicted peaks near E_F may simply be too weak to be observed in the experimental curves as the Cooper minimum is approached. The mean deviation in binding energy between corresponding peaks, where these can be identified, in theory and experiment is approximately 0.3 eV. This is of the same order as the accuracy of location of final state bands in the three step interpretation (Courths et al 1981).

Similar comments regarding the source of discrepancy between theory and experiment apply as for the silver (100) case. Relativistic corrections are again ignored, and in addition the rather severe approximations of a sudden potential step at the surface, and of constant initial and final state lifetimes, have an effect on the form of the computed spectrum (Pendry and Titterington 1978).

4.6 Summary

Angle resolved photoemission measurements of the copper (100), silver (100) and (111), and palladium (111) crystal surfaces have been made. At the HeI photon energy of 21.2 eV the results were in agreement

with previously published data, where these were available for comparison. Direct transition from calculated ground state band structures were found to predict experimental peak positions quite well and the effects of non \underline{k} -conserving transitions were in general small. For the higher photon energies up to 120 eV the time-reversed LEED theory was found to predict the trends in photoemission from the silver (100) and palladium (111) surfaces. The method was also used for all of the surfaces at 21.2 eV. In this way the validity of the theory and the accuracy of the potentials employed was checked.

The measurements formed the basis for an understanding of the electronic properties of the clean surfaces which were later used for adsorbate studies.

CHAPTER 5

AN ELECTRON SPECTROSCOPIC STUDY OF Pd OVER-
LAYERS ON Ag (100) AND (111)

- 5.1 Introduction
- 5.2 LEED and AES Results
- 5.3 Normal Emission Photoelectron Spectra
- 5.4 Work Function
- 5.5 Isolated Pd Resonance
- 5.6 E-k Dispersion Relations for Pd Monolayers
- 5.7 Photoemission Calculations
- 5.8 Discussion
- 5.9 Summary

CHAPTER 5

AN ELECTRON SPECTROSCOPIC STUDY OF Pd OVER-
LAYERS ON Ag (100) AND (111)5.1 Introduction

In this chapter is described an angle resolved photoemission study of palladium adsorbed on the (100) and (111) faces of silver. This system was chosen for several reasons. First, palladium and silver form a continuous face centred cubic solid solution in the bulk with a lattice constant which varies from 2.75 Å (Pd) to 2.89 Å (Ag). The Pd 4d and Ag 4d valence bands overlap little in energy with small d-d hybridisation. Thus at temperatures low enough to inhibit dissolution, palladium should form well ordered overlayer structures (with a 5% expansion) which do not interact strongly with the silver substrate and are particularly suited for the study of electron states of a monolayer. Electron diffraction studies of Burland and Dobson (1981) have confirmed that the growth is initially pseudomorphic. Second, both silver and palladium are well characterised metals with band structure calculations (e.g. Christensen 1972 and 1976, Podlucky et al 1979) and experimental photoelectron spectra (e.g. Lloyd, Quinn and Richardson 1977, Asonen et al 1980, Courths, Bachelier and Huffner 1981, Padmore et al 1982) of the bulk crystalline phase available. In addition theoretical calculations of the electron states of ultra-thin palladium films on silver (100) using the LCAO technique have been presented by Bisi and Calandra (1977). The local density of states of the first layer appeared to agree with the photoelectron spectra of Eastman and Grobmann (1973) even though the substrate and overlayer geometry were not defined in the experiment. Noffke and Fritsche (1981) have recently reported self-consistent calculations of the electron band structure of an unsupported palladium (100) monolayer.

The theoretical calculations for the supported and unsupported palladium monolayers are compared with the present experimental results in section 5.6. In view of the central importance of local coordination number to electronic structure care was taken to establish the precise mode of overlayer growth. This is discussed in sections 5.2, 5.3 and 5.4

5.2 LEED and AES Results

Palladium was deposited onto the (100) and (111) faces of silver, held at 20°C, while periodically monitoring the LEED pattern and the peak to peak height of the differentiated Pd $M_{4,5}N_{4,5}N_{4,5}$ (330eV) and Ag $M_{4,5}N_{4,5}N_{4,5}$ (356eV) Auger emission lines. The Auger signal versus time (As-t) curve reveals the growth mode of an overlayer (Rhead 1976) and may be used to calibrate the Auger signals as a function of coverage. In the present work uncertainty in the measured signals was attributed to their sensitivity to the position of the crystal (it was repositioned in front of the electron optics after each short evaporation period) and to fluctuations in the electron gun emission. Both factors tend to affect the adsorbate (I_{Pd}) and substrate (I_{Ag}) signals by the same relative amount. Furthermore, the sum $I_{Pd} + I_{Ag}$ was nearly independent of coverage, a consequence of similar Auger excitation probabilities and kinetic energies of the emitted electrons for palladium and silver. Accordingly the normalised palladium signals: $I'_{Pd} = 100 \frac{I_{Pd}}{I_{Pd} + I_{Ag}}$ are plotted in figure 1. This has the effect of reducing the scatter, thus making more apparent any discontinuities in the curve arising from the completion of individual atomic layers or adsorbate phases.

The form of the plot (figure 5.1a) for adsorption on the (100) surface initially follows a series of straight lines in accord

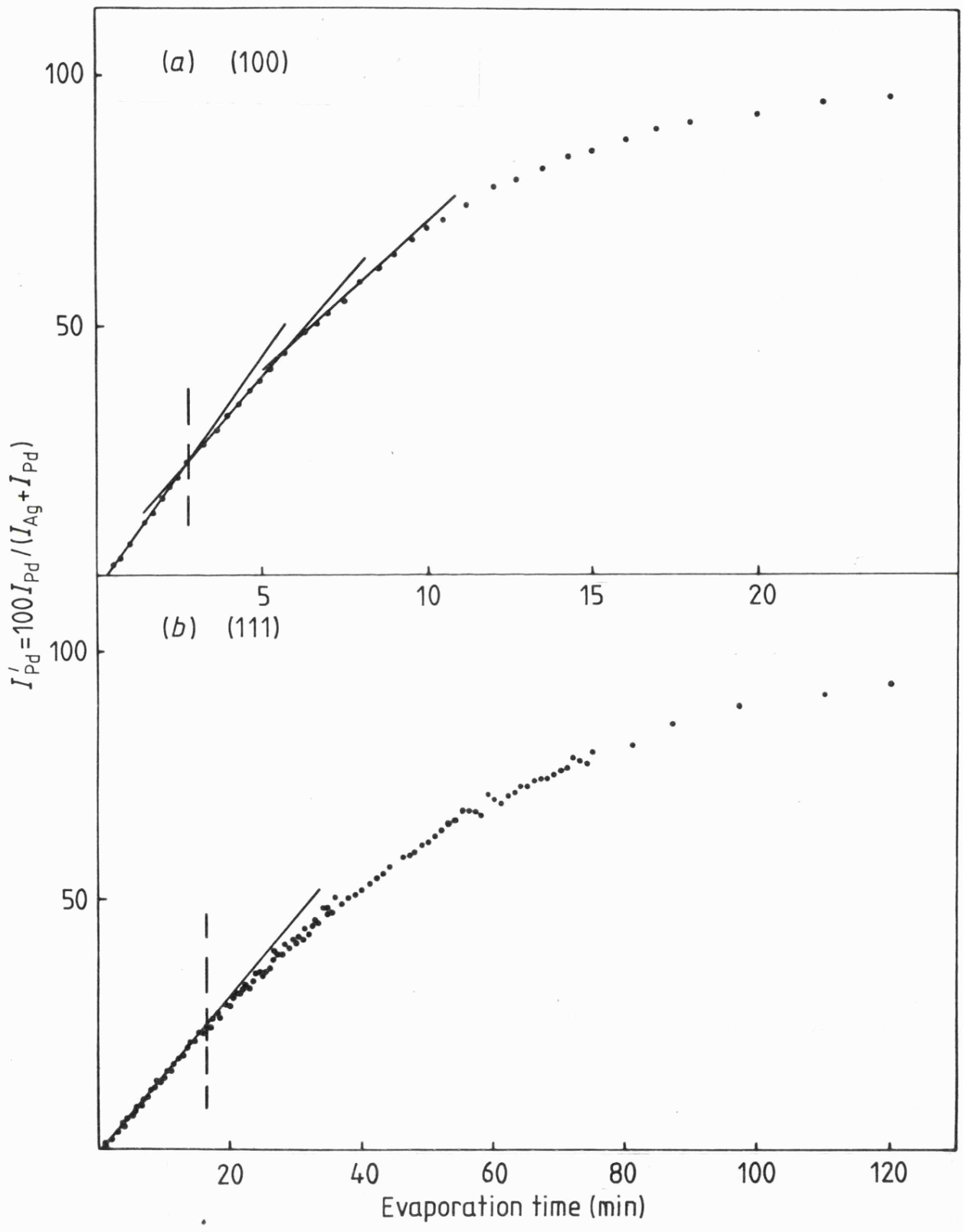


FIG 5.1

with Frank-Van der Merwe (layer by layer) growth mode. Thus the clearly defined break at $t = 2.75$ mins, $I'_{Pd} = 23.7$ was associated with the completion of the first monolayer. For adsorption on the Ag (111) surface (figure 5.1b) an initial linear region is again identified followed by a featureless curve. The break from the linear region was estimated to be at $t = 16.5$ mins, $I'_{Pd} = 24.7$ and again associated with the completion of the first monolayer.

If it is assumed that the monolayer can be regarded as a homogeneous slab of thickness d then the first break in the $As-t$ plot should occur when the palladium and silver Auger signals are given by

$$I_{Pd} = I_{Pd_{\infty}} \left(1 - \exp \frac{-d}{\lambda_{Pd}} \right)$$

and

$$I_{Ag} = I_{Ag_0} \exp \frac{-d}{\lambda_{Ag}}$$

Here I_{Ag_0} is the substrate signal at zero coverage and $I_{Pd_{\infty}}$ the adsorbate signal for an infinitely thick layer; λ_{Ag} and λ_{Pd} are the mean free paths for inelastic scattering of Auger electrons originating in the substrate and adsorbate respectively as they pass through the overlayer. With the proposed calibrations these expressions give, for electrons of energy 330 eV and 356 eV, mean free paths of 3.9 and 3.0 monolayers (ml) of palladium respectively for Pd/Ag (100), and 3.5 and 3.3 ml of palladium respectively for Pd/Ag (111). By comparison Guglielmacci and Gillet (1980), using a similar method, obtained values of 3.4 and 3.7 ml for the escape of electrons through Ag (111) and Burland and Dobson (1981), estimated a value of approximately 3.5 ml for escape through Pd (111). The empirical expression

$$\lambda (E) = \frac{538}{E^2} + 0.41(aE)^{\frac{1}{2}}$$

proposed by Seah and Dench (1979) to describe the energy dependence of

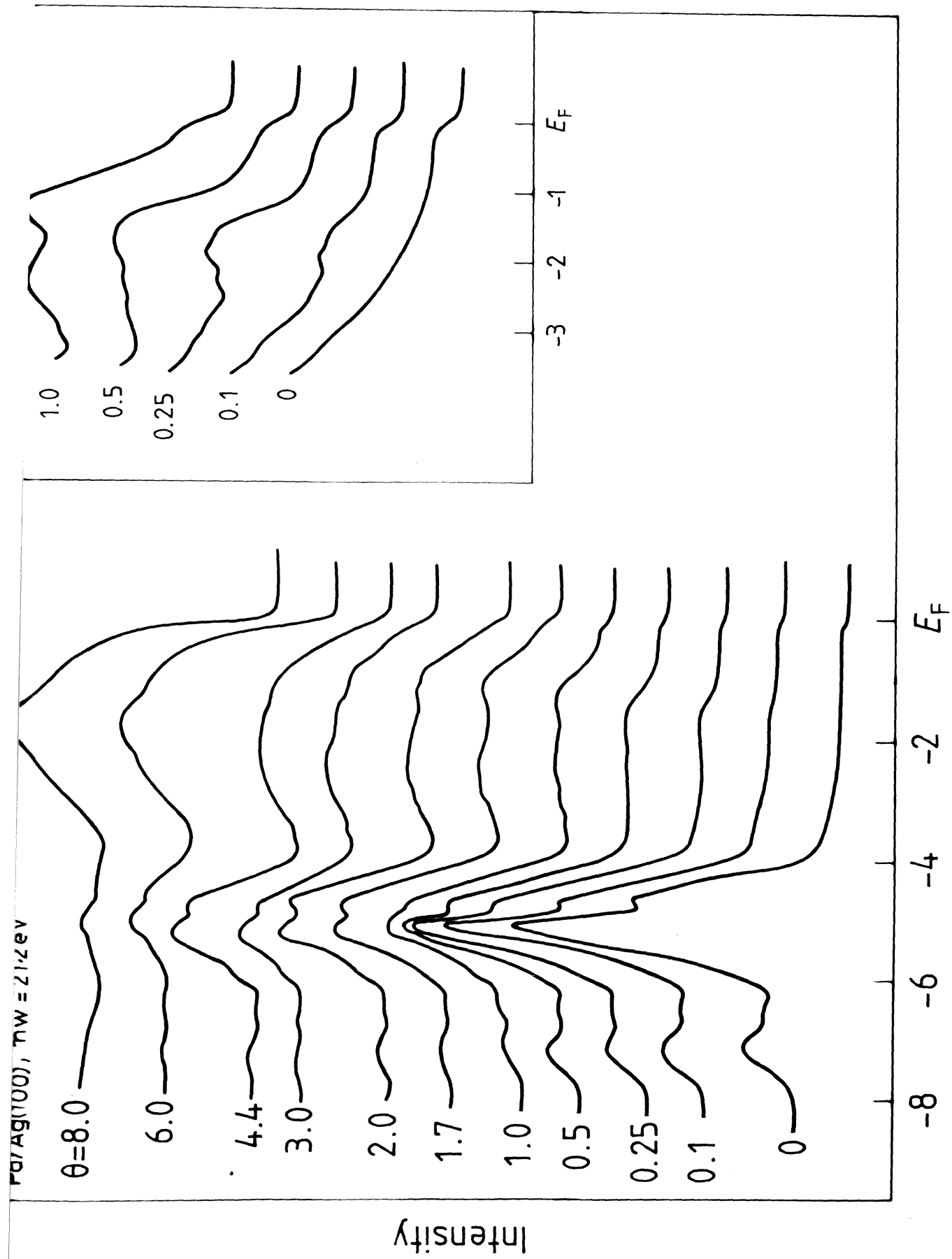
the mean free paths gives values of 3.9 and 4.0 ml respectively for the escape of electrons through a palladium film of unspecified geometry. The broad agreement between the values reinforces the calibration of the evaporation times given above. The error in the identification of the first monolayer point was estimated to be $\pm 10\%$.

During deposition on both faces the sharp $p(1 \times 1)$ substrate LEED pattern was retained beyond the first monolayer. For both the (100) and (111) substrates an increase in the background intensity was observed after approximately 3 monolayers. At 8 monolayers this was marked and the spots, though discernable, were diffuse.

Retention of the $p(1 \times 1)$ pattern throughout deposition is indicative of pseudomorphic growth of the monolayer. Bulk silver has a lattice constant 5.1% greater than bulk palladium, both metals crystallising with an f.c.c. structure. Thus a perfect epitaxial layer of palladium has an expanded lattice constant with concomitant lattice strain. The increased background intensity and reduced sharpness of the diffraction spots at higher coverages was therefore attributed to the relaxation of the overlayer to the bulk palladium structure. This is consistent with the results of Burland and Dobson (1981) where the misfit of Pd films on Ag (111) was monitored as a function of film thickness using RHEED.

5.3 Normal Emission Photoelectron Spectra

Figures 5.2 and 5.3 show the normal emission photoelectron spectra for the (100) and (111) substrates for increasing palladium coverage θ (in monolayers). The spectra were recorded with radiation of 21.2 eV photon energy [HeI] and they are plotted against the energy of the initial state; zero corresponds to the Fermi level. The region immediately below the Fermi level is shown in more detail in the insets



Energy of initial state (eV)

FIG. 5.2

for coverages up to one monolayer. The spectra recorded for the clean substrates ($\theta = 0$) are in agreement with those reported by Courths et al (1981).

For the (100) substrate (figure 2) the silver 4d band between -4 and -7 eV decreases in strength with little change in position as θ increases. This is consistent with the growth of an ordered epitaxial layer involving little charge transfer to the substrate. The most intense feature in the silver 4d-band emission (-5.1 eV) appears to be more rapidly attenuated by the overlayer than the rest of the band. Similar behaviour has been observed for overlayers on Cu (100) (Binns and Norris 1982) and attributed to the perturbation of a surface resonance. The same interpretation is believed to apply in the Ag (100) case. At low coverages ($\theta \sim 0.1$ ml) a single feature at -1.7 eV can be seen superposed on the Ag 4s band, and was attributed to emission from resonant bound 4d states localized on isolated palladium atoms adsorbed in a random p(1 x 1) lattice gas. On increasing the coverage the feature grows in strength and broadens in accord with increasing lateral overlap of the 4d wavefunctions on neighbouring palladium sites. At one monolayer three peaks can be clearly identified at -1.17, -2.30 and -3.09 eV. With further coverage the band continues to grow in strength and broadens. At 4.4 monolayers it is featureless but at 8 monolayers it shows two strong peaks and is similar to the spectrum for normal emission from the (100) surface of a palladium single crystal (Lloyd, Quinn and Richardson 1977). This supports the previous suggestion that beyond three monolayers the overlayer structure relaxes to that of the bulk.

Thus, for the (100) face, three distinct regions were identified which corresponded to well defined values of the palladium - palladium coordination number $Z_{\text{Pd-Pd}}$ and to the symmetry. At low coverages

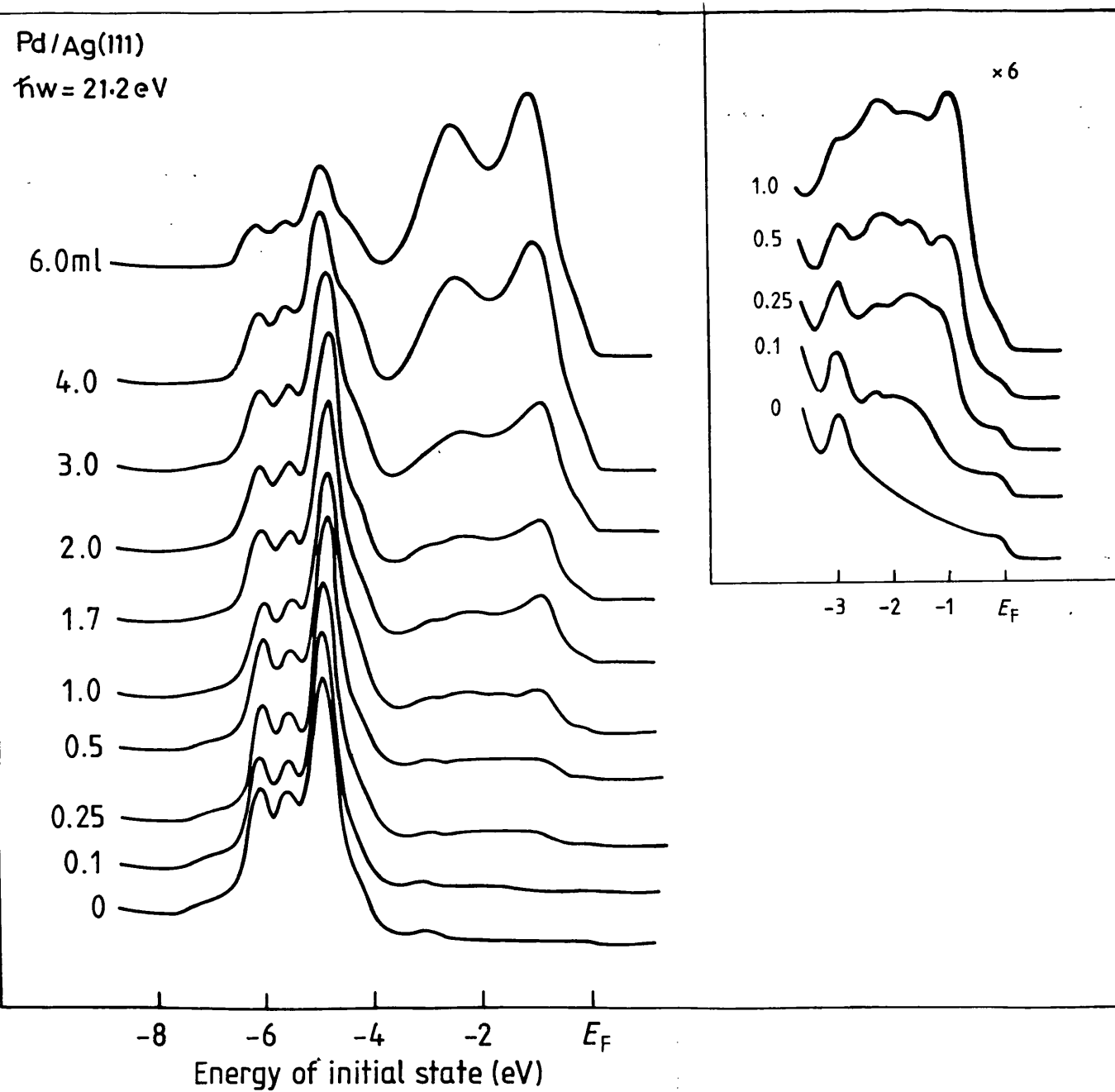


FIG. 5.3

the palladium sites are isolated and the coordination number is zero. The symmetry is non-cubic due to the surface potential but the effect on the electronic structure is small. At one monolayer the palladium - palladium coordination number is 4 and the symmetry obviously two dimensional. The perturbation of the Pd 4d states is greater since the d_{xy} orbitals extending in the plane of the substrate will penetrate the region of other palladium potential wells whereas the d_{xz} and d_{yz} orbitals which are directed out of the plane will not. For the thick layer the symmetry is three dimensional and coordination number is 12. The change from a single peak to 3 features at a monolayer and then back to two can be seen as a consequence of the increase in d-d overlap with coverage and the greater orbital degeneracy characteristic of the bulk structure in comparison with that of the monolayer. In their angle resolved photoemission study of thin silver overlayers on copper (111) Heiman Neddermeyer and Roloff (1977) also reported for $\theta < 3.1$ ml emission which was not observed for thicker films or bulk Ag (111). Measurements as a function of photoemission angle which confirm their energy band origin are described in section 3.5.

For adsorption on the (111) face (figure 5.3) similar behaviour is observed. The silver 4d band decreases in strength without major change in shape or position as the Pd 4d band develops at lower energies. The spectrum for the thick layer (6 ml) agrees with the result of Lloyd et al (1977) for clean Pd (111). Again emission from the palladium monolayer shows three peaks which do not obviously relate to features in the bulk curve. One important difference in comparison with adsorption on the (100) face is that the monolayer structure develops more rapidly. This is believed to be due to the formation of monolayer thick platelets rather than a random $p(1 \times 1)$ lattice gas. The stable adsorbate site on the (111) surface is a 3-fold hollow, shallower than the equivalent

Pd/Ag(111)
coverage = 3ml,
photon energy = 21.2eV
A = clean, as prepared surface
B = after adsorption of 50L O_2

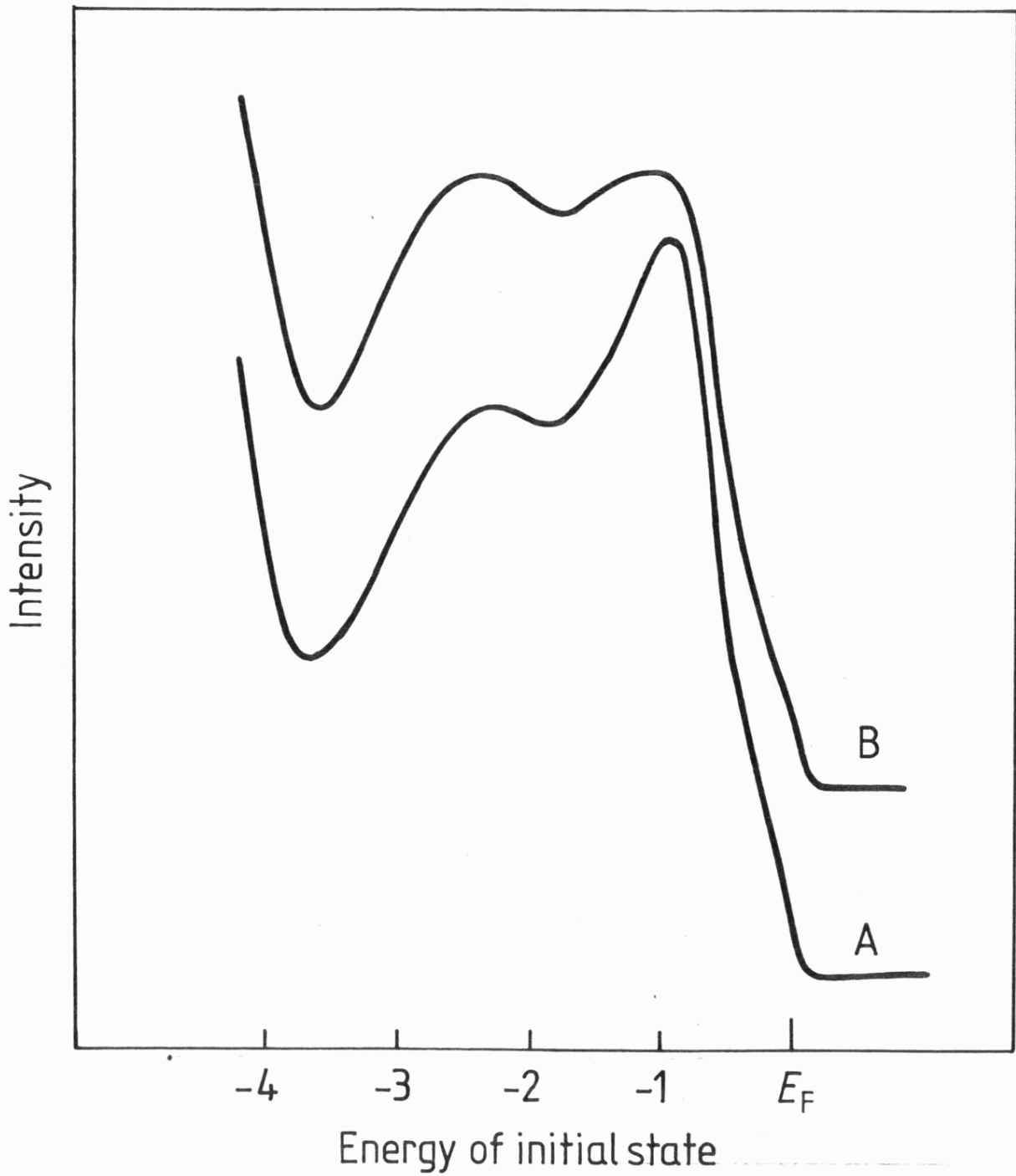


FIG. 51

4-fold hollow site on the (100) surface. It is probable that the lower surface mobility on the (100) surface prevents adatoms readily associating into platelets.

At coverages between 1 and 4 monolayers the intensity of the leading peak in the normal emission curves for Pd/Ag (111) was found to be very sensitive to surface contamination. At 3 monolayers coverage, exposure to 50 Langmuirs of oxygen caused a 20% reduction in intensity of this peak while having no noticeable effect on the other spectral features (figure 5.4). This result corresponds to the work of Weng and El-Batanouny (1980) who reported the formation of a surface resonance at $\theta \lesssim 3$ ml coverage of palladium on niobium (110) at the same binding energy as the feature discussed here.

5.4 Work Function

Figure 5.5 shows the variation with coverage of the work function ϕ . ϕ was obtained from the width W of the normal emission spectra through the expression $\phi = \hbar\omega - W$. The value for clean silver (100), 4.65 eV, is in good agreement with the published value 4.64 eV (Dweydari and Mee 1975) whereas the value for silver (111), 4.5 eV, is less than the published value of 4.7 eV (Dweydari and Mee, 1975).

With deposition of palladium on the (100) substrate ϕ initially falls to a minimum value of 4.45 eV at approximately 0.4 ml and then rises. The rise appears more steep up to 3 ml coverage than beyond. For the (111) substrate a submonolayer minimum is not observed, rather there is a steady rise in ϕ as θ is increased from zero to 8 ml. The value of 5.6 eV for the thick overlayer is close to the published value for Pd (111): (Demuth 1977). No value for Pd (100) is available in the literature. A rise in ϕ between silver and palladium

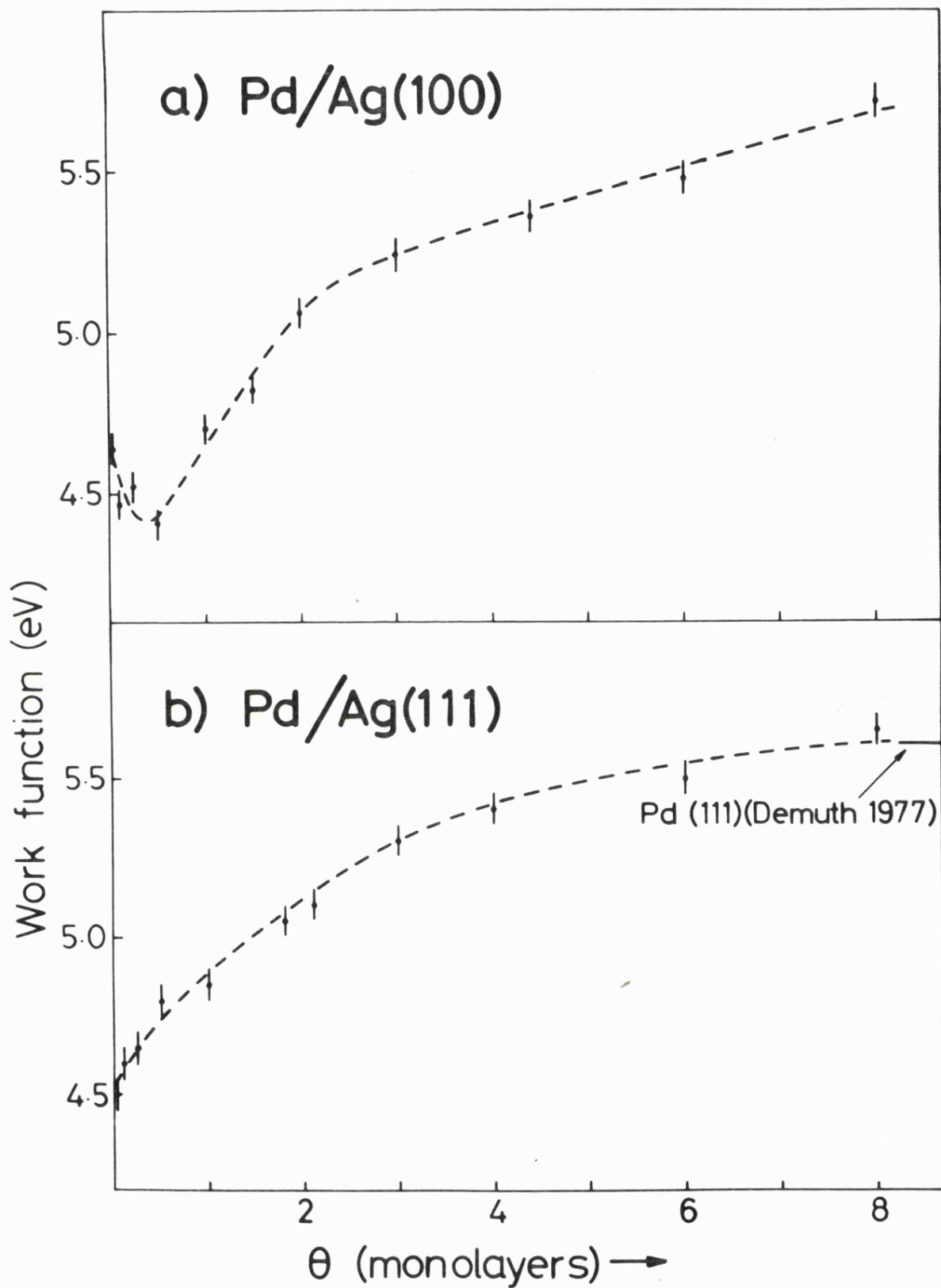


FIG. 5.5

is consistent with the slightly higher electronegativity of the latter (1.9 and 2.2 respectively, Pauling 1960).

The work function of a metal is given by:

$$\phi = \Delta \phi - \bar{\mu} ,$$

where μ is the chemical potential relative to the mean potential within the bulk and $\Delta \phi$ is the dipole at the surface due to the termination of the metal and resultant spillage of the electron cloud into the vacuum. Using a simple representation of the ionic lattice and by treating the response of the electron cloud self-consistently through the density functional method Lang (1971) explained the main features of the variation of ϕ with adsorption of an electropositive alkali metal on a transition metal. An alternative approach has been discussed by Muscat and News (1974). The theory of work function change on metal adsorption was considered in chapter 2. In the spirit of Lang's model we can associate the initial decrease in ϕ for palladium adsorption on silver (100) as the consequence of the incomplete response of the electron cloud to an adsorbate layer of lower mean electronic density \bar{n} than that of the substrate \bar{n}_s . For $\theta < 0.4$ ml the arrangement of palladium atoms on the electronically similar surface may be likened to a roughened surface which also tends to show a reduced value of ϕ . According to Lang's model the work function of the monolayer should correspond to that of bulk metal. The discrepancy between the value at $\theta = 1.0$ ml with that for the thick layer is due to the 5.1% linear lattice expansion imposed on the palladium monolayer by the underlying substrate. The rise in ϕ between $\theta = 1.0$ and 8 ml signifies a slow contraction of the overlayer lattice with increasing thickness.

The magnitude of the charge transfer from the adsorbate layer can be estimated through the classical expression (Langmuir 1932):

$$\frac{d\phi}{dS} = \mu / \epsilon_0$$

Here 2μ is the dipole moment of the adsorbate-image point charge arrangement and S is the surface density of the adsorbate. For an isolated palladium atom in a four-fold hollow site on the Ag (100) surface a value of 8% of an electron charge is obtained.

The absence of a submonolayer minimum for adsorption on the Ag (111) face is consistent with the suggestion in section 5.3 that for this face islanding occurs immediately. Thus the surface is not homogeneous and there will be regions with a work function equal to that of the palladium monolayer together with regions with the lower value of bulk silver. The measurement technique gives an average (albeit with a weighting to the lower value) and in consequence we observe a gradual rise in ϕ . Significant charge transfer with a corresponding reduced ϕ should occur only at the edges of the palladium terraces.

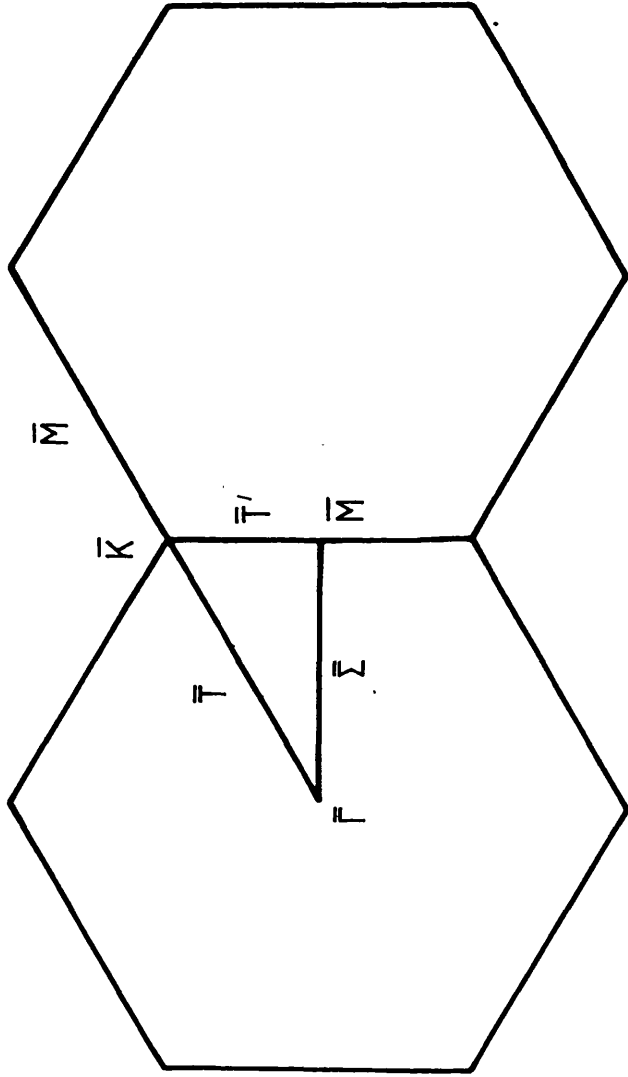
5.5 The Isolated Palladium Resonance

Figure 5.6a (solid curve) shows the palladium surface resonance measured for a coverage of 0.1 ml on the Ag (100) surface. It is contrasted in the lower figure (figure 5.6b, solid curve) with the same feature obtained by annealing at 500° C an overlayer deposited on the (111) surface to produce the bulk substitutional alloy. The concentration in the region probed by the photoemission experiment was estimated to be 3 at.%.

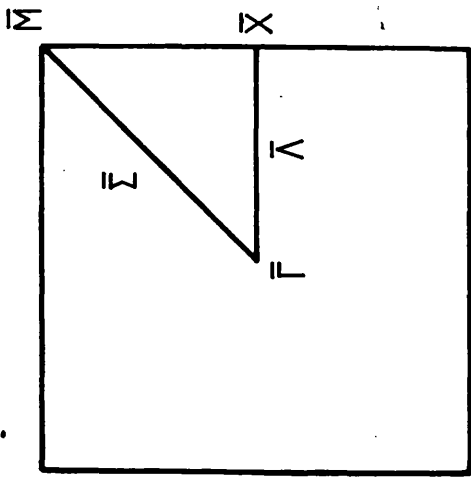
The centre of gravity of the surface resonance is at a lower initial energy (-1.74 eV) than that (-1.2 eV) of the feature reported by Eastman and Grobman for palladium overlayers adsorbed on polycrystalline silver films. Polycrystalline films tend to adopt the most dense surface structure, which for an fcc lattice is the (111) surface. The

peak discussed by Eastman and Grobmann corresponds closely in position to the strongest peak of the aggregated platelet structure for the Pd/Ag (111) system (figure 5.3). We therefore suggest that these authors were not observing dispersed palladium as they suggest, but adsorbed palladium in platelet form.

By comparison with the surface resonance the resonance in the bulk alloy (figure 6b) occurs at a slightly deeper initial energy (-2.1 eV) and has broadened from a full width half maximum of 0.78 eV to 0.94 eV. The position of the bulk resonance agrees exactly with that reported by Norris and Myers (1971). The theoretical study of Pindor et al (1980) which used the KKR-CPA approximation locates the position of the impurity level in $\text{Ag}_{.80}\text{Pd}_{.20}$ alloy at -7 eV. To date no calculation of the isolated adsorbate has been reported, the work of Bisi and Calandra (1977) referred specifically to a dense monolayer, and so the simple resonant bound state model originally described by Friedel (1958) and the Anderson (1961) was used. Following Norris and Myers the width was attributed to two factors: s-d hybridization between the extended conduction band of silver and the localized 4d orbital on palladium and to spin-orbit interaction within the palladium site. The latter is not negligible and indeed for the ad-atom case (figure 5.6a) there is evidence of a doublet. The data were fitted using two Lorentzians in the relative strength 3:2 and allowance made for the experimental broadening of 0.18 eV. Good agreement was found with a spin-orbit splitting of 0.35 eV which is less than the value quoted by Herman and Skillman (1963) but closer to that calculated by Podloucky et al (1979). The results of the analysis are shown (broken lines). The FWHM, Δ_{sd} , of the Lorentzian due to the s-d hybridization was found to be 0.3 eV for the adatom and 0.5 eV for the substitutional impurity.



(111)



(100)

FIG. 5.7

Pd/Ag(100)
 $\Theta = 1\text{ml}$
 $hw = 21.2\text{eV}$

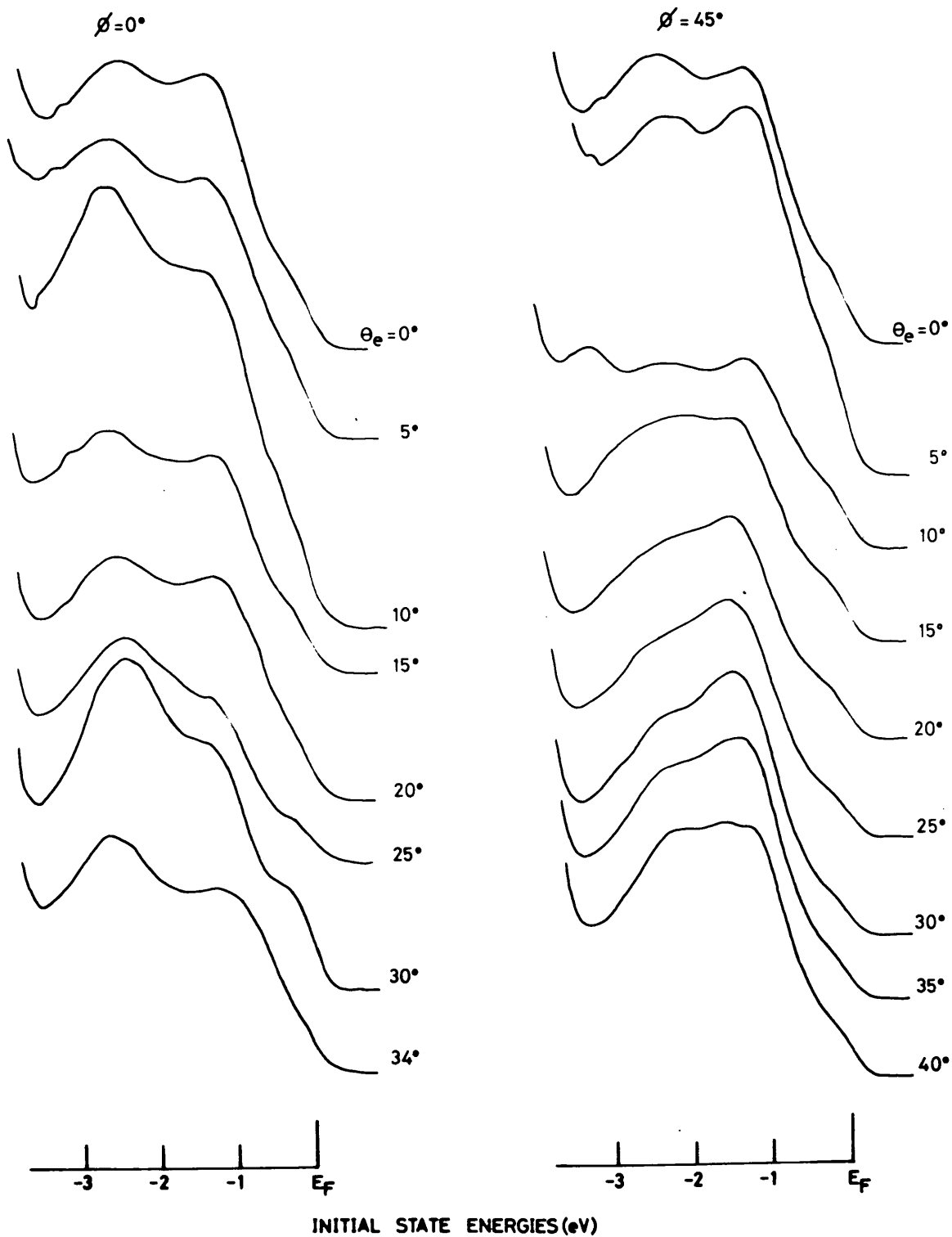


FIG. 5.8a

Within the tight binding approximation it may readily be shown that the FWHM of a density of states function with a gaussian profile is proportional to $I\sqrt{Z}$. Here Z is the coordination number and I the overlap integral $-\int \phi^*(\underline{r}) \Delta V(\underline{r}) \phi(\underline{r} - \underline{R}_\ell) d^3\underline{r}$; $\Delta V(\underline{r})$ is the difference between the crystal potential and that of a single well. In moving a palladium atom from a hollow site on the (100) surface ($Z = 4$) to a substitutional position in the bulk ($Z = 12$) an increase in the FWHM of a single hybridized level of a factor of $\sqrt{3}$ is expected. This is very close to the measured relative increase of Δsd of 1.67. The shift in the resonance to lower energies on alloying reflects the nett lowering of the potential, again through the increase in Z .

5.6 E-k Dispersion Relations for Palladium Monolayers

At palladium coverages of one monolayer angle resolved photoelectron spectra were recorded for both (100) and (111) faces. The emission angle was set at 5° intervals; normal emission corresponds to $\theta_e = 0^\circ$. The azimuthal axis was aligned along the $\bar{\Gamma}$ and $\bar{\Lambda}$ axes of the square (100) Brillouin zone and along the $\bar{\Gamma}$ and $\bar{\Sigma}$ axes of the hexagonal (111) Brillouin zone (figure 5.7). Spectra obtained with HeI (21.2 eV) radiation are shown in figure 5.8. Since the emission spectra from the Ag 4d band were observed as attenuated forms of the spectra from the clean substrates only the region between E_F and -4 eV which is dominated by emission from the Pd 4d band is shown.

For both faces the normal emission spectra show three peaks in the palladium 4d band which shift and are modulated in intensity as the emission angle is moved off-normal in accord with conservation of the one-electron wave vector \underline{k} in the optical excitation process. Since the Pd 4d bandwidth is determined predominantly by the lateral interactions

Pd/Ag(111)
 $\Theta = 1\text{ml}$
 $hw = 21.2\text{eV}$

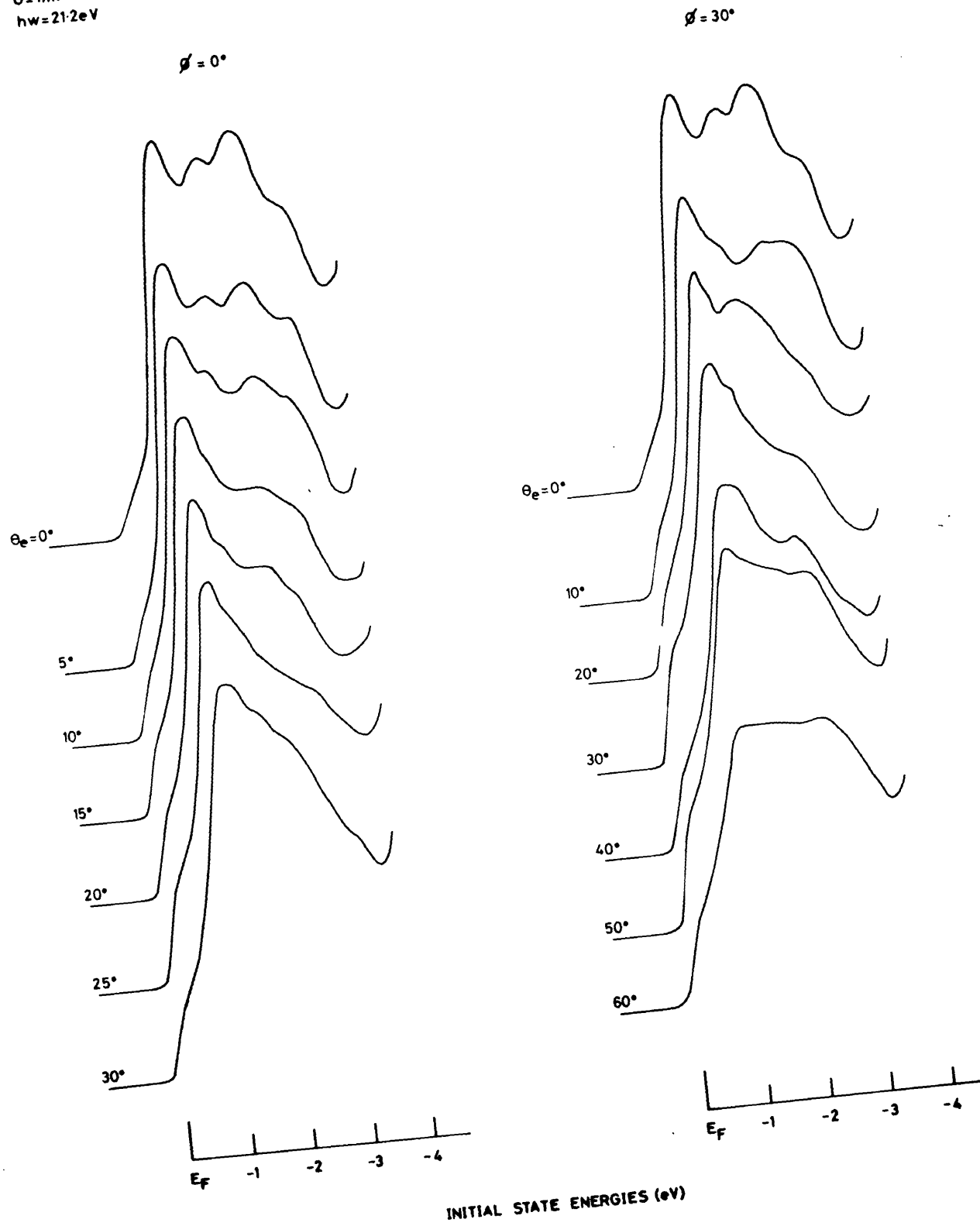


FIG. 5.8b

in the monolayer little dispersion of the electron energy with k_{\perp} , the component of k perpendicular to the surface, would be expected. Rather the band structure should be described by a two-dimensional $E - k_{\parallel}$ relation. Fig 5.9 shows normal emission spectra excited by two photon energies: 21.2 and 40.8 eV. As the analyser in this orientation can only accept electrons with the parallel component k_{\parallel} equal to zero, a variation in peak positions will reflect dispersion along the perpendicular axis. The absence of significant dispersion confirms the interpretation of the overlayer as a two-dimensional system. Accordingly each peak in the emission spectra may be assigned to a point in the $E - k_{\parallel}$ diagram through the relation

$$k_{\parallel} = \sqrt{\frac{2mE_{\text{kin}}}{\hbar^2}} \sin \theta_e$$

where θ_e is the polar angle of emission with respect to the normal and E_{kin} is the measured kinetic energy (Chapter 4, section 4.2). The same analysis has been applied to the segregated layer at the surface of a Cu-Ni alloy by Heimann et al (1981). Figs 5.10 and 5.11 show the measured dispersion relations for palladium monolayers adsorbed on the two faces; the results are plotted along the principal symmetry axes. For Pd/Ag (100) two calculations have been published with which the experimental results may be compared; for Pd/Ag (111) no calculations exist in the literature. Bisi and Calandra (1977) used a parameterised molecular orbital technique to determine the local density of states of a palladium overlayer on Ag (100). The overlayer was assumed to take the geometry of the underlying substrate plane, as observed experimentally in the present work. No account was taken of the spin-orbit interaction which, as discussed in section 5.5, is not insignificant. By considering orbitals for which more than 50% of the charge was located in the first

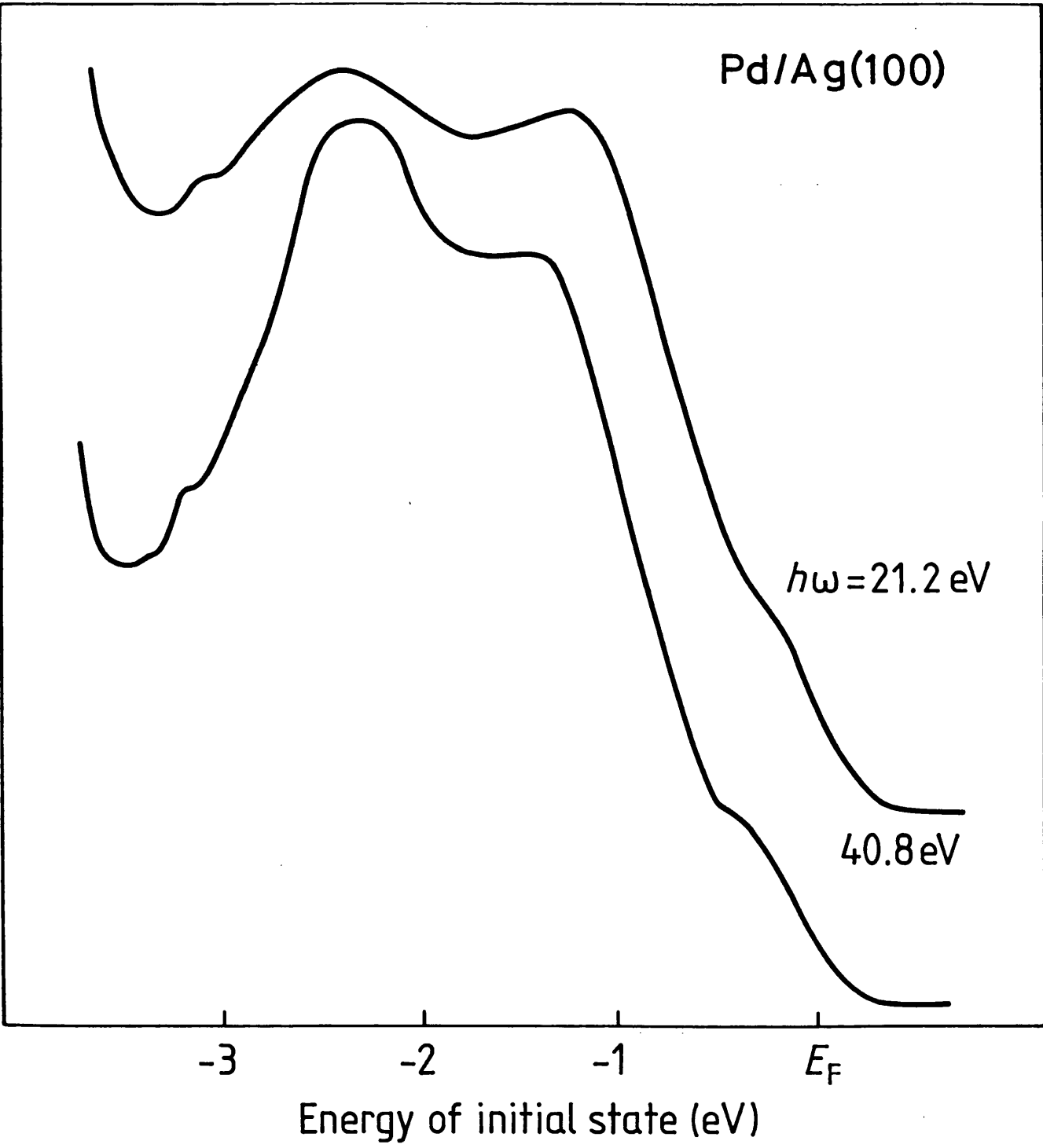
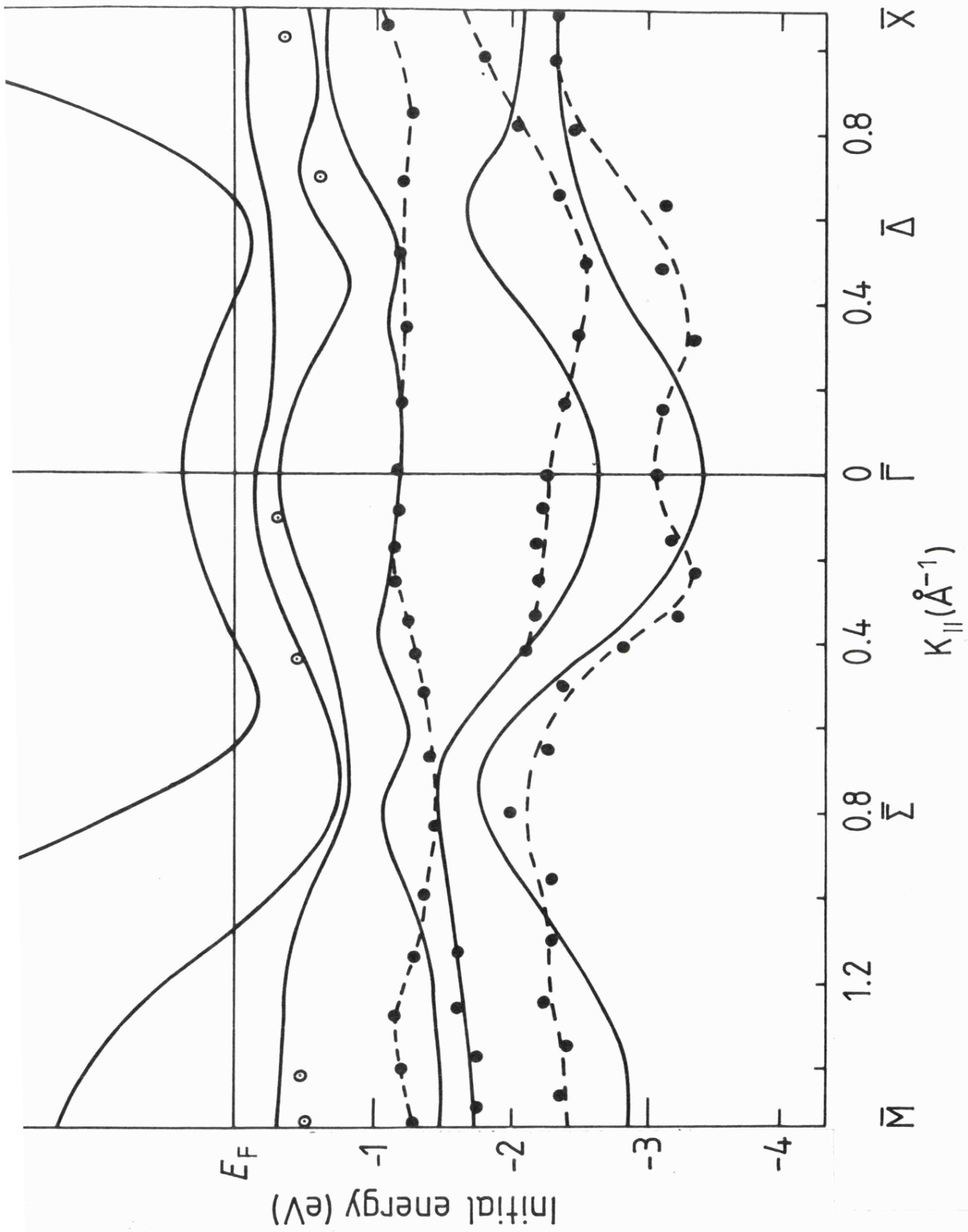


FIG. 5.9

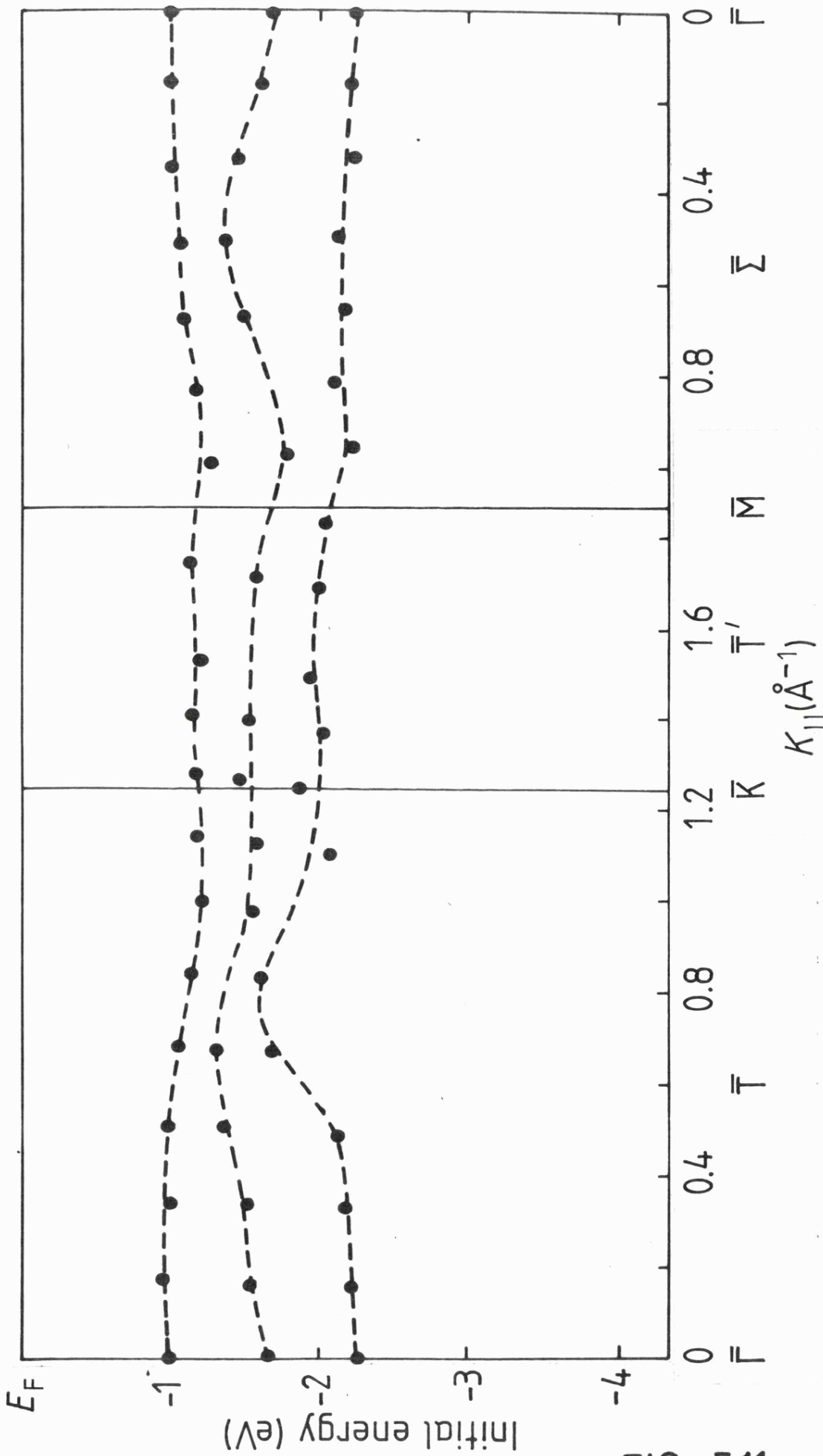
two layers dispersion relations for the adsorbate and surface states were obtained. If \underline{k} conservation is assumed these bands predict peaks in the normal emission photoelectron spectrum at - 0.8 and - 2.5 eV due to transitions from states near the $\bar{\Gamma}$ point to a continuum of final states. This compares with features in the measured spectrum at - 1.2 and - 2.4 eV. At points away from the centre of the zone, corresponding to greater angles of emission, Bisi and Calandra find a large number of rapidly dispersing bands between E_F and - 3.0 eV. Instrumental resolution does not allow a detailed comparison with experiment apart from noting that the bands lie within the measured energy range.

Recently Noffke and Fritsche (1981) have reported a self-consistent scalar relativistic calculation of the energy band structure of an isolated Pd (100) monolayer. The calculation used the linear rigorous cellular method and assumed the interatomic distance corresponded to the bulk palladium value. Their results are reproduced in fig. 5.10 for comparison. Fair overall agreement is seen, particularly near the $\bar{\Gamma}$ point and along the $\bar{\Sigma}$ axis. The unusual non-parabolic behaviour of the lowest band near the zone centre could be due to non \underline{k} -conserving transitions from a high density of states at the \bar{M} point. The similarity between theory and experiment is consistent with small charge transfer and would suggest that an isolated monolayer represents a good approximation to the supported monolayer in spite of the 5% lattice mismatch and the hybridisation with the substrate 5s-band. In their study of a segregated nickel layer on a Ni-Cu alloy Heimann et al (1981) found a 1.24 eV shift was necessary to bring theory in agreement with experiment. This was attributed to a deepening of the monolayer potential caused by neighbouring layers in the alloy. A similar correction does not appear to be necessary in the present work.



Dispersion relation for the palladium(100) monolayer

FIG. 5.10



Dispersion relation for the palladium(111) monolayer

FIG. 5.11

In the case of palladium on silver (111), off normal spectra recorded at coverages of 0.5 and 0.25 ml showed features corresponding to those observed at 1 ml. Significant dispersion at 0.25 ml provides further evidence that, on this face, palladium is initially adsorbed as small platelets, rather than a lattice gas.

5.7 Photoemission Calculations

The time-reversed LEED formalism of Pendry (1976), discussed in Chapter 2, was used to calculate the normal emission spectrum from one monolayer of palladium on silver (100) at 21.2 eV. The method has previously been used for bromine layers on copper (100) (Kar 1981) but the present work represents the first application of the theory to metal overlayers. The potentials used were those of the clean surfaces in the calculations of Chapter 4. The palladium-palladium distance in the overlayer was taken to equal that of the silver-silver nearest neighbour distance in the bulk and the overlayer-substrate distance was set equal to the mean of the bulk palladium and bulk silver interatomic spacings, corresponding to a hard sphere approximation.

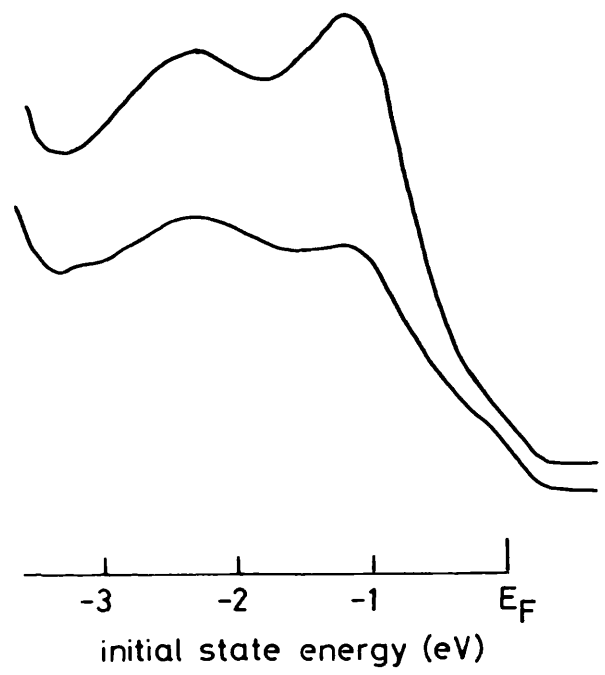
The calculated normal emission spectrum is shown in figure 5.12. The s and p polarized components are shown separately, together with their summed total spectrum. The experimental curve, on the same energy scale, is also shown and the Fermi edges are aligned. Comparison of theory and experiment shows that the gross features of the experiment are reproduced; the two peaks in the calculated spectrum correspond to emission from the silver and palladium bands. Relative to the experimental curve, theory gives too great an attenuation of the silver emission with the palladium emission assuming an exaggerated prominence. This is a lifetime effect, and is discussed in Chapters 7, 8 and 9. The energy

Pd/Ag(100)
 normal emission
 $hw=21.2\text{eV}$

experiment

$\theta_i=15^\circ$

$\theta_i=85^\circ$



the theoretical and experimental curves are on the same energy scale and the Fermi edges are aligned

theory
 — = s+p pol
 x—x = p pol
 •—• = s pol

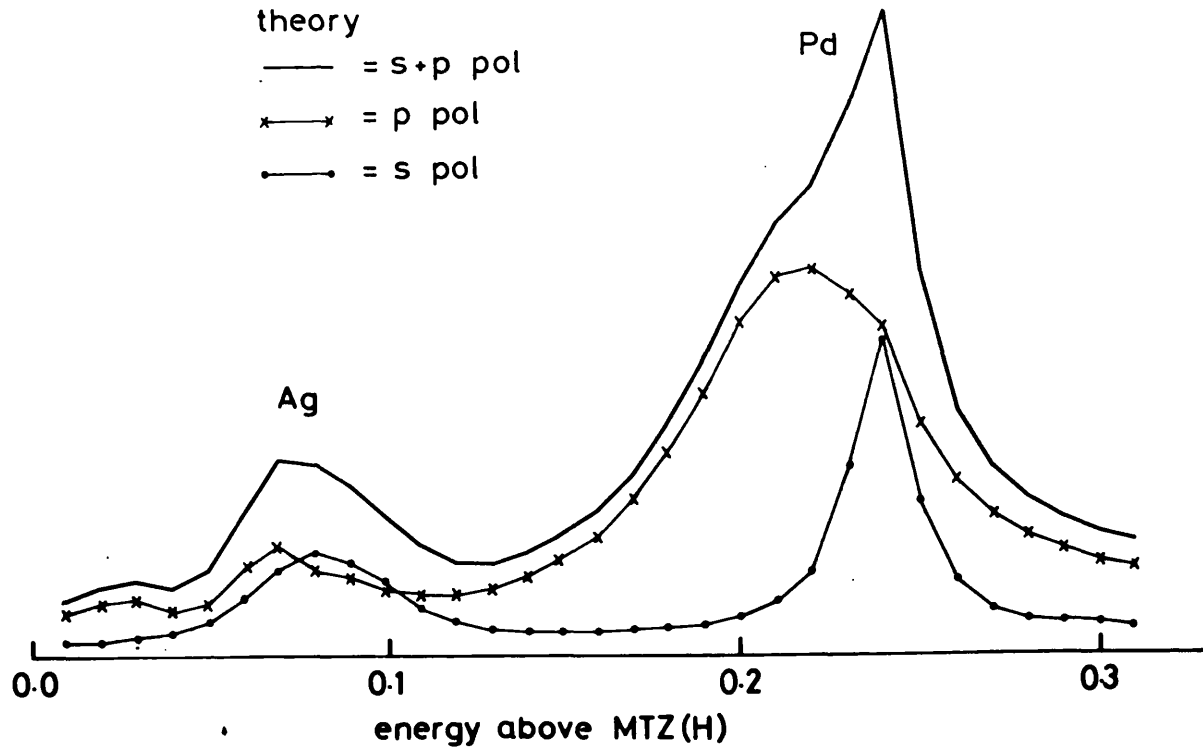


FIG. 5.12

gap between the theoretical silver and palladium emission is approximately correct.

Figure 5.12 shows that the theoretical palladium emission consists of two distinct separate features of s and p polarized origin. Lloyd et al (1977) have considered the photon angle dependence of photoemission from a copper (100) crystal and shown that s and p polarized components in emission excited using an unpolarized source may be distinguished using near normal and glancing incidence respectively. The experimental spectra of figure 5.12 were obtained using near normal (15°) and near glancing (85°) photon incidence. On going to glancing incidence the s component of the light is reduced and a corresponding reduction in intensity of the leading feature in the experimental spectrum is observed. This indicates it is of primarily s origin, as predicted by the calculation.

5.8 Discussion

The electronic structure of monolayers of noble and transition metals has been the subject of continued theoretical discussion partly since they reflect rather dramatically the change from bulk to surface behaviour. Calculations indicate the importance of self consistency if realistic estimates are to be made of electronic and magnetic properties. Contrary to this interest experimental studies have been limited to relatively few systems often without proper surface characterisation. In view of the central role of the local atomic arrangement to the electronic structure it is essential that the growth mode is well understood. For pseudomorphic systems simultaneous multilayer growth can occur in which the second layer begins before the first is completed (Barthes and Roland 1981). For Fe/Pd (111) this has been found to have a significant influence on magnetic behaviour of

the overlayer (Binns and Norris 1982). In the present study our results suggest that multiple stacking is not significant for low coverages and the monolayers are flat.

Palladium is distinguished by its nearly filled 4d shell and, in the bulk, by the high density of states at the Fermi level and consequent large Stoner enhancement factor. Theory and experiment confirm that the electronic structure is particularly sensitive to structural rearrangement (see for example Dass, Koelling and Mueller 1973 and Stritzker 1979). Using a self-consistent LCAO approximation for the isoelectronic metal nickel Tersoff and Falicov (1981) have shown that the reduction of the coordination number such as occurs at a metal-vacuum interface, is accompanied by a transfer of charge from the s to the d valence orbitals. The spectra shown in figures 5.3 and 5.4 demonstrate this effect clearly. Thus at the monolayer coverage of both the (100) ($Z_{\text{Pd-Pd}} = 4$) and (111) surfaces ($Z_{\text{Pd-Pd}} = 6$) the Pd 4d band shows little overlap with the Fermi level and can be likened to a noble metal. The same behaviour was reported for palladium adsorbed on niobium (110) surfaces by El Batanouny et al (1981). It is not until two monolayers are completed that a significant increase in the emission near E_{F} is observed corresponding to the build up of the density of Pd 4d states at this energy. This is relevant to the recent work of Brodsky and Freeman (1981) who reported a large increase in the paramagnetic susceptibility for a multilayer Pd-Au (100) structure. The effect, which was attributed to the rise in $G(E_{\text{F}})$ due to the lattice expansion imposed by the gold structure, was greatest for palladium layers 1 monolayer thick. Silver is sufficiently similar to gold (the lattice constant is 0.2% greater) for the overlayer systems described in the present study to be considered as the basic unit of such an arrangement. By contrast the present data

show that $G(E_F)$ is low at a monolayer, and that the results of Brodsky and Freeman are consistent with multiple stacking and an average coordination number $Z_{\text{Pd-Pd}}$ somewhat in excess of 4.

5.9 Summary

The growth mode and electronic structure of ultra-thin Pd layers of 0.1 to several monolayer thickness on Ag (100) and (111) have been investigated using LEED, Auger and angle-resolved photoelectron spectroscopy. In the (100) case growth was seen to proceed from a lattice gas at low coverage through a characteristic two-dimensional phase at 1 ml and then by a gradual progression to a bulk-like Pd (100) structure at 8 ml. The initial drop in work function on adsorption of palladium was explained in terms of charge transfer from palladium in a pseudo-atomic state to the substrate. After approximately half a monolayer had been deposited lateral interaction in the overlayer dominate, resulting in an increase work function which then rose to the bulk value. The gross features of the spectra recorded in normal emission from 1 monolayer of palladium were reproduced using time-reversed LEED theory. Variation of the photon incidence angle enabled identification of the corresponding s and p-polarized components of the experimental and theoretical spectra.

In the (111) case two-dimensional platelets were formed almost immediately and no initial lowering of work-function was recorded. After passing through the two-dimensional phase at 1 ml a bulk-like Pd (111) spectrum was recorded at 4 ml coverage, rather earlier than for the (100) surface. For both surfaces the off-normal photoemission spectra recorded at one monolayer coverage were interpreted in terms of a two-dimensional band-structure model. On the (100) surface fair agreement was obtained with a theoretical calculation of the electron states of an isolated monolayer. This would appear to indicate that

the substrate has relatively little effect in the electronic structure of the monolayer. Deviation from isolated monolayer behaviour was attributed to hybridization with the Ag s-band and the 5.1% lattice expansion imposed by the substrate. The difference in position and width of the resonant bound palladium 4d state on an isolated palladium atom supported on the (100) surface in comparison with that on an impurity atom in the bulk is consistent with the change in the coordination number from 4 to 12.

The work presented in this chapter has been discussed by Smith et al (1982).

CHAPTER 6

AN ELECTRON SPECTROSCOPIC STUDY OF PALLADIUM
OVERLAYERS ON COPPER (100)

- 6.1 Introduction
- 6.2 LEED and Auger Spectroscopy Results
- 6.3 Coverage Calibration
- 6.4 Photoemission Results
- 6.5 Photoemission Calculations
- 6.6 Discussion and Summary

CHAPTER 6

AN ELECTRON SPECTROSCOPIC STUDY OF PALLADIUM
OVERLAYERS ON COPPER (100)6.1 Introduction

In the previous chapter the palladium on silver system was considered and shown to exhibit two dimensional behaviour at a coverage of one monolayer. Palladium is a material for which there is evidence that its electronic and magnetic properties are particularly structure-sensitive; thus it was also of interest to study palladium adsorbed in a rather different environment than that of a perfect epitaxial overlayer.

Fujinaga (1979a, 1979b) has performed LEED and Auger spectroscopy analyses of copper-palladium alloy surfaces prepared by an evaporation and annealing technique. The results demonstrated the possibility of formation of both the ordered Cu Pd (α) and Cu₃ Pd (β) alloy phases on the (100) surface at room temperature, although growth was not followed using the As-t method of the present work. This indicated that a LEED / AES /UPS study of the growth of ultra thin palladium overlayers on copper (100) would enable study of surface alloy formation and provide the desired contrast to the palladium on silver (100) and (111) work.

The LEED and As-t results are discussed in section 6.2 and from these a coverage calibration obtained and discussed in relation to the work of Fujinaga and others (for example Binns and Norris 1982, Gonzalez et al 1980, 1981) in section 6.3. Angle resolved photoelectron spectra are presented in section 6.4 and the results of theoretical calculations given in section 6.5. Aspects of this work have been discussed by Smith et al (1981) and are summarized in section 6.6

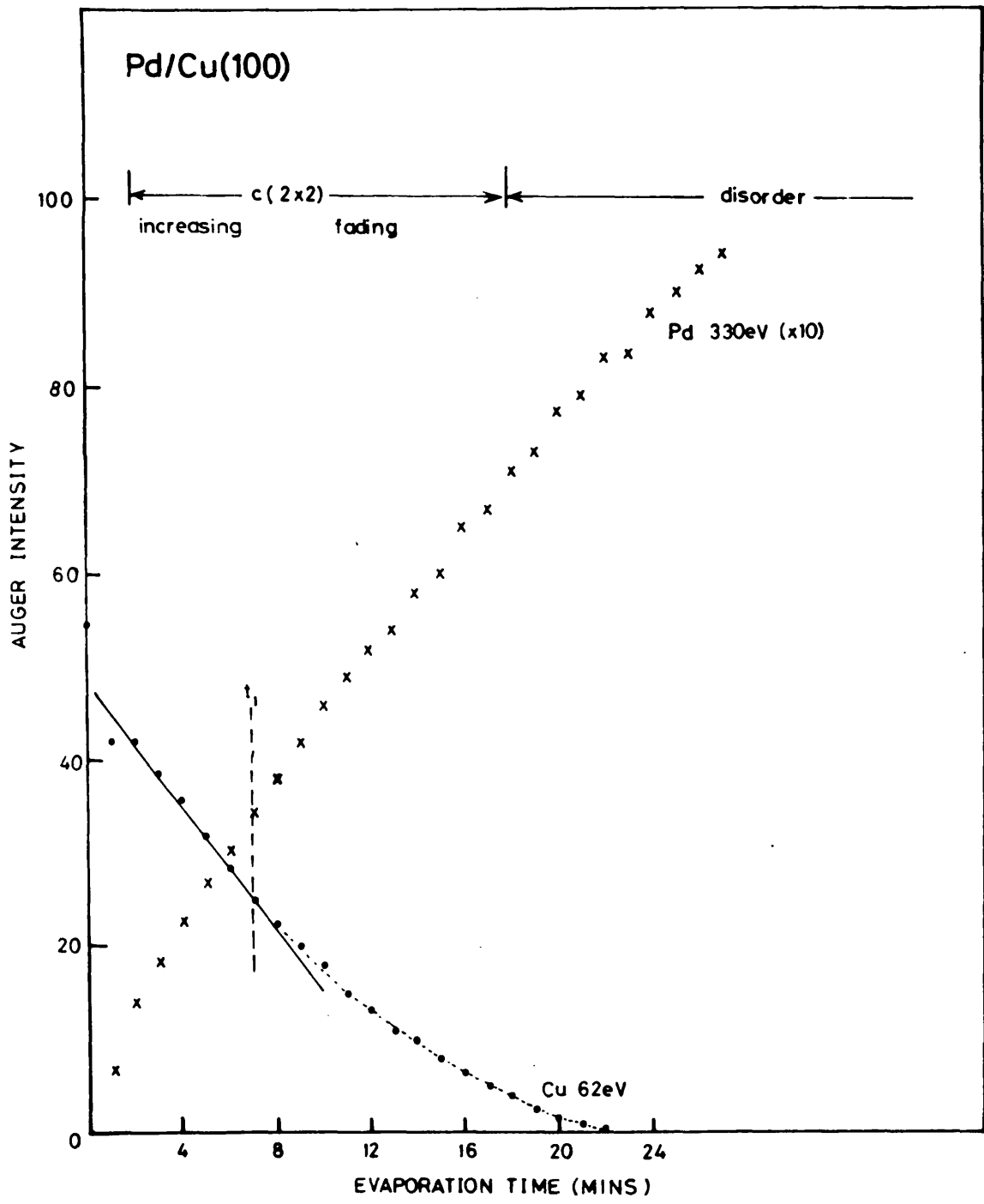


FIG. 6.1

6.2 LEED and Auger Spectroscopy Results

Palladium was deposited on to the copper (100) substrate maintained at room temperature while periodically monitoring the peak to peak heights of the differentiated palladium (330 eV) and copper (62 eV) Auger lines and observing the LEED patterns. From the results the As-t plot of figure 6.1 was obtained. For the palladium on silver system the substrate and overlayer Auger signals were seen to mirror each others behaviour and, as a result, a normalisation procedure could be applied to reduce the scatter in the experimental points. This was a consequence of the similar Auger yields and escape depths of the emission lines used and clearly cannot be applied in the case of palladium on copper. Not only are the mean free paths of the 62 eV and 330 eV electrons rather different but during deposition the copper 62 eV line was seen to go to zero intensity while the intensity in the palladium line at 330 eV was still increasing. This was at least in part due to the steeply sloping background present at low energies which distorted the line shape. Representative Auger line spectra taken in the $\frac{dN}{dE}$ mode at various times during the deposition are shown in figure 6.2. After 22 minutes of evaporation there was clearly significant copper Auger emission but distortion of the line shape results in almost zero measurable height. No attempt at background subtraction was made.

Returning to figure 6.1, the copper signal is seen to decay initially linearly with deposition time, with a break occurring at time t_1 (7 minutes). No corresponding feature is seen in the palladium curve. During deposition, extra LEED spots appeared in the initial $p(1 \times 1)$ pattern, resulting in a $c(2 \times 2)$ pattern which reached maximum intensity at time t_1 . Beyond t_1 the background slowly increased until

Pd/Cu(100)
Auger signals

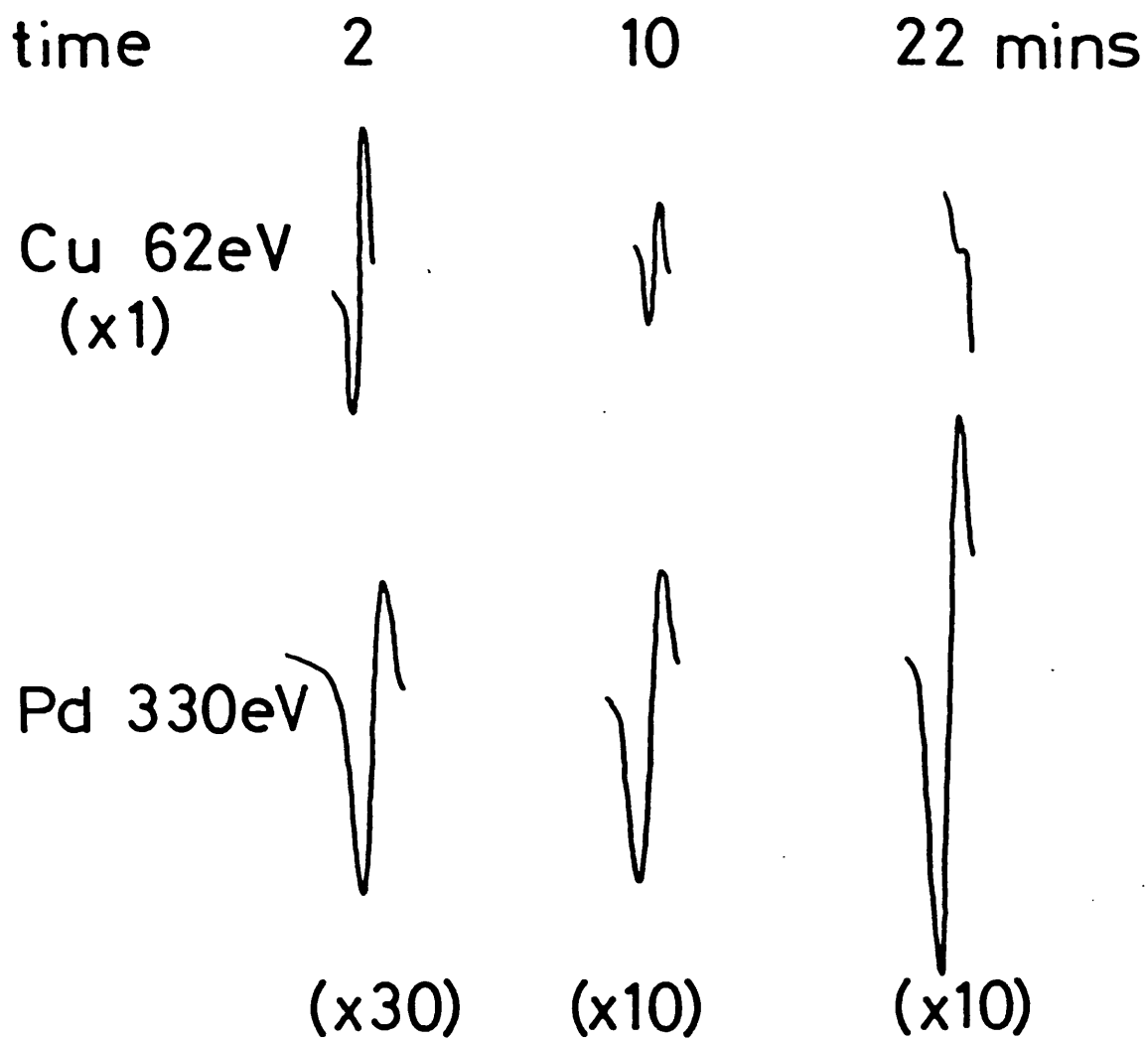
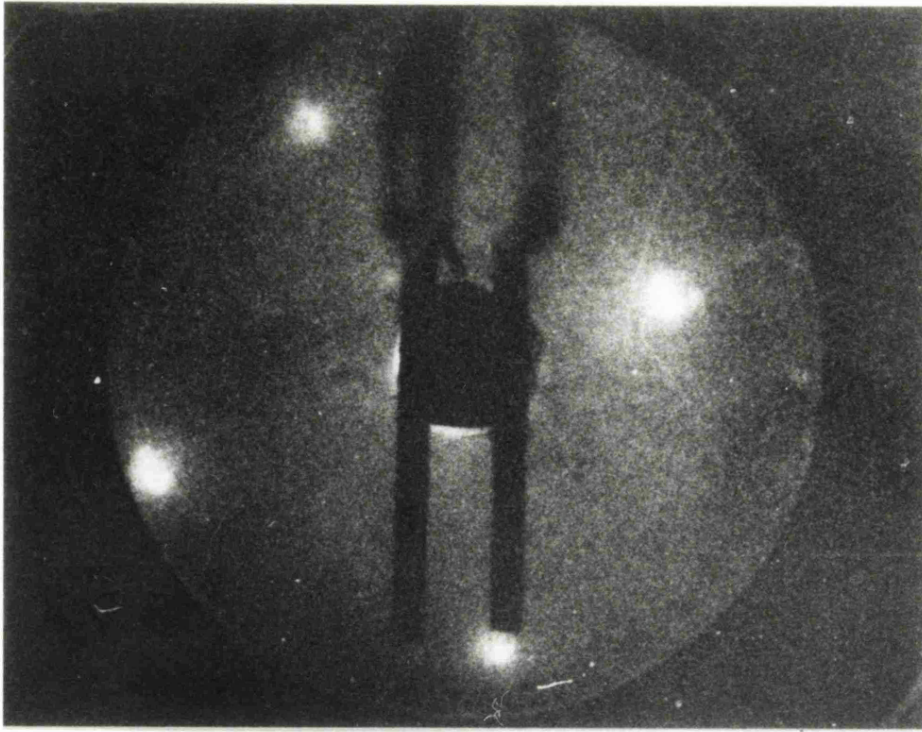


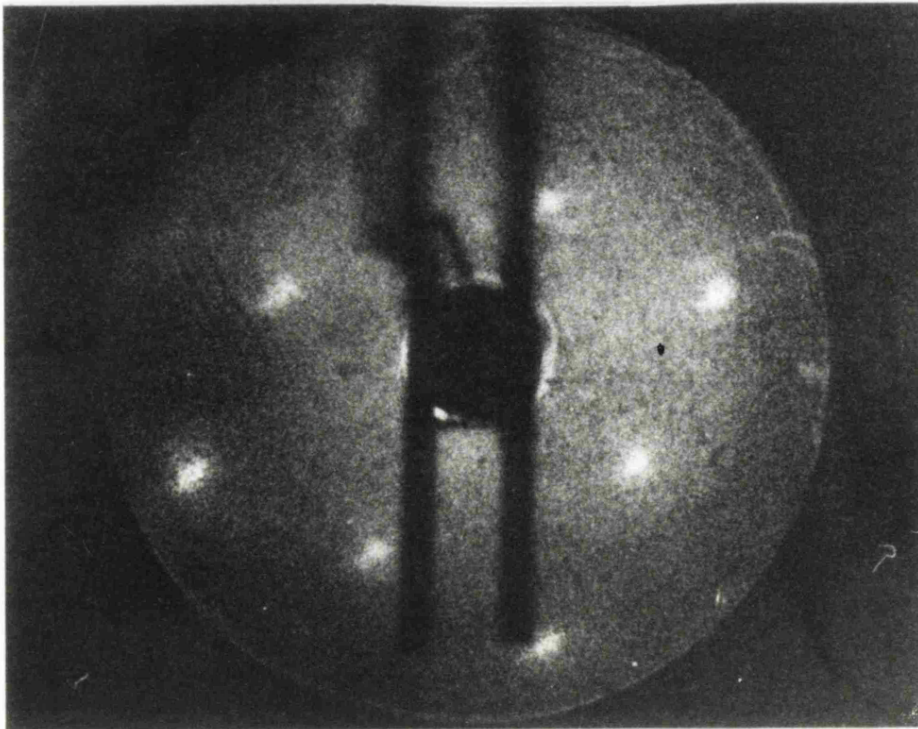
FIG. 6.2

Figure 6.3 (plate)

- (a) LEED pattern from clean Cu (100)
- (b) LEED pattern from c(2x2) palladium on Cu (100)



(a) Cu (100)



(b) C (2x2) Pd/Cu(100)

after a deposition time of approximately $2.5t_1$ the LEED pattern was completely obscured. Photographs of the $p(1 \times 1)$ and $c(2 \times 2)$ LEED structures are shown in figure 6.3.

6.3 Coverage Calibration

From the results discussed in section 6.2 it is evident that palladium initially grows on copper (100) in an ordered structure, the completion of which is marked by the maximum in intensity of the $c(2 \times 2)$ LEED pattern and the break in the decay of the copper Auger emission in the $As-t$ plot. Further palladium is adsorbed in a disordered state. This behaviour is qualitatively similar to that reported for manganese and cobalt on the same substrate (Binns and Norris 1982, Gonzalez et al 1980, 1981), however, further structure in the $As-t$ plots in both these cases could be identified and these authors interpreted their results in terms of an ordered submonolayer structure followed by layer by layer growth. In the present case no structure is seen in the overlayer growth curve, in fact the palladium signal follows an increasing exponential of the form

$$I_{Pd} = 152 (1 - \exp(-0.04 t))$$

where I_{Pd} = palladium Auger intensity (relative units)

t = time (minutes)

This is demonstrated in figure 6.4, where $\ln(152 - I_{Pd})$ is plotted against time and the data points are seen to follow the straight line quite closely. Clearly a simple layer by layer growth mode is not indicated.

The $c(2 \times 2)$ LEED pattern has two probable alternative interpretations, shown schematically in figure 6.5. The first is an ordered overlayer with palladium atoms occupying four-fold hollow sites

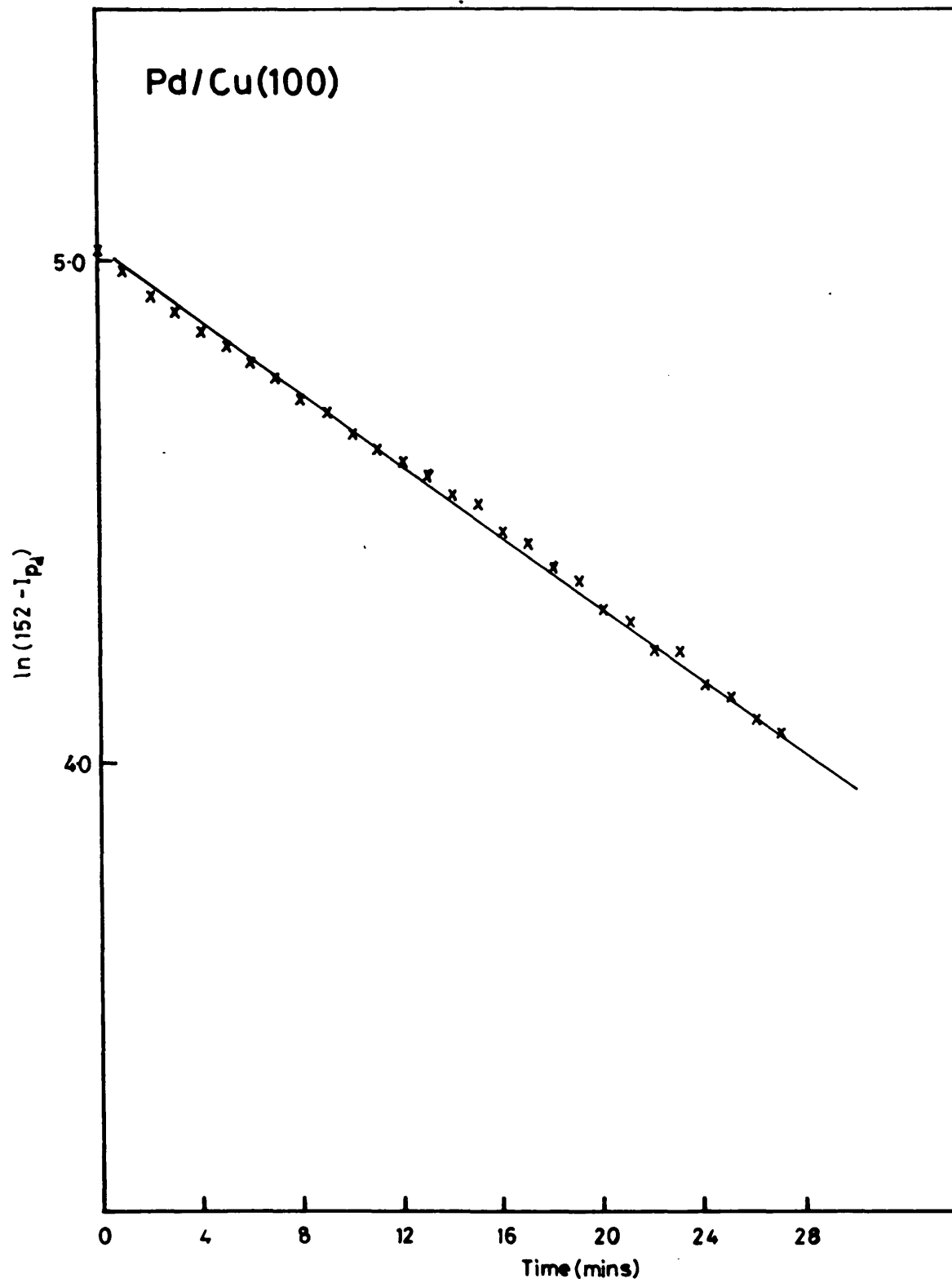
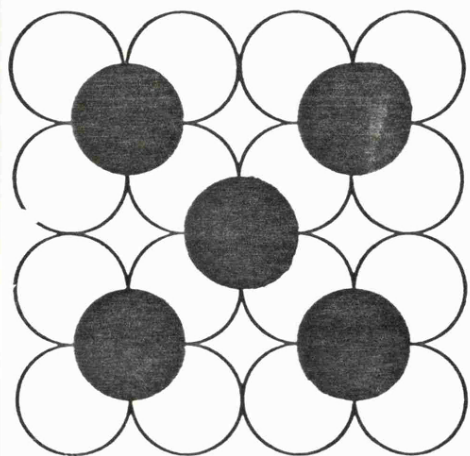


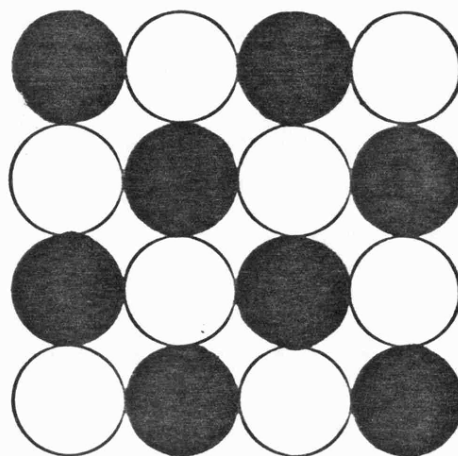
FIG. 6.4

and the other is a two dimensional surface alloy in which the palladium atoms have replaced every other copper atom to produce a simple square arrangement with copper atoms at the corners and palladium atoms at the face centres of the squares. Other overlayer structures are possible, for instance involving "bridge" or "on top" sites but the higher coordination four fold hollow is favoured when covalent bonding is not involved.

Both arrangements of figure 6.5 have identical periodicity and cannot be distinguished from the LEED pattern alone, however, when seen in conjunction with the Auger results a judgement can be made. As discussed above, lack of structure in the overlayer curve indicates that a simple layer by layer growth mode is not followed. Especially, a change in gradient would be expected at completion of the first monolayer. Evidence for interpretation in terms of the formation of an ordered surface alloy is obtained from the work of Fujinaga (1979a, 1979b) where a $c(2 \times 2)$ pattern was also formed during room temperature deposition of palladium on copper (100) during the process of alloy formation. It may be seen that the first (surface alloy) and second (copper) layers in figure 6.5b are generated by the top and middle (001) planes of the cubic unit cell of Cu_3Pd shown in figure 6.5c. The tendency to surface alloy formation at room temperature has been observed with other systems such as lead on low index faces of gold for which stable ordered alloy structures also exist in the corresponding bulk phase (Perdereau et al 1974). By contrast, copper and cobalt do not form any ordered structures in the bulk and copper and manganese show only a slight tendency to do so at high temperatures (Hansen and Anderko 1958). It is therefore proposed that palladium adsorption on copper (100) at room temperature involves formation of a surface alloy, the completion of which occurs at time t_1 in the A_s-t plot, and is followed by disordered palladium growth.

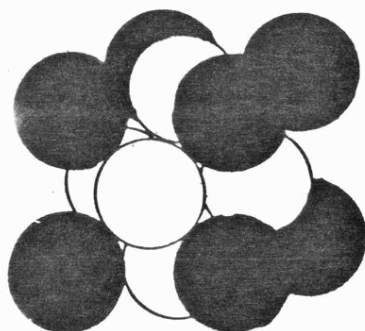


a) overlayer

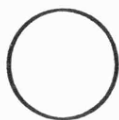


b) surface alloy

c) Cu_3Pd



Pd



Cu

FIG. 6.5

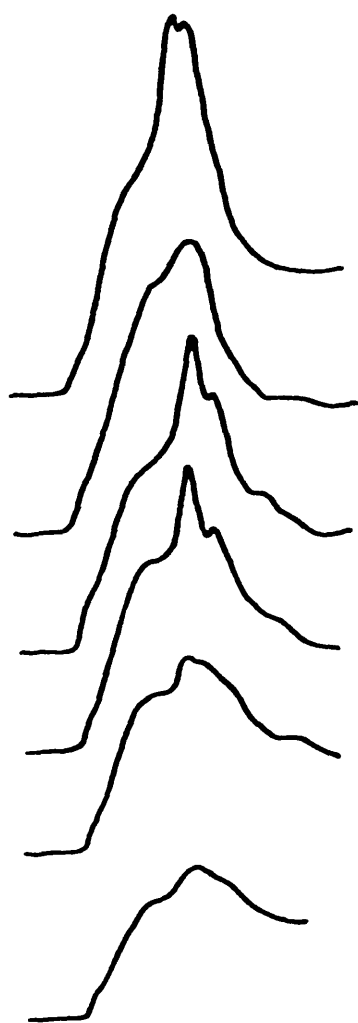
6.4 Photoemission Results

Angle resolved photoelectron spectra were recorded at 21.2 eV photon energy with the electron analyser oriented in the two principal symmetry planes, (001) and (011), normal to the substrate surface. Measurements were made with the clean substrate and palladium coverages corresponding to an evaporation time $t = t_1$ (the $c(2 \times 2)$ structure) and for $t = 2t_1$. The incident angle of the photon beam was 20° off normal and spectra were recorded at normal and several off-normal emission angles. Figures 6.6 and 6.7 show spectra for the (001) and (011) emission planes respectively.

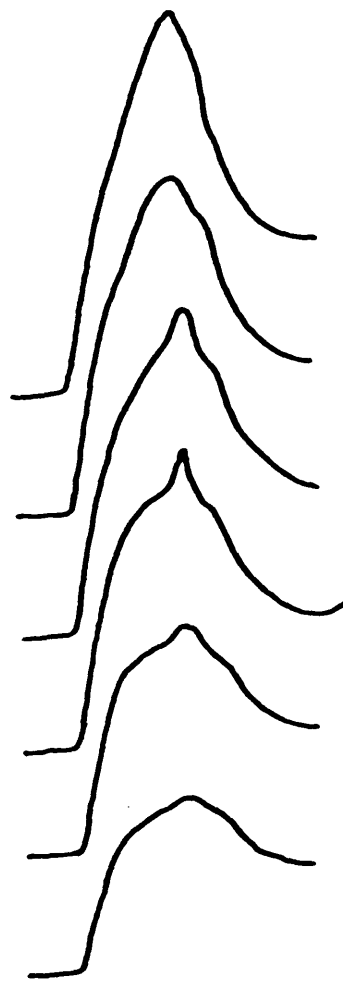
For the ordered $c(2 \times 2)$ surface (time t_1) the intensity in the copper 3d band emission lying at -2 to -5 eV is reduced, and preferential attenuation of the surface resonance discussed in Chapter 4 is observed. The sensitivity of the structure to take-off angle, reflecting conservation of the electron momentum \underline{k} in the photoexcitation process and dispersion in the initial 3d bands, is still apparent and similar to that seen for clean copper (Chapter 4, figure 4). The main effect of palladium adsorption is the broad feature which appears 1.2 eV below the Fermi level and is due to palladium 4d states. This band shows no significant variation with emission angle. Because of overlap with the copper 3d band it is difficult to separate the adsorbate related features from those of the substrate, but the full width at half maximum (FWHM) of the palladium 4d band was estimated to be 1.0 eV. With further palladium adsorption to a point where the LEED pattern indicates disorder (time t_2), the copper band becomes less structured and the palladium band is broadened. Changing the emission angle has little effect on any part of the spectra. A similar result has been reported by Lindgren and Wallden (1979) for caesium adsorbed on copper (111) and was attributed to

Pd/Cu(100)
 $hw = 21.2 \text{ eV}$
 $\phi = 0^\circ$

time = t_1



time = $2t_1$



$\theta_e = 0^\circ$

10°

20°

30°

40°

50°

┆┆┆┆┆┆
 E_F -1 -2 -3 -4 -5

┆┆┆┆┆┆
 E_F -1 -2 -3 -4 -5

ENERGY OF INITIAL STATE (eV)

FIG. 6.6

Pd/Cu(100)

$hw=21.2\text{eV}$

$\phi=45^\circ$

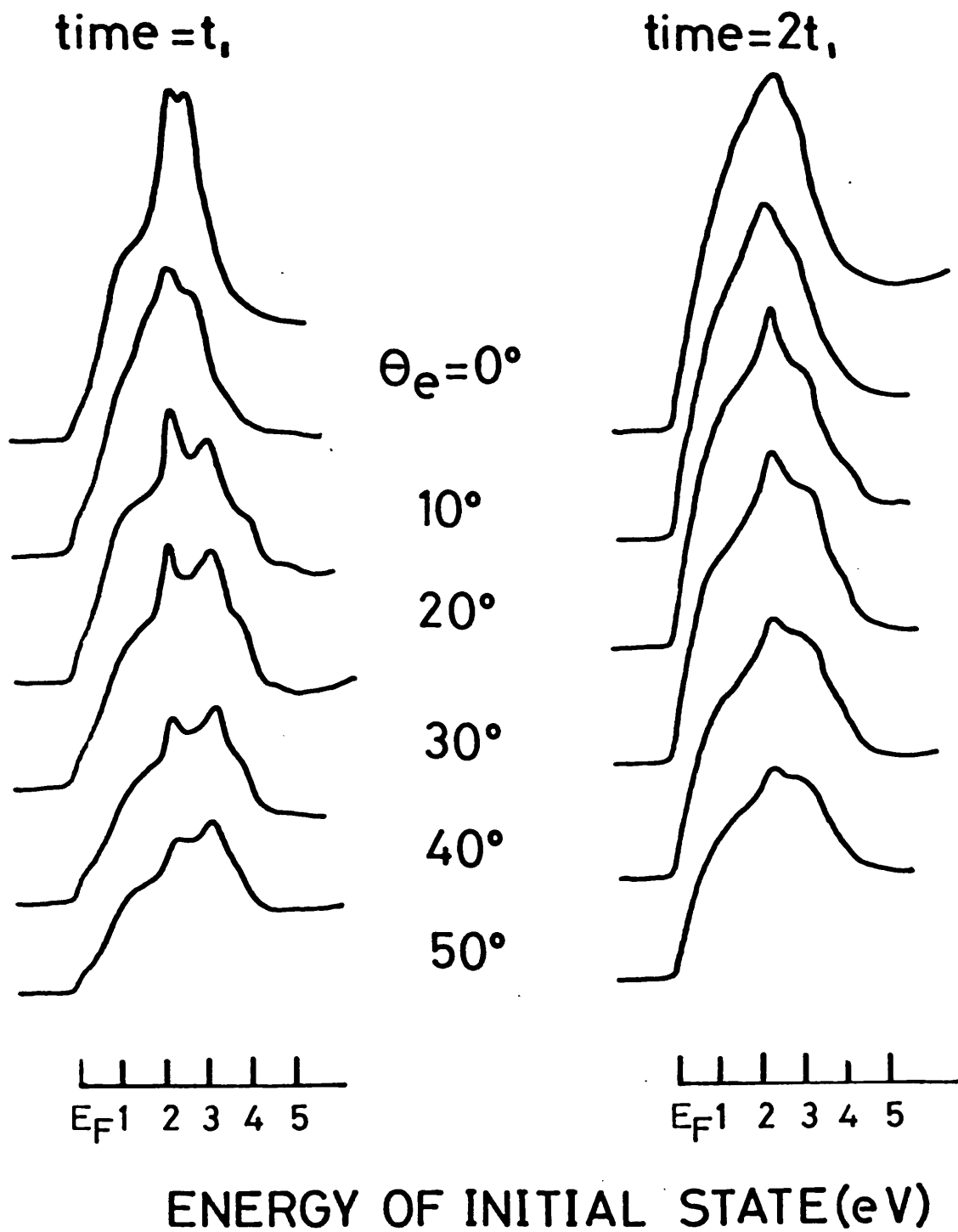


FIG. 6.7

incoherent scattering of the emergent electron wave by the disordered overlayer. Thus the detector records an angle averaged spectrum.

6.5 Photoemission Calculations

The PEOVER program for the calculation of angle resolved photoemission spectra from solids discussed in previous chapters does not allow for the inclusion of different atom types in the same layer. Additionally, a disordered layer cannot be specified in the input data stream and as a result realistic calculations for the palladium on copper (100) system could not be carried out. It was, however, of interest to investigate the effect of geometry on the theoretical photoemission from an ordered overlayer and calculations were performed for both $c(2 \times 2)$ and $p(1 \times 1)$ palladium overlayers. The theoretical curves for normal emission at 21.2 eV are shown in figure 6.8. The vertical intensity scale is the same for each spectrum and energies are measured in Hartrees from the muffin tin zero. The Fermi energy for copper is shown; it cannot be specified for the overlayers since the work function for these hypothetical structures is unknown. The potentials used were those employed in the clean surface work discussed in Chapter 4.

Referring to figure 6.8, the principal effect of going from clean copper (100) to the $c(2 \times 2)$ palladium overlayer is a marked attenuation of the copper d-band emission coupled with a change in peak shape. The presence of a strong surface resonance band running along the top of the projection of the d-bands on to the SBZ of copper has already been discussed (Chapter 4) and has been observed by several authors. The $c(2 \times 2)$ palladium overlayer will cause a perturbation of the surface potential, to which this kind of feature is particularly sensitive, resulting in the attenuation and change of shape of the substrate emission. Of course, a certain amount of attenuation due to scattering

THEORY: Pd/Cu(100)
hw=21.2eV

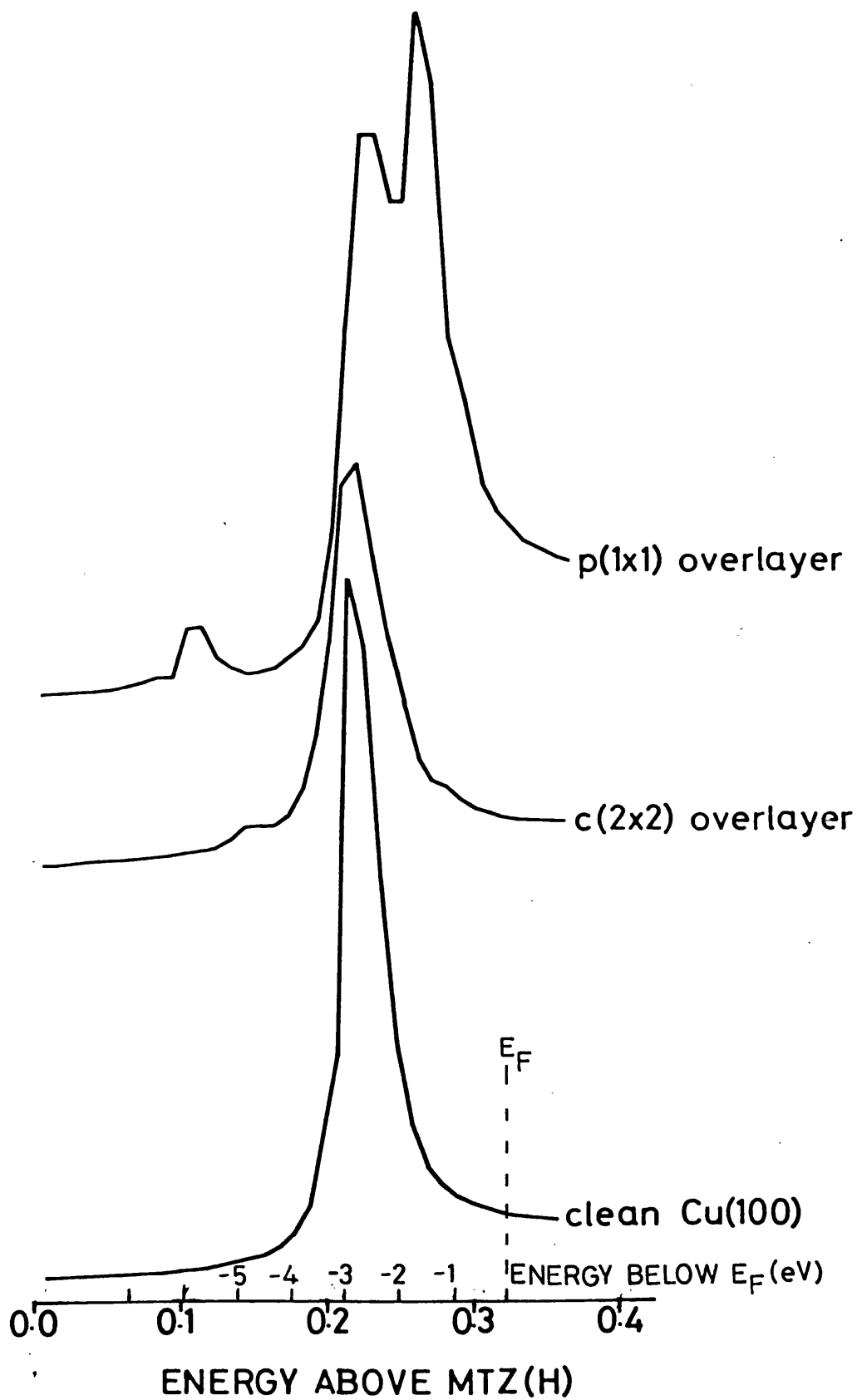


FIG. 6.8

from the overlayer is also expected. Little evidence for palladium-derived emission is seen except for the shoulders at .15H and .29H, either side of the main peak. These shoulders may be the edges of a weak and broad palladium resonance centred at approximately the same energy as the copper d-bands. In the $c(2 \times 2)$ structure there will be very little overlap between wave functions centred on adjacent palladium atoms and a broad resonance may be expected.

On going to the hypothetical $p(1 \times 1)$ case quite dramatic changes are seen. Strong palladium emission occurs with peaks at .270H and .235H. In addition, a small feature at .115H and a shoulder at .300H may be observed. It is known that calculations using PEOVER may emphasise the overlayer emission at the expense of lost intensity in the substrate signal (N. Kar, private communication; see also Chapters 5, 7 and 8 of this work) and this effect makes interpretation rather difficult in cases such as this when there can be no direct comparison with experiment. The spectrum represents a two-dimensional palladium (100) layer in which the palladium has suffered a lattice contraction of 7% (bulk interatomic spacings for palladium and copper are 2.75 \AA and 2.56 \AA respectively) and also contains components due to mixing of the palladium and copper d-bands. The .235H feature especially will contain a significant proportion of intensity originating from the copper bands which produce the strong .225H peak in clean copper (100). The weaker .115H feature has clearly originated from the shoulder at .150H in the $c(2 \times 2)$ spectrum, with a shift to lower energy (higher binding energy) and an increase in intensity with increasing coverage.

6.6 Discussion and Summary

The lack of angular dispersion of the palladium induced feature in the photoemission measurements from the $c(2 \times 2)$ surface alloy is a

consequence of the small d-d overlap between the non-adjacent palladium atoms. The position of the palladium 4d states implies that hybridisation with the copper 3d band is not the most significant factor. Thus, apart from spin orbit splitting which, at 0.5 eV (Hermann and Skillman 1963), is not negligible, the dominant interaction and contribution to the width of the palladium band in the c(2 x 2) structure is the resonance with the copper 3s states. The palladium 4d electrons may be thought of as occupying a virtual or resonant bound state as discussed by Friedel (1958) and Anderson (1961) for random alloys. Angle integrated photoemission spectra have been reported by several workers for dilute Cu-Pd alloys (Wallden 1969, Nemoshkalenko et al 1975, Huffner et al 1975). All show a palladium related feature at the same energy as found in this study. The value obtained here for the FWHM, 1.0 eV, is close to the value of 0.9 eV observed in XPS for a 5% palladium alloy (Huffner et al 1975).

To summarise, it has been shown that growth of palladium on copper (100) at room temperature involves formation of a surface alloy with an electronic structure, as revealed by photoemission, similar to that of bulk dilute Cu Pd alloys. The growth of this surface alloy probably proceeds through the diffusion of copper atoms originating from step sites across the surface during palladium adsorption. Vacancy diffusion to the surface at a sufficient rate to accommodate the adsorbed palladium atoms would not be possible at room temperature. The distorted alloy surface so formed is such that an ordered palladium layer cannot grow in registry and further adsorption results in disordered overgrowth.

CHAPTER 7

AN ELECTRON SPECTROSCOPIC STUDY
OF COPPER OVERLAYERS ON SILVER (100)

- 7.1 Introduction
- 7.2 LEED and Auger Spectroscopy
- 7.3 Coverage Calibration
- 7.4 Normal Emission Photoelectron Spectra
- 7.5 Dispersion Relation of one Monolayer
- 7.6 Photoemission Calculations
- 7.7 Discussion and Summary

CHAPTER 7

AN ELECTRON SPECTROSCOPIC STUDY
OF COPPER OVERLAYERS ON SILVER (100)7.1 Introduction

This chapter describes a LEED, Auger and angle resolved photoemission study of copper overlayers adsorbed on silver (100). The system was chosen for several reasons and shows similarities to the palladium on silver (100) adsorbate-substrate combination described in Chapter 5. The copper and silver bulk d-bands are centred at -2.7 eV and -5.1 eV respectively and show little overlap with energy so small d-d hybridization may be expected. Both copper and silver are well characterized materials; band structure calculations and photoemission spectra from their (100) crystal faces were discussed in Chapter 4. Recent transmission electron microscopy experiments have shown that copper grows on silver (100) initially as an ordered (100) layer (Bruce and Jaeger 1977). The system was the subject of an early angle integrated photoemission study (Eastman and Grobman 1973) and of a theoretical investigation (Bisi and Calandra 1977) in which the LCAO technique was used to calculate the surface DOS. Theory and experiment were not in good agreement and it was not clear if the experimental technique was in need of refinement or the (non self-consistent) theory was inadequate. The DOS and energy band structure of the isolated copper (100) monolayer have been the subject of a recent self-consistent calculation (Arlinghaus et al 1979).

There is, however, one important difference between copper and palladium overlayers on silver. For perfect epitaxial (pseudomorphic) growth on silver the copper layer would be subject to a 13% lattice expansion due to the different lattice parameters of fcc copper and

silver (3.615 \AA and 4.086 \AA respectively). This may be expected to have a significant effect on the electronic structure of such an over-layer.

Deposition was followed by LEED and Auger spectroscopy (section 7.2) and from the results the growth mode determined (section 7.3). Normal emission photoelectron spectra are presented in section 7.4 and off normal spectra at one monolayer coverage in section 7.5. The results of theoretical photoemission calculations are given in section 7.6 and the investigation is summarized in section 7.7.

7.2 LEED and Auger Spectroscopy

Copper was deposited on the (100) face of silver held at room temperature while periodically monitoring the LEED pattern and the peak to peak intensities of the differentiated silver $M_{4,5}$ $N_{4,5}$ $N_{4,5}$ (356 eV) and copper $M_{2,3}$ VV (62 eV) Auger emission lines. The plot of Auger signal vs time is shown in figure 7.1. The silver Auger intensity decay has three straight line sections with changes in gradient at times t_1 and t_2 . After time t_3 the decay follows a gently sloping curve of shallow gradient. The behaviour is approximately reflected in the increase of copper intensity, although little structure may be seen in the curve. No attempt at normalization of the Auger intensities, such as for the case of palladium on silver (Chapter 5), was made. The superposition of the copper 62 eV Auger line on the rapidly sloping secondary background made reliable measurements of the copper signal intensity difficult until significant copper emission was obtained, hence no data points were recorded until 10 minutes of evaporation.

The $p(1 \times 1)$ LEED pattern obtained from the silver (100) substrate was retained up to the second change of gradient in the As-t plot (time t_2). Slight broadening of the spots was observed

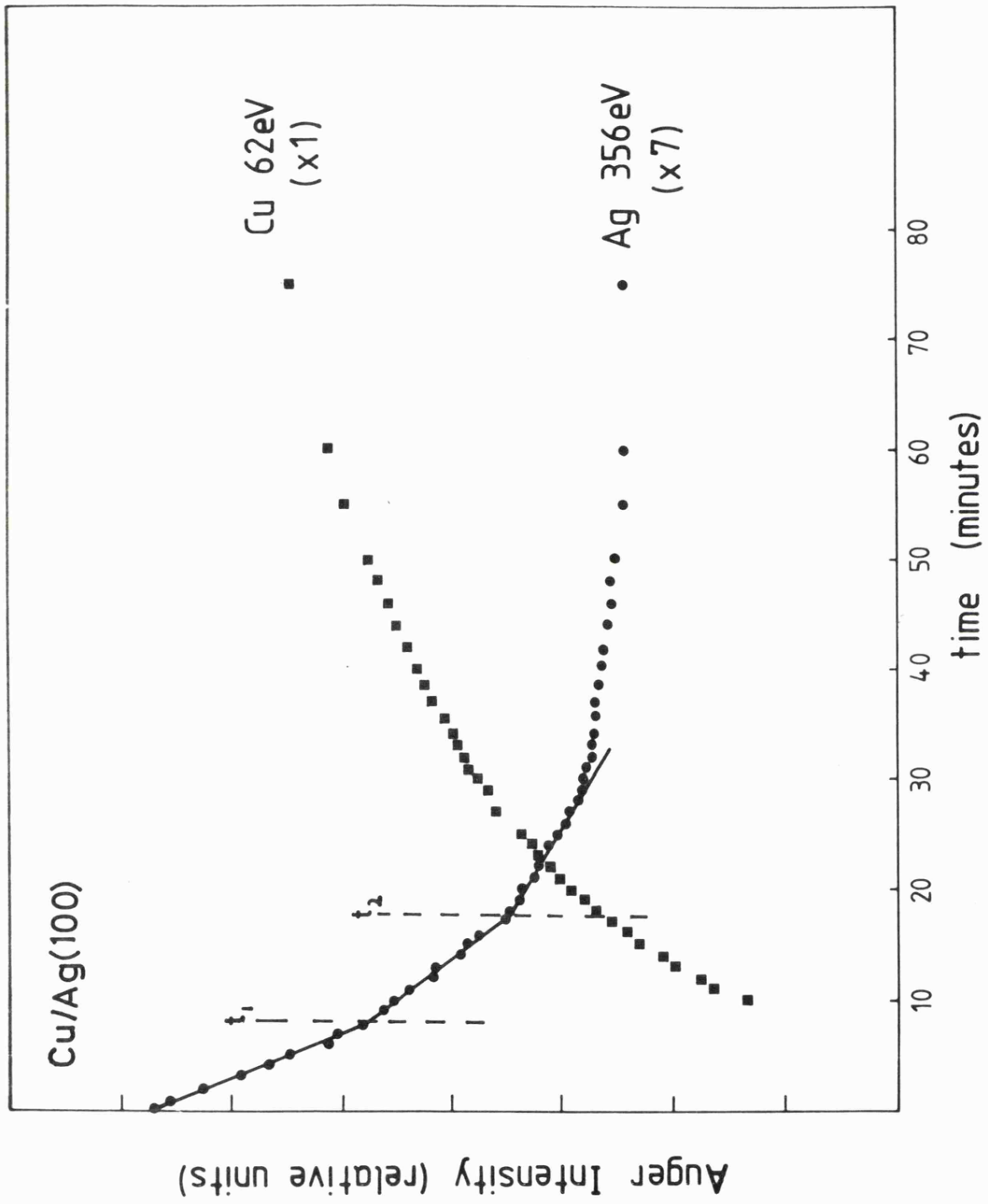


FIG. 7.1

between times t_1 and t_2 but after t_2 the deterioration was rapid resulting in very broad spots and a high background intensity after a further 15 minutes deposition.

7.3 Growth Mode and Coverage Calibration

Interpretation of overlayer growth modes (Bauer and Poppa 1972) from structure in the As-t plot (Rhead 1976) was discussed in Chapter 2. In the case of copper on silver (100) the initial piece-wise linear decay of the substrate Auger intensity indicates that the first stage of growth is layer by layer. In Chapter 2 it was shown that, according to the classical model of Frank and van der Merwe (1949) as subsequently modified by Woltersdorf (1981), this form of growth may only occur where the lattice mismatch is less than a certain critical value. Values of between 7% and 11% were obtained, depending on the substrate temperature. Both copper and silver crystallise in the fcc structure with lattice constants 3.61 \AA and 4.09 \AA respectively, the mismatch between a copper (100) layer on silver (100) is 11.6%, relative to the substrate. A simple classical growth model cannot be expected to give precise numerical results but it is clear that this lattice expansion is near the upper limit for pseudomorphic layer by layer growth. Beyond this limit the Stranski-Krastanov mode, in which layer growth is followed by islanding, often occurs and this appears to be the case for the system copper on silver (100).

During formation of the first monolayer (up to time t_1) there is perfect epitaxy, as shown by the LEED pattern. The change of gradient at t_1 indicates completion of the first monolayer. There is slight deterioration of the LEED pattern between t_1 and t_2 but the well-defined break at t_2 is evidence of an almost perfect second layer. After completion of the second layer rapid deterioration of the LEED

pattern was seen and this, together with the lack of a clean third break in the curve is indicative of a change in the growth mechanism at approximately t_3 . The large strains permissible in monolayers cannot be sustained at thicker coverages and relaxation to a bulk-like overlayer lattice constant must take place. The As-t plot indicates such relaxation to be taking place between approximately two and three deposited copper monolayers. The change to an extremely shallow gradient is typical of island formation.

The so-called universal curve for electron mean free paths proposed by Seah and Dench (1979) predicts an attenuation of 77% for electrons at the silver Auger energy on passing through one copper monolayer and 60% on passing through two copper monolayers. This compares with the experimentally observed attenuations of 72% and 52% respectively.

The observed mode of growth, namely two epitaxial layers followed by disorder and islanding, is very similar to that observed for the related iron on silver (100) system (Smith, Padmore and Norris 1982, Chapter 8 of this work) in which three monolayers were formed and relaxation during the growth of the third monolayer lead to islanding.

The most significant point concerning the growth mode is that a supported p(1 x 1) (100) monolayer of copper with a 13% lattice expansion over the bulk has been prepared. No evidence for alloying at room temperature was found.

7.4 Normal Emission Photoelectron Spectra

Angle resolved photoelectron spectra taken in normal emission at 21.2 eV (He I) are shown as a function of coverage in figure 7.2. Prominent silver 4d emission is seen in the region -4 to -7 eV. Features due to copper d-band formation occur superposed on the silver s-band in

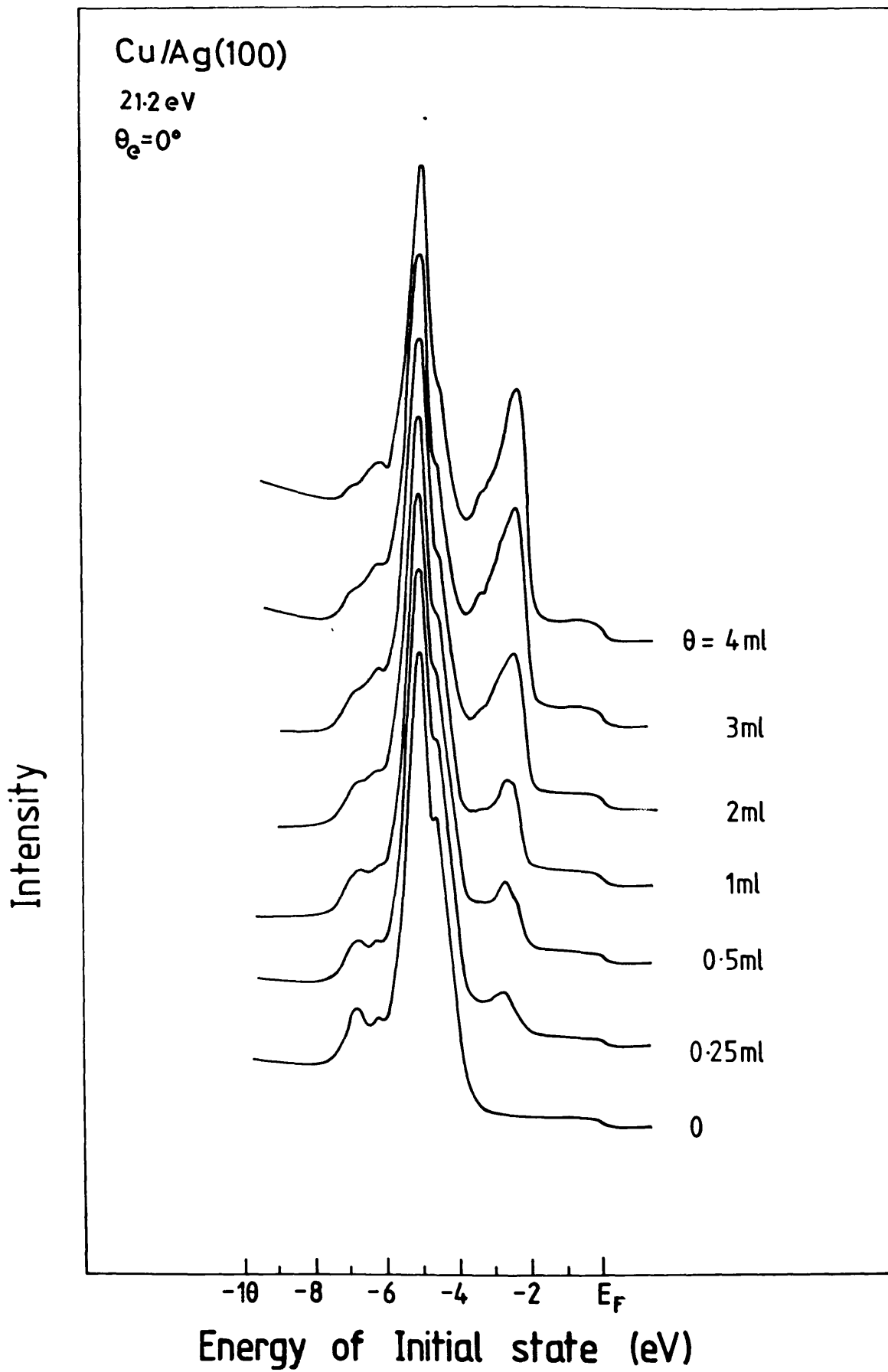


FIG. 7.2

the -2 to -4 eV energy range and increase in width and intensity with increasing copper coverage. The corresponding decrease in silver emission intensity with little change of shape or position is consistent with the growth of an ordered epitaxial layer and implies little interaction between the overlayer and substrate bands. No change in work function with coverage was found.

At low coverage (0.25 ml) a single feature of symmetric Lorentzian shape centred at -2.8 eV may be seen superposed on the silver 4s band emission. This is reminiscent of that seen for palladium on silver (100) at low coverages (Smith et al 1982) and as such may be interpreted as due to resonant bound 3d states localized on isolated copper atoms adsorbed in a random p(1 x 1) lattice gas configuration. The FWHM of 0.8 eV is similar to that observed for palladium adsorbed on the same substrate. On increasing coverage to 0.5 ml the copper emission becomes structured, showing three distinct features at -2.56, -2.75 and -3.42 eV. This is a consequence of increasing overlap of the 3d wave functions on adjacent sites as significant two dimensional islanding occurs. At one monolayer the copper emission shows structure similar to that seen at 0.5 ml, with an increase in intensity of the leading peak, which has shifted in energy to -2.47 eV. This corresponds to a two-dimensional phase not typical of either bulk copper or the isolated copper atom, whose electronic structure is discussed in the following section.

With further deposition the copper emission continues to grow in strength, the dominant effect being the increase in intensity in the feature nearest the Fermi energy. In Chapter 4 the presence of strong surface resonance contributions to the photoemission signal from bulk copper was discussed and it is probable that the increase in intensity of this feature is due to the formation of these resonances

with increasing coverage. This is consistent with the palladium on silver (111) result of Chapter 5, section 5.3, when a surface resonance was found at a coverage of three monolayers

Angle-integrated photoemission measurements from copper overlayers on a silver substrate of unspecified but presumably polycrystalline nature have been reported by Eastman and Grobman (1973). At one monolayer coverage they observed a feature described as a resonant bound state of FWHM 1.0 eV centred ~ 2.5 eV below E_F . The normal emission curve in figure 7.2 for the single monolayer shows the copper emission to be centred at -2.77 eV and of FWHM 1.1 eV. Thus the experimental result is in agreement with Eastman and Grobman although, as discussed below the present data is interpreted in terms of the development of a two dimensional energy band structure within the monolayer rather than a resonant bound state in the spirit of the Anderson (1961) model. On going from one to four monolayers coverage Eastman and Grobman observed a change in shape of the copper emission from an asymmetric Lorentzian to a bulk like form. The present measurements confirm this result to the extent that a spectrum typical of bulk copper (100) was recorded at four monolayers.

A calculation of the DOS of a pseudomorphic epitaxial copper monolayer supported on a silver (100) substrate has been presented by Bisi and Calandra (1977). Using the semi-empirical tight-binding approach of the parameterized LCAO technique a copper d-band centred at 5.4 eV below the Fermi level was obtained. This clearly does not agree with the present experimental results, with the theoretical band requiring a 2.68 eV shift towards E_F to locate it in the region indicated by the photoemission measurements. This is almost certainly the result of the 0.3 electrons per atom transferred to the substrate during the iteration process of the calculation. Charge transfer of this nature

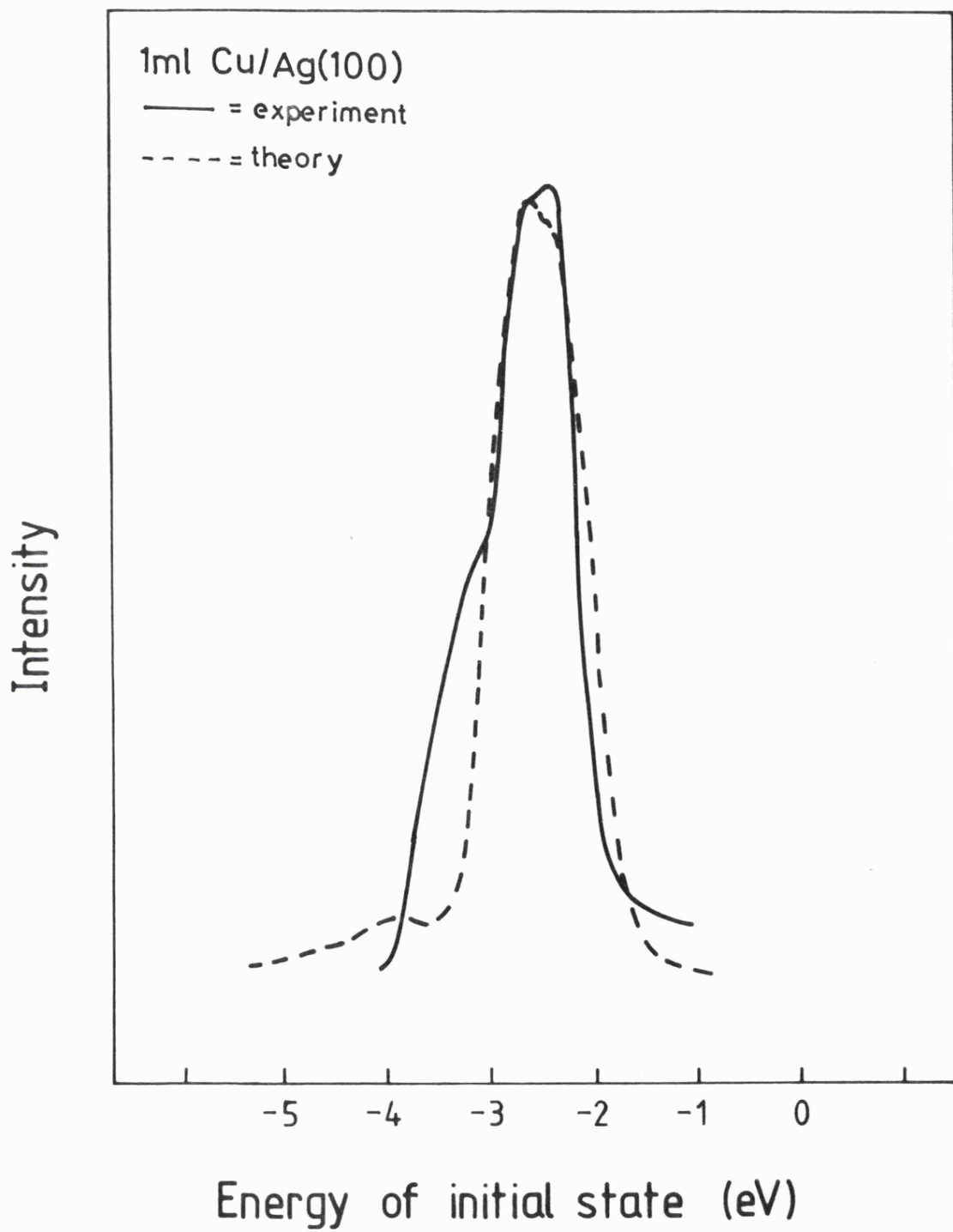


FIG. 7.3

is known to be characteristic of the LCAO technique when applied to bulk materials (Kohn et al 1976). An indication of any charge transfer between overlayer and substrate may be obtained by monitoring the work function during deposition (Lang 1971). The work function was obtained from the width of the photoelectron energy distribution curve during copper deposition and no change was seen, indicating no transfer of charge. This is the expected result since both copper and silver have an electronegativity of 1.9 (Pauling 1960) and the work functions of their (100) surfaces are similar (4.59 eV and 4.64 eV respectively) (Gartland 1972, Dweydari and Mee 1975).

The DOS of the copper monolayer as calculated by Bisi and Calandra is shown in figure 7.3. The theoretical result has been broadened by a Lorentzian of FWHM 0.2 eV, to simulate the effect of experimental resolution, and shifted by the factor 2.68 eV discussed above. Superposed on this is the experimental photoelectron difference curve obtained from one monolayer at 21.2 eV in normal emission. Quite good agreement between theory and experiment is seen, although some discrepancy in the position and intensity of the feature on the high binding energy side of the main peak is observed. In making this comparison two points should be noted. First, the experiment is angle resolved so an average over the whole Brillouin Zone is not obtained and perfect agreement with a calculated DOS should not be expected. Inspection of figure 7.4 shows there is little variation in shape and position of the copper d-band features as the analyser is moved off normal so the angle resolving aspect of the experiment, in this case, should not strongly affect the comparison with the theoretical DOS. Second, the photoelectron spectrum does not provide a direct measurement of the density of initial states. Rather, some convolution of the initial and final DOS is obtained (the so-called energy distribution

of the joint density of states, or EDJDOS). In the case of a supported layer, however, a continuum of final states is available in the bulk band structure of the substrate projected onto the surface Brillouin Zone and strong transition matrix element effects are not expected.

7.5 Dispersion Relation for the Monolayer

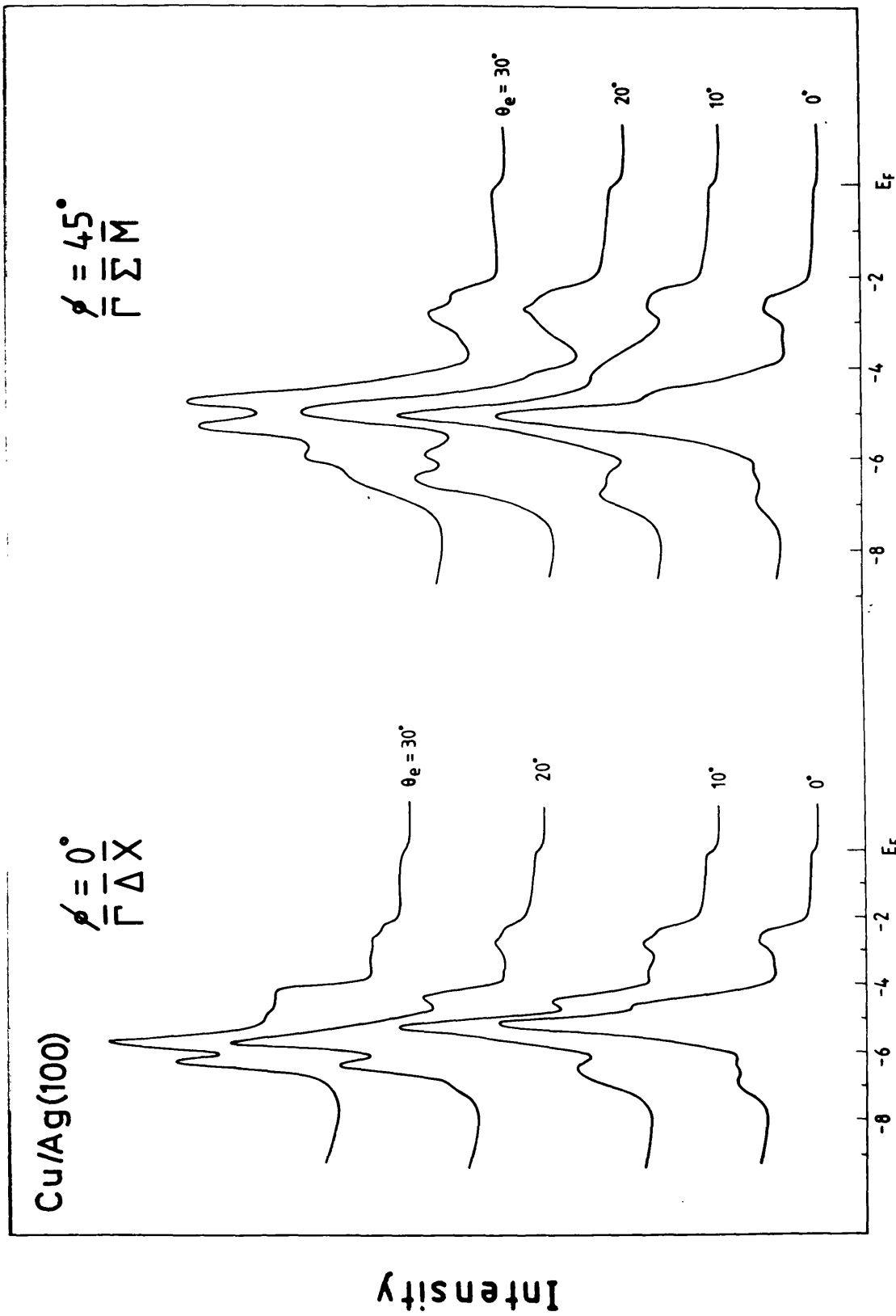
At a coverage of one copper monolayer angle resolved spectra at 21.2 eV were taken at off normal emission angles along the two principal symmetry axes of the (100) surface. Representative spectra are shown in figure 7.4. The behaviour of the silver 4d bands in angle resolved photoemission has been investigated previously and interpreted in terms of direct transitions from calculated initial states to free electron like final states (see Chapter 4, or Courths et al 1981) and need not be discussed further.

The interpretation of off normal photoelectron spectra in terms of the two dimensional band structure of the overlayer has been discussed previously (Chapters 4 and 5). For an epitaxial monolayer whose electron states show no hybridization with the substrate high-occupancy (in this case 4d) bands the overlayer electron states have no dispersion with k_{\perp} , the component of the one electron momentum vector perpendicular to the surface, and the energy bands are a function of k_{\parallel} , the parallel component, only. As such, they may be mapped directly from the spectra using the relation

$$k = \frac{1}{\hbar} \sqrt{2m E_{kin}} \sin \theta_e$$

using the notation of Chapter 5.

The method has recently been applied to the copper enriched (111) surface of a Ni_{0.84}Cu_{0.16} alloy by Heiman et al (1981). Two dimensional dispersion in fair agreement with the calculated bands for



Energy of Initial State (eV)

FIG. 7.4

a copper (111) monolayer isolated in space (Jepson et al 1978) was observed. The theoretical bands required a 1.24 eV shift to higher binding energy to produce agreement with the experiment and this was attributed to a deepening of the monolayer potential due to the underlying layers.

Copper on silver (100) represents a better approximation to an isolated monolayer since, experimentally, the copper and silver d-bands show little overlap and further, photoemission spectra taken in normal emission at 21.2 eV and 40.8 eV show features in the copper emission at approximately the same initial state energies. In normal emission the analyser accepts only those photoelectrons for which $k_{\parallel} \sim 0$. No change in peak positions between photon energies indicates no dispersion in k_{\perp} (the component of k accepted by the analyser in normal emission) and shows the essentially two dimensional nature of the films.

The effect of lattice spacing on the band structure is important and must be taken into consideration here. Using a tight binding approach to the d-bands of a transition metal based upon the Korringa-Kohn-Rostoker formulation Heine (1967) has shown the width of a non-hybridized d-band to be given by

$$\Delta \propto W (kR)^{-5}$$

where $k^2 = E_d$, the energy of the d-resonance above the bottom of the free-electron band

R = radius of the sphere inscribed in one atomic cell

W = escape probability, constant for a given band.

This may be written

$$\Delta = \frac{1}{2} M^2 R^{-5}$$

with M = the reduced matrix element

The validity of this R^{-5} bandwidth dependence for the noble metals copper,

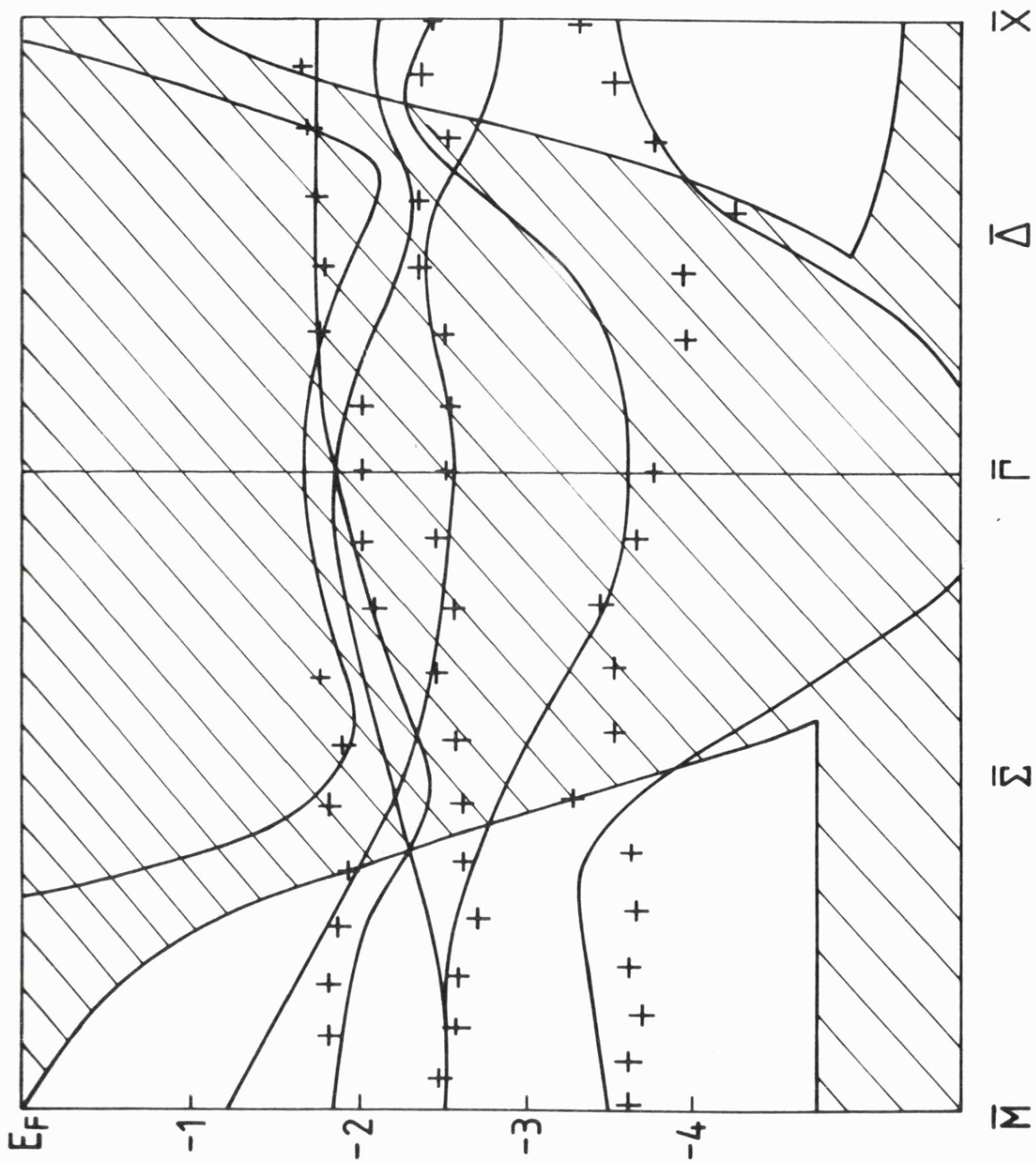


FIG. 75

silver and gold has been verified in a series of KKR band structure calculations using different lattice spacings by Jacobs (1968).

In the present case of an epitaxial copper layer on silver (100) the copper-copper distance in the overlayer is 13% greater than the natural bulk crystalline lattice spacing and so the experimental bandwidth has to be increased by a linear scaling factor of $(1.13)^5 \approx 1.8$ to account for this effect. The experimental E vs k_{\parallel} dispersion for the copper monolayer, after scaling, is shown in figure 7.5. Also shown are the theoretical energy bands for a copper (100) monolayer, as calculated self consistently by Arlinghaus et al (1979). In order to bring the calculated bands into the energy region occupied by the scaled experimental points they have been rigidly shifted by 1.20 eV to higher binding energy. The shift is of similar magnitude to that used by Heiman and co-workers (1981) and is presumably of the same origin.

The shifting and broadening process described above appears to bring the experimental and theoretical dispersions into fair agreement, although the theoretical curves are often separated by energies less than the resolution (~ 150 meV) of the analyser and so detail in these regions could not be distinguished in the spectra. The hatched area of figure 7.5 corresponds to the bulk band structure of silver projected on to the (100) surface Brillouin Zone. The projected s-band is seen to overlap significantly with the two dimensional copper bands along both the $\bar{\Delta}$ and $\bar{\Sigma}$ directions. Hybridization with these states may account for some discrepancies and especially for the poor agreement between theory and experiment at ~ -4 eV along $\bar{\Gamma}\bar{X}$.

7.6 Photoemission Calculations

As for palladium on silver the formalism of Pendry (1976) as implemented by Hopkinson et al (1979) was used to investigate the angle resolved photoemission for copper overlayers on silver (100). In this

Cu, 21.2eV, normal emission

— = Cu lattice

- - - = Ag lattice

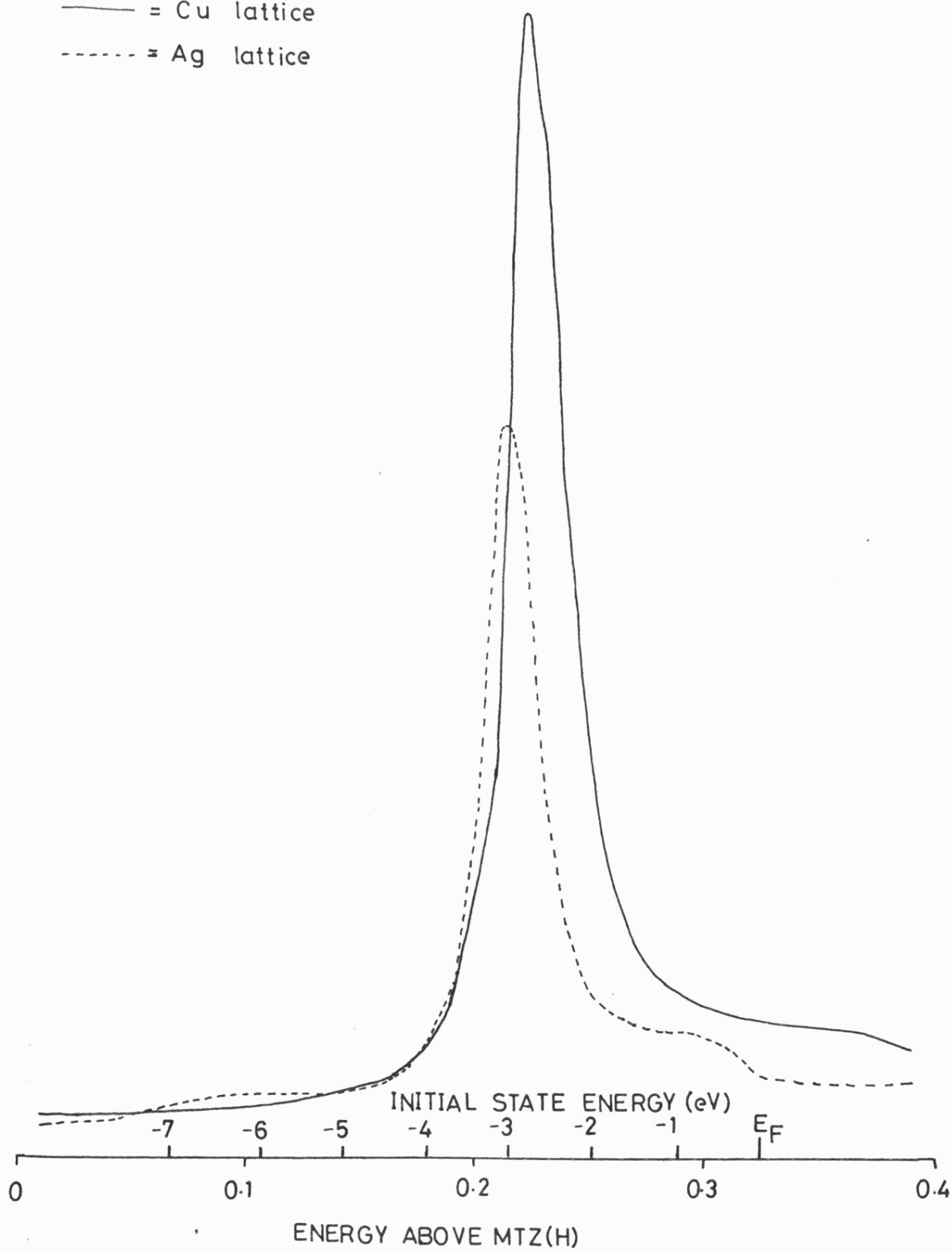


FIG. 7.6

case rather more extensive calculations were carried out involving variation of lattice constant, overlayer-substrate distance, photon energy dependence and modification of the overlayer potential. Throughout, the muffin tin potentials for copper and silver described in Chapter 4 were used.

The LEED and Auger results suggested that the first copper monolayer deposited on silver (100) took the lattice constant of silver. It was therefore of interest to investigate the effect of lattice constant variation on the bulk overlayer material before proceeding to the monolayer case. Figure 7.6 shows the calculated normal emission spectrum at 21.2 eV for both natural bulk copper and for a copper crystal rigidly expanded by 13%, that is, with a nearest-neighbour distance corresponding to that found in bulk fcc silver. The lattice expansion is seen to result in a change in shape and width of the copper 3d emission peak. This is consistent with simple tight binding theory and is the result of reduced overlap between the d-like wavefunctions on neighbouring atoms. The reduction in intensity of 49% does not have such a ready explanation. The reduction in the overall number of atoms contributing to the spectrum due to the lattice expansion is only 34%. It is possible that expansion of the lattice causes a reduction in the back-scattered component of the photocurrent as a result of reduced cross-sections. Alternatively, the lattice expansion and concomitant lowering of the d-levels in energy results in reduced overlap with the propagating plane wave-like states in the flat interstitial regions of the muffin tins. The reduced transition matrix element then results in reduced photoemitted intensity.

Spectra calculated for one epitaxial p(1 x 1) monolayer of copper on silver (100) in normal emission at 21.2 eV (HeI) is shown in figure 7.7. The copper layer was taken to be lying in the plane where the next silver layer would be expected in a continuous crystal, i.e.

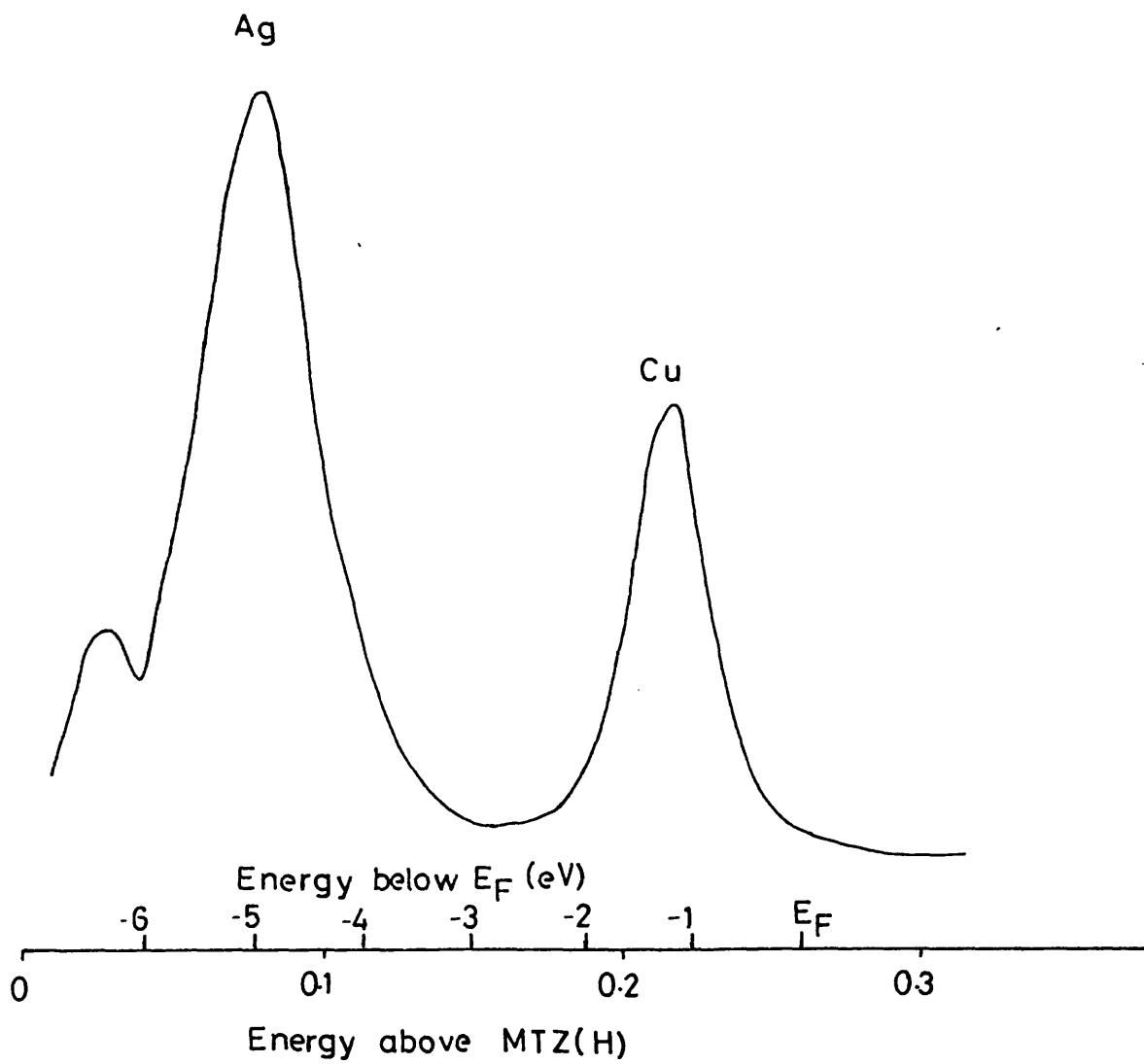


FIG. 7.7

the overlayer-substrate distance was half the bulk substrate lattice constant. Expansion of the overlayer relative to bulk copper is likely to modify the electron lifetime from the bulk value and to allow for this in the calculations the electron lifetime was estimated from the As-t plot as follows. The mean free path, λ , of silver Auger electrons through the copper monolayer was 3.0 ml (section 7.3). In the usual notation the Heisenberg Uncertainty Principle states

$$\Delta p \Delta x \geq \hbar$$

In the limit $\Delta x = \lambda$, $\Delta p \lambda = \hbar$

and $p = \sqrt{2m^* E}$

$$\Delta p = - \frac{\sqrt{m^*}}{2E} \Delta E$$

so
$$\Delta E = - \frac{\hbar}{\lambda} \sqrt{\frac{2E}{m^*}}$$

giving a value for the inverse lifetime of -0.05 H , assuming $m^* = m$, the electron rest mass. Although the shapes of the calculated copper and silver emissions in figure 7.7 are approximately curved there is disagreement in intensity and relative energy position compared to the one monolayer curve of figure 7.2. The copper emission intensity is enhanced relative to the silver, even though the cross-section for 3d levels at this energy is an order of magnitude less than that for 4d levels (Kennedy and Manson 1972). Agreement could be improved here by the use of a more reliable d-state cross section, as has been noted previously (Padmore et al 1982), or possibly by the use of energy dependent lifetimes.

It is evident that, compared with experiment, the copper emission shown in figure 7.7 is located too near the Fermi energy. The experimental separation of the copper and silver d-band maxima is 2.46 eV, or 0.09 H. Theory gives a separation of 0.24 H, and the error of 0.05 H is equal to the difference between the inner potentials of copper and

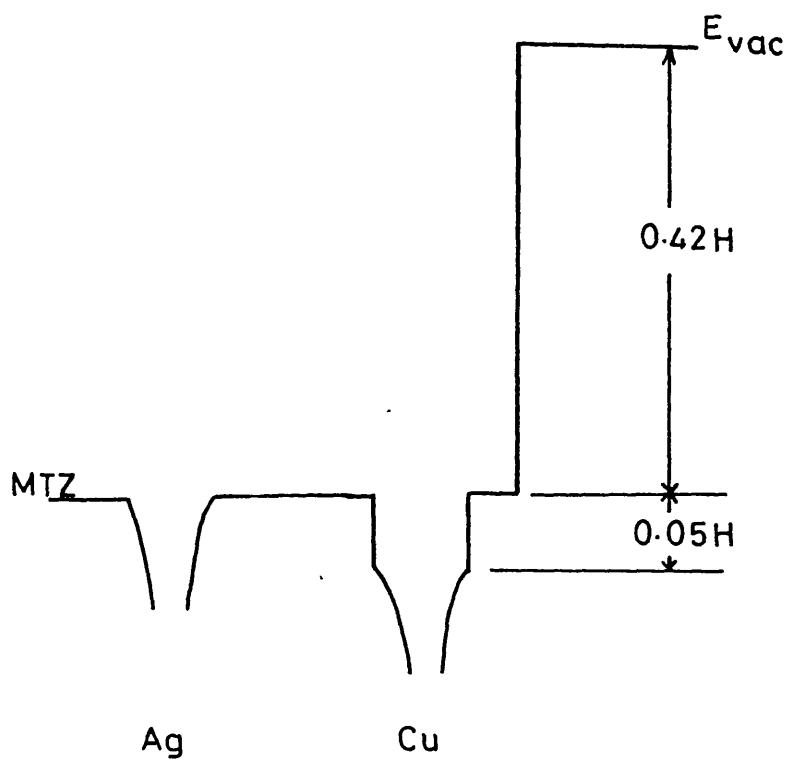


FIG. 7.8

silver (0.47 H and 0.42 H respectively). In the PEOVER program energies are referred to the muffin tin zero and only one inner potential may be specified even though different materials may be involved. This results in distortion of the theoretical energy separations of emission from substrate and overlayer materials with different inner potentials. The problem is similar to that occurring in alloys, where the shifted muffin tin or the charge renormalized atom may be used. A discussion has been given by Bansil et al (1974) in their calculation of the complex energy bands of α -brass. The fact that the error in the calculated energy separation in figure 7.7 is equal to the difference in inner potentials indicates there is no significant charge transfer in the experiment, in which case a rigid shift of the overlayer potential within the muffin tin may be used. The resultant potential with a step of 0.05 H applied at the muffin tin radius of the overlayer atoms is shown in figure 7.8 and the calculated spectra using this modified potential for photon energies of 21.2 and 40.8 eV are shown in figure 7.9(a). The theoretical and experimental 21.2 eV spectra are now in good agreement, as shown in figure 7.9(b) and discussed by Binns et al (1982). On going from 21.2 to 40.8 eV significant changes in the spectra are observed. The change to a double peak structure of the silver emission is characteristic of this energy. There is no predicted shift or change in shape of the overlayer emission between the two photon energies. This indicates no dispersion with the component of the momentum vector perpendicular to the surface (k_{\perp}) and is consistent with the interpretation of the monolayer spectra on a two dimensional basis discussed in the previous section. The increase in intensity of the copper emission at 40.8 eV, although exaggerated relative to experiment, is a consequence of the rising 3d photoionization cross-section in this energy range.

Cu/Ag(100)

theory

$\theta = 1\text{ml}$

— = 21.2eV

- - - = 40.8eV

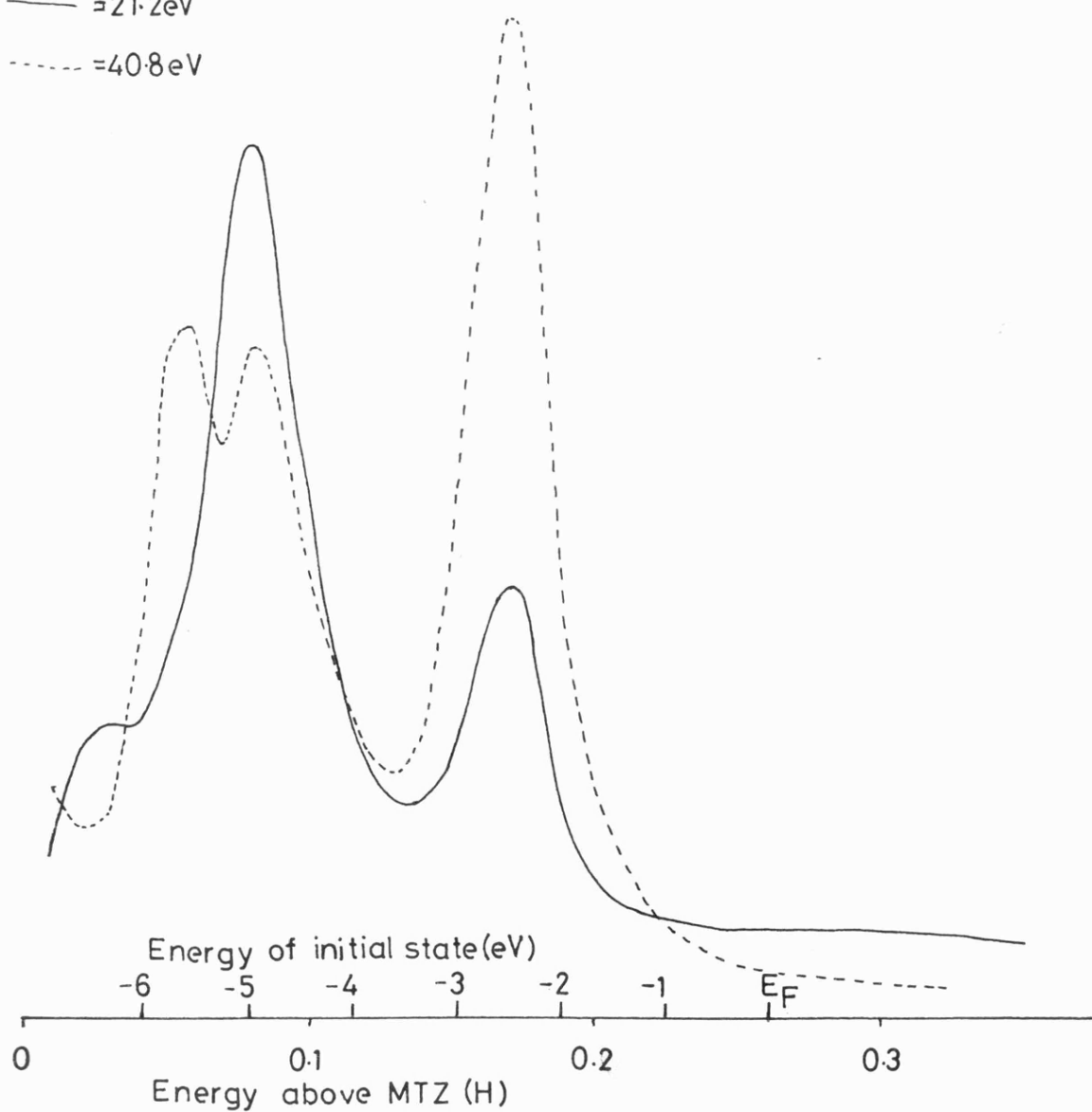


FIG. 7.9a

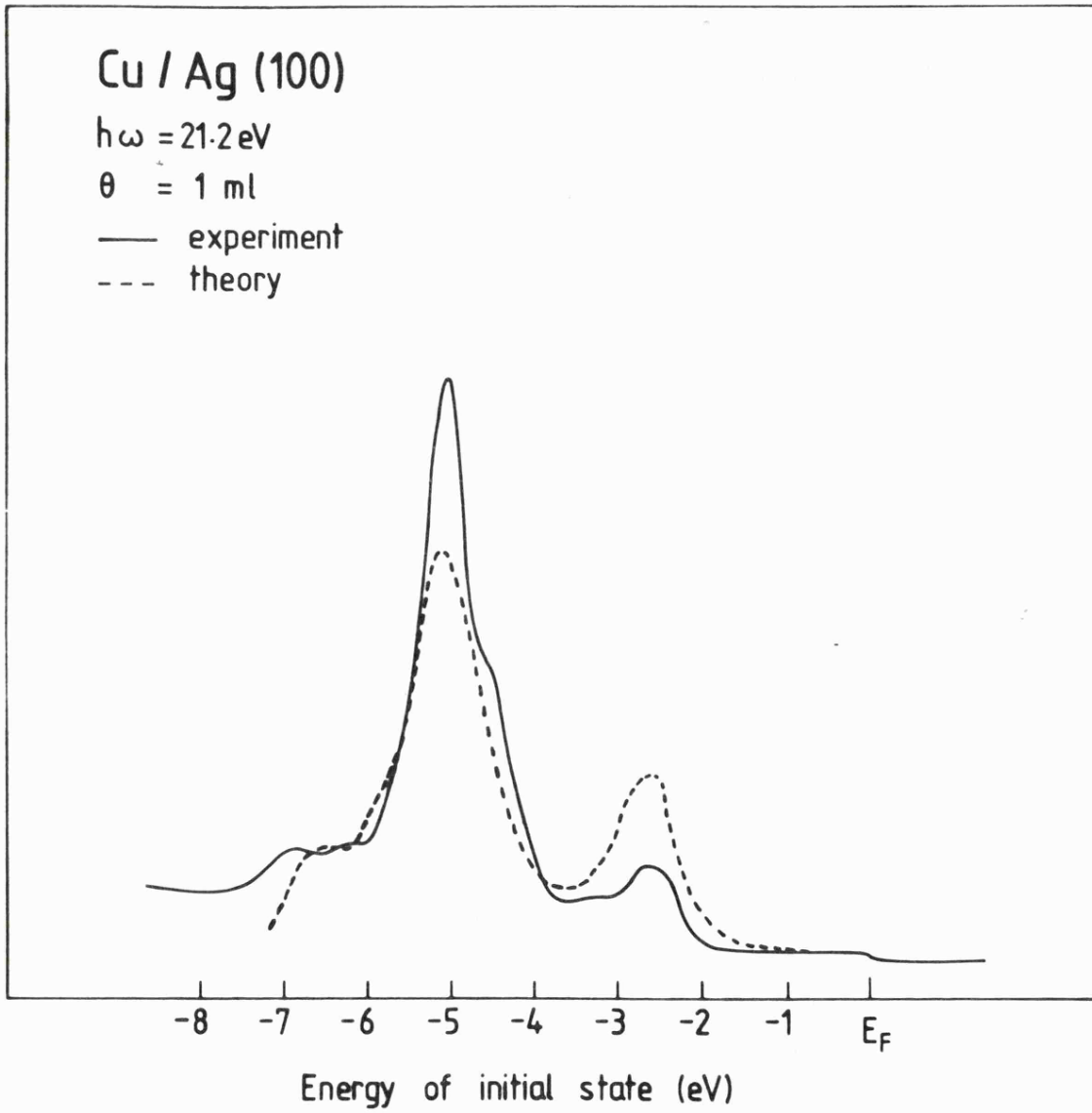


FIG. 7.9b

The effect of increasing the overlayer-substrate distance from 0.4 through 0.5 and 0.7 to 2.0 times a substrate lattice constant on the monolayer spectra was investigated. The results for normal emission using the modified potential are shown in figure 7.10. The figure shows that moving the copper layer both towards and away from the substrate relative to the 0.5 position results in movement of the emission towards the Fermi energy. Moving the atoms closer together (the 0.4 position) results in increased overlap between the wavefunctions on overlayer and substrate sites with a consequent reduction in binding energy, in accord with tight binding theory. In addition, a small increase in the width of the copper emission, as expected, may be detected in the $d = 0.4$ curve. In the spectrum calculated for the 2.0 position the monolayer is at the distance from the surface expected for the 4th layer in the ideal Frank-van der Merwe growth and its interaction with the substrate is very much reduced. The calculated copper emission in this spectrum is therefore representative of emission from a monolayer isolated in space with a 13% lattice expansion relative to the bulk. The 0.7 curve represents a state intermediate between the adsorbed and isolated monolayer. In the previous section (section 7.5) it was found necessary to apply a rigid shift of 1.2 eV to higher binding energies to a theoretical band structure to obtain energy agreement with the experimentally derived points in $E-k_{\parallel}$ space and this was attributed to a deepening of the monolayer potential due to the underlying layers, after Heimann et al (1981). The movement of the theoretical copper upwards in energy with increasing separation from the substrate is indicated to be a consequence of reduced interaction with the substrate potential.

The feature on the high binding energy side of the silver 4d emission peak has surface sensitive character. Figure 7.2 shows its

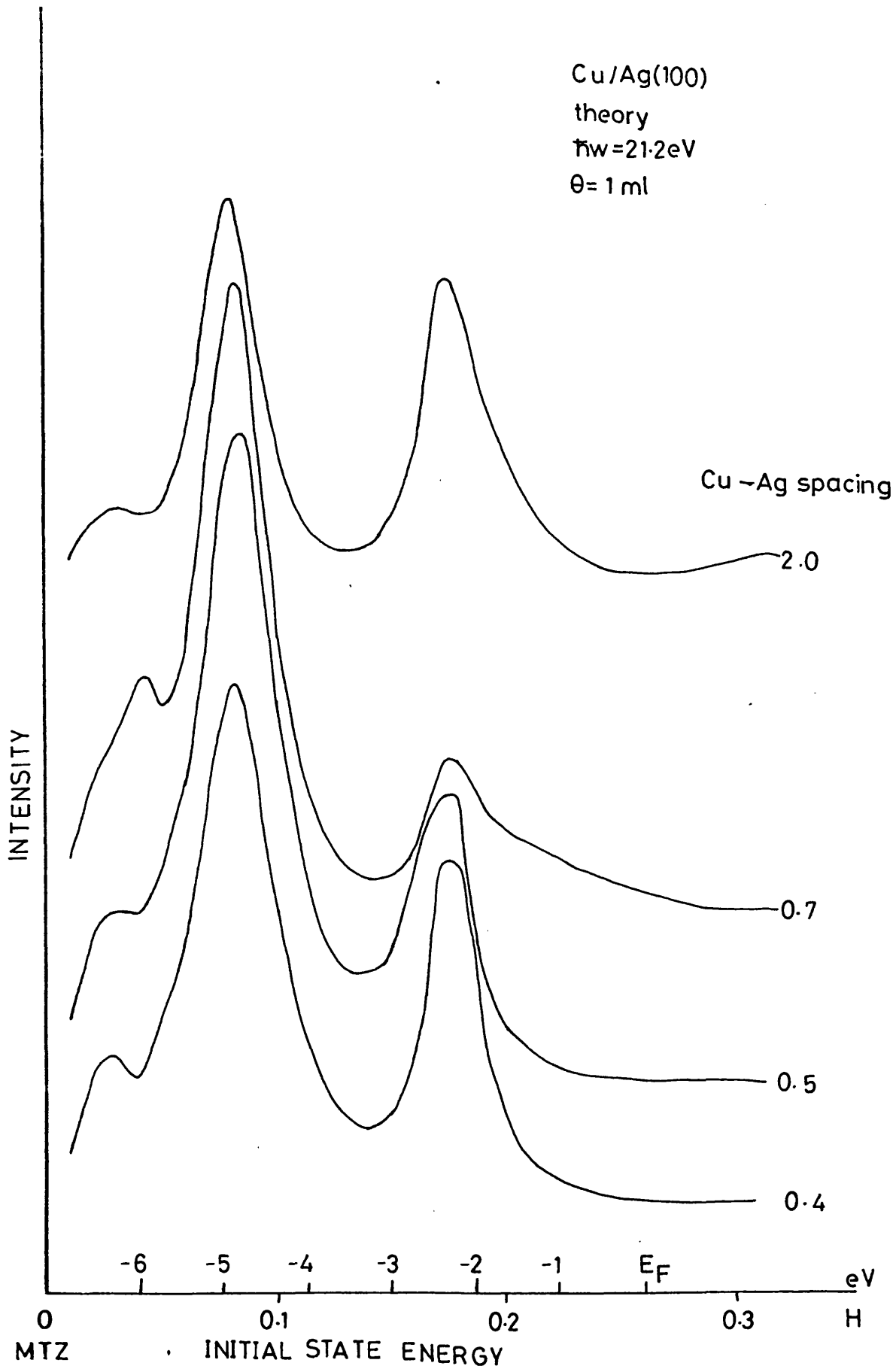


FIG. 7.10

rapid attenuation on increasing coverage up to one monolayer beyond which no further change is seen; this behaviour is typical of a surface resonance. The presence or absence of surface states or resonances is dependent upon the nature of the surface potential and geometry used in the calculation, which normally must be self-consistent, however, the monolayer behaviour is approximately reproduced in the 0.5 curve of figure 7.10. Movement of the overlayer to the 0.4 or 0.7 position reduces agreement with experiment, indicating that the distance of 0.5, corresponding to an unrelaxed epitaxial layer, is correct. The shape of this feature in the silver emission of the 2.0 curve is in agreement with the calculated spectrum for bulk silver (Chapter 4, figure 4.12) and confirms the view that at this distance the overlayer is effectively isolated from the substrate.

Agreement between PEOVER results and experimental spectra is evidence that both the experimental information on geometry and coverage, and the theoretical potentials, lifetimes and surface barriers, are correct. As such, this provides a determination of both the geometric and electronic structure of the system.

7.7 Discussion and Summary

LEED and Auger spectroscopy have been used to investigate the growth of copper overlayers on silver (100). The form of the As-t plot indicated that copper was initially adsorbed epitaxially, following a form of the Stranski-Krastanov growth mode in which the growth of two epitaxial monolayers was followed by disorder and island formation. This is consistent with recent measurements on iron overlayers on silver (100) (Smith et al 1982) and is a consequence primarily of the lattice expansion suffered by the first epitaxial monolayer.

Two approaches to the interpretation of angle-resolved photoemission data was taken, namely comparison of experimental spectra with the time-reversed LEED formalism of Pendry (1976) and comparison of experimental E vs k_{\parallel} points with the calculated isolated monolayer band structure (Arlinghaus et al 1979). It proved possible to simulate the experimental spectrum by calculations using the standard copper and silver potentials with an epitaxial overlayer geometry in which the copper overlayer was fixed at the position of the next silver (100) layer in an infinite crystal. After application of a rigid shift, equal in sign and magnitude to the difference between the bulk internal potentials, agreement in emission shape and energy position was obtained. This implies that charge transfer does not play a significant part and, within the muffin tin region, the bulk atomic potential may be used. Adjustment of the parameters of the calculation until good agreement between theory and experiment was reached provided confirmation of the geometry and electronic structure of the overlayer.

From the band-mapping point of view, it was found necessary to shift the theoretical band structure of the isolated copper monolayer and to broaden the experimental bandwidth according to tight binding theory before correspondence was obtained between theory and experiment. A detailed comparison between theoretical and experimental bands was not possible due to the finite resolution of the experiment but occupation of the predicted regions of E - k_{\parallel} space was indicated. This is further evidence of the minor role of substrate-overlayer interaction in these systems and is consistent with previous results on segregated CuNi (111) surfaces (Heimann et al 1981) and on palladium overlayers on silver (100) and (111) (Smith et al 1982).

Inspection of the layer terms in the PEOVER calculation of the photoemission from one monolayer of copper on silver (100) at 21.2 eV

showed that the peak at 0.08 H was 94% due to silver emission and the peak at 0.17 H was 81% due to emission from the surface barrier and the copper overlayer. The remaining 19% of emission contained in the copper-derived feature was due to the silver s-band which although not sharply structured may slightly modify the copper overlayer band structure.

The results at one monolayer were compared with a recent LCAO calculation of the DOS of one epitaxial pseudomorphic copper monolayer on silver (100) (Bisi and Calandra 1977). The shape of the difference spectrum was in fair agreement with theory, though the theoretical energy position of the first (copper) layer DOS maximum was in error by 2.68 eV. This was a result of charge transfer in the calculation, which was not observed either experimentally or in the photoemission calculations.

CHAPTER 8AN ELECTRON SPECTROSCOPIC STUDY OF IRON
OVERLAYERS ON SILVER (100)

- 8.1 Introduction
- 8.2 LEED and Auger Spectroscopy
- 8.3 Growth Mode
- 8.4 Work Function
- 8.5 Photoemission at 21.2 eV (HeI)
 - 8.5.1 Three Monolayer Coverage
 - 8.5.2 One Monolayer Coverage
- 8.6 Photoemission at 40.8 eV (HeII)
- 8.7 Photoemission Calculations
 - 8.7.1 Three Monolayer Coverage
 - 8.7.2 One Monolayer Coverage
- 8.8 Photoemission using Synchrotron Radiation
 - 8.8.1 The 3s Levels
 - 8.8.2 Valence Band Emission
- 8.9 Summary

CHAPTER 8AN ELECTRON SPECTROSCOPIC STUDY OF IRON
OVERLAYERS ON SILVER (100)8.1 Introduction

The electronic structure of iron has been the subject of much recent theoretical and experimental investigation (for example, Callaway and Wang 1977, Wang and Freeman 1980, Anderson et al 1977, Schulz et al 1979, Eastman et al 1981). Particular interest has been focussed on magnetic properties, including that of thin films and overlayers (Noffke and Fritsche 1981, Keune et al 1977, Bergmann 1981, Gradmann and Isbert 1980). To date, only one photoemission study of iron overlayers has been reported (Binns et al. 1982).

This chapter presents the results of an electron spectroscopic study of the growth and electronic structure of iron overlayers on silver (100). For bulk iron the fcc phase, with interatomic spacing 2.57 \AA , is observed only between 900 and 1400°C , below 900°C iron has a bcc crystal structure with an interatomic spacing of 2.48 \AA . Silver is fcc with an interatomic spacing of 2.89 \AA , which corresponds to a 14% lattice mismatch over bcc iron and 11% over fcc iron in the case of (100) oriented films. The LEED and Auger spectroscopy data are given in section 8.2 and the growth mode discussed in section 8.3. The change of work function on iron adsorption is described in section 8.4. Angle resolved photoelectron spectra were recorded for various iron coverages at photon energies of 21.2 eV (HeI) and 40.8 eV (HeII) and these are discussed in sections 8.5 and 8.6. Although the iron on silver system is not ideally suited to the PEOVER program, calculations of the photoemission spectra were made and are presented in section 8.7. Section 8.8 describes the results of photoemission measurements made using synchrotron radiation at 120 and

160 eV. The investigation is summarized in section 8.9. A more complete discussion of surface magnetism, incorporating the results of this and the subsequent chapter concerning nickel overlayers, is given in Chapter 9.

8.2 LEED and Auger Spectroscopy

The As-t plot for the deposition of iron onto silver (100) at room temperature is shown in figure 8.1. Three straight line sections are visible in the substrate signal decay and breaks occur at times t_1 , t_2 and t_3 . After time t_3 a slow monotonic decrease of substrate signal and increase of overlayer signal was observed. The Fe 47 eV peak is superposed on a steeply sloping secondary background which distorts the measured peak intensity at low coverages. It was therefore not possible to measure reliably the Fe signal until after time t_1 , but from then on it mirrored the Ag signal behaviour with changes in gradient discernable at times t_2 and t_3 .

During deposition the substrate p(1 x 1) LEED pattern persisted with clear, distinct spots until time t_2 . Between t_2 and t_3 a slight deterioration in the pattern was noted with a gradual rise in background intensity. After t_3 the p(1 x 1) pattern rapidly became indistinct and disappeared.

8.3 Growth Mode

The growth of iron on silver (100) at room temperature has been discussed by Smith et al (1982). The LEED and Auger results indicate that Fe adsorption on Ag (100) at room temperature proceeds via a layer-by-layer mode for the first three layers, with the breaks in the As-t plot (t_1 , t_2 and t_3) indicating completion of the first, second and third monolayers respectively. It can be seen from the plot that the time required for the third monolayer to form was slightly longer than that

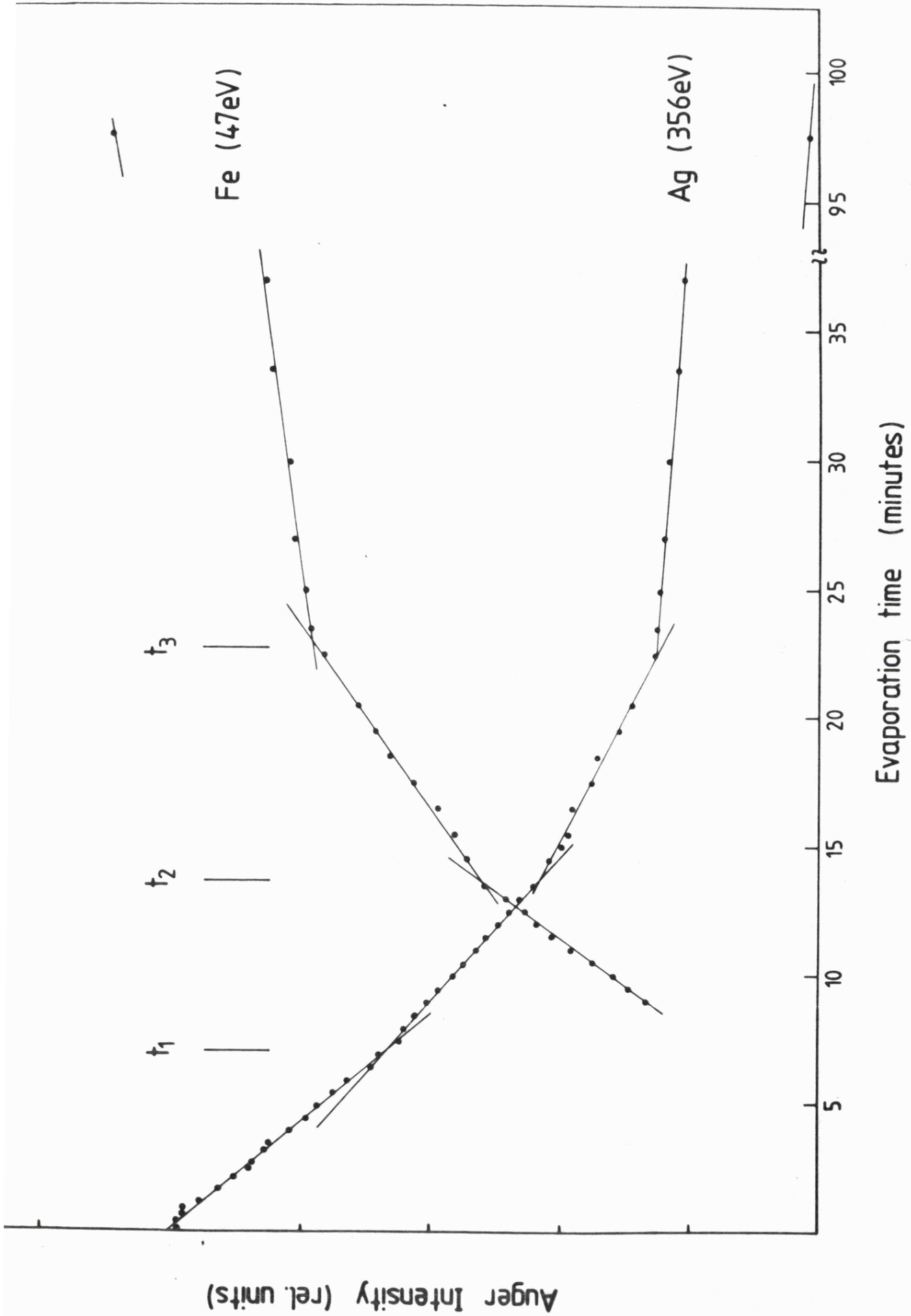


FIG. 8.1

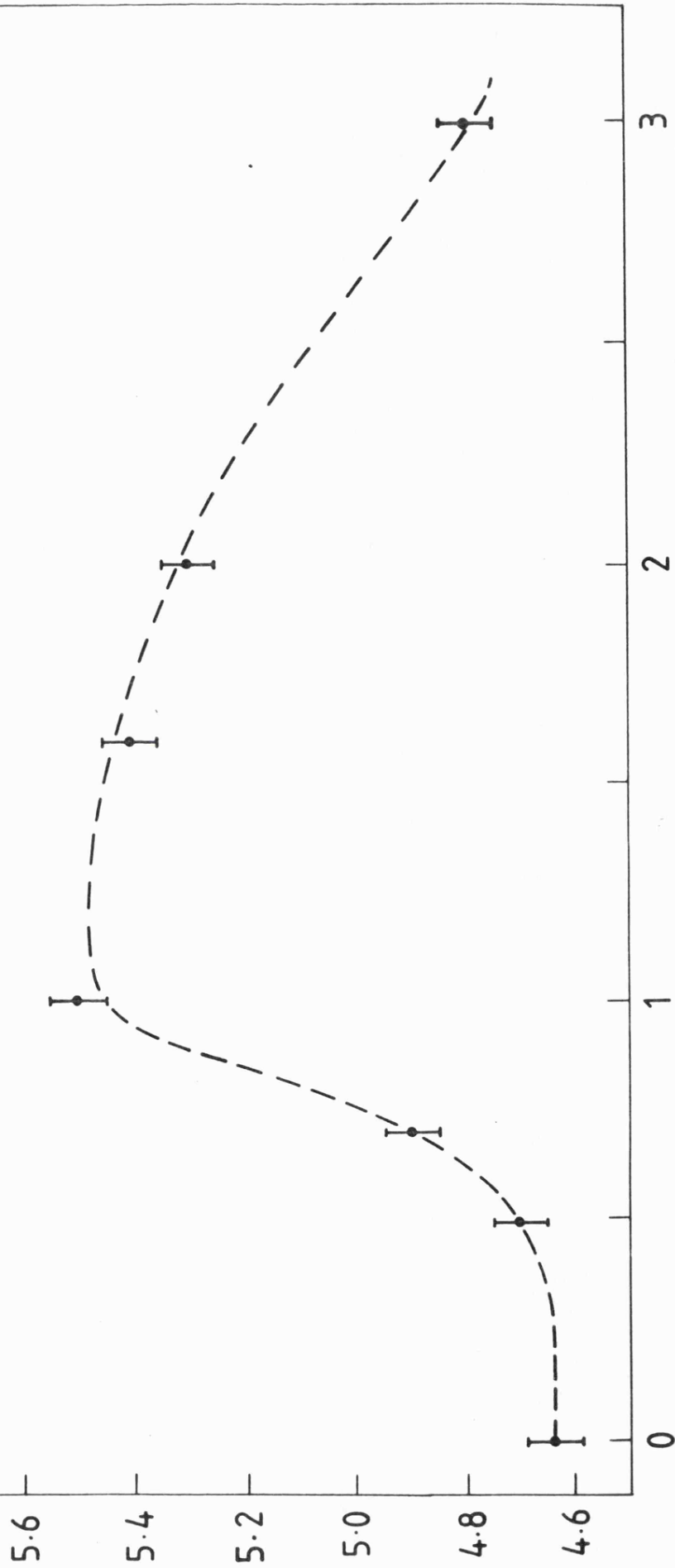
for the first and second monolayers. If we assume no change in sticking probability and a constant deposition rate this indicates denser packing in the third layer, corresponding to the reduced ordering observed in the LEED pattern between times t_2 and t_3 . The first two monolayers are in registry with the substrate but strain due to the 11% lattice expansion over that of bulk fcc Fe results in some relaxation in the third layer. This breakdown of periodicity causes subsequent depositions to follow disordered island growth. Thus growth appears to follow Frank-van der Merwe theory for three monolayers after which islanding occurs as in the Stranski-Krastanov model. The two epitaxial Fe layers plus the strained third layer correspond to fcc Fe with a lattice expansion of 12% over the high temperature bulk fcc allotrope.

This expansion of 12%, corresponding to a mismatch of 11%, is at the upper critical value in the Frank-van der Merwe theory of layer growth discussed in Chapter 2, so the formation of islands at some coverage is expected. The mode is very similar to that observed for copper overlayers on the same substrate (Chapter 7) where two monolayers were also formed before relaxation took place.

8.4 Work Function

During iron deposition the work function ϕ was obtained from the width of the normal emission 21.2 eV photoelectron spectrum shown plotted against coverage in figure 8.2. There is initially little variation from the clean substrate value of approximately 4.6 eV but after 0.3 monolayer coverage a rapid rise was observed, reaching a peak of 5.5 eV at one monolayer. As deposition proceeded the work function fell and at three monolayers the value of 4.8 eV is close to the values of between 4.6 and 4.8 eV reported in the literature for bulk Fe (Cardwell 1953, Kobayashi and Kato 1969, Ueda and Shimizu 1972).

Work function (eV)
FIG. 8.2



Fe coverage (monolayers)

Both the uniform positive background model of adsorbate-induced work function changes (Lang 1971) and the virtual level model (Newns 1969, Muscat and Newns 1974) discussed in Chapter 2 have been applied to alkali metal adsorption systems with some success. The theories predict charge transfer from overlayer to substrate resulting in an initial lowering of work function at low coverages with the bulk overlayer work function being reached at one monolayer coverage. This has been confirmed experimentally in a number of cases (Anderson and Jostell 1974, Broden and Bonzel 1970, Gerlach and Rhodin 1970). As the electronegativity of Fe is only slightly less than that of Ag (1.8 and 1.9 respectively) (Pauling 1960) similar but less dramatic behaviour may be expected in the present work but this is clearly not the case. The initial flat region of the curve up to $\frac{1}{4}$ monolayer indicates that charge transfer does not play an important role.

According to the Lang model (1971), at one monolayer coverage the work function of bulk overlayer material is obtained, so the present results predict a value of 5.5 eV for fcc Fe with a lattice constant of 2.39 \AA . As the coverage is increased the work function remained approximately constant up to two monolayers. Then as the third, distorted, monolayer was built up relaxation of the lattice commenced and the work function dropped. In this region there is increasing overlap between the electronic wave functions as the interatomic spacing reduces which leads to a higher electron density \bar{n} but the work function is found to decrease, in contrast to the prediction of the theoretical models. It should also be noted that an increase in surface roughness at this coverage due to the distorted third monolayer could cause the same effect (Lang and Kohn 1971). It is suggested that an improved model of work function change including the effects of s-d hybridisation

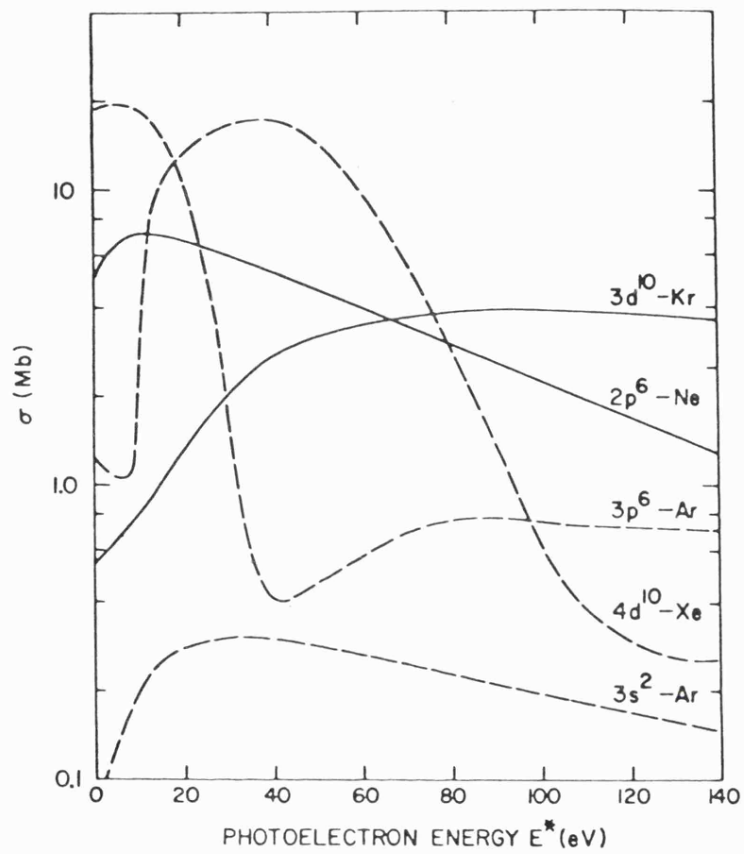


Figure 17.11 Calculated photoemission cross sections for the photoionization cross sections of outer shell electrons after Kennedy and Manson (1972)

FIG. 8.3

is required before results on transition metal overlayer systems, such as presented here, can be reliably interpreted.

The work function at a particular coverage was found to be an extremely sensitive measure of the quality of the overlayers. Reductions of ~ 0.1 eV due to contamination by the residual atmosphere of the vacuum chamber were detected on layers one hour old. In this work care was taken to obtain good vacuum conditions and this was found to be essential; on repeating the experiments at 10^{-9} mbar pressure a smoothly varying structureless As-t plot was recorded.

8.5 Photoemission at 21.2 eV

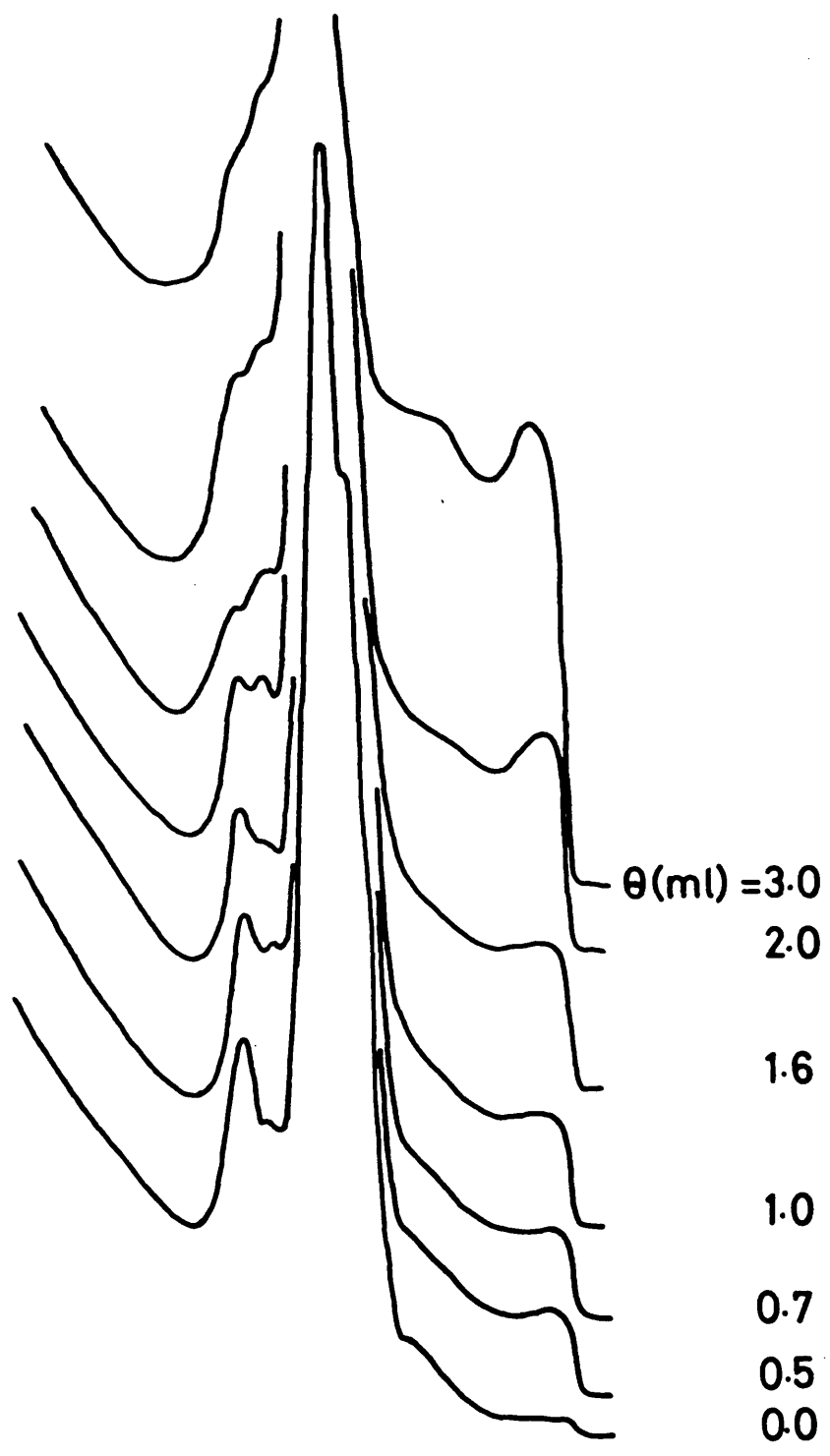
At the HeI photon energy of 21.22 eV the cross-section for photoionization of 3d electrons is an order of magnitude below that for 4d electrons, as shown in figure 8.3 (Kennedy and Manson 1972). At this energy therefore the photoemission was dominated by the substrate signal with features in the overlayer emission being difficult to discern. Nevertheless, in view of the existence of published 21.2 eV spectra for bulk iron (for example Pessa et al 1976, Schulz et al 1979) and the current interest in the electronic structure of iron monolayers (Noffke and Fritsche 1981, Calloway and Wang 1977) it was felt worthwhile pursuing this line of investigation. The measurements are also relevant to the recent surface magnetism measurements of Gradmann and Isbert (1980), Bergmann (1981) and to the "dead layers" controversy (Walker et al 1972, Leiberman et al 1969) which is discussed further in the following chapter.

Angle resolved spectra were taken in normal emission for coverages of between 0 and 3 monolayers and off normal spectra in the two principal symmetry axes of the substrate were recorded at a coverage of one monolayer. The normal emission spectra are shown in figure 8.4 and

Fe/Ag(100)

hw=21.2eV

normal emission



-13 -12 -11 -10 -9 -8 -7 -6 -5 -4 -3 -2 -1 E_F

Initial State Energy (eV)

FIG. 8.4

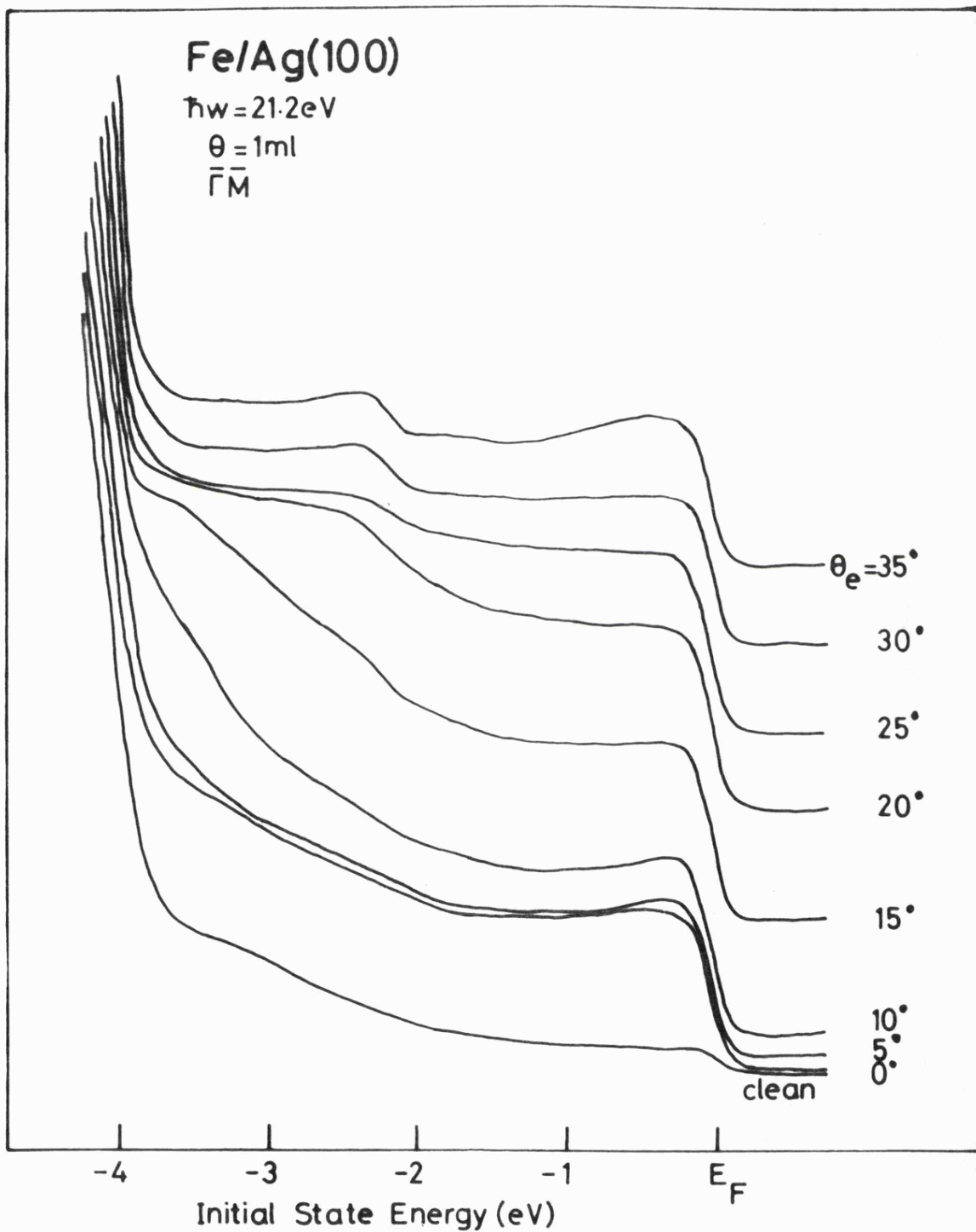


FIG. 8.5a

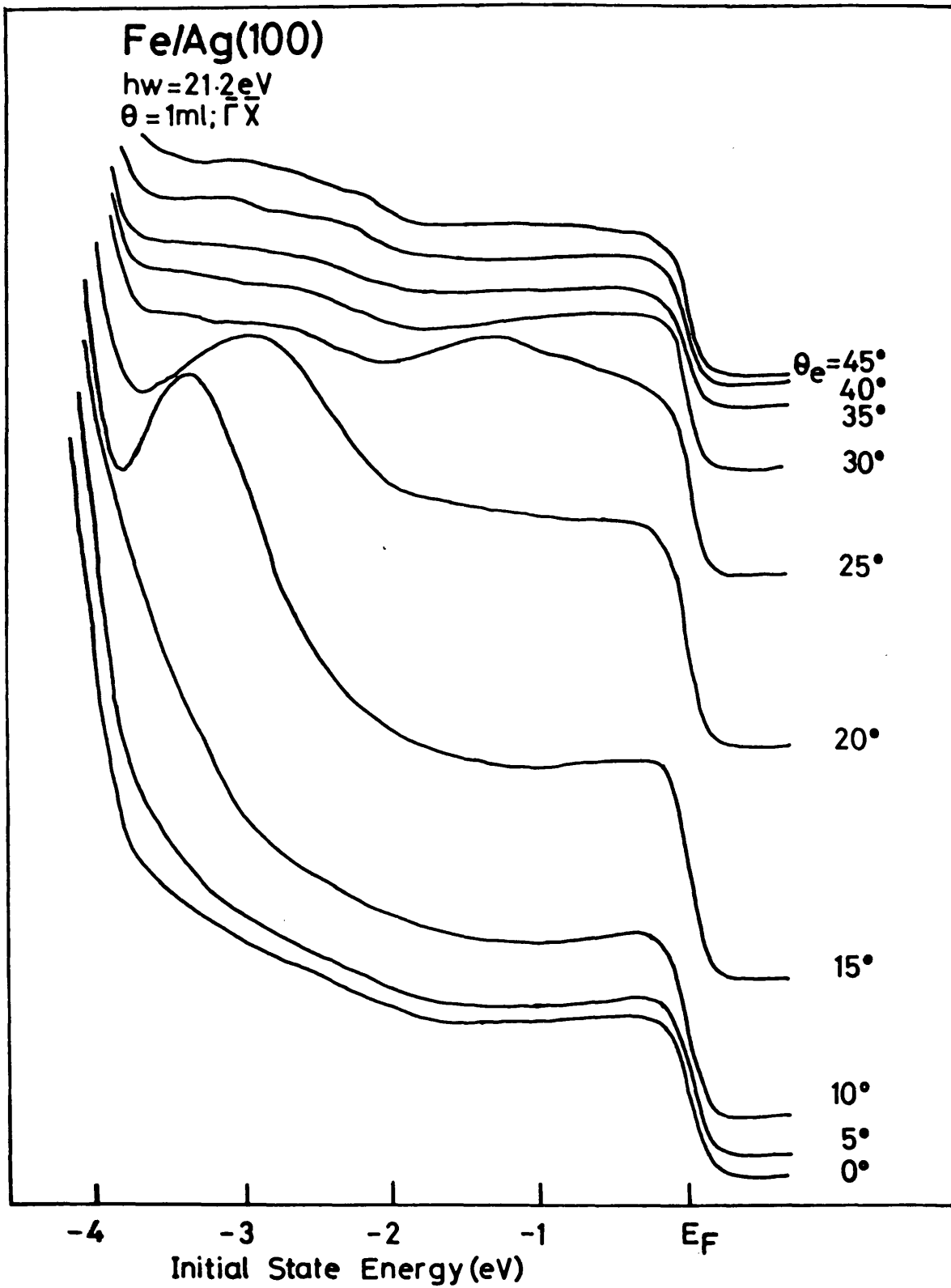


FIG. 8.5b

the off normal spectra in figure 8.5. In each case the vertical scale is grossly exaggerated in order to bring features in the iron emission into view, and the main silver peak at -4.9 eV has been omitted from the diagrams for clarity. The spectra in normal emission show a smooth progression from the clean surface with a feature developing near E_F and an increase in the emission superposed on the silver s-band from 0 to -4 eV. The spectra recorded at coverages of 3 and 1 monolayers are discussed in subsections 8.5.1 and 8.5.2 respectively.

Exaggeration of the vertical scale in figure 8.4 results in enhancement of the detailed structure to the left (high binding energy) side of the main silver 4d emission peak. Two features are seen, at -6.90 eV and -6.36 eV and these were interpreted in Chapter 4 as due to a direct transition from the lower s-like band and a DOS feature from the Γ_{8+} point respectively. On increasing coverage a progressive preferential attenuation of the direct transition feature is observed. Examination of the copper and palladium on silver (100) data (Chapters 7 and 5) also reveals the effect. This preferential attenuation raises speculation on the nature of the -6.90 eV peak since other features in copper (100) and silver (100) which exhibit particular sensitivity to adsorption have been associated with surface resonances. There is continued controversy over the location of the surface resonance running in the d-bands of the silver (100) SBZ (see Chapter 4) and the present evidence may be an indication of its position. Further discussion is given in Chapter 10.

8.5.1 Three Monolayer Coverage

The 21.2 eV difference spectrum for the normal-emission curve of clean silver (100) and 3 monolayers of iron on silver (100) is shown in figure 8.6. Below -4 eV the steeply sloping silver (100) d-band

— = 3 ml Fe/Ag(100), 21.2eV difference curve
- - - = Bulk Fe(100) at 21.2eV (Schulz et al 1979)

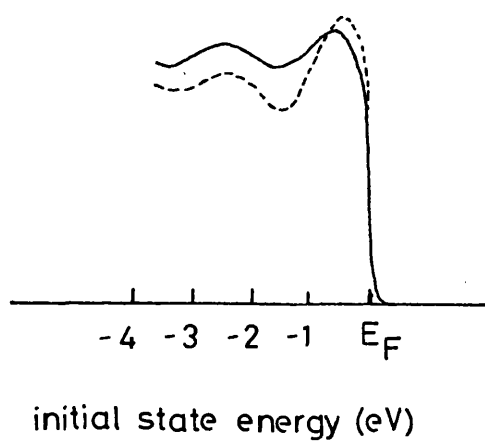


FIG. 8.6

emission made subtraction difficult so no points beyond this energy are recorded. Two distinct features are observed in the difference curve, at -0.64 eV and -2.50 eV and the shape of the difference curve is similar to the spectrum obtained from bulk Fe (100) at 21.2 eV by Schulz et al (1979). It should be emphasized that the results of Schulz and co-workers were obtained from bulk bcc iron at room temperature, which has a different crystal structure to the expanded fcc overlayer under discussion. The workers, however, found that the photoemission spectra from the (100), (110) and (111) surfaces of bulk iron at both 21.2 eV and 40.8 eV are very similar and were in close correspondence to earlier measurements on polycrystalline iron films (Pessa et al 1976). Generally the recorded spectral features could not be assigned to direct transitions from the calculated initial state bands of Tawil and Callaway (1973). They concluded that the spectra from iron reflected the one dimensional density of states.

Further evidence is given by the present 3 monolayer curve which shows features corresponding to bulk iron even though the crystal structure is different. Callaway and Wang (1977) have provided the combined spin-up and spin-down density of states for ferromagnetic iron. Their results show prominent features at 0.7 and 2.8 eV below E_F , at approximately the same energies as the structure observed in the 3 monolayer difference spectrum. This also implies the spectra are providing a measurement of the DOS. The results of the various photoemission measurements and calculations discussed above are summarized in figure 8.7, together with the present experimental results.

Thus, it appears that while the noble metals copper, silver and palladium, considered so far in this thesis, may be adequately described by direct transitions from calculated initial states with indirect

Photoemission from Iron

Source	$\hbar\omega$ (eV)	Binding Energies (eV)	
3-nl Fe/Ag(100) (present work)	21.2	$.64 \pm .06$	$2.50 \pm .1$
	40.8	$.46 \pm .07$	$2.60 \pm .1$
	120	$.69 \pm .08$	$2.52 \pm .15$
Polycrystalline Fe (Pessa et al 1976)	21.2	$.58 \pm .03$	$2.4 \pm .2$
	16.8	$.60 \pm .07$	$2.6 \pm .2$
Fe (100)	21.2	$.48 \pm .05$	$2.3 \pm .1$
	40.8	$.57 \pm .05$	$2.3 \pm .1$
Fe (110)	21.2	$.43 \pm .05$	$2.5 \pm .1$
	40.8	$.44 \pm .05$	$2.3 \pm .1$
Fe (111) (Schulz et al 1979)	21.2	$.68 \pm .05$	$2.6 \pm .1$
	40.8	$.72 \pm .05$	$2.4 \pm .1$
Ferromagnetic Fe DOS (Callaway & Wang 1977)		.74	2.8

Figure 8.7

transitions playing a minor role, DOS effects dominate in the case of iron at this photon energy. For direct transitions to be observed the broadening of the component of wave-vector normal to the surface, Δk_{\perp} , must be much less than the dimensions of the BZ. One contribution to Δk_{\perp} is the electron mean free path (final state lifetime) λ , $\Delta k_{\perp} \sim 1/\lambda$, however, photoemission from nickel, with λ approximately the same as in iron, has been successfully interpreted in terms of direct transitions. In iron the contribution to \underline{k} -broadening due to the hole lifetime is longer than in the noble metals (Hochst et al 1976) and also than in nickel (Hochst et al 1977, Pendry 1978). Thus the hole lifetime of the order of 1 eV in iron causes effective wave-vector broadening and results in the breakdown of the \underline{k} -selection rule.

An alternative interpretation of photoemission from bulk iron, in which structure in the photoelectron spectra is seen as originating from direct \underline{k} -conserving transitions has been used by several workers (Eastman et al 1980, Turner and Erskine 1982). These experiments have generally been performed along carefully selected lines of the BZ and using the polarization properties of synchrotron radiation to select emission from the required initial states.

8.5.2 One Monolayer Coverage

The off-normal photoelectron spectra recorded at 21.2 eV for one monolayer of iron on silver (100) are shown in figures 8.5a and 8.5b. For clarity the silver 4d emission below -4 eV has been omitted from the diagrams to enable the iron emission to be shown on an enhanced vertical (photoemitted intensity) scale. Comparison with the curves recorded for clean silver (100) (Chapter 4, figure 4.13) shows that the angular variation seen in the spectra is dominated by the HeI- β satellite of the silver d-bands, and the variations in the silver s-band emission. The iron contribution to the spectra is in the form of an increased

Fe MONOLAYER

----- majority spin

———— minority spin

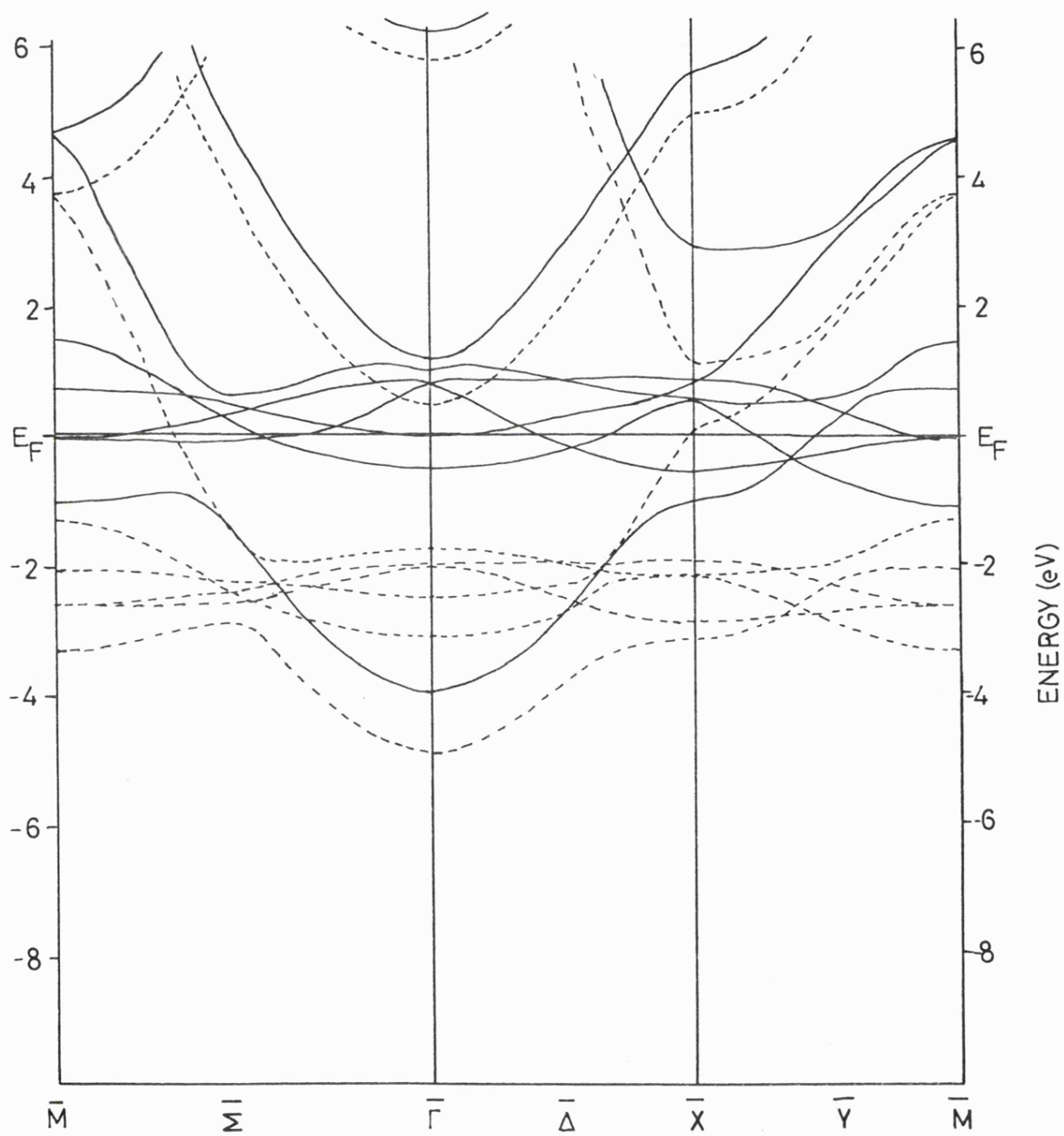


FIG. 8.8

emission near the Fermi level and a relatively smooth feature superposed on the silver s-band emission. The results of a recent Linear Rigorous Cellular (LRC) calculation of the spin-split energy bands of a (100) iron monolayer are shown in figure 8.8 (J.Noffke, private communication 1981). A large number of rapidly dispersing majority and minority spin bands are contained in the region 0 to -4 eV and are often separated by energies less than the resolution of the present experiment. The normal emission difference curve is shown in figure 8.9, along with predicted peak positions using the theoretical energy band positions at the $\bar{\Gamma}$ point. The single spin-down band at ~ -0.5 eV and the four spin-up bands between -1.9 eV and -3.2 eV correspond to the observed emission although an accurate assignment of peak positions to the theoretical energy bands does not seem possible. Indeed, it was shown in the previous section that photoemission from iron is dominated by the density of states. An additional factor must be the lattice expansion of the experimental supported monolayer. For copper overlayers on silver (100) (Chapter 7) an attempt was made to correct for this by adjustment of the bandwidth but in the case of iron overlayers the d-band lies across the Fermi energy and as such is not measurable in the experiment. In the case of nickel overlayers (Chapter 9) calculations for both natural and 10% expanded monolayers were available from which the bandwidth dependence could be checked. Thus, it does not seem possible to map the two-dimensional band structure of iron overlayers using angle-resolved photoemission at 21.2 eV, unlike the case of palladium and copper monolayers.

8.6 Photoemission at 40.8 eV

The theoretical cross-section data reproduced in figure 8.3 predict an increase in the intensity of 3d emission relative to emission from 4d levels on changing the photon energy from 21.2 eV (HeI) to 40.8 eV

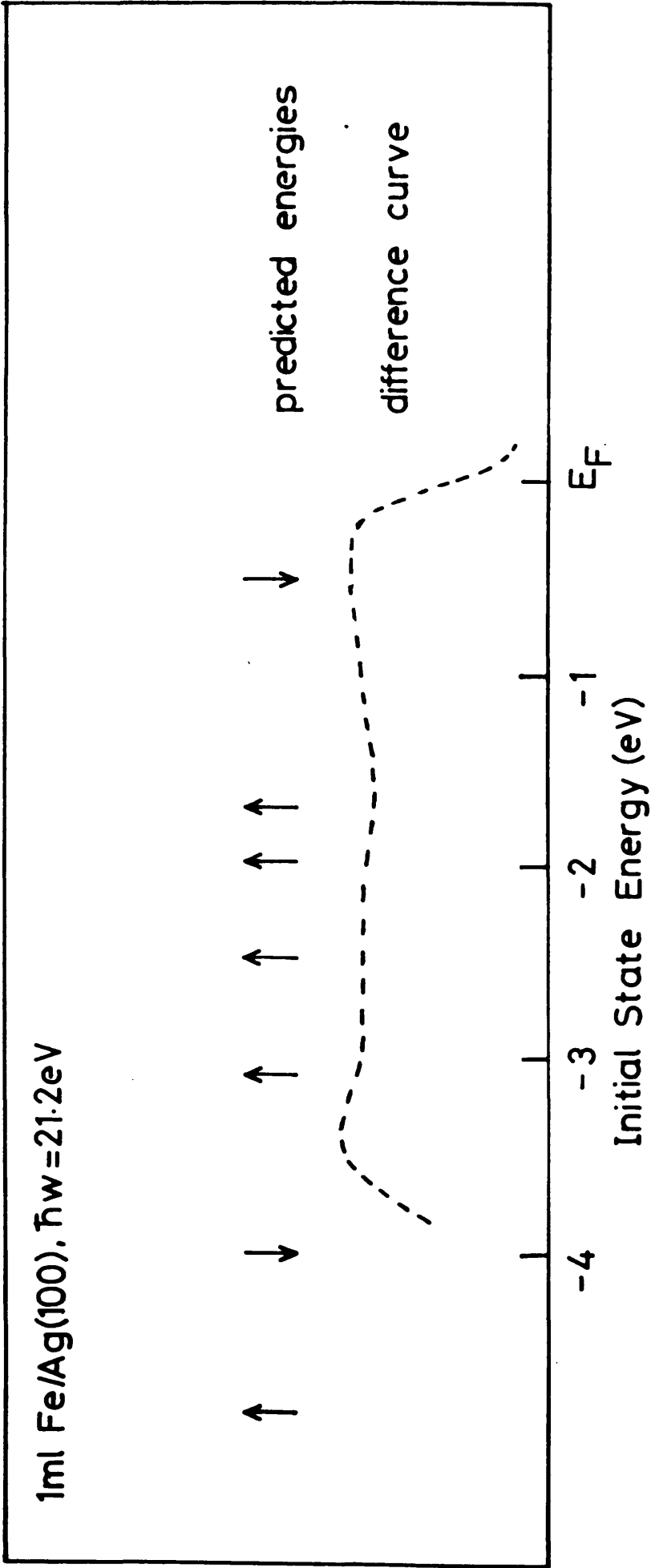


FIG. 8.9

(HeII). Measurements were made on iron overlayers on silver (100) using the HeII resonance line in order to exploit the advantageous cross section at this energy. Figure 8.10 shows the clean substrate normal emission spectrum together with those for coverages of one and three iron monolayers at 40.8 eV. Also shown are the corresponding difference curves. Although the cross-section at this energy was more favourable the intensity of He-II radiation obtained from the discharge lamp was two orders of magnitude below that for HeI and resulted in a reduced signal to noise ratio for the 40.8 eV spectra.

The spectrum for three monolayers of iron on silver (100) is very similar to that obtained at 21.2 eV; the peak positions are as given in figure 8.7. In their study of photoemission from the crystal faces of bulk iron Schulz et al (1979) obtained similar spectra from the (100), (110) and (111) faces at 21.2 eV and 40.8 eV, as discussed previously. The similarity between the HeI and HeII spectra from three monolayers of iron adsorbed on silver (100) is further evidence for the interpretation of photoemission from iron in terms of the density of states, as proposed by Schulz et al, rather than by direct transitions.

Features in the one monolayer spectrum are rather difficult to discern. The overall effect of increased emission near the Fermi level and over the silver s-band region is similar to that seen at 21.2 eV.

8.7 Photoemission Calculations

The calculation of photoelectron spectra using the PEOVER program for iron overlayers on silver presents additional complications compared to copper and palladium overlayers. The constant initial and final state lifetime approximation has been discussed in previous chapters; in the case of iron and silver whose initial state lifetimes are different this becomes severe as only one lifetime may be specified for all the layers of the calculation. The internal potentials, U_0 , of bulk iron

Fe/Ag(100)
 $h\nu = 40.8\text{eV}$
normal emission

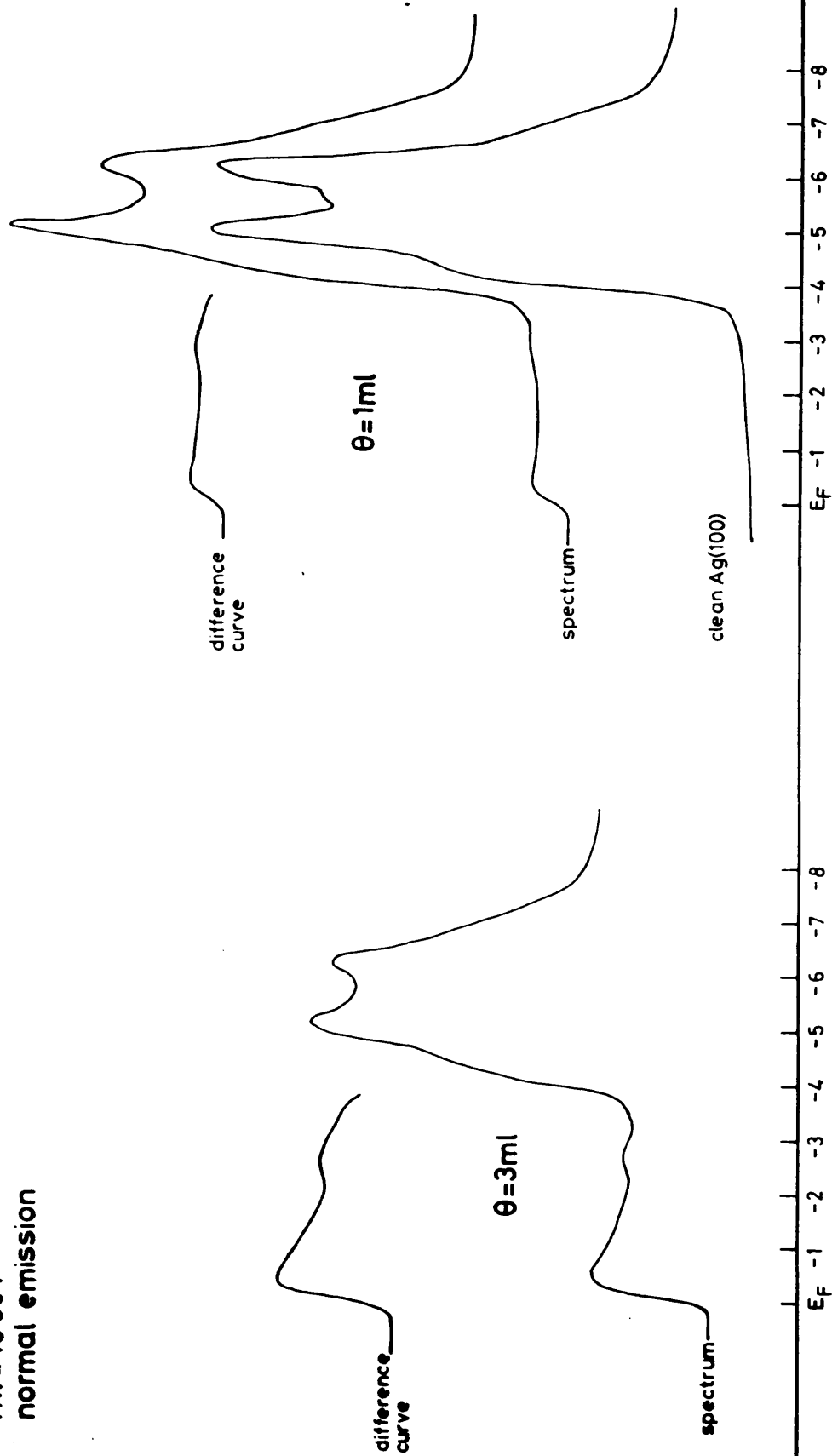


FIG. 8.10

(0.58H) and silver (0.42H) differ by rather more than in the case of copper on silver, where a rigid shift of the copper potential by an energy equal to this difference was found to bring theory and experiment into agreement. The significant change in work function, a component of U_0 , on iron adsorption is a complicating factor and it is not clear how to compensate for this. If the work function change is a result of charge transfer sufficiently large to modify the shape of the overlayer potential within the muffin-tin region then the non-self-consistent approach of PEOVER will fail.

The most serious difficulty, however, is ferromagnetism, which must occur at some coverage of iron. The calculation does not include exchange splitting so any spectral structure resulting from ferromagnetism cannot be reproduced in the theory.

8.7.1 Three Monolayer Coverage

The first three monolayers of iron adsorbed on silver (100) take the crystal structure of the underlying substrate lattice and hence correspond to fcc iron with a 12% lattice expansion over the natural fcc allotrope formed between 900°C and 1400°C. It is difficult to estimate the effect of this change of structure and lattice parameter on the energy bands and magnetic properties of iron. Calculations for iron overlayers on silver using PEOVER are also problematic, as discussed above, so an attempt to understand the photoemission from three adsorbed layers of iron on silver was made through calculations for bulk fcc iron expanded to the silver lattice constant. It has already been noted (section 8.5) that the difference spectrum at this coverage strongly resembles spectra taken from bulk ferromagnetic iron samples.

The potential used was that of Moruzzi et al (1978) which was interpolated onto the Hermann-Skillman grid required by PEOVER. A hole lifetime of 0.02H, somewhat smaller than the value of ~ 1 eV (.037H)

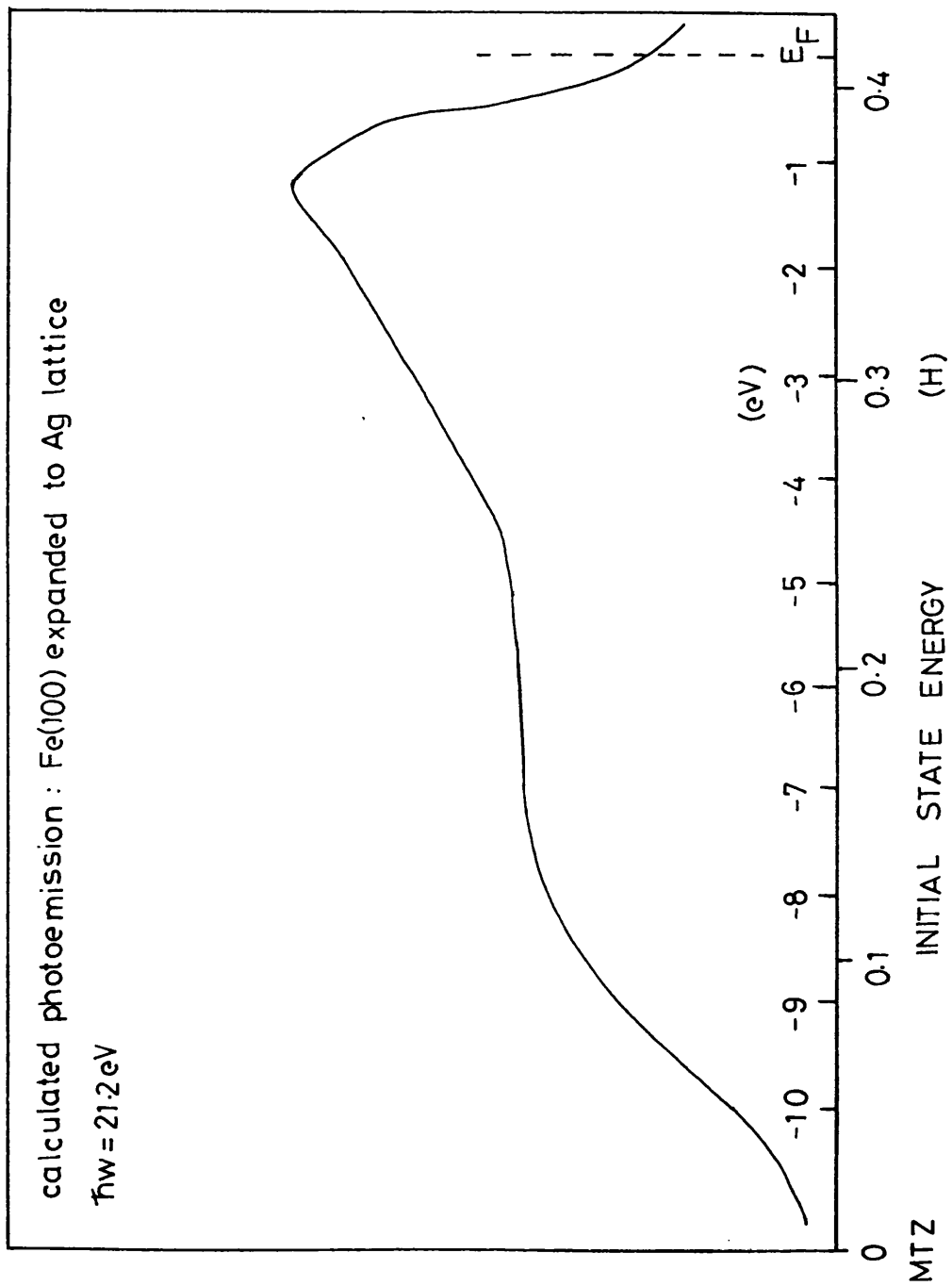


FIG. 8.11

suggested by Schulz et al (1979), gave the best agreement between theory and experiment and was the value taken in all the calculated spectra shown in this section. The step at the surface-vacuum interface of height $0.58H$ was taken as lying at the outer muffin-tin radius of the surface layer. Spectra were rather insensitive to this position.

The calculated normal emission spectrum for the expanded fcc iron at 21.2 eV is shown in figure 8.11. Subtraction of the estimated work function of 4.7 eV from the internal potential gave the position of the Fermi energy as $0.41H$ above the MTZ. The principal feature of this spectrum is a strong asymmetric peak centred 1.2 eV below E_F with a featureless background at higher binding energies and a sharp drop in intensity at E_F . This corresponds to expanded fcc iron in a non-ferromagnetic state. The experimental curve (figure 8.6) shows two clearly defined peaks whereas the non-ferromagnetic calculated spectrum shows only one. Thus the non exchange split calculation, giving a single peak, does not reproduce the experimental data. The experimental double peak may therefore be associated with ferromagnetism, with the two features arising from the exchange split minority and majority spin partial densities of states. This result indicates that the three monolayers of iron adsorbed onto silver (100) with the fcc lattice of the substrate are ferromagnetic with an exchange splitting of 1.9 eV, the separation of the two features in the experimental curve.

Calculations were attempted for three epitaxial layers of iron adsorbed on silver, but severe attenuation of the substrate signal was found and realistic results not obtained. From the layer terms of the calculated photocurrent it was determined that 96% of the theoretical emission was due to the first three (iron) layers of the model crystal. The difficulties of realistically modelling photoemission from iron overlayers on silver were discussed above, and the approach was not continued at this coverage.

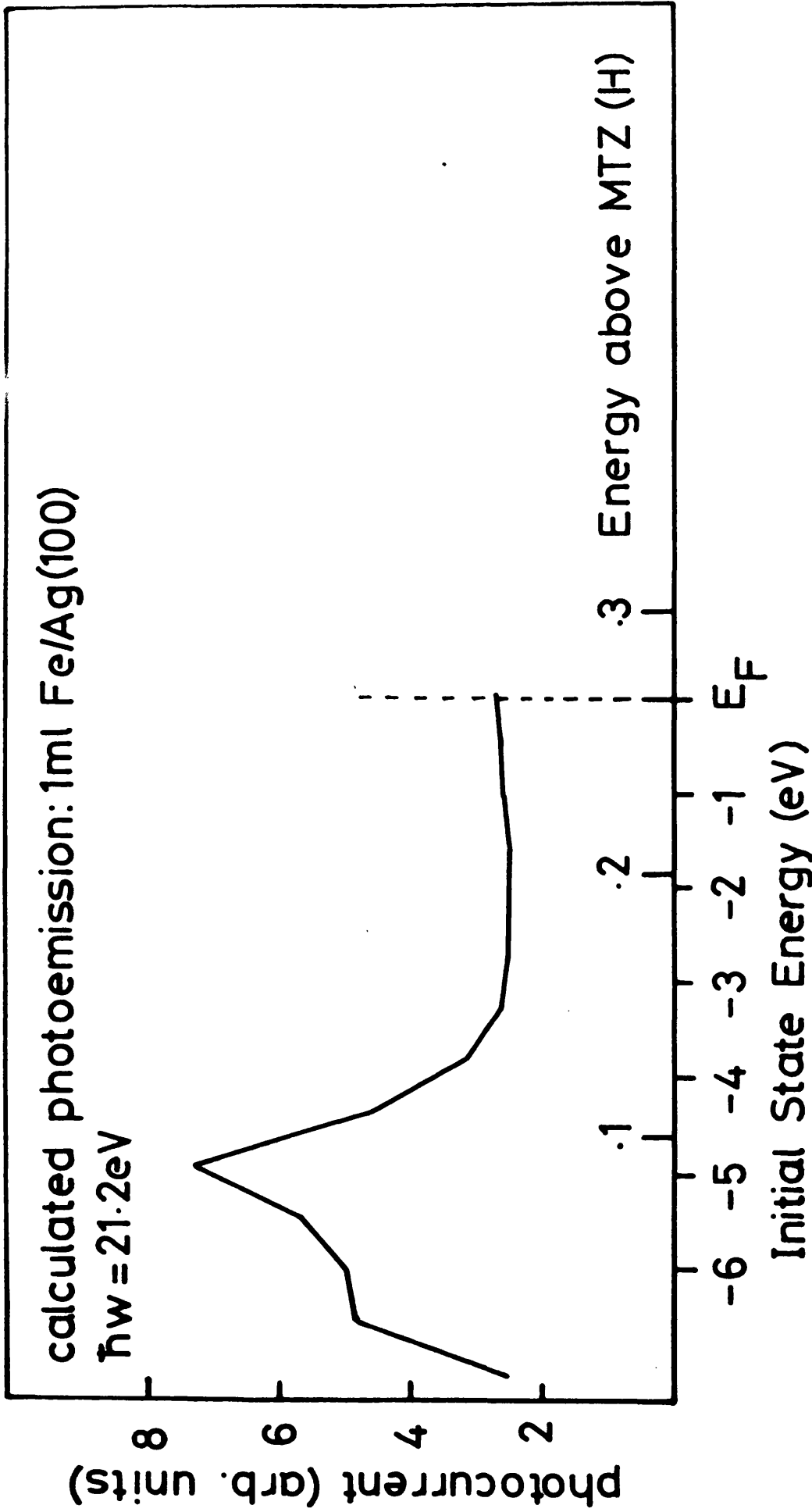


FIG. 8.12

8.7.2 One Monolayer Coverage

The calculated normal emission photoelectron spectrum for one iron overlayer on silver (100) at 21.2 eV is shown in figure 8.12. The iron potential was rigidly shifted by 0.15H to higher binding energy to compensate for the difference in internal potential between overlayer and substrate. Electron and hole lifetimes of 0.10H and 0.01H respectively, appropriate to the silver substrate, were used and the silver potential and geometry were as described in previous chapters. Compared to the clean silver spectrum (Chapter 4, figure 4.12) the effect of iron adsorption is to attenuate and change the shape of the substrate emission and to increase emission over the region occupied by the silver s-band in the clean substrate spectrum. Apart from over-attenuation of the substrate emission the spectrum is in approximate agreement with experiment. The flat iron emission between 0.14H (~ -4 eV) and E_F is similar to that seen in the experimental curve. As both theory and experiment are rather featureless a comparison is difficult to make and the magnetic state of this overlayer was not investigated.

8.8 Photoemission using Synchrotron Radiation

Synchrotron radiation from the Daresbury SRS was used to extend the study of photoemission from iron overlayers on silver (100) into the higher energy region available with this light source. Spectra were taken in normal emission using 120 eV light to stimulate valence band emission and 160 eV light to follow the behaviour of the iron 3s and silver 4s core levels during overlayer growth. A photon energy of 120 eV was chosen for the valence band spectra because at this energy the silver 4d emission passes through the Cooper minimum whereas the iron 3d emission intensity is still high and therefore dominates the spectra (figure 8.3). The iron 3s and silver 4s core levels appear at binding energies between 90 and 100 eV. As subtraction of the background

was necessary to obtain the line shapes it was desirable that these levels appeared at relatively high kinetic energies where the background was not rapidly varying. It was also necessary to avoid overlap with the iron Auger line at 47 eV kinetic energy. The photon energy of 160 eV was chosen as a suitable compromise, taking into account the output function of the monochromator at these energies.

Spectra showing the core level and valence band regions are discussed separately in sections 8.8.1 and 8.8.2 below.

8.8.1 The 3s Levels

Spectra taken in normal emission for various coverages of iron on silver (100) at 160 eV photon energy over the binding energy range 85 to 105 eV are shown in figure 8.13. The data are unsmoothed and are normalised to the secondary background. The dominant feature at zero coverage is the silver 4s emission, centred at a binding energy of approximately 96.5 eV. On deposition of iron this feature is rapidly attenuated and a peak due to iron 3s emission centred around 90.5 eV builds up in intensity, equalling the silver 4s intensity at one monolayer coverage and dominating the spectrum thereafter. This behaviour is shown more clearly in figure 8.14, in which the smoothly varying secondary background has been subtracted from the curves of figure 8.13. It can be seen from figure 8.14 that there is significant overlap between the iron 3s and silver 4s peaks and to obtain information concerning the iron 3s line shape it was necessary to subtract from each curve the contribution to the emission from the silver 4s level (curve 0 in figure 8.14) after allowing for attenuation by the overlayer. The results of this subtraction are shown in figure 8.15. Although there is some noise in the curves of figure 8.15 a satellite of the iron 3s line can be clearly seen at coverages above one monolayer. There is also some evidence for its

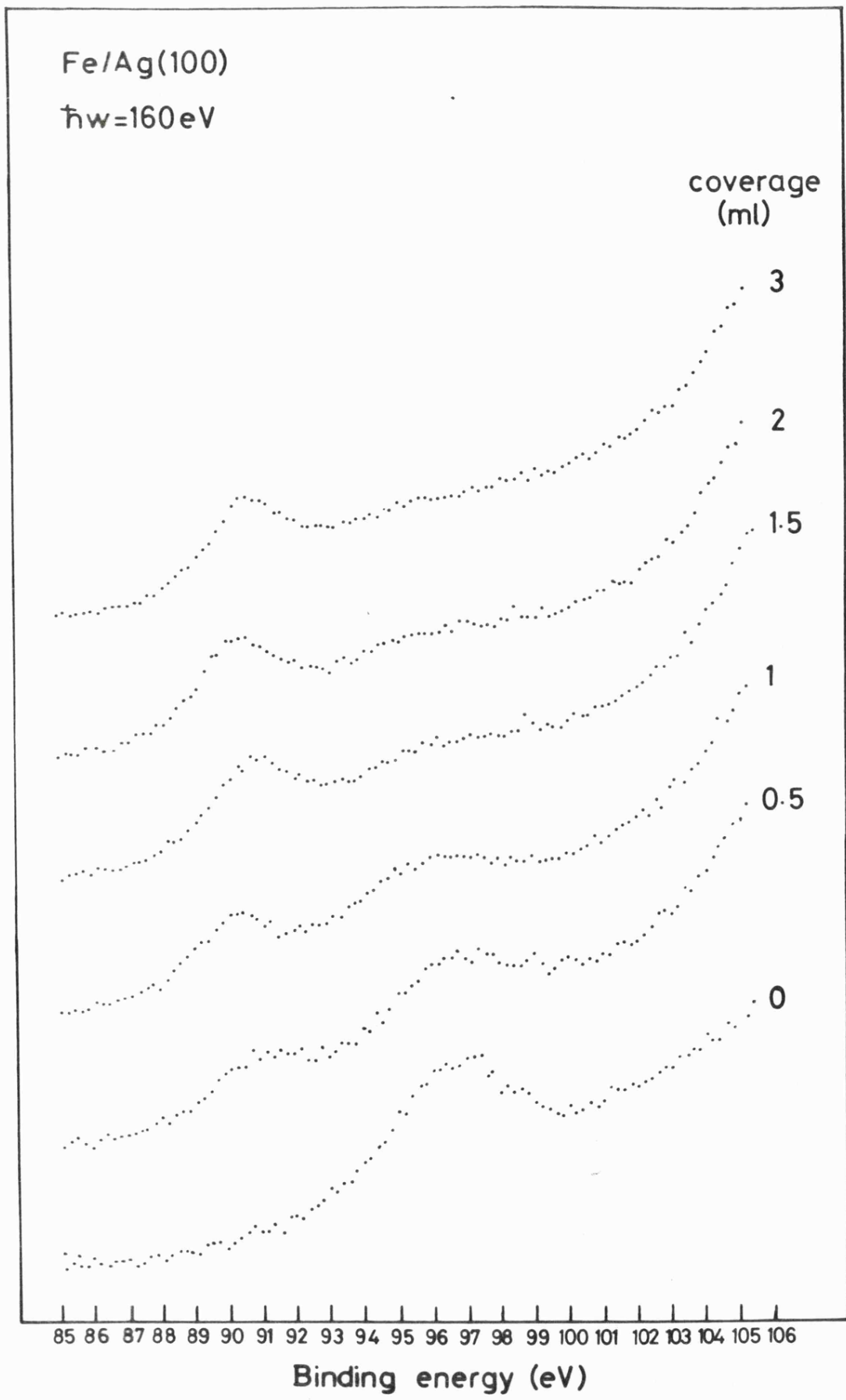


FIG. 8.13

Fe/Ag(100)

$\hbar\omega=160\text{eV}$

secondary background subtracted

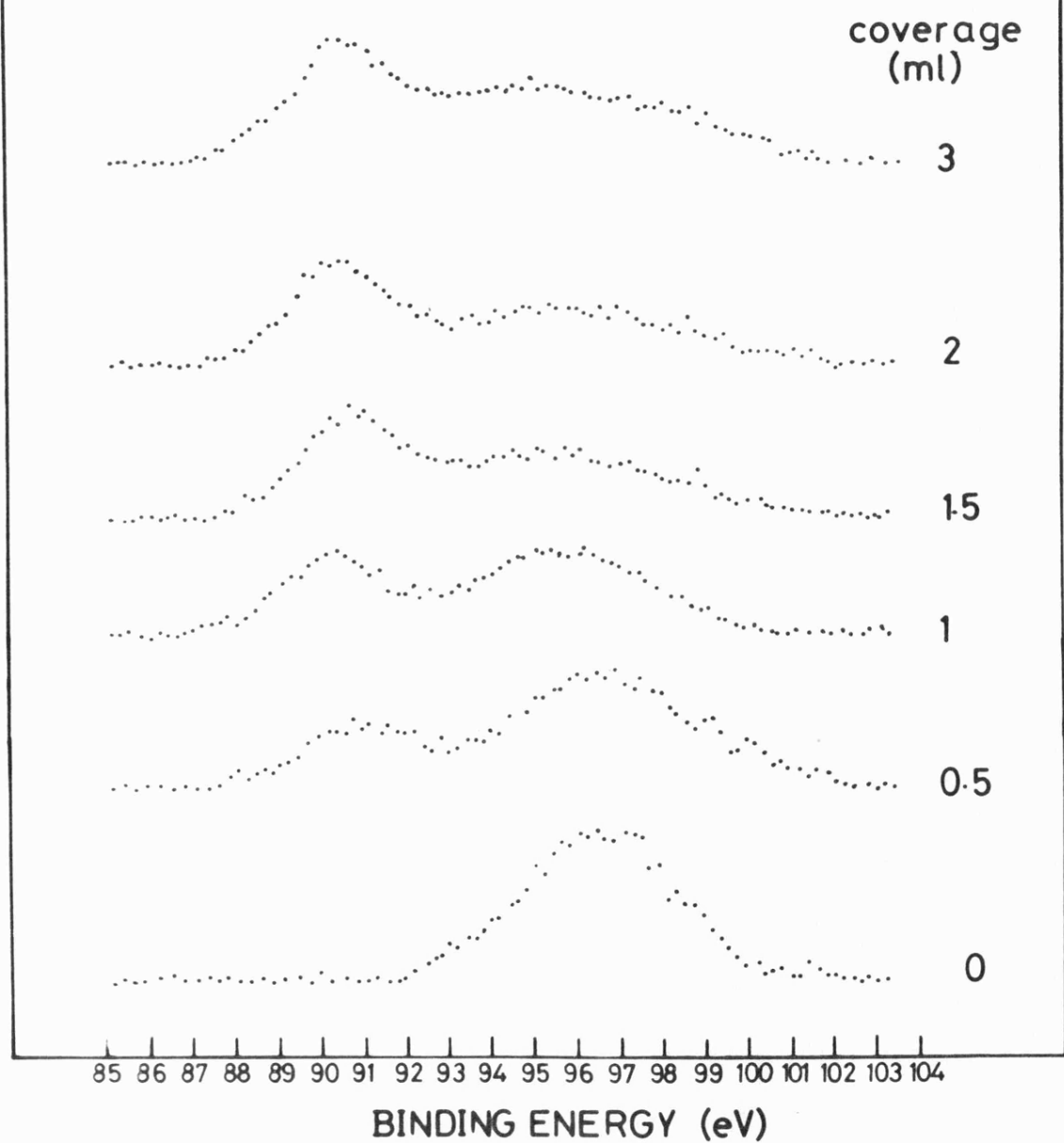


FIG. 8.14

Fe/Ag(100)

$\hbar\omega = 160\text{eV}$

secondaries and
silver 4s subtracted

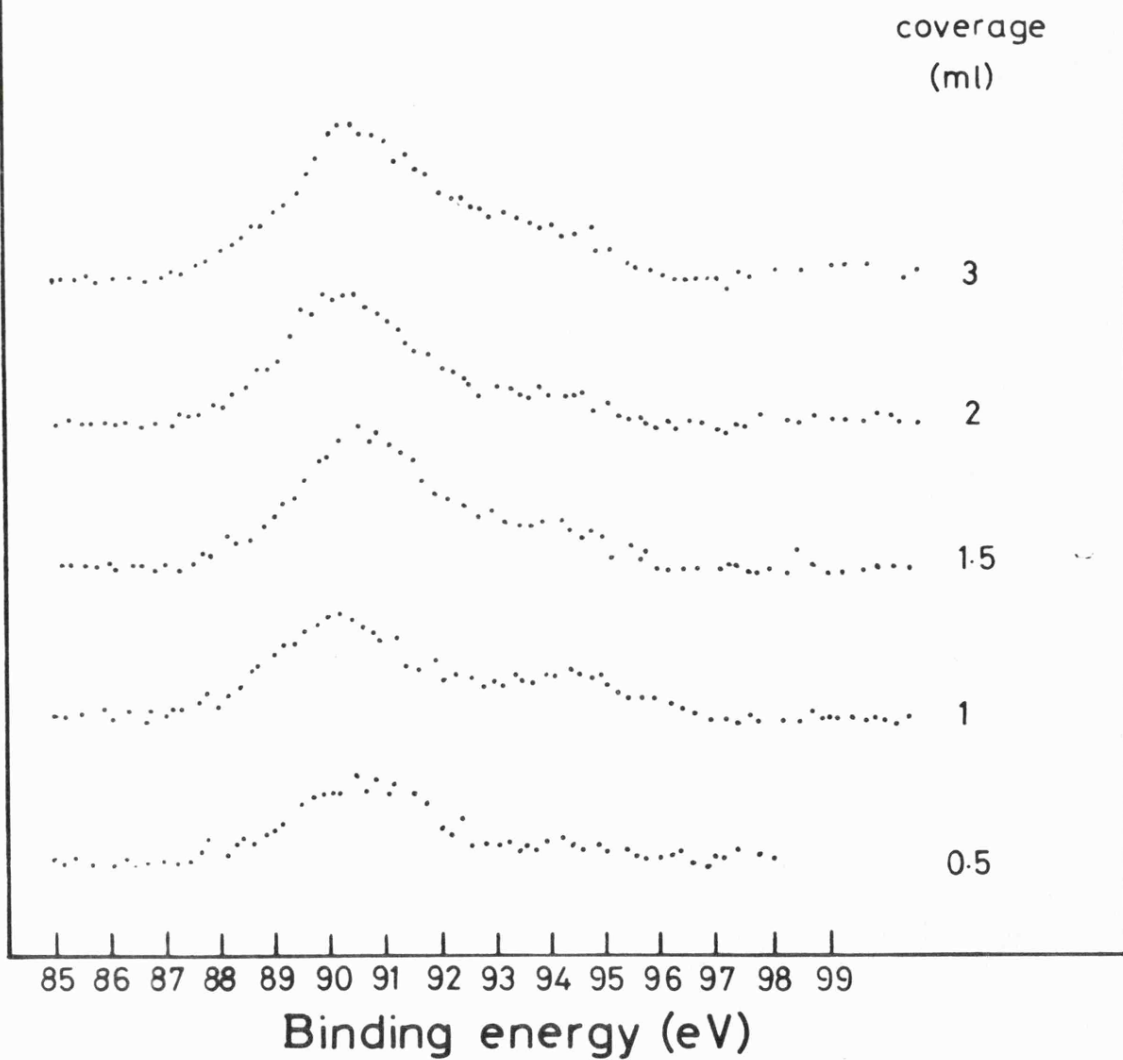


FIG. 8.15

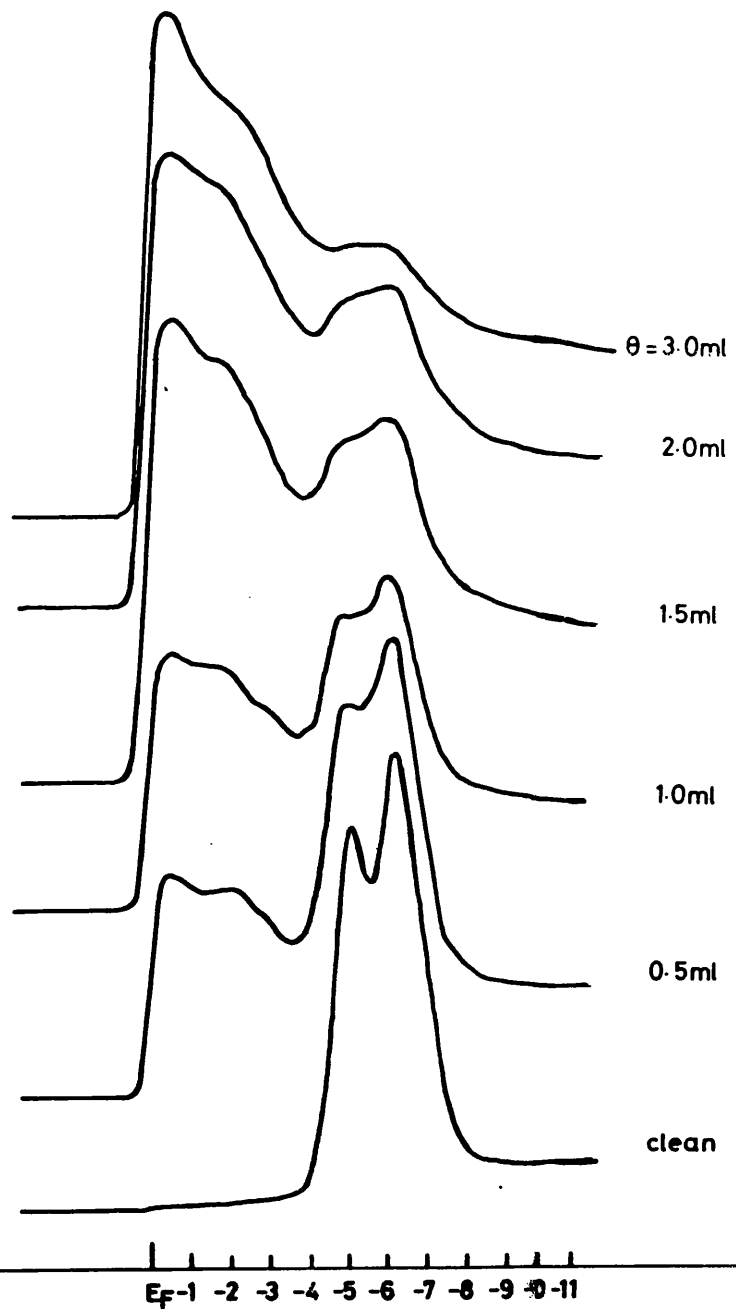
existence at 0.5 monolayers although the noise level in this spectrum is rather high.

Multiplet splitting of core levels in XPS due to the localized moment of a ferromagnetic material has been reported by several workers (see for example McFeely et al 1974, Joyner et al 1980). The splitting may be related to the magnetic moment using the method of Kowalczyk (1976) which is based on the Van Vleck (1934) formalism. The one monolayer spectrum of figure 8.15 shows a multiplet splitting of $4.4 \pm .1$ eV, which corresponds to a magnetic moment of $2.1 \pm .1 \mu_B$ from the calibration of Joyner et al (1980). This is the magnetic moment of an iron atom in a supported, expanded, fcc (100) monolayer, which has not been previously measured. It is, however, close to the accepted value of $2.3 \mu_B$ for bulk iron. On increasing the iron coverage a change in the spectral shape of the iron 3s emission occurs and the satellite appears to move closer to the main peak. The division of intensity between the two exchange-split peaks remains constant above one monolayer coverage. At three monolayers the splitting has a reduced value of $4.0 \pm .1$ eV, giving a moment of $1.7 \pm .1 \mu_B$ representing the value for iron atoms in an expanded fcc lattice. The reduction in moment with increased iron-iron coordination is expected (Noffke and Fitsche 1981).

It is not possible, from the core-level splitting alone, to distinguish between the possible magnetic states of the overlayer. Using a high sensitivity torsion magnetometer Gradmann and Isbert (1980) found ferromagnetism in iron films deposited on $\text{Cu}_{1-x}\text{Au}_x(111)$ surfaces which showed a transition from weak ($0.6 \mu_B/\text{atom}$) to strong ($2.6 \mu_B/\text{atom}$) ferromagnetism when the gold content of the substrate, and hence the lattice expansion of the epitaxial overlayer, was increased. Iron overlayers on copper (110) have also been shown to be ferromagnetic (Wright 1971) whereas on the (100) surface of copper antiferromagnetic layers

Fe/Ag(100)

$\hbar\omega = 120\text{eV}$



FIG

were found (Keune et al 1977). A more complete discussion of the literature is given in the following chapter (Chapter 9).

8.8.2 Valence Band Emission

Spectra taken in normal emission with a photon energy of 120 eV showing the development of the iron valence band emission with increasing coverage are given in figure 8.16. Because of the improved cross section at this energy compared to the HeI and II spectra shown in sections 8.5 and 8.6 features in the overlayer emission may be readily distinguished, even at coverages as low as 0.5 ml. Difference curves obtained at 120 eV between clean silver (100) and coverages of iron of 0.2 and 1.0 monolayers are shown in figure 8.17.

At 0.2 monolayers the difference spectrum shows two features at initial state energies of -0.9 eV and -2.8 eV, and the data have been modelled in figure 8.17 by two Lorentzians of equal intensity and FWHM 1.1 eV separated by 1.9 eV and broadened by 0.3 eV to represent experimental resolution. The model curve fits the data quite well and this seems to imply that, at this coverage, the electronic structure of the overlayer consists of the isolated 3d resonance broadened by interaction with the substrate s band and exchange split by an amount

$\delta E_x = 1.9$ eV. The result is consistent with the calculation of Podloucky et al (1980) who observed formation of well defined spin-split Lorentzian shaped 3d virtual bound states near the Fermi energy for the isolated iron atom adsorbed in silver. The exchange splitting was calculated to be 2.1 eV. Similar, but non-exchange split, resonances were observed for palladium overlayers at 0.1 ml coverage, however, it is possible that at 0.2 ml a significant proportion of the adsorbed iron atoms may be in two dimensional islands and an alternative interpretation of the observed emission is formation of a primitive valence band structure within these islands.

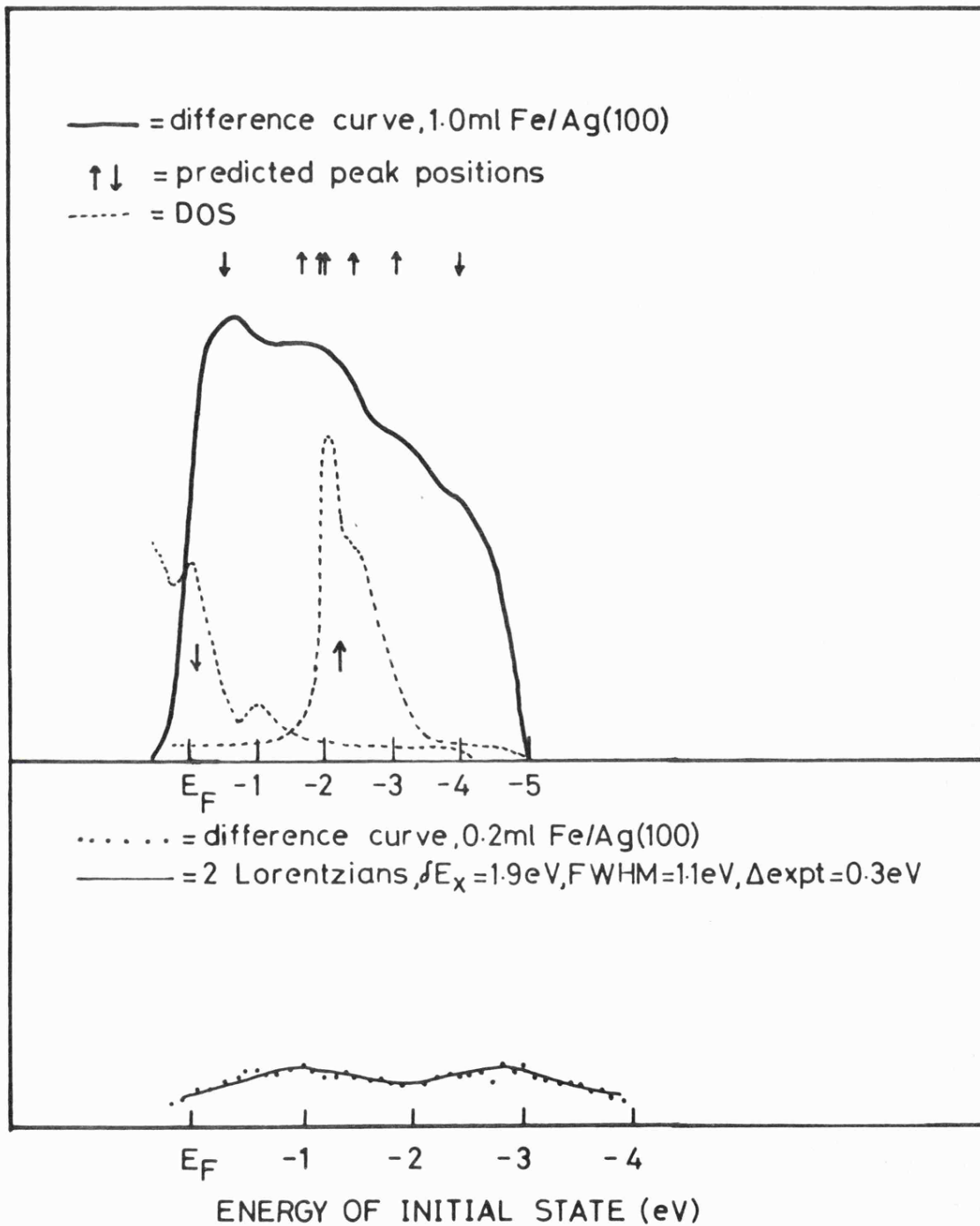


FIG. 8.17

At 0.5 monolayers, the iron band is well developed with three features clearly distinguishable in the emission at initial state energies of -0.56, -2.23 and -2.95 eV. On increasing the coverage to 1.0 ml the spectral shape is retained with only small movements in the three peak positions to -0.67, -2.10 and -2.91 eV respectively. The one monolayer difference curve is shown in figure 8.17 together with the predicted peak positions from initial states at the $\bar{\Gamma}$ point in the spin split energy band calculation shown in figure 8.8 and the corresponding DOS. Although significant Brillouin Zone averaging due to lifetime effects and experimental resolution will occur here the predicted peak positions are seen to correspond quite well to features in the difference spectrum with the feature nearest E_F being of minority-spin origin and the strong feature at -2.11 eV being due to emission from majority-spin states. Also shown are the corresponding exchange-split PDOS. The non-perfect agreement is probably due to the lattice expansion of the overlayer. Mermin and Wagner (1966) have shown that a perfectly two dimensional system is inherently unstable in the presence of long wavelength spin waves and thus cannot sustain ferromagnetism at finite temperatures. The present measurements appear to contradict this result, however, there is some interaction with the substrate s-band and the system is not perfectly two dimensional, also photoemission provides a measure of short range order only so a single-domain layer is not necessarily indicated.

With further increases in coverage the shape of the iron emission rapidly approaches that of bulk iron. Above 1.5 ml a two-peak structure occurs, typical of that seen from the various single crystal faces of bulk ferromagnetic iron at lower photon energies (Schulz et al 1979). At 3 ml the peak positions are -0.69 eV and -2.52 eV (figure

8.7); from the arguments of the previous sections of this chapter these may be associated with the minority and majority spin densities of states respectively, implying an exchange splitting of the valence band of 1.83 eV, similar to that of 1.9 eV inferred from the HeI and HeII data.

8.9 Summary

The results of an investigation of the growth and electronic structure of ultra-thin iron overlayers on silver (100) using LEED, AES and angle-resolved UVES with both noble gas discharge and synchrotron radiation sources are summarized; further discussion in conjunction with the results for nickel overlayers on silver (100) is included in Chapter 9.

Growth was found to follow a form of the Stranski-Krastanov mode in which three epitaxial layers preceded the formation of islands. This is similar to that observed for copper overlayers on silver and is a result of the similar lattice mismatch between overlayer and substrate in both cases.

During deposition the work function was found to rise rapidly from the clean surface value of approximately 4.6 eV, reaching a peak of 5.5 eV at one monolayer coverage after which it dropped to a value of 4.8 eV typical of bulk iron at three monolayers. This is in contrast to the predictions of both the uniform positive background and the virtual level models of work function change on metal adsorption and it is suggested that an improved model is required before results on transition metal overlayers such as presented here may be reliably interpreted.

Photoemission measurements at 21.2 eV and 40.8 eV were made on various iron coverages and comparisons made with theoretical spectra. At three monolayers the iron emission was similar to that seen for the bulk crystal faces of bcc iron and for polycrystalline iron at various noble gas energies by Schulz et al (1979). This was taken as giving additional evidence for these authors' conclusions that photoemission from iron could be understood in terms of calculated densities of states.

The difference spectrum at three monolayers was compared with calculated spectra from expanded fcc iron. The theoretical spectra, using a non-exchange split potential, showed a single feature, compared to two features in the experimental curves. This was interpreted as evidence of the ferromagnetic nature of the film, with the two features arising from the exchange-split partial densities of spin-up and spin-down states. The value of exchange splitting of 1.9 eV is in good agreement with previous experimental values for bulk iron of 1.5 eV to 1.9 eV (Eastman et al 1980, Pessa et al 1976). The band structure of bcc ferromagnetic iron has been calculated by Callaway and Wang (1977), who found a substantial variation of the exchange splitting over the d-bands. For a von Barth-Hedin potential (von Barth and Hedin 1972) they found a value of 1.3 eV near the bottom of the band and 2.2 eV near the top of the band. The corresponding values for a Kohn-Sham-Gaspar potential (Gaspar 1964, Kohn and Sham 1965) were 1.6 eV and 2.7 eV. The isolated monolayer calculation of Noffke (figure 8.8) gives an exchange splitting of 0.8 eV for the lower s-p like band and 2.5 eV for the d-like bands at the $\bar{\Gamma}$ point. At one monolayer the iron emission was almost structureless and although emission corresponding to predicted peak positions using a spin-split iron monolayer calculation was seen it was not possible to make a reliable assignment of spin-up and spin-down bands at this coverage.

To overcome the cross-section problem encountered at noble gas discharge photon energies and provide access to the iron 3s core levels, synchrotron radiation from the Daresbury SRS was used. At 120 eV characteristic structure in the one monolayer spectrum corresponding to the exchange-split DOS of an isolated monolayer could be discussed. Increasing coverage to 3 ml produced a spectrum typical of the bulk crystal faces of iron and an exchange splitting of 1.83 eV was inferred,

in agreement with the HeI measurements. At all coverages the iron 3s level was found to have a satellite, interpreted as due to the local moment on the atom. Using a published calibration the magnetic moment was obtained from the exchange splitting. Values of $2.1 \pm .1 \mu_B$ at one monolayer and $1.7 \pm 1 \mu_B$ at three monolayers were found.

Thus it appears that all coverages of iron on silver (100) investigated were magnetically ordered.

CHAPTER 9AN ELECTRON SPECTROSCOPIC STUDY OF NICKEL
OVERLAYERS ON SILVER (100)

- 9.1 Introduction
- 9.2 LEED and Auger Spectroscopy
- 9.3 Growth Mode
- 9.4 Photoemission Spectra
- 9.5 Photoemission Calculations
- 9.6 Magnetism in Overlayers
- 9.7 Summary

CHAPTER 9AN ELECTRON SPECTROSCOPIC STUDY OF NICKEL
OVERLAYERS ON SILVER (100)9.1 Introduction

Following the investigation of the growth and electronic properties of iron overlayers on silver (100) discussed in the previous chapter, it was of interest to extend the work to nickel overlayers on the same substrate. Experimental energy bands and exchange splittings have been found to agree reasonably well with ground state calculations for iron but discrepancies exist for the strong ferromagnet nickel (Eastman et al 1980) with both the d-band width in PES and the experimental exchange splitting being smaller than the calculated values. This suggests that a one-electron scheme may be inadequate for an accurate description of the electronic properties of nickel and many-body effects may be important. Nickel has been the subject of several recent energy band calculations (Wang and Callaway 1977, Dempsey et al 1978) and emphasis has been placed on the surface magnetism and spin polarization (Wang and Freeman 1980a, 1980b, Wang et al 1982). Self-consistent calculations show no evidence for the magnetically "dead" layers of Leiberman et al (1969, 1970, 1972) reported for electro-deposited nickel films. The band structure and DOS of nickel monolayers have been given by Noffke and Fritsche (1981) and the effect of lattice expansion on the moment considered. Photoemission spectra from single crystal nickel surfaces have been reported by Heiman and Neddermeyer (1976) for 21.2 eV photons and by Heiman et al (1981), Eastman et al (1980) and Himpsel et al (1979) for synchrotron radiation in the energy range 6 to 30 eV and by Kanski et al (1980) for the 30 to 80 eV photon energy range.

In this chapter the results of a LEED and AES investigation of the growth of nickel overlayers on silver (100) are presented in

section 9.2 and a discussion of the growth mode given in section 9.3. Photoemission spectra as a function of nickel coverage are given in section 9.4, where their interpretation in terms of the two-dimensional band structure is discussed. The results of photoemission calculation are shown in section 9.5. Magnetism in overlayers has recently been a rapidly expanding field and is briefly reviewed, with particular emphasis on iron and nickel, in section 9.6. The work is summarized in section 9.7.

9.2 LEED and Auger Spectroscopy

The variation of the nickel (60 eV) and silver (356 eV) Auger signal intensities during nickel deposition onto silver (100) at room temperature is shown in figure 9.1. Three straight line sections occur in the silver substrate intensity decay, with breaks at times t_1 , t_2 and t_3 . After t_3 no further structure was seen in the plot and the silver Auger intensity fell to zero at a time corresponding to approximately $9t_1$. The nickel intensity shows a change to a very slow increase at deposition time t_3 , but the changes of gradient at t_1 and t_2 in the substrate curve are not reflected in the overlayer. This is believed to be a consequence of the steeply sloping secondary background at this energy and the increased surface sensitivity of this line over the substrate 356 eV line.

During deposition the $p(1 \times 1)$ substrate LEED pattern was retained up to t_1 . Beyond this coverage there was rapid deterioration in the pattern and at a point mid-way between t_2 and t_3 there was a very high background intensity and the spots could no longer be discerned.

9.3 Growth Mode

The LEED and Auger results for the growth of nickel overlayers on silver (100) are very similar to those recorded for iron on silver (100)

AUGER SIGNAL vs TIME Ni/Ag(100)

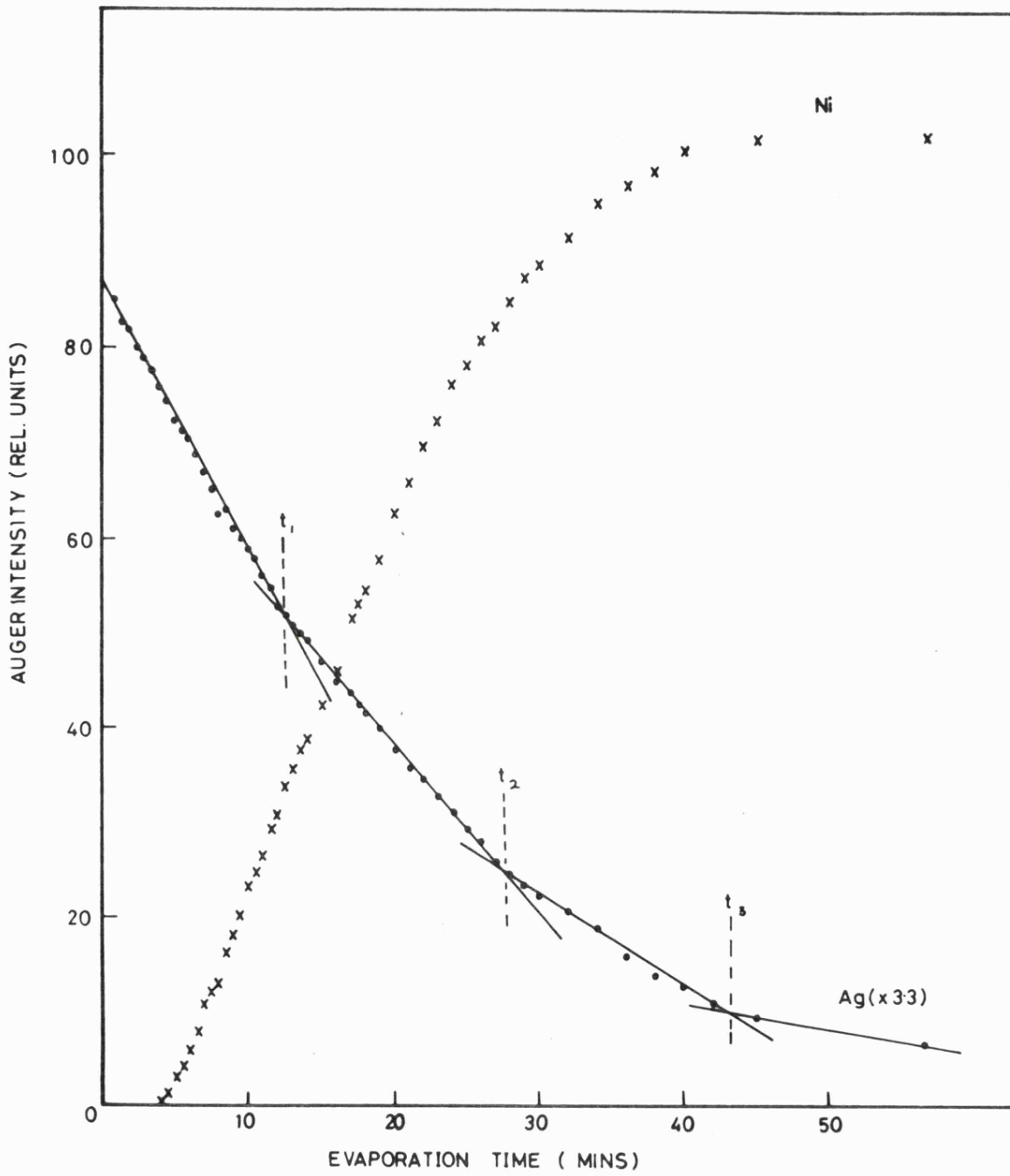


FIG. 9.1

(Smith et al 1982) and copper on silver (100). The piece-wise linear decay of the silver substrate signal indicates layer-by-layer growth, with the breaks at t_1 , t_2 and t_3 associated with the completion of the first, second and third monolayers respectively. The LEED results indicate that the first monolayer is pseudomorphic, after which growth is disordered. In the bulk both nickel and silver crystallise in the fcc structure with lattice constants of 3.524 \AA and 4.086 \AA respectively. Thus a pseudomorphic nickel (100) monolayer on silver (100) will have an expansion relative to bulk nickel of 15.7%, and a lattice mismatch relative to the substrate of 13.8%. This exceeds the upper critical limit for epitaxial pseudomorphic layer-by-layer growth in the Frank and van der Merwe (1949) model. From the LEED pattern it appears that relaxation of the overlayer from this expanded lattice occurs during formation of the second layer.

On the time scale of figure 6.1, t_1 corresponded to 12.5 minutes, t_2 to 27.7 minutes and t_3 to 43.2 minutes. Therefore $t_2 - t_1$, at 15.2 minutes, is greater than t_1 , and $t_3 - t_2$, at 15.5 minutes, is greater than $t_2 - t_1$. If the rate of arrival and the sticking coefficient are assumed constant these results show that more material was required to form the second monolayer than the first, and slightly more for the third than the second. Since the time taken for a given monolayer to form is proportional to the number of atoms that are accommodated in it, and this is inversely proportional to the square of the mean atomic spacing, these results show that the mean interatomic spacing in the second layer is reduced by 10% relative to that in the first layer. The corresponding reduction in the third layer is 11% relative to the first layer. Lattice expansion was shown to have a significant effect on the properties of copper overlayers on silver (100) in Chapter 8.

The substrate Auger intensity is attenuated by 59.8% relative to the clean surface value by adsorption of one nickel monolayer. The dependence of Auger intensity on coverage may be modelled in a simple growth mode independent way by an exponential decay, and in the case of nickel on silver (100) this gives a value for λ , the mean free path, of 1.94 monolayers, or 4.84 Å. In this energy range λ has a broad minimum and shows little variation with energy (Seah and Dench 1979) so this value of 1.94 ml may be used to obtain the final state lifetime for photoemission (see section 9.5).

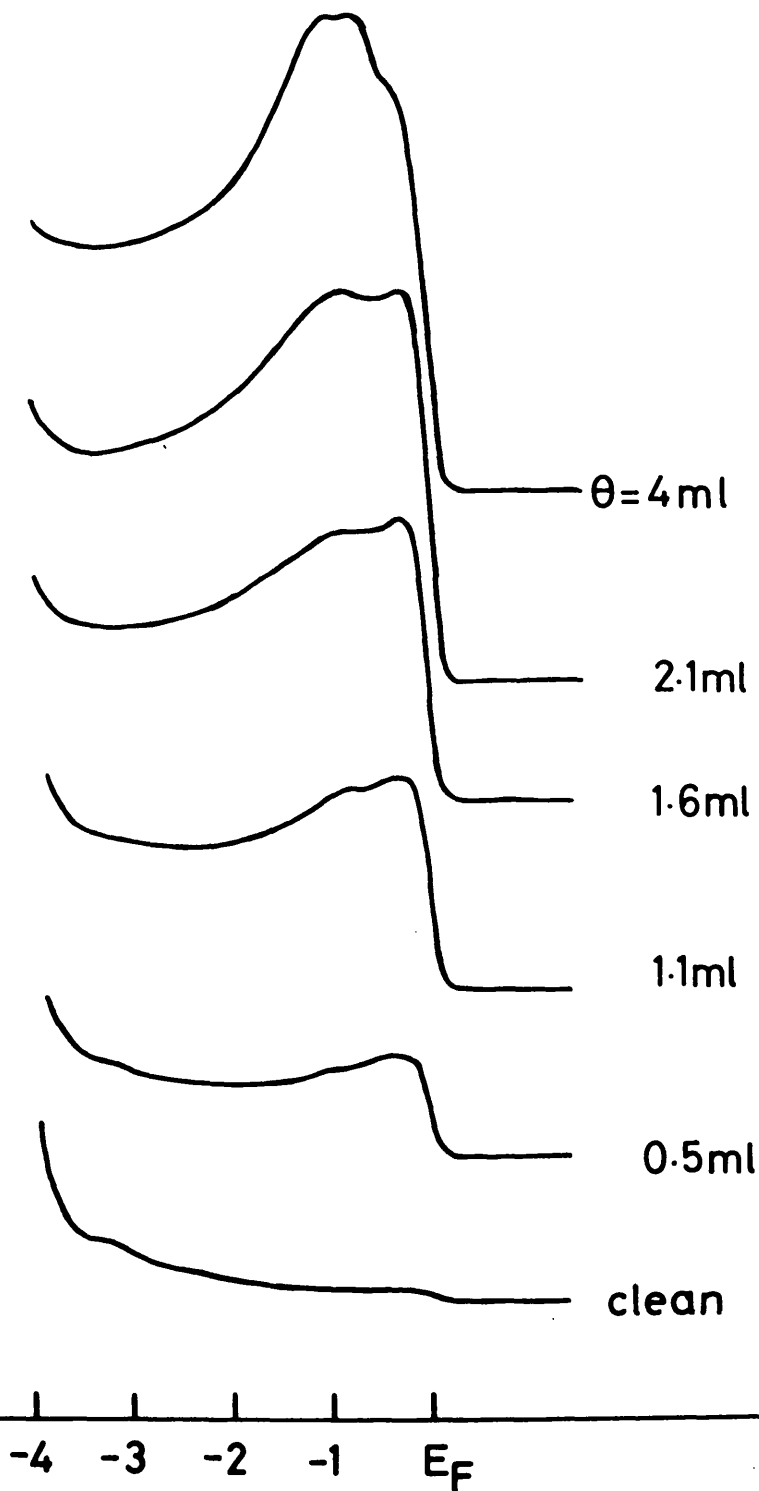
In summary, the growth of nickel overlayers on silver (100) at room temperature follows a form of the Stranski-Krastanov mode with the growth of three monolayers followed by a change to island formation. The first nickel layer is epitaxial and takes the silver lattice constant, corresponding to a 15.7% expansion over bulk fcc nickel, and further layers are disordered with a relaxed interatomic spacing.

9.4 Photoemission Spectra

Photoemission spectra taken at noble gas discharge energies from overlayers of nickel on silver (100) are presented in this section. Due to limited experimental time a less complete data set than for the previously investigated overlayer-substrate combinations was acquired and further work on this system, particularly using synchrotron radiation, would be desirable.

Figure 9.2 shows normal emission spectra taken at 21.2 eV for various coverages of nickel. No change in work function and hence no charge transfer was seen on deposition. The behaviour of the silver d-band emission was similar to that observed during copper and iron deposition, with enhanced attenuation of the surface sensitive feature on the high binding energy side of the 4d emission peak. The similarity

Ni/Ag(100)
 $\hbar\omega = 21.2\text{eV}$



Energy of Initial State (eV)

FIG. 9.2

between the 1 ml and 0.5 ml spectra indicates that two-dimensional islands formed below one monolayer coverage. For coverages of 2.1 ml and below a doublet structure in the nickel emission is seen, with the higher binding energy peak increasing in intensity with coverage. Both peaks show a consistent movement towards the Fermi energy with increasing coverage; the peak nearest E_F has binding energies of 0.42 eV, 0.32 eV, 0.27 eV and 0.24 eV for coverages of 0.5 ml, 1.1 ml, 1.6 ml and 2.1 ml respectively. A corresponding shift from 1.05 eV to 0.83 eV in the higher binding energy peak on going from 0.5 ml to 2.1 ml occurs. On increasing the coverage from 2.1 ml to 4.0 ml the higher binding energy feature increases in intensity further, dominating the spectrum, and splits into a doublet. The form of the spectrum seen at this coverage is typical of bulk nickel (100) and corresponds well to that observed by Heimann and Nedermeyer (1976). These authors attributed all three spectral features to direct transitions from the calculated ground state band structure of Wang and Callaway (1974).

In a recent paper Noffke and Fritsche (1981) have presented the spin dependent DOS for a nickel monolayer, together with the spin magnetic moment per atom for the (100) monolayer and the (100) monolayer linearly expanded by 10%. The band structures used to obtain these values are shown in figures 9.3 to 9.5 (J. Noffke, private communication). Figure 9.3 shows the non-magnetic monolayer, figure 9.4 the magnetic monolayer, and figure 9.5 the magnetic monolayer with the lattice constant expanded by 10%.

In normal emission $\underline{k}_{\parallel} = 0$ and direct transitions from the $\bar{\Gamma}$ point of the SBZ are detected, if DOS effects in the spectra are small. Before predicted peak positions from the band structure may be compared with the experimental curves it is necessary to take into account the

Ni MONOLAYER

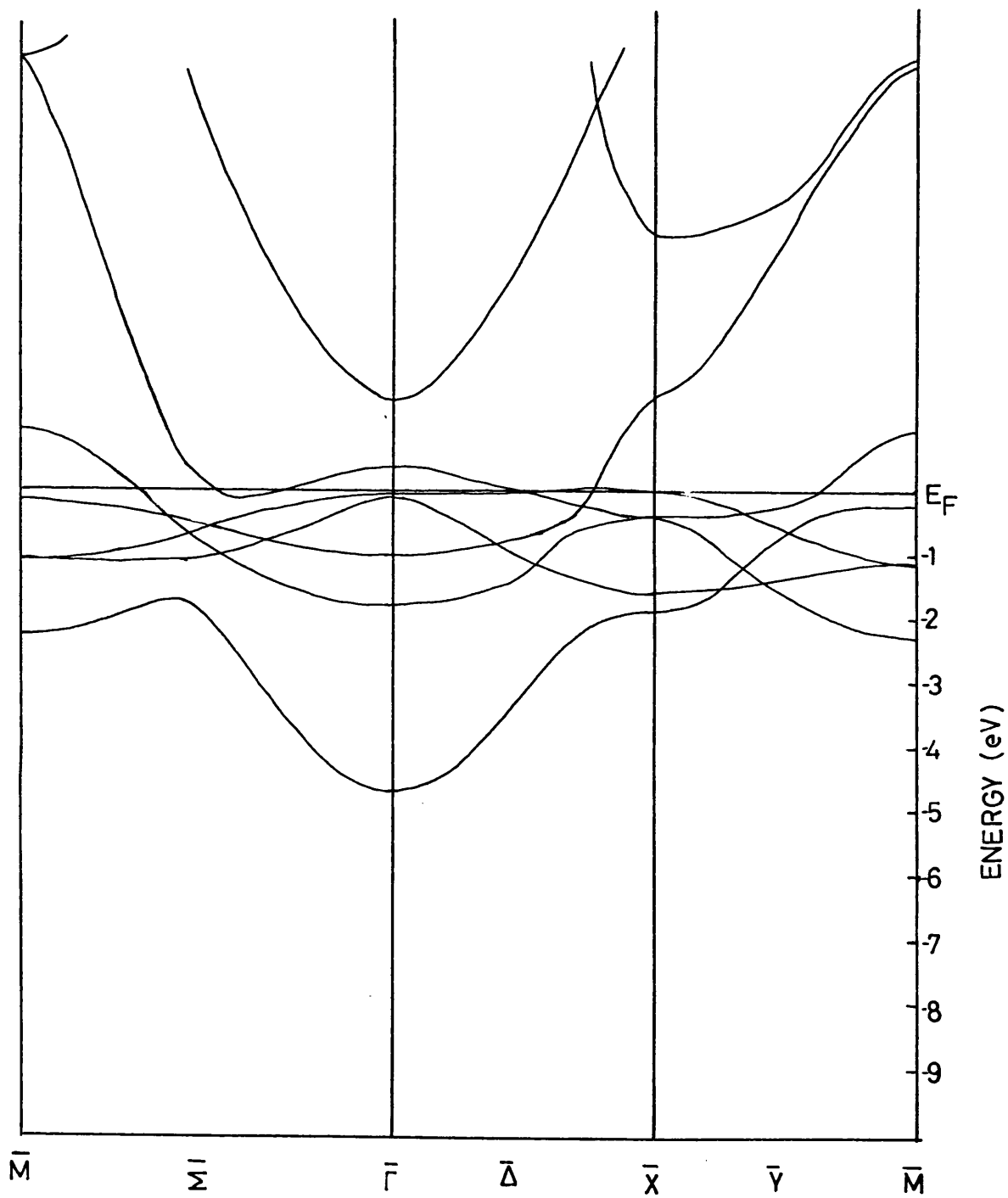


FIG. 9.3

EXCHANGE SPLIT Ni MONOLAYER

--- = spin down

— = spin up

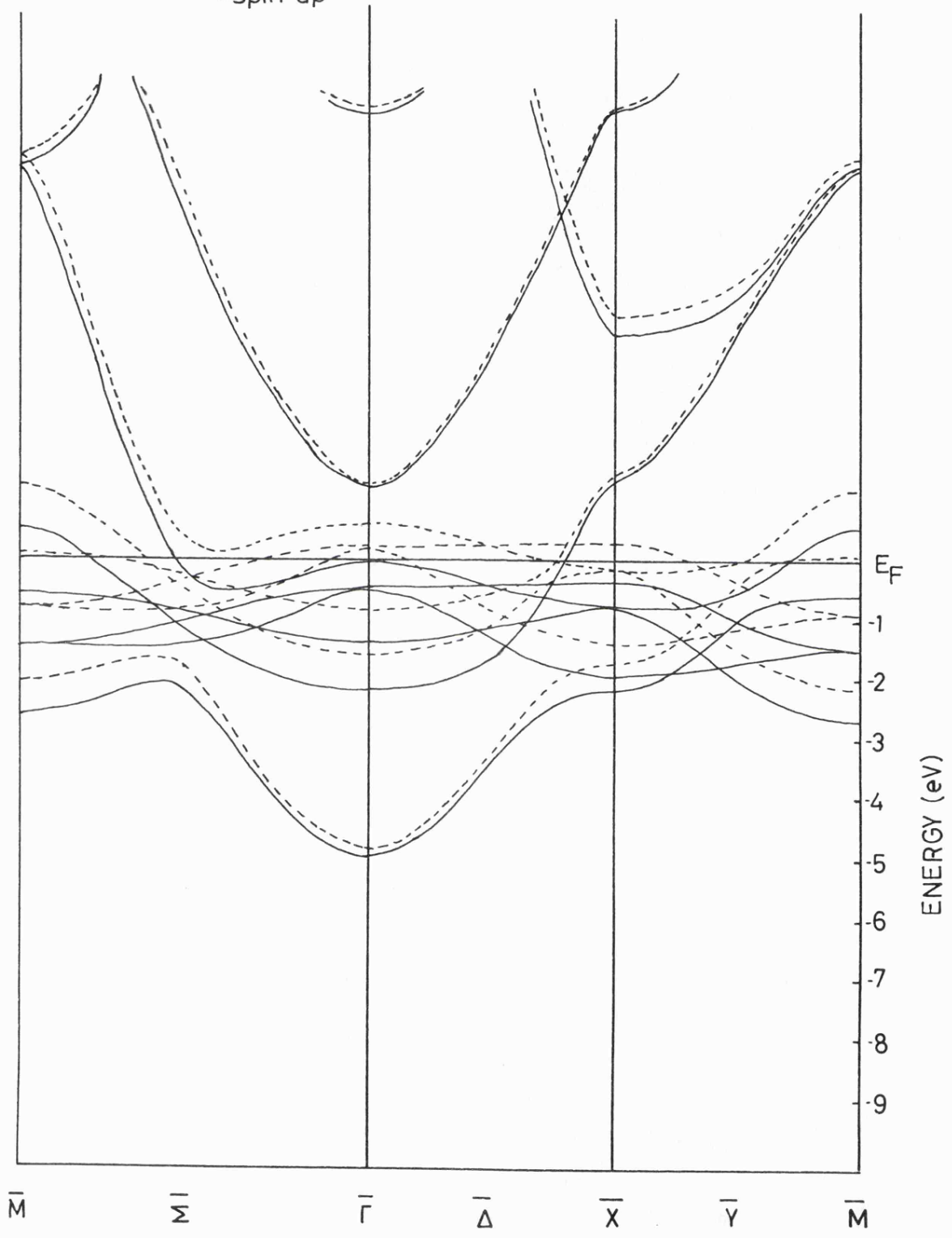


FIG. 9.4

Ni MONOLAYER +10% EXPANSION

— = spin up
- - - = spin down

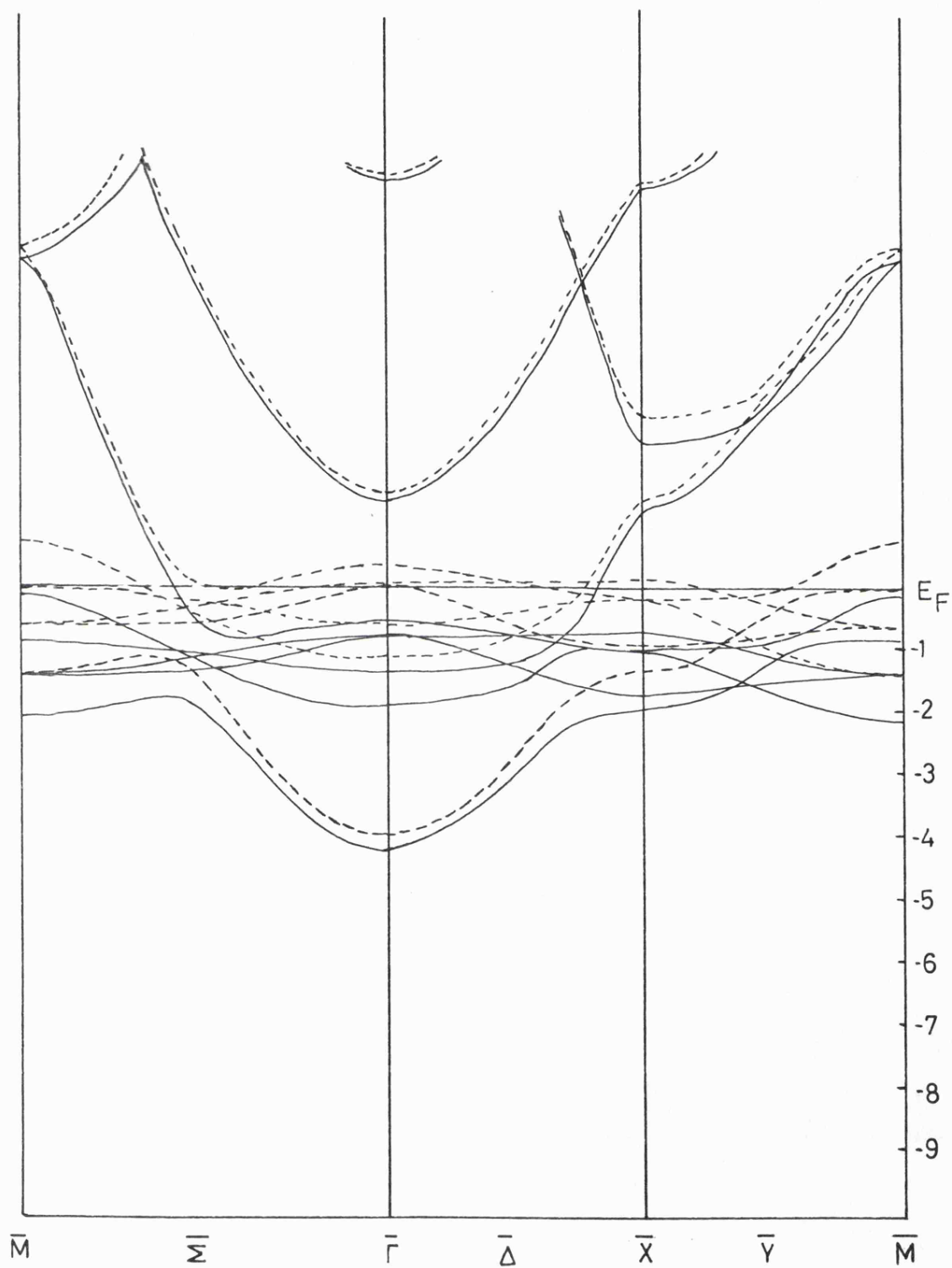
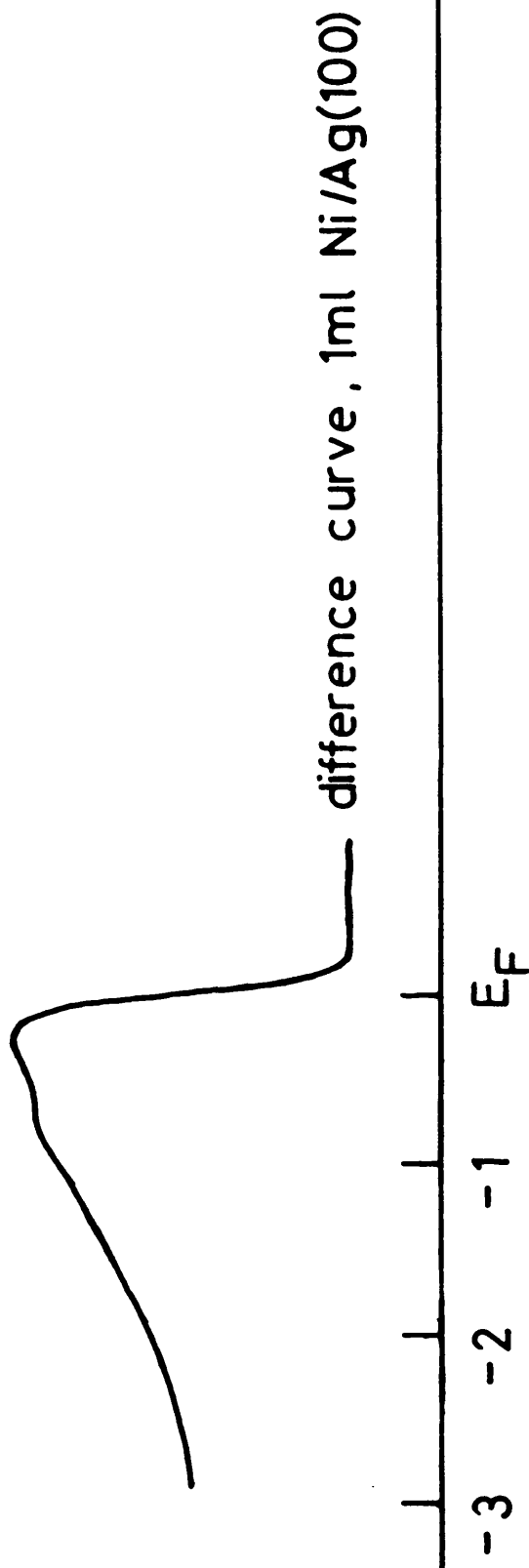


FIG. 9.5

large (15.7%) lattice expansion of the pseudomorphic nickel (100) monolayer adsorbed on silver (100). Comparison of figures 9.4 and 9.5 show that on application of a 10% lattice expansion the centres of the spin-up and spin-down bands remain in approximately the same energy position and the shapes are little changed, but there is significant bandwidth reduction by a factor of 1.6 for both spin-up and spin-down cases. In the previous chapter concerned with copper overlayers on silver (100) (Chapter 7) use was made of the derivation by Heine (1967) of the dependence of the width of a tight binding d-band inversely on the fifth power of interatomic spacing. In the present case an expansion to 1.10 times the original lattice constant resulted in a calculated self-consistent bandwidth reduction by a factor 1.6, and $(1.10)^5 = 1.61$, confirming the proposed relationship. Thus for the case of nickel on silver (100) it is justified to treat the electronic structure of the overlayer with a 15.7% lattice expansion as a perturbation of the 10% expanded layer and further reduce the spin-up and spin-down bandwidths by a factor $(1.157 / 1.10)^5 = 1.29$ about their original band centres. The same procedure has been applied to the non-exchange split band structure and the predicted energy positions of peaks for both the split and non-split band structures for the expanded lattice shown in figure 9.6, together with the normal emission difference spectrum for one monolayer at 21.2 eV. A similar spectrum was obtained at 40.8 eV and is not shown. The two peaks in the experimental curve do not appear to correspond exactly with either set of predicted peaks, however, further evidence indicates the magnetic nature of the film. The high density of states observed at the Fermi energy for all coverages including the monolayer is typical of ferromagnetism (Stoner 1948). The DOS of the exchange-split nickel (100) monolayer presented by Noffke and Fritsche (1981) shows a large peak in the minority spin partial DOS just below E_F , with a very low contribution

$\uparrow \uparrow \downarrow \uparrow \downarrow$ magnetic monolayer +15.7%
 $| | | |$ non-magnetic monolayer +15.7%



initial state energy (eV)

FIG. 9.6

of majority spins whereas at approximately 1 eV below E_F there is a large majority spin contribution. It is thus possible to assign the two peaks in the experimental curve to the minority and majority spin DOS, indicating an exchange splitting of 0.6 eV at the top of the d-band for the 15.7% expanded monolayer. The calculated exchange splitting of the 10% expanded monolayer of figure 9.5 is 0.9 eV for the d-bands at $\bar{\Gamma}$ and is 0.7 eV for the non-expanded layer (figure 9.4). Recent calculations of the magnetic exchange splitting in bulk nickel using self-consistent spin-polarized bands have, in general, overestimated the value relative to experiment and it has been suggested that the one-electron model is inadequate for describing the electronic properties of nickel (Heiman et al 1982, and references therein). Although many body effects may be of importance expansion of the crystal lattice and reduction of the coordination number have been shown to result in an increased moment (Noffke and Fritsche 1981). The accepted experimental splitting for bulk nickel is 0.3 eV (Eastman et al 1978, Himpsel et al 1979, Eberhardt and Plummer 1980), a similar value being found for nickel (110) surface states (Eberhardt et al 1980).

9.5 Photoemission Calculations

Photoemission spectra for nickel overlayers on silver (100) were calculated using the Pendry (1976) theory in the form of the PEOVER program described in previous chapters. The nickel potential was obtained from C-G Larsson (private communication 1982). Using the same potential Kanski et al (1980) have calculated the photoemission spectra for nickel (100) over the photon energy range 30 to 80 eV; good agreement between theory and experiment was found and consequently calculations for bulk nickel will not be presented here. The calculated normal emission photoelectron spectrum for one monolayer of pseudomorphic nickel adsorbed

CALCULATED PHOTOEMISSION; 1 ml Ni/Ag(100), $h\nu = 21.2\text{eV}$

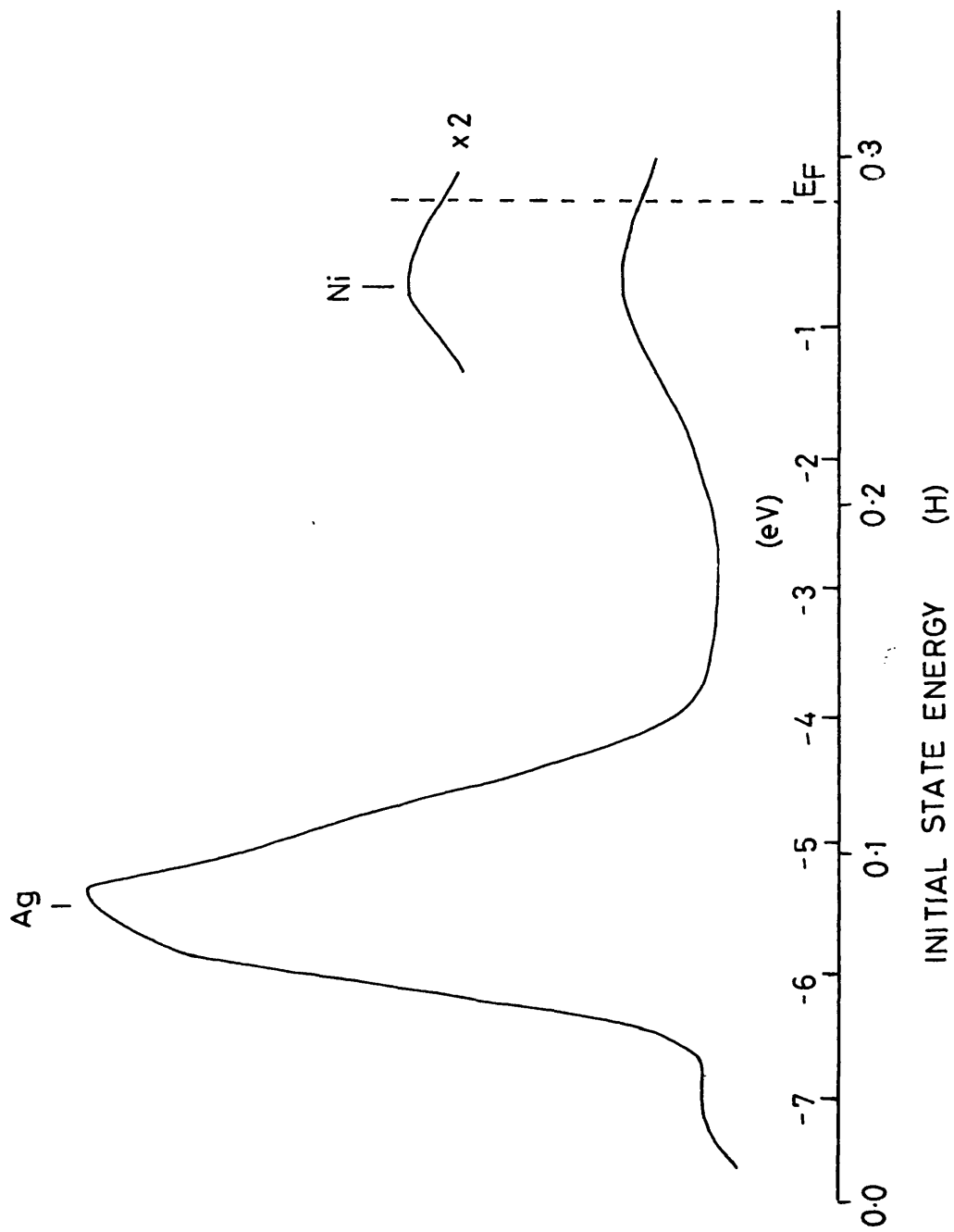


FIG. 9.7

on silver (100) is shown in figure 9.7. The silver potential is that used by Padmore et al (1982) described in Chapter 4. To obtain the best agreement between theory and experiment a realistic value of the electron lifetime was estimated from the Heisenberg Uncertainty Principle and the A_s-t plot in the manner applied to copper on silver (100). The value of $0.14\hbar$ obtained from this is larger than values for the other overlayers and accounts for the enhanced attenuation of the silver surface sensitive emission peaks mentioned earlier. Other values were as for bulk silver (Chapter 4).

Overall, there is agreement between theory and experiment in figure 9.7, compared with the one monolayer curve of figure 9.2. Adsorption of nickel results in a broadening of the structure in the silver d-band and an increase in the DOS at E_F . There is no sign of a double-peaked structure in the emission just below E_F . Without the inclusion of spin polarized potentials the possibility of magnetism in the overlayer cannot be investigated but the lack of a calculated doublet when such a structure appears in the experiment may be taken as evidence of exchange splitting of the bands of the overlayer. The various adjustable parameters in PEOVER (for example, surface barrier height and position, electron and hole lifetimes, etc) are unlikely to cause formation of such a doublet, their principal effects being variation of position, width and relative intensities of the spectral features.

Although this conclusion is based on a limited data set, the evidence seems to indicate that nickel is adsorbed in a magnetic state at one monolayer and higher coverages on silver (100).

9.6 Magnetism in Overlayers

The work on nickel and iron overlayers adsorbed on silver (100) reported in this thesis, and that of iron overlayers on palladium (111) of Binns et al (1982) and cobalt on copper (111) of Miranda et al (1982),

are the only photoemission studies of well characterized magnetic overlayer systems to date. Many of the increasing number of magnetic experiments performed on similar systems are performed at atmospheric pressure, even though the structures may have been prepared at UHV. The role of so-called "passivating layers" applied to protect the ultra-thin layer in question has yet to be evaluated.

Interest in the modifications of magnetic properties of the ferromagnets iron and nickel at surfaces and in thin films was stimulated by the early work of Lieberman et al (1969, 1970, 1972). The ferromagnetic flux was measured as a function of thickness of films deposited electrochemically from aqueous solution and "dead layers", which did not contribute to the flux, were observed. For cobalt, nickel and iron extrapolated to zero temperature two dead layers were found. This was interpreted as s-d electron transfer in the neighbourhood of the surface resulting in a reduced DOS near E_F and hence a reduced moment in the spirit of the Stoner model. The number of dead layers was found to be independent of the substrate used, even though the results of the present work and many other studies indicate the substrate has a profound effect on the geometry, and hence the electronic structure, of the overlayer. It is likely that deposition from aqueous solution resulted in imperfect or contaminated films; experiments on evaporated films using the Mossbauer effect showed no evidence of the dead layers (Walker et al 1972, Varma and Hoffman 1971, 1972). The subject has been reviewed by Gradman (1974) who concludes that most of the available experimental results contradict the existence of magnetically dead layers. Recent self-consistent results show that the presence of a copper film on nickel (100) causes a copper-induced moment reduction in the first and second nickel layers, but no dead layers were found (Tersoff and Falicov 1981). A single copper layer gave an almost ideal (surface insensitive) interface.

Experiments on iron, nickel and cobalt films prepared in UHV and measured in situ have been performed by Bergmann (1979, 1981) using the Anomalous Hall Effect (AHE). Suppression of the magnetisation for thin films of iron and cobalt on an amorphous $\text{Pb}_{75}\text{Bi}_{25}$ alloy surface was not found but for nickel on the same substrate 2.5 atomic layers were required before a divergence in susceptibility and a resulting magnetic moment were detected. Modification of the nickel d-bands by hybridisation with the substrate was seen as causing this effect; on application of a further $\text{Pb}_{75}\text{Bi}_{25}$ layer to a 5.6 atomic layer nickel film a reduction in the moment due to suppression of the magnetisation of the upper surface was observed. No surface characterisation of the $\text{Pb}_{75}\text{Bi}_{25}$ amorphous alloy was used, and the growth mode of the nickel layers was not investigated.

Gradmann and Isbert (1980) have used Mossbauer spectroscopy to investigate the magnetic properties of iron overlayers grown epitaxially on $\text{Cu}_{1-x}\text{Au}_x$ (111) surfaces characterised in situ by LEED and Auger spectroscopy. By increasing the gold content of the substrate they were able to control its lattice parameter and hence the expansion of the epitaxial overlayer relative to bulk iron. Films of two and three atomic layers thickness were investigated as a function of lattice parameter and a transition from weak ferromagnetism ($0.6 \mu_B$ / atom) at $x = 0$ (Cu(111)) to strong ferromagnetism ($2.6 \mu_B$ / atom) on an expanded substrate was recorded. The results were interpreted as evidence for a change from antiferromagnetism to ferromagnetism with increasing lattice expansion. fcc iron films have also been investigated by Keune et al (1977). Mossbauer spectroscopy of thin ($\sim 18 \text{ \AA}$) films prepared on Cu (100) showed anti-ferromagnetic ordering at low temperature with paramagnetism seen at room temperature (above the Neel temperature). The growth mode of the layers was not investigated and substantial islanding may have occurred.

The only studies which have combined LEED and Auger determination of the growth mode and structure of the overlayer with photoemission measurements are those of Binns et al (1982) for iron overlayers on palladium (111) and Miranda et al (1982) for cobalt layers on copper (111). Comparison of the photoemission spectra with a calculated spin-dependent DOS indicated that the adsorbed epitaxial cobalt monolayer on copper (111) was ferromagnetic, with an exchange splitting very similar to that of bulk cobalt. Binns and co-workers found that iron was adsorbed on palladium (111) in a simultaneous multilayer (Barthès and Rolland 1981) mode and at submonolayer coverages significant amounts of the second and higher layers were present. At an equivalent coverage of 0.5 ml they estimated the overlayer to consist of clusters of typically 10 iron atoms each with approximately two atoms in the second layer. To create a perfect two dimensional layer 0.6 ml was deposited at 160K and annealed at 370K for five minutes. Iron diffusion into the substrate did not occur. Annealing was found to remove the multiplet splitting due to exchange interaction of the iron 3s level, and to reduce the DOS at the Fermi level. Thus a perfectly flat iron layer on palladium (111) is either a weak ferromagnet, or is non-magnetic. Strong ferromagnetism could be induced by covering the monolayer with a dilute lattice gas of iron atoms (C. Binns, private communication). These results indicate the importance of a precise knowledge of the overlayer structure in this kind of experiment.

A summary of the more recent UHV studies of magnetic overlayers is given in figure 9.8. Included are the results of the present work on nickel and iron overlayers on silver (100). Iron monolayers are found to be ferromagnetic on polycrystalline silver, silver (100), polycrystalline palladium copper (111) and copper-gold (111), antiferromagnetic on copper (100) and non-magnetic on palladium (111). Following Keune et al

System	Techniques	Magnetic state of layer(T_c)	local moment (μ_B)	Coverage
Fe/Pd (111) Binns et al (1982)	LEED, AES, PES	F N	2.3 -	Simultaneous Multilayer Flat Monolayer
Co/Cu (111) Miranda et al (1982)	LEED, AES, PES	F	bulk Co	Monolayer
Fe/Ag (100) Ni/Ag (100) (present work)	LEED, AES, PES	F F	2.1 1.7	1 Monolayer 3 Monolayers Monolayer and above
Fe/Cu (100) Keune et al (1977)	TEM, Mossbauer	AF (80K)		18 Å
Fe/polycrystalline Pd Bergman (1981)	AHE	N F	-	< .1 monolayer > .5 monolayer
Ni/Pb ₇₅ Bi ₂₅ Bergmann (1973)	AHE	F		> 2.5 monolayers
Fe/polycrystalline Ag Walker et al(1972)	Mossbauer	F		1 monolayer
Fe/Cu (111) Kummerle & Gradmann (1977)	LEED, AES, torsion magnetometer	F	.58	2 ml
Fe/Cu _{1-x} Au _x (111) Gradmann & Isbert (1980)	LEED, AES, torsion magnetometer	F (300K)	.6 to 2.6	2 ml, as a function of lattice expansion

F = Ferromagnetic
N = Non Magnetic
AF = Anti ferromagnetic

Figure 9.8

(1977), it is likely that the apparent discrepancies in the results may be resolved by taking into consideration the substrate orientation, the growth mode and/or island size, and the lattice expansion suffered by the overlayer. Systematic investigation of the effects of variations in these parameters after the manner of Gradmann and Isbert (1980) are desirable. In addition, the importance of the growth mode cannot be overestimated, as demonstrated by Binns et al (1982).

9.7 Summary

The LEED patterns and As-t plot for the growth of nickel overlayers on silver (100) at room temperature indicated that the first monolayer was adsorbed epitaxially, taking the crystal structure of the substrate, and thus had a 15.7% expansion relative to bulk nickel. The longer time required for formation of the second monolayer relative to the first, and the deterioration of the LEED pattern, was evidence of relaxation taking place in the second monolayer. Further layers were disordered and no structure in the As-t plot was seen after three deposited monolayers, indicating island formation.

The HeI photoemission spectra at coverages of 2.1 ml and below showed a doublet structure in the nickel-derived emission which did not correspond well with predicted peak positions from isolated monolayer band structure calculations, even after allowing for the effects of the overlayer lattice expansion. The doublet was also not predicted in a photoemission calculation using a non-exchange split potential even though other spectral features were reproduced. This was interpreted as evidence for ferromagnetism in the overlayer, with a measured exchange splitting of 0.6 eV, rather higher than that reported for the bulk (Heimann et al 1981). Expansion of the monolayer lattice constant and reduction of the coordination number are expected to increase the magnetic moment and hence the exchange splitting (Noffke and Fritsche 1981).

The picture emerging from a review of relevant experiments on magnetic overlayers is extremely complex. The magnetic state of the layer appears to be a function of overlayer and substrate orientation and geometry, of any lattice expansion imposed on the layer by the substrate, and of the growth mode and local atomic environment in the overlayer. A systematic survey of overlayer systems with controlled variation of these parameters is desirable. A review of recent experimental and theoretical advances has been given by Allan (1981).

CHAPTER 10DISCUSSION, SUMMARY AND CONCLUSIONS

- 10.1 Introduction
- 10.2 Overlayer Growth Modes
- 10.3 Overlayer Electronic Structure
- 10.4 Two-Dimensional Energy Bands
- 10.5 Surface States
- 10.6 Calculation of Photoelectron Spectra
- 10.7 Suggestions for Further Work
 - 10.7.1 Experimental Development
 - 10.7.2 Theoretical Development

CHAPTER 10DISCUSSION, SUMMARY AND CONCLUSIONS10.1 Introduction

The LEED, Auger and photoemission measurements reported in this thesis represent a survey of the growth and electronic properties of iron, nickel, copper and palladium overlayers on silver (100). Palladium overlayers on silver (111) and copper (100) were also studied. In this chapter the results of these investigations are summarized and trends in the structural and electronic properties brought out. The lattice mismatch between the overlayer and substrate bulk materials has been shown to be a dominant factor governing growth mode and this is discussed in section 10.2. The electronic structures of the various overlayers are the subject of section 10.3, and two-dimensional energy bands and surface states are considered in sections 10.4 and 10.5. Photoemission and the bulk energy band structures of the substrate materials was reviewed in Chapter 4, and magnetism in overlayers in Chapter 9. The present work represents the only documented attempts known of by the author to calculate realistic photoemission spectra from adsorbed metal overlayers and their comparison with experimental results. The photoemission calculations are discussed in section 10.6. Suggestions for further work, both experimental and theoretical, are made in section 10.7.

10.2 Overlayer Growth Modes

The growth modes of the overlayer-substrate combinations studied in this thesis are summarized in table 10.1. Palladium on copper (100), for which the overlayer bulk spacing is larger than the substrate and hence shows a negative mismatch, forms a $c(2 \times 2)$ surface alloy and does not fall into the sequence shown by the other materials. Palladium, iron, copper and nickel all form one epitaxial pseudomorphic monolayer when

System	Mismatch	Growth Mode	Comments
Pd/Cu(100)	-7.6%	Surface Alloy	c(2x2) surface alloy followed by disordered simultaneous multilayer
Pd/Ag(111)	4.8%	Frank-van der Merwe	p(1x1) monolayer followed by epitaxial simultaneous multilayer
Pd/Ag(100)	4.8%	Frank-van der Merwe	p(1x1) layer by layer with relaxation after ~ 4 monolayers
Fe/Ag(100)	10.9% (fcc Fe)	Stranski-Krastanov	2 p(1x1) epitaxial layers, 1 layer with increased atom density, then islands
Cu/Ag(100)	11.5%	Stranski-Krastanov	2 p(1x1) epitaxial layers followed by disorder and islands
Ni/Ag(100)	13.8%	Stranski-Krastanov	p(1x1) monolayer followed by 2 layers with increased atom density and disorder, then island formation

Table 10.1

initially adsorbed on silver (100), and palladium also does so on silver (111). The classical Frank-van der Merwe model of overlayer growth described in Chapter 2, as modified by Woltersdorf (1981), gives an upper critical lattice misfit of 11% beyond which layer growth cannot be sustained. This value is supported by the present data to the extent that iron, copper and nickel overlayers on silver (100) with mismatches of 10.9%, 11.5% and 13.8% respectively grow in the Stranski-Krastanov mode in which islands form after initial layer growth whereas palladium on both the (100) and (111) silver faces where the mismatch is 4.8% follows the Frank-van der Merwe mode. Further, as the mismatch increases through the series iron, copper, nickel there is a reduction in the number of layers which grow epitaxially before island formation. This is a consequence of increased strain in the layer and is also in agreement with the classical theory, which has been shown to have general applicability to metal overlayers on both metallic and non-metallic substrates (Woltersdorf 1981). The temperature dependence of the growth mode of silver on palladium was investigated by Guglielmacci and Gillet (1982) and the number of layers grown before island formation found to reduce with increasing temperature. The critical misfit reduces with increasing temperature due to thermal activation of dislocation formation and so an increase in temperature produces a similar effect to that of an increase in overlayer lattice expansion seen in the present work.

In most cases the growth modes derived in this work are consistent with those observed for related systems for which LEED and Auger measurements have been carried out, where these are available in the literature. For palladium on silver the work of Guglielmacci and Gillet (1980, 1982) on the inverse system silver on palladium may be quoted. For both the (100) and (111) surfaces layer-by-layer growth was observed at room temperature. In addition, layer growth was observed by Burland and

Dobson (1981) who used RHEED to monitor the misfit of palladium films on silver (111) and gold (111) as a function of film thickness.

The tendency to surface alloy formation on deposition of palladium onto copper (100) was expected from the LEED/AES results of Fujinaga (1979), although the related systems cobalt on copper (100) (Gonzalez et al 1981) and manganese on copper (100) (Binns and Norris 1982) formed $c(2 \times 2)$ overlayers rather than the $c(2 \times 2)$ surface alloy observed for palladium. Cobalt and manganese showed no tendency to form a bulk ordered alloy with copper at room temperature whereas for palladium both the CuPd and Cu_3Pd phases occur (Hansen and Anderko 1958). The formation of surface alloys has been observed with other systems such as lead on the low-index faces of gold for which stable ordered alloy structures also exist in the corresponding bulk phase (Perdereau et al 1974).

The Stranski-Krastanov growth mode observed in the present work for copper, nickel and iron layers on silver (100) has been widely reported for various overlayer-substrate combinations. Systems exhibiting this form of growth at room temperature include lead and tin on aluminium (111) (misfits of 22% and 11%) (Argile and Rhead 1980), silver on molybdenum (100) and tungsten (110) (misfits 6% and 5%) (Venables et al 1980), lead on silver (111) (misfit 21%) (Takayanagi 1981) and lead and thallium on copper (100) (misfits 37% and 35%) (Barthes and Rhead 1979, Binns and Norris 1982). From these results and from several review articles (for example Bauer and Poppa 1972, Woltersdorf 1981) it appears that the classical model of Frank and van der Merwe (1949) forms an adequate basis for the qualitative prediction of metal overlayer growth modes. It is important to note that the very large misfits quoted for some of the systems above does not necessarily correspond to a large strain since the overlayer may be re-oriented relative to the substrate.

Layer	Measured m.f.p.(ml)	Seah & Dench m.f.p.(ml)
Pd (100)	3.0	4.0
Pd (111)	3.3	4.0
Cu (100)	3.0	3.8
fcc Fe (100)	2.5	3.9
Ni (100)	1.9	3.8

Table 10.2

From the various A_s-t plots produced during this work it is possible to estimate the mean free paths for electrons at the silver Auger energy (356 eV) passing through the overlayer material. The results are shown in table 10.2, together with values estimated using the Seah and Dench (1979) empirical formula. The empirical expression appears to consistently overestimate the mean free path, although all values are within a factor of two. This is probably a function of the increased lattice spacing of the overlayer relative to the bulk materials for which the empirical relationship was established. Further, attenuation by a single monolayer is only approximately comparable to the exponential attenuation experienced in a bulk material, as shown by the piece-wise linear form of the A_s-t plots.

Throughout this work only simple overlayer structures were seen in LEED. All the metal deposits formed an initial $p(1 \times 1)$ epitaxial monolayer with no ordered submonolayer structures observed, with the exception of palladium on copper (100) where a $c(2 \times 2)$ surface alloy was formed. This is in contrast with many studies in which a wide variety of submonolayer structures were found (see the review by Biberian and Somorjai 1979) and is a consequence of the similar natures of the materials used. With the exception of iron, all crystallise naturally in the fcc structure of the substrate materials at room temperature with lattice spacings within approximately 10% of each other. Initial growth was either a $p(1 \times 1)$ lattice gas or the formation of pseudomorphic monolayer platelets at submonolayer coverages.

10.3 Overlayer Electronic Structure

The use of angle resolved photoemission enabled the development of the electronic structure of an overlayer to be followed through characteristic phases of differing dimensionality. Aspects of the electronic

structure of low dimensional metallic systems have been discussed by Binns et al (1982). At extremely low coverages of the $p(1 \times 1)$ lattice gas of palladium adsorbed on silver (100) a single spin-orbit split resonant bound state could be identified and by fitting Lorentzians to the difference spectrum the magnitude of the spin-orbit coupling (0.35 eV) and the hybridisation with the substrate s-band (0.30 eV) estimated. A similar but non-spin orbit split feature was seen for low coverages of copper on silver (100) and for iron on silver (100) at a photon energy of 120 eV a doublet was seen at 0.2 ml. This was tentatively identified as arising from a magnetic exchange split resonant bound state. The exchange splitting of 1.9 eV was similar to the value predicted for an isolated interstitial iron impurity in silver (Podloucky et al 1980).

On increasing the coverage two dimensional islands were formed and the development of a band structure within these islands observed. Dispersion of the features in palladium emission for palladium overlayers on silver (111) could be discerned at 0.25 ml and at 0.5 ml the dispersion was that of the monolayer with a reduced bandwidth. At one monolayer the two dimensional dispersion of the monolayer bands of palladium on silver (100) and silver (111) and copper on silver (100) could be plotted out and compared with calculated isolated monolayer band structures. The validity of this procedure and the degree of agreement with theory is discussed in section 10.4 below. Although photoemission probes only short range order and it is not clear if the difference between ferromagnetic and antiferromagnetic ordering can be distinguished, measurements made on well characterised overlayers can give valuable information. The controversial results at present available on magnetic overlayers were discussed in Chapter 9, section 9.6.

For palladium on silver (100) an increase in the number of features in the overlayer emission were detected on going from one to two

monolayers coverage, probably as a result of scattering of the palladium d-states between the parallel layers. The theoretical basis for such an effect has recently been proposed by Loly and Pendry (1982). A similar increase in the number of spectral features has been observed for xenon layers on aluminium (111) but explained in terms of a layer dependent shift in the emission lines from the rare gas (Mandel et al 1982).

When the coverage was increased beyond one monolayer bulk-like spectral features were seen to develop rapidly; at 3 ml a surface sensitive feature was detected for palladium on silver (111) corresponding to that observed by Weng and El-Batanouny (1980) in their study of palladium growth on niobium (110). Bulk-like emission was seen from three monolayers of copper, iron and palladium on silver (100), and four monolayers of nickel on silver (100).

10.4 Two Dimensional Energy Bands

With the advent of layer KKR, self-consistent local orbital (SCLO), and linear rigorous cellular (LRC) methods, among others, the calculation of band structures for thin slabs of material has reached a high degree of precision with the effects of surface states, spin-orbit coupling and magnetic exchange splitting being included in state of the art work. The prototype slab calculation is that of an isolated monolayer, a structure not readily open to experimental investigation. An experimental monolayer must be supported on a substrate and the interaction between the electron states of the overlayer and the substrate govern the degree to which this structure approaches the perfect two-dimensional nature of an isolated monolayer. A standard test is to observe the dispersion of the overlayer bands with k_{\perp} (the component of momentum normal to the surface) by varying the photon energy in normal

emission photoelectron spectroscopy. Systems which show flat bands in the \underline{k} direction include transition metal intercalates (Beal 1979), rare gas monolayers on palladium (100) (Hermann et al 1980), chalcogenide layers on aluminium (111) (Jacobi et al 1980), segregated layers at the (111) surface of a CuNi alloy (Heimann et al 1981) and it is believed that the transition metal overlayers on silver (100) and silver (111) of the present work also exhibit this behaviour.

Experimental two dimensional dispersion relations were obtained for palladium on silver (100) and silver (111), and for copper on silver (100). In the case of palladium on silver (111) no calculations exist in the literature with which the results may be compared. For palladium on silver (100) the experimentally-derived points in $E-\underline{k}_{//}$ space were compared with the self-consistent scalar relativistic isolated monolayer bands of Noffke and Fritsche (1981). Fair overall agreement was seen between theory and experiment, especially at the $\bar{\Gamma}$ point and along the $\bar{\Sigma}$ direction of the (100) SBZ. The similarity between theory and experiment was consistent with small charge transfer and suggested that, in this case, the supported layer represented a good approximation to an isolated monolayer in spite of the 5% lattice mismatch and hybridisation with the substrate 5s band. The 11.5% lattice mismatch between the (100) planes of bulk copper and silver was found to have a significant effect on the comparison between theory and experiment for the two-dimensional energy bands of the copper monolayer adsorbed on silver (100). Using the (interatomic spacing)⁻⁵ bandwidth dependence proposed by Heine (1967) the experimental width was scaled accordingly and a rigid shift of 1.2 eV to higher binding energy applied to align the experimental points with the self-consistent theoretical bands of Arlinghaus et al (1979). Again, fair overall agreement was found although predicted bands separated by less than the energy resolution of the analyser could not be distinguished.

Hybridisation with the substrate s-band may have accounted for some discrepancy between theory and experiment, especially the poor agreement at higher binding energies along the $\bar{\Gamma}$ \bar{X} direction.

The photon energy dependence of the cross-section for photoemission was such that, at one monolayer, spectra at 21.2 eV (HeI) from iron and nickel overlayers on silver (100) were dominated by the substrate emission. For iron in particular, features in the overlayer emission were difficult to discern and all apparent dispersion in the off-normal spectra could be traced to variations in the substrate s-band and to the HeI- β satellite of the substrate d-band emission. As a result, mapping of the two-dimensional energy bands of the overlayer was not possible, although features in the difference spectrum appeared to coincide with those predicted from an exchange split monolayer band structure. To obtain reasonable intensity in the iron emission the photon energy was increased to 120 eV using synchrotron radiation but the angular resolution of the analyser was such that at this energy a sample over a significant region of the BZ was obtained and the spectra reflected the DOS. The band-mapping experiment was not attempted for nickel overlayers.

10.5 Surface States

In principle all the electron states of an overlayer may be considered to be surface states since they are localized in the surface layer of the composite overlayer/substrate material and show two-dimensional dispersion, however, this section is concerned with surface states of the bulk materials and their modification on adsorption of metal overlayers. A discussion of the clean copper and silver surfaces and their intrinsic surface states was given in Chapter 4, sections 4.3 and 4.4. In photoemission, surface states are generally detected by observing the spectra before and after adsorption of an overlayer material,

preferential attenuation of a certain feature indicating its surface sensitive nature. Verification of two-dimensional dispersion in ARPES then confirms the feature as a surface state. A systematic survey of photoemission from the copper (100) surface was carried out by Heimann et al (1979) and the surface state bands near the \bar{M} point predicted by Gay et al (1979) detected. In the present work preferential attenuation of the principal copper (100) feature at 2.7 eV in HeI normal emission was seen on adsorption of palladium. The calculation of Gay and co-workers showed high densities of surface states at $\bar{\Gamma}$ at 2.20 eV and 2.98 eV, with attenuation of the experimental 2.7 eV feature corresponding to the predicted energy of 2.98 eV. The experimental angle-resolved spectrum shows a weak shoulder at 2.16 eV due to a high DOS at the \bar{M} point. Angle integrated PES show an intensity maximum at this energy which shows surface sensitive behaviour (Binns 1981), confirming the results of Gay and co-workers.

There does not appear to be such satisfactory agreement between theory and experiment for surface states on the silver (100) surface. For normal emission at 21.2 eV several surface sensitive features may be identified. Adsorption of palladium, copper, iron and nickel produces attenuation of the features in the spectrum at 6.36 eV and 6.90 eV, with the 6.90 eV feature being attenuated relatively rapidly compared to that at 6.36 eV. This behaviour was shown in Chapter 8, figure 8.4, and was discussed in section 8.5. The surface sensitive nature of the most intense silver (100) peak at 5.06 eV is shown in figure 5.2 where adsorption of palladium up to one monolayer causes rapid attenuation of the feature. Smith et al (1980) have calculated the electronic structure of silver (100) with particular reference to surface states using the method of Gay et al (1979). Their predicted binding energies for surface states at $\bar{\Gamma}$ are 3.27, 3.42, 4.20, 5.27 and 5.88 eV. The experimentally observed surface sensitive

features of the present work lie at 5.06, 6.36 and 6.90 eV respectively and clearly there is not immediate agreement with the results of Smith et al (1980). Application of a rigid shift to the theoretical surface states of ~ 1 eV to higher binding energy results in approximate agreement between theory and experiment for the three states of higher binding energy. The calculated work function was 4.2 eV and the error here compared to the experimental value of 4.65 eV is not large enough to account for this 1 eV shift. The calculations also predicted a surface state at \bar{M} which could not be located in ARPES (Lindroos et al 1982) and it appears that further refinements of the already sophisticated theoretical techniques are required before surface states may be accurately predicted.

10.6 Calculation of Photoelectron Spectra

Throughout this work the time-reversed LEED formalism of Pendry (1976) as implemented by Hopkinson et al (1979) has been used to calculate photoemission spectra for both the clean and adsorbate covered surfaces studied. The program in the form available at Daresbury Laboratory is known as "PEOVER" and has been used for a variety of studies of clean metal surfaces. Pendry and Hopkinson (1978) have investigated photoemission and the effects of inverse lifetime in nickel and copper, emission from copper, nickel and palladium in the higher ($\lesssim 90$ eV) photon energy range has been studied (Kanski et al 1980, Nilsson et al 1980, 1981) and the method has been used to probe surface states on silver (100) (Lindroos et al 1982) and as a basis for monitoring the temperature dependence of photoemission from metals (Larsson and Pendry 1981). The only documented calculation of photoemission from an overlayer system is that of Kar (1981), whose results for bromine on copper (100) compared favourably with the data of Richardson and Sass (1981).

The program derives the photoemission spectrum directly from the geometric and electronic input parameters without proceeding via a

calculated band structure and as such is a direct test of the potential; in addition information contained in the relative intensities of features which is usually ignored in band structure mapping is used. In the present work the program was applied to synchrotron radiation excited photoemission from silver (100) (Padmore et al 1982) and palladium (111) (Binns et al 1982). Photoemission from all the substrate materials and overlayer-substrate combinations described in this thesis was also modelled using the theory, with the most successful application being to the copper on silver (100) system. In this case a series of calculations was performed involving variation of the geometry and of the potential, initial and final state lifetimes and surface barrier. The resultant normal emission spectrum at 21.2 eV showed a degree of correspondence between theory and experiment that is very encouraging for future work.

The photoemission calculations have highlighted certain effects of the approximations in the photoemission program. Energy-independent initial and final state lifetimes result in distortion of the relative magnitudes of overlayer and substrate emission, an effect compounded by the photoionization cross-section for the different overlayer and substrate bands. In addition, the overlayer and substrate materials may have different lifetimes and this cannot be allowed for. Surface states are extremely sensitive to the form of the surface barrier and the abrupt step potential used in PEOVER must be regarded as a rather severe approximation in this context, although good results are obtained for bulk states. The band structures obtained from the program correspond closely to the results of self-consistent calculations using the same potential. For the heavier elements silver and palladium some lack of agreement between theory and experiment may be due to spin-orbit interaction which, at $\sim .4$ eV, is not negligible and cannot be provided for in the calculation at present. In the calculations for iron and nickel the more serious

problem of ferromagnetism was encountered. The large ferromagnetic valence band exchange splitting (≈ 2 eV in iron) could not be included in the calculations; indeed, lack of agreement between theory and experiment was taken to be evidence of ferromagnetism.

Energy dependent lifetimes and an improved cross section have been included in photoemission calculations (Pendry and Hopkinson 1978, Kanski et al 1981), some suggestions for further modifications are made in the following section.

10.7 Suggestions for Further Work

An adsorbed metal monolayer represents a particularly significant state of matter, whose electronic properties may be radically different from the bulk material. These properties are very dependent on the particular geometry and orientation of the layer under investigation. Photoemission remains the best probe of electronic structure despite its inherent limitations but it is essential that photoemission studies are carried out on well-characterised surfaces and overlayers. Experiments using a quartz crystal thickness monitor without additional structural probes are inadequate; such experiments would not detect the structural differences of the magnetic as-deposited and non-magnetic annealed iron layers of Binns et al (1982) for example.

The adsorbed metal overlayer represents the basic unit of the layered ultra-thin coherent structure (LUCS) which are currently attracting attention (Jahlborg and Freeman 1980, Schuller 1980) and appear to have interesting or unusual magnetic and superconducting properties (Schuller and Falco 1979, Banerjee et al 1982, Brodsky and Freeman 1980, Brodsky 1982). The importance of accurate surface science measurements on these systems has been demonstrated by the results of Chapter 5 concerning palladium overlayers on silver (100) where a low DOS at E_F at 1 ml was

found in contradiction to the proposed explanation of Brodsky and Freeman (1980) for their observed increase in the paramagnetic susceptibility of a palladium-gold (100) multilayer structure.

The importance of good surface characterisation for magnetic overlayer measurements has been discussed (Chapter 9); with the considerations above in mind suggestions are now made for further experimental and theoretical development of the work of this thesis.

10.7.1 Experimental Development

The first stage of investigation of the properties of an overlayer is characterisation of the growth mode and this requires As-t plots of high quality and low noise. The production of such plots would be facilitated by an automated monitoring device such as used by Guglielmacci and Gillet (1980) in which the Auger intensity is continuously monitored during deposition using a multiplexed cylindrical mirror analyser (CMA).

The present double-crucible design of evaporator (Chapter 3) appears to be suitable for temperatures up to 1150 to 1200°C. It has been proposed that vanadium may become magnetic if subjected to a lattice expansion such as by adsorption on a crystal surface or when in fine cluster form (Akoh and Tasaki 1978, Yokoyama et al 1981) so a photoemission study of vanadium layers on silver (100) would be of interest. Ruthenium overlayers on copper (100) are of interest for their catalytic properties, however, for materials such as these very high evaporation temperatures are required, on or above the limit of the present device. Preliminary measurements on an electron beam heated device indicate that very high temperatures may be reached (vanadium rod was melted) but further work is required to investigate the reliability and temperature stability of such a device.

Experiments that should be carried out using the present equipment include a photoemission study of the magnetic nature of nickel films on

silver (100) (Chapter 8). Use should be made of dipole selection rules and the polarization of synchrotron radiation exploited in order to suppress unwanted emission and highlight direct transitions from the exchange split overlayer bands at selected points of the SBZ.

Loly and Pendry (1982) have recently suggested a mechanism to account for the increase in the number of spectral features seen in photoemission from certain overlayer systems on increasing the coverage above the monolayer. Their example calculations cited the silver on palladium (100) system as favourable for this study and measurements using HeI radiation could proceed at once. The calculations, claiming to remove the limits to accurate band structure determination by photoemission, ignored the effect of spin-orbit interaction and predicted peaks of width $\lesssim 150$ meV, rather narrower than is usually seen in photoemission from a solid material.

In view of the rapidly increasing number of experiments being carried out on magnetic overlayers (reviewed in Chapter 9) it is of importance to introduce direct magnetic measurements into the vacuum chamber. Anomalous Hall Effect measurements, after Bergmann (1982), or Mossbauer studies seem suited to this kind of work although the experimental difficulties might be prohibitive at this stage. Refinement of sample manipulation to include liquid helium cooling would be required, and the introduction of magnets into the experimental region poses problems for electron spectroscopy. Possibly provision of two chambers, one for in situ magnetic measurements and one for surface characterisation, linked by a gate valve and sample transfer mechanism (at liquid helium temperature) may enable these problems to be overcome. Alternatively, detection of the spin polarization of the photoemitted electron, after the manner of Eib and Alvarado (1976), Dempsey and Kleinman (1977) and Clauberg et al (1981), may give sufficient information concerning the magnetic state of

a well characterised overlayer.

10.7.2 Theoretical Development

Calculations of photoemission from adsorbed metal overlayers should be continued. The work described in Chapter 7 on copper overlayers on silver(100) shows that it is possible to obtain good agreement between theoretical and experimental spectra using the standard version of PEOVER. There appears to be two routes for the development of these calculations to take: first, the approximations in the program must be improved, and second, an increased flexibility to enable more complex systems to be studied is required.

Surface states and resonances are extremely sensitive to the form of the surface barrier and the step form of the barrier assumed in the calculation of photoelectron spectra is quite a severe approximation. An exponential or parameterised fit to surface state bands, after Gurman (1976) would seem appropriate. The provision of energy dependent lifetimes of the initial and final state has been shown to improve agreement between theory and experiment for bulk materials (Pendry and Hopkinson 1973, Kanski et al 1981), and these effects must be included in the calculation if accurate positions, widths and intensities of overlayer and substrate emission bands are to be predicted. A related question is the temperature dependence of photoelectron spectra. A model of temperature dependence has been developed by Larsson and Pendry (1981) and is suitable for incorporation into the program. Improved cross-sections for photoemission are also available and should be incorporated (Nilsson et al 1981).

To extend the range of materials that can be studied adaptation of the input format to include spin-split potentials is desirable. In this way the effect of spin-orbit interaction, and of the much larger

magnetic exchange splitting of the ferromagnets, on the spectra could be investigated. In addition, provision for more than one atom type per layer would enable study of alloys, and with random positioning the random substitutional alloys could be investigated. Extension of this to disordered overlayers and materials would, however, be extremely complex.

Given reliable muffin-tin potentials the agreement between theory and experiment could be used as a check of overlayer structure and geometry in the manner of photoelectron diffraction experiments. A "reliability factor" similar to those used in LEED calculations would need to be defined.

The systems studied in this thesis were specifically chosen to have minimal overlayer-substrate charge transfer, however, this will not generally be the case. A study of the effects of charge transfer on the potential, such as by self-consistent calculation of the work function, is indicated. To this end calculations of the electronic structure of overlayer-substrate combinations, similar to those of Bisi and Calandra (1977) would be of assistance. More sophisticated self-consistent techniques, however, are required. The layer R.A.P.W. program currently under development at Daresbury Laboratory would seem ideally suited to this purpose.

REFERENCES

1. H. Akoh and A. Tasaki. J. Appl. Phys. 49 (1978) 1410
2. G. Allan. Surface Sci. Reports 1 (1981) 121
3. S.L. Altmann. "Band Theory of Metals", Pergamon, Oxford (1970)
4. O.K. Anderson, J. Madsen, U.K. Poulsen, O. Jepsen and J. Kollar, Physica 86-88B (1977) 249
5. P.W. Anderson. Phys. Rev. 124 (1961) 41
6. S. Anderson and W. Jostell. Surface Science 46 (1974) 625
7. C. Argile and G.E. Rhead. Thin Solid Films 67 (1980) 299
8. F.J. Arlinghaus, J.G. Gay and J.R. Smith. Phys. Rev. B20 (1979) 1332 and refs. therein
9. F.J. Arlinghaus, J.G. Gay and J.R. Smith. Phys. Rev. B23 (1981) 5152
10. N.W. Ashcroft and D.C. Langreth. Phys. Rev. 155 (1967) 682
11. N.W. Ashcroft and W.L. Schaich, in Proceedings of the Density of States Symposium (NBS, 1969)
12. H. Asonen, M. Lindroos, M. Pessa and N. Dahlback. Solid State Commun. 35 (1980) 69
13. P. Auger. J. Phys. Radium 6 (1925) 205
14. R. Z. Bachrach, in "Crystal Growth" Ed B.R. Pamplin, 2nd Ed., Chap. 6 pp 221-274 (1981)
15. I. Banerjee, Q.S. Yang, C.M. Falco and I.K. Schuller, Solid State Commun. 41 (1982) 805
16. A. Bansil, H. Ehrenreich, L. Schwartz and R.E. Watson. Phys. Rev. B9 (1974) 445
17. U. von Barth and L. Hedin. J. Phys. C5 (1972) 1629
18. M-G Barthes and G.E. Rhead. Surface Science 80 (1979) 421
19. M-G Barthes and G.E. Rhead. J. Phys. D13 (1980) 747
20. M-G Barthes and A. Rolland. Thin Solid Films 76 (1981) 45
21. E. Bauer. Z. Crystallogr. 110 (1958) 372
22. E. Bauer and H. Poppa. Thin Solid Films 12 (1972) 167
23. A.R. Beal. "Intercalated Layer Materials" 251-305, Ed. F. Levy (Reidel 1979)

24. C.N. Berglund and W.E. Spicer. Phys. Rev. 136 (1964) A 1030
25. G. Bergmann. Phys. Rev. Letts 41 (1978) 264
26. G. Bergmann. Physics Today (August 1979) 25 and refs. therein
27. G. Bergmann. Phys. Rev. B23 (1981) 3805
28. J.P. Biberian and G.A. Somorjai. J. Vac. Sci and Technol. 16 (1979) 2073
29. C. Binns. Leicester University Ph.D. Thesis (1981)
30. C. Binns and C. Norris. Surface Science 115 (1982) 395
31. C. Binns and C. Norris. Surface Science 116 (1982) 338
32. C. Binns, C. Norris, I. Lindau, M.L. Shek, B. Pate, P.M. Stefan and W.E. Spicer. Solid State Commun. (1982)
33. C. Binns, C. Norris, G.C. Smith, H.A. Padmore and M-G Barthes-Labrousse. Proceedings 5th European Conf. on Surface Science (ECOSS-5), Gent (1982); in special issue of Surface Science
34. C. Binns, G.C. Smith, C. Norris, H.A. Padmore and G.P. Williams. to be published
35. O. Bisi and C. Calandra. Surface Science 67 (1977) 416
36. J.S. Blakemore. "Solid State Physics", W.B. Saunders & Co. London, 2nd Ed. (1974)
37. F. Bloch. Z. Physik 52 (1928) 555
38. M. Born and J.R. Oppenheimer. Ann. Physik 84 (1927) 457
39. G. Broden and H.P. Bonzel. Surface Science 19 (1970) 403
40. M. Brodsky. Phys. Rev. B25 (1982) 6060
41. L.A. Bruce and H. Jaeger. Philos Mag. 36 (1977) 1331
42. G.A. Burdick. Phys. Rev. 129 (1963) 138
43. G.N. Burland and P.J. Dobson. Thin Solid Films 75 (1981) 383
44. J. Callaway and C.S. Wang. Phys. Rev. B16 (1977) 2095
45. M. Cardona and L. Ley (Eds). "Photoemission in Solids: 1, General Principles", Springer-Verlag, New York (1978)
46. A. Cardwell. Phys. Rev. 92 (1953) 554
47. N.E. Christensen. Phys. Stat. Solidi (b) 54 (1972) 551
48. N.E. Christensen. Phys. Rev. B14 (1976) 3446

49. N.E. Christensen. Solid State Commun. 37 (1981) 57
50. N.E. Christensen. Solid State Commun. 38 (1981) 309
51. M.I. Chodorow. Ph.D. Thesis, M.I.T. (1939)
52. M.F. Chung and L.H. Jenkins. Surface Science 22 (1970) 479
53. R. Clauberg, W. Gudat, E. Kisker, E. Kuhlman and G.M. Rothberg. Phys. Rev. Letts 47 (1981) 1314
54. K. Codling. Nucl. Inst. and Methods 172 (1980) 137
55. R. Courths. Solid State Commun. 40 (1981) 529
56. R. Courths, V. Bachelier and S. Huffner. Solid State Commun. 38 (1981) 887
57. S.G. Das, D.D. Koelling and F.M. Mueller. Solid State Commun. 12 (1973) 89
58. C.J. Davisson and L.H. Germer. Phys. Rev. 30 (1927) 705
59. D.G. Dempsey, W.R. Grise and L. Kleinman. Phys. Rev. B18 (1978) 1270
60. D.G. Dempsey and L. Kleinman. Phys. Rev. Letts 39 (1977) 1297
61. J.E. Demuth. Chem. Phys. Letts 45 (1977) 12
62. S. Dushman. "Scientific Foundations of Vacuum Techniques", Wiley, New York (1949)
63. A.W. Dweydari and C.H.B. Mee. Phys. Stat. Solidi (a) 27 (1975) 223
64. D.E. Eastman and W.D. Grobman. Phys. Rev. Letts 30 (1973) 177
65. D.E. Eastman, F.J. Himpsel and J.A. Knapp. Phys. Rev. Letts. 40 (1978) 1514
66. D.E. Eastman, F.J. Himpsel and J.A. Knapp. Phys. Rev. Letts. 44 (1980) 95
67. W. Eberhardt and E.W. Plummer. Phys. Rev. B21 (1980) 3245
68. W. Eberhardt, E.W. Plummer, K. Horn and J. Erskine. Phys. Rev. Letts. 45 (1980) 273
69. E. Eib and S.F. Alvarado. Phys. Rev. Letts. 37 (1976) 444
70. M. El-Batanouny, M. Strongin, G.P. Williams and J. Colbert. Phys. Rev. Letts. 46 (1981) 269
71. B. Feuerbacher, B. Fitton, R.F. Willis (Eds), "Photoemission and the Electronic Properties of Surfaces", Wiley-Interscience, New York (1978)

72. F.C. Frank and J.H. van der Merwe. Proc. Royal Soc. (London) A198 (1949) 205, 216
73. A. Franks, K. Lindsey, J.M. Bennett, R.J. Speer, D. Turner and D.J. Hunt. Philos. Trans. A277 (1975) 503
74. J. Friedel. Nuovo Cim. Suppl. 7 (1958) 287
75. L. Fritsche, M. Rafatmehr, R. Glocker and J. Noffke. Z. Physik B33 (1979) 1
76. Y. Fujinaga. Surface Science 84 (1979) 1
77. Y. Fujinaga. Surface Science 86 (1979) 581
78. R. Gaspar. Acta. Phys. Acad. Sci. Hung. 3 (1954) 263
79. P.O. Gartland. Phys. Norv. 6 (1972) 201
80. J.G. Gay, J.R. Smith and F.J. Arlinghaus. Phys. Rev. Letts. 42 (1979) 332
81. M. Gell-Mann and M.L. Goldberger. Phys. Rev. 91 (1953) 398
82. R.L. Gerlach and T.N. Rhodin. Surface Science 19 (1970) 403
83. I. Gonzalez, R. Miranda, M. Salmeron, J.A. Verges and F. Yndurain. Proc. 3rd European Conf. on Surface Science (ECOSS-3) Cannes (1980); Phys. Rev. B24 (1981) 3245
84. K. Goto, K. Ishikawa, T. Koshikawa and R. Shimizu. Surface Science 47 (1975) 477
85. U. Graismann. Appl. Phys. 3 (1974) 161
86. U. Graismann and H.O. Isbert. J. Mag. and Mag. Mater. 15-18 (1980) 1109
87. D.E. Gray (Ed), American Institute of Physics Handbook, Third Ed. (1972) McGraw-Hill, New York
88. B. Gruzza and E. Gillet. Thin Solid Films 68 (1980) 345
89. J.M. Guglielmacci and M. Gillet. Thin Solid Films 68 (1980) 407
90. J.M. Guglielmacci and M. Gillet. Surface Science 105 (1981) 386
91. J.M. Guglielmacci and M. Gillet. J. Cryst. Growth 57 (1982) 155
92. J.M. Guglielmacci and M. Gillet. Thin Solid Films 88 (1982) 247
93. C. Guillot, Y. Ballu, J. Paigne, J. Lecante, K.P. Jain, P. Thiry, R. Pinchaux, Y. Petroff and L.M. Falicov. Phys. Rev. Letts. 39 (1977) 1632
94. S.J. Gurman. J. Phys. C9 (1976) L609

95. R.W. Gurney. Phys. Rev. 28 (1926) 341
96. E.P. Gyftopoulos and J.D. Levine. J. Appl. Phys. 33 (1962) 67
97. M. Hansen and K. Anderko. "Constitution of Binary Alloys", 2nd Ed, McGraw-Hill, New York (1958)
98. G.V. Hansson and S.A. Flodstrom. Phys. Rev. B18 (1978) 1572
99. L.A. Harris. J. Appl. Phys. 39 (1968) 1419
100. D.R. Hartree. Proc. Cambridge Phil. Soc. 24 (1928) 89
101. A. Haug. "Theoretical Solid State Physics", Vol. 1, Pergamon, Oxford (1972)
102. D.W.O. Heddle. J. Phys. E4 (1971) 589
103. F. Herman and S. Skillman. "Atomic Structure Calculations", Prentice-Hall, London (1963)
104. K. Hermann, J. Noffke and K. Horn. Phys. Rev. B22 (1980) 1022
105. C. Herring. Phys. Rev. 57 (1940) 1169
106. P. Heimann, J. Hermanson and H. Miosga. Phys. Rev. B20 (1979) 3059
107. P. Heimann, J. Hermanson, H. Miosga and H. Neddermeyer. Solid State Commun. 37 (1981) 519
108. P. Heimann, F.J. Himpsel and D.E. Eastman. Solid State Commun. 39 (1981) 219
109. P. Heimann and H. Neddermeyer. J. Phys. F6 (1976) L257
110. P. Heimann, H. Neddermeyer and H.F. Roloff. Phys. Rev. Letts. 37 (1976) 775
111. P. Heimann, H. Neddermeyer and H.F. Roloff. Proc. 3rd Intern. Vac. Congr. and 3rd Intern. Conf. on Solid Surfaces, Vienna (1977)
112. V. Heine. Phys. Rev. 153 (1967) 673
113. F.J. Himpsel and D.E. Eastman. Phys. Rev. B18 (1978) 5236
114. F.J. Himpsel, J.A. Knapp and D.E. Eastman. Phys. Rev. B19 (1979) 2919
115. H. Hochst, A. Goldmann and S. Hufner. Z. Phys. B24 (1976) 245
116. H. Hochst, S. Hufner and A. Goldmann. Z. Phys. B26 (1977) 133
117. J.F.L. Hopkinson, J.B. Pendry and D.J. Titterton. Comp. Phys. Commun. 19 (1980) 69; Daresbury Preprint DL/SCI/P190T (July 1979)

118. M.R. Howells. Nucl. Inst. and Methods 172 (1980) 123
119. M.R. Howells, D. Norman, G.P. Williams and J.B. West. J. Phys. E11 (1978) 199
120. S. Hufner, G.K. Wertheim, J.H. Wernick. Solid State Commun. 17 (1975) 1585
121. D.C. Jackson, T.E. Gallon and A. Chambers. Surface Science 36 (1973) 381
122. J.D. Jackson. "Classical Electrodynamics", Wiley, New York, (1962)
123. K. Jacobi, C.V. Muschwitz and K. Kambe. Surface Science 93 (1980) 310
124. R.J. Jacobs. J. Phys. C1 (1968) 1296, 1307
125. J.F. Janak. Phys. Rev. B9 (1974) 3985
126. T. Jarlborg and A.J. Freeman. Phys. Rev. Letts 45 (1980) 653
127. O. Jepsen, J. Madson and O.K. Anderson. Phys. Rev. B18 (1978) 605
128. D.J. Joyner, O. Johnson and D.M. Hercules. J. Phys. F10 (1980) 169
129. T. Kanaji, Y. Taki and T. Urano. Jpn. J. Appl. Phys. 19 (1980) 371
130. E.O. Kane. Phys. Rev. Letts. 12 (1964) 97
131. J. Kanski, P.O. Nilsson and C-G Larsson. Solid State Commun. 35 (1980) 397
132. N. Kar. J. Phys. C14 (1981) 2185
133. D. Kashchiev. J. Cryst. Growth 40 (1977) 29
134. S.R. Kelemen and I.E. Wachs. Surface Science 97 (1980) L370
135. D.J. Kennedy and S.T. Manson. Phys. Rev. A5 (1972) 227
136. W. Keune, R. Halbauer, U. Gonser, J. Lauer and D.L. Williamson. J. Appl. Phys. 48 (1977) 2976
137. C. Kittel. "Introduction to Solid State Physics", Wiley, London, 5th Ed (1976)
138. H. Kobayashi and S. Kato. Surface Science 18 (1969) 341
139. K.S. Kohn, D.G. Dempsey, L. Kleinman and E. Caruthers. Phys. Rev. B13 (1976) 1515

140. W. Kohn and N. Rostoker. Phys. Rev. 94 (1954) 1111
141. W. Kohn and L.J. Sham. Phys. Rev. 140 (1965) A1133
142. D.M. Kolb, W. Boeck, K-M Ho and S.H. Liu. Phys. Rev. Letts. 47
(1981) 1921
143. J. Koringa. Physica 13 (1947) 392
144. T. Koshikawa, T. von dem Hagen and E. Bauer. Surface Science
109 (1981) 301
145. S.P. Kowalczyk. Thesis (1976) Berkeley (LBL report no. 4319)
146. W. Kummerle and U. Gradmann. Solid State Commun. 24 (1977) 33
147. C. Kunz, in "Photoemission and the Electronic Properties of
Surfaces", B. Feuerbacher, B. Fitton and R. Willis (Eds) Wiley,
New York (1978)
148. C. Kunz, in "Photoemission in Solids", L. Ley and M. Cardona (Eds),
Vol. 11, Chap. 6, Springer-Verlag, Berlin (1979)
149. J.J. Lander. Phys. Rev. 91 (1953) 1382
150. N.D. Lang. Phys. Rev. B4 (1971) 4234
151. N.D. Lang and W. Kohn. Phys. Rev. B3 (1971) 1215
152. I. Langmuir. J. Am. Chem. Soc. 54 (1932) 2798
153. C-G Larsson and J.B. Pendry. J. Phys. C14 (1981) 3089
154. L.B. Leder and J.A. Simpson. Rev. Sci. Instrum. 29 (1958) 571
155. J.E. Lennard-Jones. Proc. Phys. Soc. 52 (1940) 38
156. L.N. Liebermann, D.R. Fredkin and H.B. Shore. Phys. Rev. Letts.
22 (1969) 539
157. L.N. Liebermann, J. Clinton, D.M. Edwards and J. Mahon. Phys. Rev.
Letts. 25 (1970) 232
158. L.N. Liebermann and J. Clinton. Proc. 18th Ann. Conf. on Mag.
and Mag. Mater., AIP Conf. Proc. 10 (1972) 1531
159. D. Liebowitz and N.J. Shevchik. Phys. Rev. B17 (1978) 3825
160. D. Liebowitz and N.J. Shevchik. Phys. Rev. B18 (1978) 1630
161. A. Liebsch. Phys. Rev. Letts. 32 (1974) 1203
162. I. Lindau and S.B.M. Hagstrom. J. Phys. E4 (1971) 936
163. S.A. Lindgren and L. Wallden. Phys. Rev. Letts. 43 (1979) 460

164. M. Lindroos, H. Asonen, P. Pessa and N.V. Smith. Solid State Commun. 39 (1981) 285
165. M. Lindroos, P. Huttunen, M. Pessa, G.V. Hansson, U.O. Karlsson and A.H. El-Farrash. J. Phys. F12 (1982) L71
166. B.A. Lippmann and J. Schwinger. Phys. Rev. 79 (1950) 469
167. D.R. Lloyd, C.M. Quinn and N.V. Richardson. Surface Science 63 (1977) 174
168. D.R. Lloyd, C.M. Quinn and N.V. Richardson. Solid State Commun. 22 (1977) 721
169. P.D. Loly and J.B. Pendry. Imperial College Preprint SST/8182/21; submitted to J. Phys. C, July 1982
170. T. Mandel, W.D. Schneider, W. Fischer and G. Kaindl. Proc. 5th European Conference on Surface Science (ECOSS-5) Gent (1982); in special edition Surface Science
171. L.F. Mattheiss. Phys. Rev. A133 (1964) 1399
172. F.R. McFeely, S.P. Kowalczyk, L. Ley and D.A. Shirley. Solid State Commun. 15 (1974) 1051
173. N.D. Mermin and H. Wagner. Phys. Rev. Letts. 17 (1966) 1133
174. R. Miranda, F. Yndurain, D. Chandesris, J. Lecante and Y. Petroff. Phys. Rev. B25 (1982) 527
175. K.P. Miyake, R. Kato and H. Yamashita. Sci. Light 18 (1969) 39
176. V.L. Moruzzi, J.F. Janak and A.R. Williams. "Calculated Electronic Properties of Metals", Pergamon, New York (1978)
177. I.H. Munro. Daresbury Laboratory Technical Memorandum DL/SCI/TM 23E, October (1981)
178. J.P. Muscat and D.M. Newns. J. Phys. C7 (1974) 2630
179. R.G. Musket, W. McLean, C.A. Colmenares, D.M. Makowiecki and W.J. Siekhaus. Applications of Surf. Sci. 10 (1982) 143
180. V.V. Nemoshkalenko, M.G. Chudinov, V.G. Aleshin, Y.N. Kucherenko and L.J. Sheludchenko. Solid State Commun. 16 (1975) 755
181. D.M. Newns. Phys. Rev. 178 (1969) 1123
182. P.O. Nilsson, J. Kanski and C-G Larsson. Solid State Commun. 36 (1980) 11
183. P.O. Nilsson, C-G Larsson and W. Eberhardt. Phys. Rev. B24 (1981) 1739
184. J. Noffke and L. Fritsche. J. Phys. C14 (1981) 89

185. C. Norris and H.P. Myers. J. Phys. F1 (1971) 62
186. M. Ohno and G. Wendin. J. Phys. C15 (1982) 1787
187. H.A. Padmore, C. Norris, G.C. Smith, C-G Larsson and D. Norman.
J. Phys. C15 (1982) L155
188. B.R. Pamplin (Ed), Special Issue of Progress in Crystal Growth, on
the subject of MBE (1980)
189. L. Pauling. "The Nature of the Chemical Bond", 3rd ed, Cornell
University Press, New York (1960)
190. J. Perdureau, J.P. Biberian and G.E. Rhead. J. Phys. F4 (1974)
798
191. J.B. Pendry, "Low Energy Electron Diffraction", Wiley-Interscience,
New York (1974)
192. J.B. Pendry. J. Phys. C8 (1975) 2413
193. J.B. Pendry. Surface Science 57 (1976) 679
194. J.B. Pendry, in "Photoemission and the Electronic Properties of
Surfaces", B. Feuerbacher, B. Fitton and R.F. Willis (Eds)
Wiley-Interscience, New York (1978)
195. J.B. Pendry and J.F.L. Titterington. J. Phys. F8 (1978) 1009
196. M. Pessa, P. Heimann and H. Neddermeyer. Phys. Rev. B14 (1976)
3433
197. M. Pessa, M. Lindroos and R. Lindstrom. Solid State Commun. 32
(1979) 585
198. L. Pincherle. "Electronic Energy Bands in Solids", Macdonald,
London (1971)
199. A.J. Pindoor, W.M. Temmerman, B.L. Gyorffy and G.M. Stocks. J. Phys.
F10 (1980) 2617
200. D. Pines. "Elementary Excitations in Solids", Benjamin, New York
(1963)
201. R. Podloucky, R. Lasser, E. Wimmer and P. Weinberger. Phys. Rev.
B19 (1979) 4999
202. R. Podloucky, R. Zeller and P.H. Dederichs. Phys. Rev. B22 (1980)
5777
203. P.A. Redhead. "The Physical Basis of Ultra-High Vacua", Chapman
and Hall, London (1968)
204. N.V. Richardson and J.K. Sass. Surface Science (1981)
205. G.E. Rhead. J. Vac. Sci and Technol. 13 (1976) 603
206. H.F. Roloff and H. Neddermeyer. Solid State Commun. 21 (1977) 561

207. J.W.A. Sachtler, J.P. Biberian and G.A. Somorjai. Surface Science 110 (1981) 43.
208. W.L. Saich and N.W. Ashcroft. Phys. Rev. B3 (1971) 2452
209. W. Schlenk and E. Bauer. Surface Science 93 (1980) 9
210. I.K. Schuller. Phys. Rev. Letts. 44 (1980) 1597
211. I.K. Schuller and C.M. Falco. "Inhomogeneous Semiconductors - 1979" AIP Conf. Proc. 58 (1979) 197
212. A. Schulz, R. Courths, H. Schulz and S. Hufner. J. Phys. F9 (1979) 241
213. M.P. Seah and W.A. Dench. Surface and Interface Analysis 1 (1979) 2
214. A. Sepulveda and G.E. Rhead. Surface Science 66 (1977) 436
215. N.J. Shevchick and D. Liebowitz. Phys. Rev. B16 (1977) 2395
216. J.C. Slater. Phys Rev. 51 (1937) 846
217. J.C. Slater. Phys. Rev. 81 (1951) 385
218. G.C. Smith, C. Norris and C. Binns. Proc. 5th Interdisciplinary Surface Science Conf. (ISSC-5), Liverpool (1981); Vacuum 31 (1981) 523
219. G.C. Smith, C. Norris, C. Binns and H.A. Padmore. J. Phys. C31(1982)
220. G.C. Smith, H.A. Padmore and C. Norris. Surface Science 119 (1982) L287
221. J.R. Smith, F.J. Arlinghaus and J.G. Gay. Phys. Rev. B22 (1980) 4757
222. E.C. Snow. Phys. Rev. 171 (1968) 785
223. D.P. Spears, R. Melandor, L.G. Petersson and S.B.M. Hagstrom. Phys. Rev. B21 (1980) 1462
224. E.C. Stoner. Repts. Prog. Phys. 11 (1948) 43
225. B. Stritzker. Phys. Rev. Letts. 42 (1979) 1769
226. K. Takayanagi. Surface Science 104 (1981) 527
227. I. Tamm. Z. Physik 76 (1932) 849
228. R.A. Tawil and J. Callaway. Phys. Rev. B7 (1973) 4242
229. N.J. Taylor. Rev. Sci. Instrum. 40 (1969) 792
230. J. Tersoff and L.M. Falicov. Phys. Rev. B24 (1981) 754; Lawrence Berkeley Lab. Preprint LBL-13624 (1981)
231. P. Thiry, D. Chandesris, J. Lecante, C. Guillot, R. Pinchaux and Y. Petroff. Phys. Rev. Letts. 43 (1979) 82

232. L.N. Thorp and E.J. Scheibner. *J. Appl. Phys.* 38 (1967) 3320
233. G.G. Tibbets, J.M. Burkstrand and J.C. Tracy. *Phys. Rev.* B15 (1977) 3652
234. H. Tokutaka, K. Nishimori and K. Takashima. *Surface Science* 86 (1979) 54
235. D. Tombouljian and P.L. Hartman. *Phys. Rev.* 102 (1956) 1423
236. A.M. Turner and J.L. Erskine. *Phys. Rev.* B25 (1982) 1983
237. K. Ueda and R. Shimizu. *Jpn. J. Appl. Phys.* 11 (1972) 916
238. Varma and R.W. Hoffman. *J. Appl. Phys.* 42 (1971) 1727
239. Varma and R.W. Hoffman. *J. Vac. Sci and Technol.* 9 (1972) 177
240. J.F. van der Veen, F.J. Himpsel and D.E. Eastman. *Phys. Rev.* B22 (1980)
241. J.A. Venables, P. Akhter and J. Derrien. *Proc. 3rd European Conf. on Surface Science (ECOSS-3) Cannes* (1980)
242. J.A. Venables, J. Derrien and A.P. Janssen. *Surface Science* 95 (1980) 411
243. J.H. van Vleck. *Phys. Rev.* 45 (1934) 405
244. J.C. Walker, C.R. Guarnieri and R. Semper. *Proc. 18th Ann. Conf. on Mag. and Mag. Mater., AIP Conf. Proc.* 10 (1972) 1539
245. L. Wallien. *Solid State Commun.* 7 (1969) 593
246. C.S. Wang and J. Callaway. *Phys. Rev.* B9 (1974) 4897
247. C.S. Wang and J. Callaway. *Phys. Rev.* B15 (1977) 298
248. C.S. Wang and A.J. Freeman. *Phys. Rev.* B19 (1979) 793
249. C.S. Wang and A.J. Freeman. *Phys. Rev.* B21 (1980) 4585
250. C.S. Wang and A.J. Freeman. *J. Mag. and Mag. Mater.* 15-18 (1980) 869
251. C.S. Wang, R.E. Prange and V. Korenman. *Phys. Rev.* B25 (1982) 5766
252. R.E. Weber and W.T. Peria. *J. Appl. Phys.* 38 (1967) 2425
253. S.P. Weeks. *Phys. Rev.* B17 (1978) 1738
254. P.S. Wehner, R.S. Williams, S.D. Kevan, D. Denley and D.A. Shirley. *Phys. Rev.* B19 (1979) 6164
255. G. Wendin. *Solid State Commun.* 38 (1981) 197
256. S-L Weng and M. El-Batanouny. *Phys. Rev. Letts.* 44 (1980) 612

257. J.B. West, K. Codling and G.V. Marr. J. Phys. E7 (1974) 137
258. J.B. West and G.P. Williams. Daresbury Laboratory Technical Memorandum DL/SRF/TM 11, March (1978)
259. D. Westphal, D. Spanjaard and A. Goldmann. J. Phys. C13 (1980) 1361
260. J.G. Wright. Philos. Mag. 24 (1971) 217
261. J. Woltersdorf. Thin Solid Films 85 (1981) 241
262. E.A. Wood. J. Appl. Phys. 35 (1964) 1306
263. J. Wormald. "Diffraction Methods" (OCS10) Clarendon Press, Oxford (1973)
264. J. Yarwood. "High Vacuum Technique", Chapman and Hall, London (1967)
265. G. Yokoyama, N. Hirashita, T. Oguchi, T. Kambara and K.I. Gondaira. J. Phys. F11 (1981) 1643
266. J.M. Ziman, "Principles of the Theory of Solids", Cambridge University Press, Cambridge (1972).

APPENDIX 1Publications

"Comparison of theory and experiment for angularly resolved photoemission from Ag (001) in the photon energy range 40 to 100 eV".

H.A. Padmore, C. Norris, G.C. Smith, C-G Larsson and D. Norman,
J. Phys. C15, (1982) L155-L158, Daresbury Preprint DL/SCI/P 308E,
October 1981.

"A photoemission study of ultra-thin palladium overlayers on low-index faces of silver".

G.C. Smith, C. Norris, C. Binns and H.A. Padmore, J. Phys. C31 (1982)

"The electron states of ultra-thin Pd overlayers on Cu (100) and Ag (111)".

G.C. Smith, C. Norris and C. Binns, Vacuum 31, 10-12 (1981) 523.

"The growth of Fe overlayers on Ag (100)".

G.C. Smith, H.A. Padmore, and C. Norris, Surface Science 119 (1982)
L287-L291

"Photoemission from low-dimensional systems".

C. Binns, C. Norris, G.C. Smith, H.A. Padmore and M.G. Barthes-Labrousse.
Proc. 5th European Conference on Surf. Sci. (ECOSS-5), Gent 1982, To be
published in Surface Science.

To be published:-

"Photoemission from a Cu monolayer on Ag (100): a comparison with time
reversed LEED theory".

G.C. Smith, C. Norris and C. Binns.

"Experimental and theoretical study of Fe and Ni adsorbed on Ag (100)".

G.C. Smith, H.A. Padmore, C. Norris, C. Binns and G.P. Williams.

"Normal photoemission from Pd (111) in the energy range 40 to 120 eV:
comparison with theory".

C. Binns, G.C. Smith, C. Norris, G.P. Williams and M-G. Barthes-Labrousse.

APPENDIX 2Data set for Photoemission Calculations

A typical input data set for the PEOVER photoemission program is presented. The JCL required for running the program on the CRAY-1 computer at Daresbury Laboratory with the operating system in use on 28 July 1982 is shown, together with overlayer and substrate geometries and potentials, and output control information. The data set chosen is that used to generate the normal emission spectrum for one monolayer of copper on silver (100) shown in figure 7.9 using the modified Chodorow copper potential (Chodorow 1939) and the silver potential of Padmore et al (1982). The file is described below:

<u>Line numbers</u>	<u>Data</u>
10 to 320	The CRAY JCL required to run the program. User, job number, output file and various control parameters are specified.
330	The lattice parameter of the crystal in atomic units.
340	The inward surface normal referred to Cartesian axes z, x, y.
350 to 360	Perpendicular vectors to complete the orthogonal coordinate system used in the program.
370 to 380	Two vectors forming the sides of the unit cell of the first layer referred to z, x, y.
390	Displacement of the origin of the next layer into the crystal from the origin of the current layer, relative to the vectors specified in lines 340 to 360.
400	From left to right: Largest l -value in the spherical wave expansion; Order of the rotation axis normal to the surface passing through atomic centres; Maximum number of layers used in calculation of the reflection coefficients for the outgoing electrons. Number of shells in the layer summations.

<u>Line numbers</u>	<u>Data</u>
410	Number of layers used in calculation of reflection coefficients at low energies.
	Number of layers used in calculation of reflection coefficients at high energies.
420	The height of the step potential at the surface in Hartrees.
In this case lines 330 to 360 and 390 to 420 are ignored, as they refer to an overlayer. The values taken are those specified for the substrate.	
430	Atomic number of the atom.
	Muffin tin radius in atomic units.
440	Number of points on which the potential is tabulated.
	First point beyond the muffin tin radius.
	Point beyond which the grid intervals do not increase.
450 to 1240	The grid points (r) and radial potential ($rV(r)$) of the overlayer in Hartrees. The Hermann-Skillman grid is used.
1250	E. Representing end of current data.
1260 to 1350	Repeat of the information contained in lines 330 to 420, now referring to the substrate.
1360	The substrate atomic number and muffin tin radius.
1370	Specification of the substrate potential.
1380 to 2170	The grid points and radial potential of the substrate.
2180	E. End of current data.
2190	E. Indicates the last specified layer repeats throughout the crystal.
2200	End of surface structure and potential data input.
2210	An identifier and heading, printed with any output.
2220	Controls calculation method of the X matrix.
	Controls amount of output.
	Controls method of calculation of electron wavefunctions.
	Controls calculation of Bloch wave vectors.

<u>Line number</u>	<u>Data</u>
	Number of points for which timing information is printed.
	Controls calculation or reading of <u>g</u> -vectors.
	Number of layer types related to previous layer types.
2230	Number of beams used in plane wave representation.
	Hole inverse lifetime (Hartrees).
	Electron inverse lifetime (Hartrees).
	Displacement of the first layer from the surface barrier.
2240	Energy start, increment and finish values (Hartrees).
2250	Photon energy in Hartrees.
	Polar angles in degrees of the emitted electron beam.
	Polar axes in degrees of the incident photon beam.
	Angle in degrees between the <u>A</u> vector of the photon beam and the intersection of the surface with the plane perpendicular to the photon beam containing the <u>A</u> -vector.
2260	Repeat of 2250 with only the changed polarization angle coded.
2280 to 2290	Specify end of data.

```

JOB, JN=QIICASP, US='4100,QII', T=59, M=600.
ASSIGN, DN=DUMMY.
COPYF, J=DUMMY.
DISPOSE (DN=DUMMY, DC=ST, DF=CB, TEXT='DSN=QII. OUTCA. DATA, 'I
, DCB=(RECFM=FB, LRECL=80, BLKSIZE=3120), DISP=(NEW, CATLG), 'I
, SPACE=(TRK,(1,1)), UNIT=3330-I, VOL=SER=DL0295', MF=DL, WAIT)
END.
EXIT.
COPYF (J=INPUT)
REIND (DN=INPUT)
ASSIGN (DN=INPUT, A=FT05)
COPYF (J=FT04)
REIND (DN=FT04)
ASSIGN (DN=FT07)
ACCESS, DN=PHOTO, P DN=PEOVER, ID=GATH.
LDR, DN=ZBLD:PHOTO.
END.
EXIT.
REIND (DN=FT07)
DISPOSE (DN=FT07, DC=ST, DF=CB, TEXT='DSN=QII. OUTCA. DATA, 'I
, DISP=OLD', MF=DL, WAIT)
/EOF
/DATASET IN USE OR JOB FAILED
/EOF

BLOCK DATA
COMMON /ST/ IST(65000)
COMMON /WS/ IWS(55000)
DATA IST(1)/65000/
DATA IWS(1)/55000/
END

/EOF 7.720 0.0 0.0 0.0
1.0 0.0 0.0
0.0 1.0 0.0
0.0 0.0 1.0
0.0 0.0 0.5
0.5 -0.5 0.5
0.5 -0.5 0.0
128 4 4 256 9
0.4700 16
29.00000 81
200.126 81 2.40529
-0.23942E+02
-0.14552E-02
-0.20794E+02
-0.29105E-02
-0.23584E+02
-0.53210E+02
-0.23280E+02
-0.29105E-03
-0.28912E+02
-0.17463E-02
-0.28764E+02
-0.34925E-02
-0.23523E+02
-0.64031E-02
-0.23213E+02
-0.28971E+02
-0.11642E+02
-0.28324E+02
-0.26194E-02
-0.28644E+02
-0.52389E-02
-0.28341E+02
-0.81494E-02
-0.58210E-03
-0.28883E+02
-0.20373E-02
-0.28734E+02
-0.40747E-02
-0.28463E+02
-0.69352E-02
-0.28157E+02
00000010
00000020
00000030
00000040
00000050
00000060
00000070
00000080
00000090
00000100
00000110
00000120
00000130
00000140
00000150
00000160
00000170
00000180
00000190
00000200
00000210
00000220
00000230
00000240
00000250
00000260
00000270
00000280
00000290
00000300
00000310
00000320
00000330
00000340
00000350
00000360
00000370
00000380
00000390
00000400
00000410
00000420
00000430
00000440
00000450
00000460
00000470
00000480
00000490
00000500
00000510
00000520

```


0.33499E+01
 0.0
 0.35362E+01
 0.0
 0.36479E+01
 0.0
 0.37225E+01
 0.0
 0.37087E+01
 0.0
 0.40950E+01
 0.0
 0.42813E+01
 0.0
 0.44675E+01
 0.0
 0.4538E+01
 0.0
 0.46401E+01
 0.0
 0.50263E+01
 0.0
 0.34617E+01
 0.0
 0.36479E+01
 0.0
 0.38342E+01
 0.0
 0.40205E+01
 0.0
 0.42067E+01
 0.0
 0.43930E+01
 0.0
 0.45793E+01
 0.0
 0.47655E+01
 0.0
 0.49518E+01
 0.0
 0.51381E+01
 0.0
 0.33872E+01
 0.0
 0.35734E+01
 0.0
 0.37597E+01
 0.0
 0.39460E+01
 0.0
 0.41322E+01
 0.0
 0.43185E+01
 0.0
 0.45040E+01
 0.0
 0.46910E+01
 0.0
 0.48773E+01
 0.0
 0.50636E+01
 0.0
 0.0
 0.34989E+01
 0.0
 0.36852E+01
 0.0
 0.38715E+01
 0.0
 0.40577E+01
 0.0
 0.42440E+01
 0.0
 0.44303E+01
 0.0
 0.46165E+01
 0.0
 0.48028E+01
 0.0
 0.49891E+01
 0.0
 0.51753E+01
 0.0
 0.34244E+01
 0.0
 0.36107E+01
 0.0
 0.37970E+01
 0.0
 0.39832E+01
 0.0
 0.41695E+01
 0.0
 0.43558E+01
 0.0
 0.45420E+01
 0.0
 0.47283E+01
 0.0
 0.49146E+01
 0.0
 0.51008E+01
 0.0

E 7.720
 1.0 0.0 0.0
 0.0 1.0 0.0
 0.0 0.0 1.0
 0.0 0.5 0.5
 0.0 -0.5 0.0
 0.5 4 256 9 10

200.0
 47.00000 81
 2.72943
 0.47000E+02
 0.51519E+03
 0.46822E+02
 0.13738E+02
 0.46638E+02
 0.27477E+02
 0.46264E+02
 0.44649E+02
 0.45886E+02
 0.72126E+02
 0.45133E+02
 0.10647E+02
 0.44396E+02
 0.16142E+01
 0.42985E+02
 0.23012E+02
 0.41662E+02
 0.34002E+01
 0.39254E+02
 0.47774E+01
 0.17173E+03
 0.46894E+02
 0.10304E+02
 0.46712E+02
 0.20607E+02
 0.46414E+02
 0.37780E+02
 0.46037E+02
 0.58383E+02
 0.45433E+02
 0.92733E+02
 0.46833E+01
 0.43395E+02
 0.43533E+02
 0.20264E+01
 0.28131E+02
 0.42857E+02
 0.40130E+02
 0.42245E+01
 0.37949E+02
 0.46965E+02
 0.68691E+03
 0.46705E+02
 0.15456E+02
 0.46564E+02
 0.30911E+02
 0.46189E+02
 0.48084E+02
 0.45735E+02
 0.78995E+02
 0.44984E+02
 0.11334E+01
 0.44106E+02
 0.17516E+01
 0.42713E+02
 0.24335E+01
 0.41155E+02
 0.36750E+01
 0.38803E+02
 0.50483E+01
 0.34346E+02
 0.46858E+02
 0.12021E+02
 0.46675E+02
 0.44042E+02
 0.46339E+02
 0.41215E+02
 0.45962E+02
 0.45233E+02
 0.99603E+02
 0.44542E+02
 0.44769E+01
 0.43250E+02
 0.21638E+01
 0.41919E+02
 0.31255E+01
 0.39711E+02
 0.44993E+01
 0.37535E+02

00001050
 00001060
 00001070
 00001080
 00001090
 00001100
 00001110
 00001120
 00001130
 00001140
 00001150
 00001160
 00001170
 00001180
 00001190
 00001200
 00001210
 00001220
 00001230
 00001240
 00001250
 00001260
 00001270
 00001280
 00001290
 00001300
 00001310
 00001320
 00001330
 00001340
 00001350
 00001360
 00001370
 00001380
 00001390
 00001400
 00001410
 00001420
 00001430
 00001440
 00001450
 00001460
 00001470
 00001480
 00001490
 00001500
 00001510
 00001520
 00001530
 00001540
 00001550
 00001560
 00001570


```

0.25360E+01 -0.78717E-01 0.26580E+01 -0.67116E-01 0.26800E+01 000021100
-0.56281E-01 0.27020E+01 -0.46212E-01 0.27240E+01 -0.36911E-01 000021120
0.27459E+01 0.0 0.27679E+01 0.0 0.27899E+01 000021130
0.0 0.28119E+01 0.0 0.28339E+01 0.0 000021300
0.23558E+01 0.0 0.23778E+01 0.0 0.28998E+01 000021400
0.0 0.29218E+01 0.0 0.29438E+01 0.0 000021500
0.29657E+01 0.0 0.29877E+01 0.0 0.30097E+01 000021600
0.0 0.30317E+01 0.0 0.30537E+01 0.0 000021700
E /EUF AC 2 CU/AG(100) 21.2EV 0 0 0 000021800
0.01 21 -0.01 0 0 0 000021900
0.7792 0.01 0.01 0.39 -0.10 0 0.37125 000022000
0.0 0.0 0.0 0.0 60.0 0.0 0.0 000022100
E /EOJ 0.0 0.0 0.0 90.0 0.0 0.0 0.0 000022200
0.0 0.0 0.0 0.0 0.0 0.0 0.0 000022300
0.0 0.0 0.0 0.0 0.0 0.0 0.0 000022400
0.0 0.0 0.0 0.0 0.0 0.0 0.0 000022500
0.0 0.0 0.0 0.0 0.0 0.0 0.0 000022600
0.0 0.0 0.0 0.0 0.0 0.0 0.0 000022800
0.0 0.0 0.0 0.0 0.0 0.0 0.0 000022900

```

ABSTRACT

The growth and electronic structure of Fe, Ni, Cu and Pd overlayers on Ag (100), and Pd overlayers on Ag (111) and Cu (100) have been investigated using LEED, Auger electron spectroscopy (AES) and angle resolved photoemission spectroscopy (ARPES). Calculations of the photoemission spectra from the adsorbed overlayers and the clean substrates are reported.

LEED and AES showed that Pd was initially adsorbed on Cu (100) as a $c(2 \times 2)$ surface alloy whereas the other overlayer-substrate combinations formed pseudomorphic monolayers. Pd on Ag (100) and Ag (111) showed continuous layer growth but for Fe and Ni islands were formed after three monolayers and for Cu after two monolayers had been deposited. The differences in growth mode can be understood in terms of a classical theory in which lattice mismatch plays an important role.

ARPES from the clean Cu (100), Ag (100), Ag (111) and Pd (111) surfaces at 21.2 eV photon energy can be interpreted by direct transitions from calculated ground state band structures. For clean Ag (100) and Pd (111) normal emission photoelectron spectra were recorded over the energy region 40 to 120 eV. Spectra were calculated using the time reversed LEED description and good agreement between theory and experiment obtained.

The development of overlayer structure through characteristic phases of different dimensionality was followed using ARPES. At low coverages a single spin-orbit split Pd resonance on Ag (100) occurred, and a similar exchange-split Fe resonance was observed. For Cu and Pd monolayers on Ag (100) the experimental two-dimensional band structures were in fair agreement with calculated isolated monolayer bands. Photoemission calculations reproduced the spectra from these adsorbed monolayers using bulk atomic potentials, particularly good agreement being obtained for the Cu monolayer. ARPES using synchrotron radiation identified the magnetic state of the Fe monolayer on Ag (100) and a valence band exchange splitting of 1.8 to 1.9 eV was inferred. Magnetic ordering in the Ni monolayer on Ag (100) was also indicated. Throughout the study the orientation and lattice expansion imposed on the overlayer by the substrate was shown to have a significant effect on overlayer electronic structure.